SCUOLA DI DOTTORATO
UNIVERSITÀ DEGLI STUDI DI MILANO-BICOCCA

Università degli studi di Milano-Bicocca
Department of Biotechnology and Bioscience

PhD program in Converging Technologies for Bimolecular Systems
Cycle XXXVI

Characterization of the nanocarrier-mediated targeting in a murine model of lung inflammation and fibrosis

Morelli Annalisa

Registration number: 765790

Tutor and supervisor: Dr. Paolo Bigini

Coordinator: Prof. Paola Branduardi

ACADEMIC YEAR 2022/2023

SCUOLA DI DOTTORATO
UNIVERSITÀ DEGLI STUDI DI MILANO-BICOCCA

The research presented in this thesis was performed at the Laboratory of Nanobiology, Department of Biochemistry and Molecular Pharmacology of the Institute of Pharmacological Research Mario Negri under the supervision of Dr. Paolo Bigini.

© 2023 Annalisa Morelli
All rights reserved. No part of this publication may be reproduced, stored in a retrieval system, or transmitted, in any form or by any means, electronically, mechanically, by photocopying, recording or otherwise, without the prior written permission of the author.

ACKNOWLEDGMENTS

I would like to acknowledge and give my deepest gratitude to my supervisor Dr. Paolo Bigini who made this work possible. For the idea of starting this project which allowed me to embrace my career in nanomedicine. His guidance, advice and optimism carried me through all this journey. Thanks for always having kind words and making me believe in my abilities.

I extend my sincere thanks to Prof. Paola Branduardi for accepting me into the XXXVI TeCSBi program. Her great enthusiasm and dedication in organizing all the TeCSBi activities represent a great source of inspiration for my career. Thanks also to my PhD fellows and TeCSBi organizers.

Thanks to Laura and Giulia, for being my PhD mates and best support in Mario Negri, especially during the last steps of this journey, it was not easy, but we did it.

To all my colleagues who have shared this journey with me in these years, Ada, Jennifer, Luca, Mara, Leonardo, Martina C., Rebecca, Anita and Grazia. A special thanks to Giulia and Martina, for their help, moral support and company. Also, I would like to express my gratitude to the entire Department of Biochemistry and Molecular Pharmacology.

To Monica and Sara, my dear friends, for always being there for support in the challenging times, for the kind words, precious advice and shared moments of laughter and smiles have meant a lot to me.

I must thank my parents, Roberta and Fabio, my sister Miriam, and my entire family for their continuous and endless support, for the invaluable advice and for always be there in the moments of need.

To Riccardo, my best friend, confidant and love, you have been my pillar of strength. For always being by my side, offering all the support, for all the advice and for always have the right words in the right moment. I am endlessly grateful for your presence in my life.

COLLABORATIONS

- The evaluation of the clinical impact and the examination of the histopathological sections from the bleomycin animal model used in Chapter 2 and 4, were assessed in collaboration with Dr. Valeria Codullo, Dr. Federica Meloni and Dr. Patrizia Morbini, Department of Internal Medicine, Policlinico San Matteo Foundation, Pavia, Italy and Department of Molecular Medicine, Unit of Pathology, University of Pavia and Foundation IRCCS Policlinico S. Matteo, Pavia, Italy.

- The synthesis and characterization of the ANANAS nanoparticles used in Chapter 3 and 4, were synthesized in collaboration with Prof. Margherita Morpurgo, Dr. Elisa Schiavon, Dr. Simone Bernardotto, Dr. Andrea Mattarei and Dr. Martina Stocco, Department of Pharmaceutical and Pharmacological Sciences, University of Padova, Italy.

- The quantification of Dexamethasone levels in lung and off-target organs by HPLC-MS described in Chapter 3 was carried out in collaboration with Dr. Alice Passoni, Dr. Alessia Lanno and Dr. Renzo Bagnati, Laboratory of Mass Spectometry, Department of Environmental Health Sciences, Istituto di Ricerche Farmacologiche Mario Negri IRCCS, Italy.

- Confocal microscopy analysis in Chapter 3, were in collaboration with Dr. Stefano Fumagalli and Dr. Joe Kelk, Department of Neurosciences, Istituto di Ricerche Farmacologiche Mario Negri IRCCS, Italy.

- The in vitro study on SARS-CoV-2 in Chapter 4, were in collaboration with Dr. Ilaria Frasson, and Dr. Sara Richter, Department of Molecular Medicine (DMM), University of Padova, Italy. Dr. Silvia Faravelli, Dr. Alberta Pinnola, Dr. Anselmo Canciani and Dr. Federico Forneris, The Armenise-Harvard Laboratory of Structural Biology, Department of Biology and Biotechnology, University of Pavia, Italy.

- The toxicity evaluation and cytokines determination performed in Chapter 4, were in collaboration with Dr. Laura Pasetto and Valentina Bonetto, Department of Neuroscience, Istituto di Ricerche Farmacologiche Mario Negri IRCCS, Italy

TABLE OF CONTENTS

ABSTRACT

Lung disorders are becoming a heavy burden for global health both in terms of mortality, morbidity and for the burden for caregivers and increased patient management costs. Among lung pathologies, pulmonary fibroses play a main role on their total incidence. It is interesting to underline that a broad range of clinical disorder, such as tumour, toxicant agent exposure, cardiac impairment, autoimmune diseases, infections, share a common downstream process associated with progressive fibrosis. This common pattern is extremely important in the field of pharmacology because a strategy aimed at delivering anti-inflammatory and/or anti-fibrotic drugs in lungs could strongly reduce the clinical worsening occurring in many different disorders. The clinical progression of fibroses induces parenchymal injury, inflammation and collagen accumulation. Fibrogenesis is a dynamic process characterized by extracellular matrix production, activation of myofibroblasts, and epithelial mesenchymal transition (EMT) induced by inflammatory cytokines. During EMT, the protective layer facilitating oxygen and carbon dioxide exchange gradually diminishes, resulting in respiratory impairment that often leads to patient mortality. Diminishing the signalling associated with cytokine release emerges as one of the primary approaches to impede or at least slow pulmonary dysfunction. One potential target in this regard is modulating the functional expression of activated macrophages, which play a pivotal role in fibrosis by acting as tissue sentinels and producing numerous pro-fibrotic factors. Unfortunately, nearly all therapies commonly employed in clinical practice, especially anti-inflammatory and immune-modulatory agents, have failed in clinical trials due to their low specificity and side effects associated with the spread of these drugs to off-target organs. To overcome this impasse, in my thesis project, I first developed and fully characterized a reliable model of bleomycin-induced acute fibrosis in mice. I systematically compared different fibrogenesis protocols, selecting the one that most closely resembled human pathology in terms of clinical and pathological features. I also examined macrophage responses during the progressive stages of fibrosis. After establishing a reliable model replicating the human disorder, I compared the effects of steroid treatment when administered freely or incorporated into biodegradable and biocompatible nanocarriers. I also evaluated their kinetics depending on the route of administration (systemic or via inhalation).

Parameters such as lung tropism, distribution in other organs, penetration into macrophages, and drug release were carefully investigated. The results demonstrated that the use of nanocarriers via intranasal administration was the optimal approach to reach the target. Finally, I applied this approach to test an innovative method for delivering angiotensin-converting enzyme 2 (ACE2) as a decoy system for preventing SARS-CoV-2 infection. Before conducting in vivo studies, we established the in vitro ability of the nanodecoy to reduce viral infectivity by 80-90% within minutes. In vivo studies confirmed the safety and affinity of these decoys for lung parenchyma and macrophages. Overall, this work represent a starting point for the treatment of lung disorders and pave the way for the next steps: 1) the chronic treatment with nanoassemblies functionalized with corticosteroids for the evaluation of therapeutic efficacy and amelioration of the clinical symptoms in the mouse model and 2) the and determination of *in vivo* efficacy in the prevention of SARS-CoV-2 infection in infected mice. The advancement of nanotechnology-based strategies will provide innovative solutions in the management of major lung diseases that affect millions of people worldwide every year.

ACRONYMS AND ABBREVIATIONS

2,3-DPG	2,3-diphosphoglycerate
α-SMA	Alpha smooth-muscle actin
ACE2	Angiotensin-converting enzyme 2
AECs	Alveolar epithelial cells
AEC1	Alveolar type I cells
AEC2	Alveolar type II cells
AMs	Alveolar macrophages
ANANAS	Avidin-Nucleic Acid Nano ASsemblies
ARDS	Acute respiratory distress syndrome
ATP	Adenosine Triphosphate
BBS	Biotin binding site
BLM	Bleomycin
BPD	Bronchopulmonary dysplasia
BSC	Basal Stem cell
CCL	Chemokine (C-C motif) ligand
CCR	Chemokine receptor
CF	Cystic fibrosis
CME	Clathrin-mediated endocytosis
CO_2	Carbon Dioxide
COL1a1	Collagen 1a1
COPD	Chronic obstructive pulmonary disease
CT	Computed tomography
CTD-ILD	Connective tissue diseases-Interstitial lung disease
DAB	3,3 - Diaminobenzidine
DC	Dendritic cells
DEX	Dexamethasone
DNA	Deoxy ribonucleic acid

ECM	Extracellular matrix
ELISA	Enzyme Linked ImmunoSorbed Assay
EMT	Epithelial-mesenchymal transition
EtOH	Ethanol
EPR	Enhanced permeability and retention
FDA	Food and Drug Administration
FEV1	Forced expiratory volume at one second
FF	Fibroblastic foci
FGF	Fibroblast growth factor
FVC	Forced vital capacity
H^+	Hydrogen ion
HCO_3-	Bicarbonate ion
H_2CO_3	Carbonic acid
H&E	Haematoxylin and eosin
H_2O	Water
H_2O_2	Hydrogen peroxide
HPLC-MS	High-Performance Liquid Chromatography mass spectrometry
IBA1	Ionized calcium-binding adapter molecule 1
IFN-γ	Interferon γ
IGF	Insulin-like growth factor
IL	Interleukin
ILD	Interstitial Lung Disease
IMs	Interstitial macrophages
i.n.	Intranasal administration
iNOS	Inducible nitric oxide synthase
i.p.	Intraperitoneal administration
IPF	Idiopathic pulmonary fibrosis
i.v.	Intravenous administration
LPS	Lipopolysaccharide

MHC-II	Major histocompatibility complex class II
MMP	Matrix metalloproteinase
MPS	Mononuclear phagocyte system
MRI	Magnetic resonance imaging
NK	Natural killer cells
NO	Nitric Oxide
NPs	Nanoparticles
NSCLC	Non-small-cell lung cancer
PAMPs	Pathogen-associated molecular patterns
PBS	Phosphate buffer solution
PBMCs	Peripheral-blood mononuclear cells
PDGF	Platelet-derived growth factor
PEG	Polyethylene glycol
PF	Pulmonary fibrosis
PNEC	Pulmonary neuroendocrine cell
RBD	Receptor-binding domain
RES	Reticuloendothelial system
RNA	Ribonucleic acid
ROS	Reactive oxygen species
RT	Room temperature (25 °C)
RT-PCR	Real time polymerase chain reaction
SARS-CoV-2	Severe Acute Respiratory Syndrome Coronavirus 2
SCLC	Small cell lung carcinoma
SD	Standard deviation
SEM	Standard error mean
TAMs	Tumor associated macrophages
TEM	Transmission electron microscopy
TGF-β	Tumour growth factor β
Th	T helper cells

TIMPs	Tissue inhibitors of metalloproteinases
TLR	Toll-like receptor
TMPRSS2	Transmembrane protease serine 2
TNF-α	Tumour necrosis factor α
UIP	Usual interstitial pneumonia
VEGF	Vascular endothelial growth factor

CHAPTER 1

Introduction

1.1 The Respiratory System

The human lungs pump vital oxygen through airways and into the bloodstream every second of every day. Without this ability, humans could not survive on Earth. The respiratory system is the network of organs and tissues that provides the fundamental ability to breathe. The circulatory system, which is made up of the heart and blood vessels, supports the respiratory system by bringing blood to and from the lungs. It helps deliver nutrients and oxygen from the lungs to tissues and organs throughout the body. These parts work together to move oxygen and clean out waste gases like carbon dioxide. These actions encompass not only muscular movements but also cellular and chemical processes.

The respiratory system consists of two divisions: upper airways and lower airways. The transition between these two divisions is located where the pathways of the respiratory and digestive systems cross, just at the top of the larynx (or voice box). The upper airway system comprises the nose and the paranasal cavities (or sinuses), the pharynx (or throat), and the larynx. The lower airway system is further divided into the proximal (trachea, bronchi and bronchioles) and distal airway (respiratory bronchioles and alveoli). All the airways branch extensively within the lungs (Figure 1.1).[1]

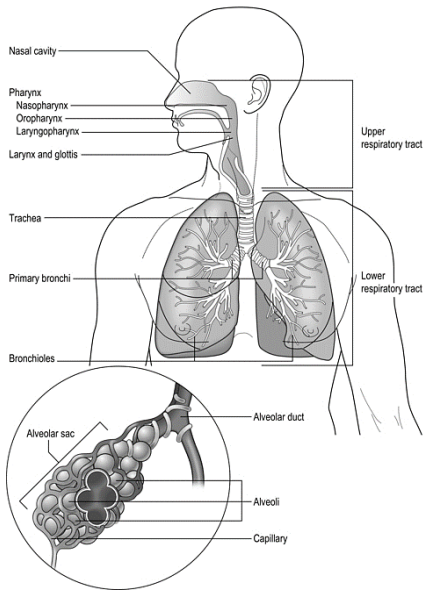

Figure 1.1 Schematic diagram of the respiratory system. Image source: clinicalgate.com

1.1.1 Morphology of the Upper Airways

The upper airways, including the nose, sinuses, pharynx, and larynx, play a crucial role in filtering and warming the air that enters the respiratory tract. This process is essential for removing dust and debris from inhaled air, safeguarding the lungs from potentially infectious foreign agents.[1]

1.1.1.1 The Nose

The nose is the external protuberance of an internal space, the nasal cavity. The external nose is a visible pyramidal structure, situated in the midface, with its base on the facial skeleton and its apex projecting anterior. The inferior surface of the nose is pierced by two piriform openings, the nares (nostrils, anterior nasal apertures), which are bound laterally by the alae of the nose. The superior bony part of the nose, including its root, is covered by thin skin.[2] The nasal structure consists of paired nasal bones forming the upper part of the external nose and paired cartilage forming the lower part. It connects the external environment through the vestibule, divided into left and right canals by the nasal septum. Each canal opens through a nostril on the face and into the pharynx via the choana. These nasal spaces connect with air-filled cavities in the skull called paranasal sinuses, which are present in the maxilla, frontal, ethmoid, and sphenoid bones. Additionally, they connect with the lacrimal apparatus in the eye's corner through the nasolacrimal duct (Figure 1.2). Sinus cavities in the skull have two main functions: they help maintain a manageable weight for the head due to their air-filled nature, and they function as resonance chambers for the human voice.[1,3]

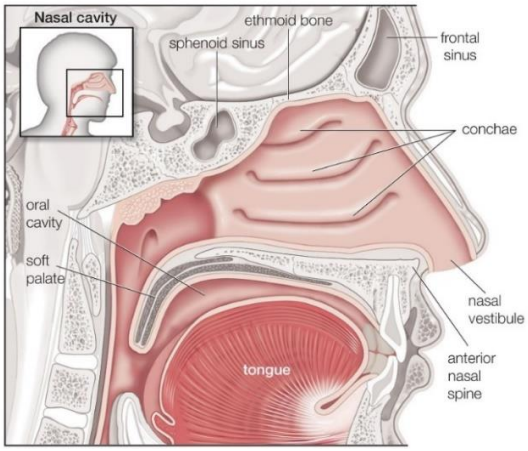

Figure 1.2 Sagittal view of the human nasal cavity. Image source: Encyclopædia Britannica, Inc. 2012

The nasal lining has a mucosal epithelial layer with an underlying submucosal layer. The respiratory mucosa consists of pseudostratified columnar epithelium containing goblet cells, ciliated and nonciliated columnar cells with microvilli, and, occasionally, intraepithelial mast cells, eosinophils, and lymphocytes.[4] They clean, moisten, and warm the inspired air, preparing it for intimate contact with the delicate tissues of the gas-exchange area. During expiration through the nose, the air is dried and cooled, a process that saves water and energy. Two regions of the nasal cavity have a different lining. The vestibule, at the entrance of the nose, is lined with stratified squamous epithelium that bears short thick hairs called vibrissae. In the roof of the nose, the olfactory organ with its sensory epithelium checks the quality of the inspired air. About two dozen olfactory nerves convey the sensation of smell from the olfactory cells through the bony roof of the nasal cavity to the central nervous system.[1,3]

1.1.1.2 The Pharynx

The pharynx is the superior expanded part of the alimentary system posterior to the nasal and oral cavities, extending inferiorly past the larynx. The pharynx extends from the cranial base to the inferior border of the cricoid cartilage anteriorly and the inferior border of the C6 vertebra posteriorly. The pharynx is widest (approximately 5 cm) opposite the hyoid and narrowest (approximately 1.5 cm) at its inferior end, where it is

continuous with the esophagus. The flat posterior wall of the pharynx lies against the prevertebral layer of deep cervical fascia.

The pharynx is divided into three parts (Figure 1.3):

• Nasopharynx: posterior to the nose and superior to the soft palate. The nasopharynx has a respiratory function. The nose opens into the nasopharynx through two choanae (paired openings between the nasal cavity and the nasopharynx). The roof and posterior wall of the nasopharynx form a continuous surface that lies inferior to the body of the sphenoid bone and the basilar part of the occipital bone. In the posterior wall of the nasopharynx is located a lymphatic organ, the pharyngeal tonsil.[1,2]

• Oropharynx: posterior to the mouth. The oropharynx has a digestive function, in particular in the compless process of deglutition. It is bounded by the soft palate superiorly, the base of the tongue inferiorly, and the palatoglossal and palatopharyngeal arches laterally. It extends from the soft palate to the superior border of the epiglottis. The palatine tonsils are collections of lymphoid tissue on each side of the oropharynx in the interval between the palatine arches.[2]

• Laryngopharynx: posterior to the larynx, extending from the superior border of the epiglottis and the pharyngo-epiglottic folds to the inferior border of the cricoid cartilage, where it narrows and becomes continuous with the esophagus. Its posterior and lateral walls are formed by the middle and inferior pharyngeal constrictor muscles. Internally, the wall is formed by the palatopharyngeus and stylopharyngeus muscles. The laryngopharynx communicates with the larynx through the laryngeal inlet on its anterior wall.[2] It represents the site where the pathways of air and food cross each other: air from the nasal cavity flows into the larynx, and food from the oral cavity is routed to the esophagus directly behind the larynx. The epiglottis, a cartilaginous, leaf-shaped flap, functions as a lid to the larynx and, during the act of swallowing, controls the traffic of air and food.[1]

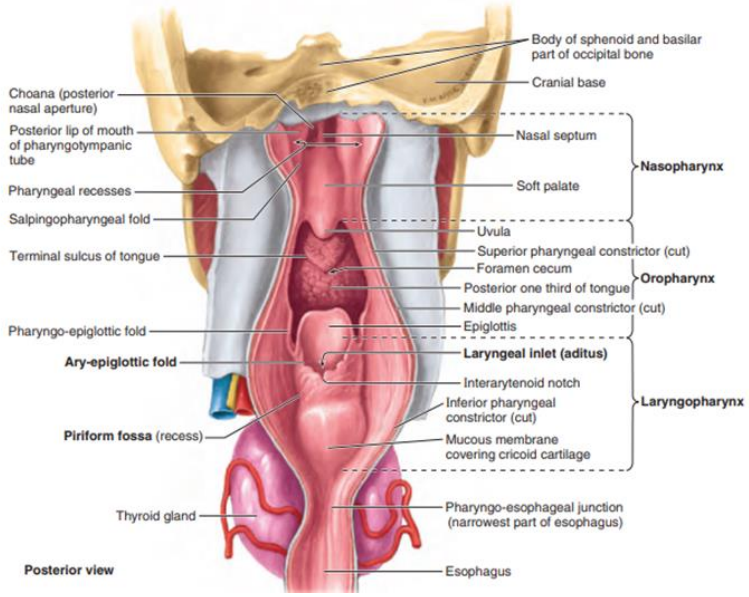

Figure 1.3 Anterior wall of pharynx. Image source: Moore, Clinically oriented anatomy. 2014

1.1.1.3 The Larynx

The larynx is a complex organ located in the front of the neck, above the trachea and below the pharynx. It has dual functions, serving as a pathway for air to reach the lungs and as the organ responsible for producing sound. The larynx is made up of nine cartilages connected by membranes and ligaments, including four major cartilages (thyroid, cricoid, paired arytenoids, and epiglottis) and three sets of minor cartilages (cuneiform, corniculate, and triticeal) (Figure 1.4).[2] The major cartilages provide structural support, while the minor cartilages allow flexibility for protecting the airway during swallowing. The hyoid bone, although not technically part of the larynx, is involved in muscular attachments. The vocal cords, located behind the thyroid cartilage, span the laryngeal lumen and are connected to the arytenoid cartilages. The vocal cords are elastic ligaments that can change shape, length, and tension. The epiglottis is attached to the back of the thyroid cartilage and helps protect the airway. The cricoid cartilage, situated below the thyroid cartilage, has a signet-ring shape and is joined to the thyroid cartilage through ligaments.[5] The laryngeal muscles can be classified into two groups: intrinsic muscles, which directly or indirectly affect the shape and tension of the vocal

cords, and extrinsic muscles, which move the entire larynx up or down. The intrinsic muscles are attached to the skeletal components of the larynx, while the extrinsic muscles connect the laryngeal skeleton to the hyoid bone, pharynx, and sternum.[1]

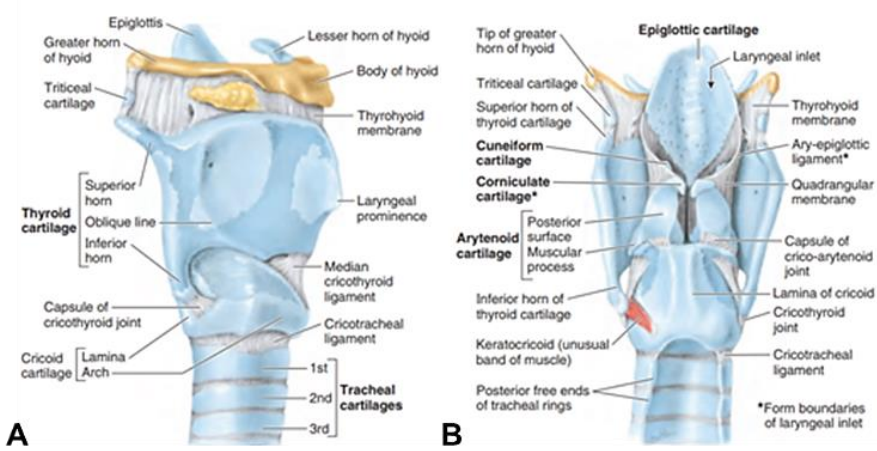

Figure 1.4 Skeleton of larynx. A) Right lateral view. B) Posterior view. Image source: Moore, Clinically oriented anatomy. 2014

1.1.2 Morphology of the Lower Airways

The major structures of the lower airways include trachea, the stem bronchi, and all the airways and lungs. The first two of these provide a canal for the passage of air to the lungs, while the lungs themselves receive the air and facilitate the process of gas exchange.

1.1.2.1 The Trachea and the airway tree

The sub-laryngeal airway constitutes the tracheobronchial tree. The trachea, extending from the larynx into the thorax, terminates inferiorly as it divides into right and left main bronchi, one each for the left and right lung passing inferolaterally to enter at the hila. It transports air to and from the lungs, and its epithelium propels debris-laden mucus toward the pharynx for expulsion from the mouth. The trachea is a fibrocartilaginous tube, supported by incomplete cartilaginous tracheal cartilages (rings), that open toward the back and are embedded in a dense connective tissue occupying a median position in

the neck.[6] The dorsal wall contains a strong layer of transverse smooth muscle fibres that spans the gap of the cartilage. At its lower end, the right main bronchus has a larger diameter, is oriented more vertically, and is shorter than the left main bronchus. The structure of the stem bronchi closely matches that of the trachea (Figure 1.5). The interior of the trachea is lined by the typical respiratory epithelium. The mucosal layer contains mucous glands.[1,2]

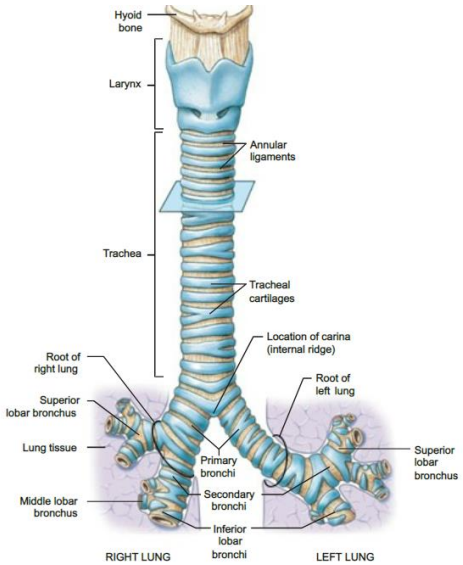

Figure 1.5 Anterior view of the anatomy of the trachea and primary bronchi. Image source: Pearson education. 2015

Functionally, the intrapulmonary airway system can be subdivided into three zones: a proximal, conducting zone; a terminal, gas-exchanging zone; and a transitional zone in between, where both functions grade into one another. Just below the level of the aortic arch, the tracheal carina marks the bifurcation of the right and left main bronchi. Within the lungs, the bronchi branch in a constant fashion to form the branches of the tracheobronchial tree. The branches of the tracheobronchial tree are components of the root of each lung (consisting of branches of the pulmonary artery and veins as well as the bronchi). Each main primary bronchus divides into secondary lobar bronchi, two on the left and three on the right, each of which supplies a lobe of the lung. Each lobar bronchus divides into several tertiary segmental bronchi that supply the

bronchopulmonary segments. Beyond the tertiary segmental bronchi, there are 20 to 25 generations of branching conducting bronchioles that eventually end as distal bronchioles, the smallest conducting bronchioles.[2] A bronchus becomes a membranous bronchiole when cartilage completely disappears from its wall. This occurs when the diameter of the airway decreases to about 1 mm. The terminal membranous bronchiole leads into the acinus, the functional unit of the lung, which consists of the respiratory bronchiole, alveolar ducts, alveolar sac, and grape-like clusters of alveoli. Each respiratory bronchiole gives rise to 2-11 alveolar ducts, each of which gives rise to 5-6 alveolar sacs, sorrounded by four or more alveoli formed by multifaceted and cup-shaped compartments with diameters of 150 to 500 µm. The orifices of alveoli along the alveolar ducts and alveolar sacs are formed by thick elastic and collagen bundles that are the continuum of bronchial and bronchiolar elastic bundles. In the alveoli, the respiratory epithelium gives way to a particularly flat lining layer that permits the formation of a thin air–blood barrier (Figure 1.6).[7]

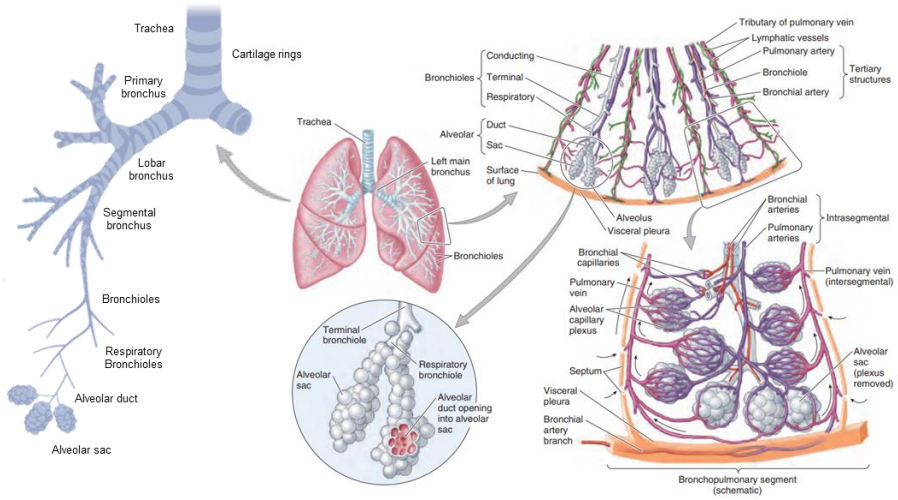

Figure 1.6 Internal structure and organization of the tracheobronchial tree. Image source: Moore, Clinically oriented anatomy. 2014

1.1.2.2 The Lung

Humans have two lung organs, a right and a left, which are located in the thoracic cavity and are responsible for adding oxygen to and removing carbon dioxide from the blood.

The thoracic cavity is divided into three compartments: right and left pulmonary cavities, bilateral compartments that contain the lungs and pleurae (lining membranes) occupying the majority of the thoracic cavity, and the mediastinum, a compartment between the two pulmonary cavities, which contains essentially all other thoracic structures (the heart, thoracic parts of the great vessels, thoracic part of the trachea, esophagus, thymus and lymphonodes). Each lung is connected with the trachea by its main bronchus, with the heart by the pulmonary arteries and bordered inferiorly by the diaphragm, dome-shaped muscle plate that separates thoracic and abdominal cavities.[1,2]

Each pulmonary cavity is lined by a pleural membrane (pleura) that also reflects onto and covers the external surface of the lungs occupying the cavities. The pleura is a membrane of fibrous tissue containing a single layer of mesothelium. It aligns the interior of the thoracic cavity and is arranged into two layers, parietal and visceral, that are continuous at the hilum of the lung via the pulmonary ligament. Depending on the subjacent structures, the parietal pleura can be subdivided into three portions: mediastinal, costal, and diaphragmatic pleurae. The pulmonary ligament hangs inferiorly from the hilum of each lung as a double fold of pleura and creates an empty space that allows for the expansion of vessels in the lung hilum as the diaphragm descends with inspiration. The pleural space contains a small amount of serous fluid between its outer parietal and inner visceral layers to maintain apposition during respiration (Figure 1.7).[8]

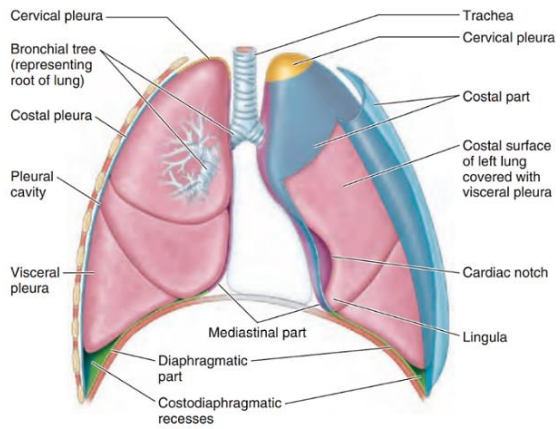

Figure 1.7 Divisions of thoracic cavity and lining of pulmonary cavities. Image source: Moore, Clinically oriented anatomy. 2014

Lungs fully occupy the pulmonary cavities and each lung has: an apex, the blunt superior end of the lung ascending above the level of the first rib into the root of the neck, a base, the concave inferior surface of the lung, opposite the apex, resting on the diaphragm, two or three lobes, created by one or two fissures, three surfaces (costal, mediastinal, and diaphragmatic) and three borders (anterior, inferior, and posterior).[2] The right lung is divided into three lobes (upper, middle, and lower) that are demarcated from one another by a diagonal (major) fissure that separates the lower from the upper and middle lobes, and a horizontal (minor) fissure that separates the middle from the upper lobe. The left lung is composed of an upper and lower lobe separated by a single oblique fissure and features a marked cardiac notch in its anterior border owing to the asymmetrical placement of the heart. The lingula, which represents the anterior-inferior division of the left upper lobe, overrides the left cardiac ventricle, and is the counterpart of the right middle lobe.[7] The lung lobes are subdivided into smaller units, the pulmonary segments. There are 10 segments in the right lung and 8 to 10 segments in the left lung, depending on the classification. Unlike the lobes, the pulmonary segments are not delimited from each other by fissures but by thin membranes of connective tissue containing veins and lymphatics (Figure 1.8).[1] The general name for the functional tissue of the lungs is parenchyma. The vast majority of the volume is alveolar tissue surrounding air spaces.[9]

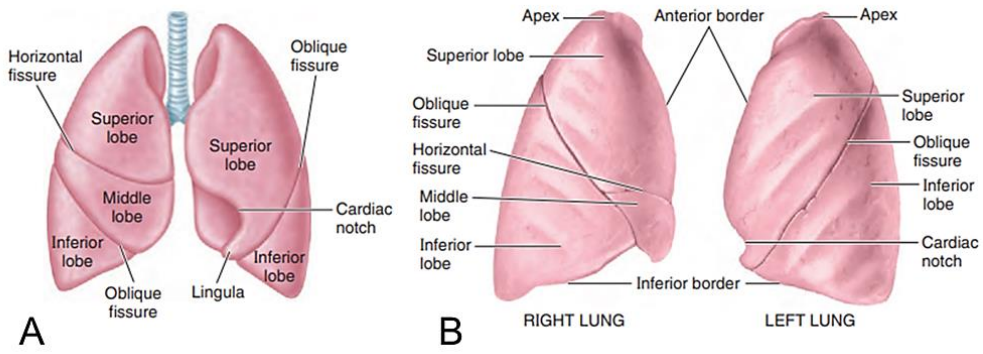

Figure 1.8 A) Anterior view and **B)** lateral views of the lobes and fissures of the lungs. Image source: Moore, Clinically oriented anatomy. 2014

The lung has two distinct but not completely separate vascular systems: a low-pressure pulmonary system and a high-pressure bronchial system. The pulmonary (or lesser) circulation is responsible for the oxygen supply of the organism. Blood, low in oxygen content but laden with carbon dioxide, is carried from the right heart through the pulmonary arteries to the lungs. The pulmonary trunk arises from the right ventricle and quickly divides into left and right main pulmonary arteries, which further divide into lobar arteries.[7] On each side, the pulmonary artery enters the lung with the stem bronchus and then divides rapidly, branching simultaneously and running parallel courses following the airway tree with a similar diameter at each level.[10] After numerous divisions, small arteries accompany the alveolar ducts and split up into the alveolar capillary networks. The oxygenated blood from the capillaries is collected by venules and drained into small veins. These do not accompany the airways and arteries but run separately in narrow strips of connective tissue delimiting small lobules. The interlobular veins then converge on the intersegmental septa. Finally, near the hilum the veins merge into large venous vessels that follow the course of the bronchi.[1] Two pulmonary veins, a superior and an inferior pulmonary vein on each side, carry oxygen-rich blood from corresponding lobes of each lung to the left atrium of the heart. The pulmonary veins run independently of the arteries and bronchi in the lung, coursing between and receiving blood from adjacent bronchopulmonary segments as they run toward the hilum.[2]

The bronchial circulation has a nutritional function for the walls of the larger airways and pulmonary vessels, making up the root of the lungs, the supporting tissues of the lungs, and the visceral pleura. The two left bronchial arteries and the right bronchial artery originate from the aorta or from an intercostal artery. They split up into capillaries surrounding the walls of bronchi and vessels and also supply adjacent airspaces. Most of their blood is naturally collected by pulmonary veins.[1] The most distal branches of the bronchial arteries anastomose with branches of the pulmonary arteries in the walls of the bronchioles and in the visceral pleura (Figure 1.9).[2]

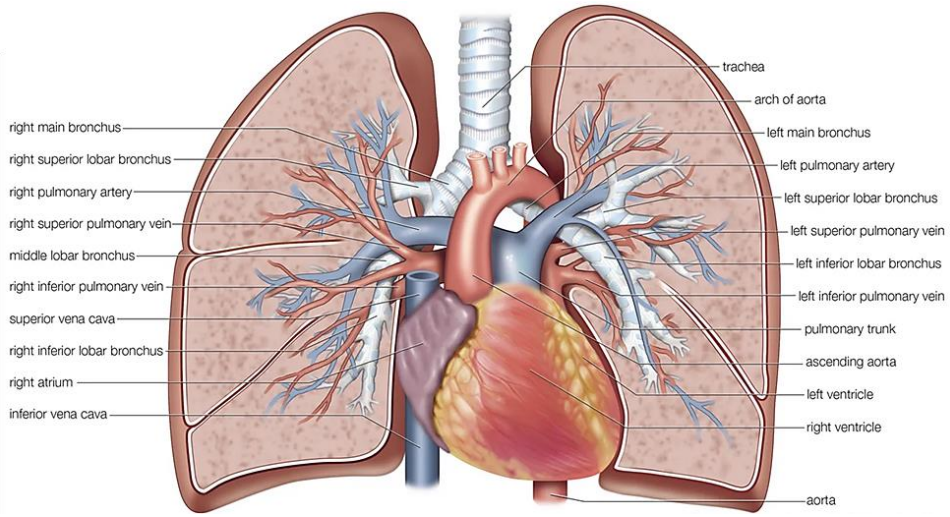

Figure 1.9 The vasculature of the lung. Image source: Encyclopædia Britannica, Inc. 2010

1.1.2.3 Pulmonary gas exchange

The gas-exchange tissue proper is called the pulmonary parenchyma, while the supplying structures, conductive airways, lymphatics, and non-capillary blood vessels belong to the non-parenchyma. The gas-exchange region begins with the alveoli of the first generation of respiratory bronchioles. The lungs are a collection of some 300 million small gas-filled alveoli, comprising a surface area of 130 m^2,[11] the walls of which are made up of little more than a rich capillary network supported by a very thin interstitial matrix. Each alveolus expands with fresh gas (high in O_2 and low in CO_2) that has flowed down the bronchial tree from the mouth during inspiration. The alveoli then reduce in volume during expiration, returning gas (lower in O_2 and higher in CO_2) up the bronchial tree to the mouth in a process called ventilation.[12] Gas exchange between the alveolar gas and blood takes place largely across the alveolar epithelium and pulmonary capillary bed after which the blood flows into venules, which are almost indistinguishable in structure from arterioles,[10] and it occurs by simple passive diffusion. There is no active transport involved in alveolar gas exchange, and the process of diffusion requires no energy expenditure by the organism (Figure 1.10).

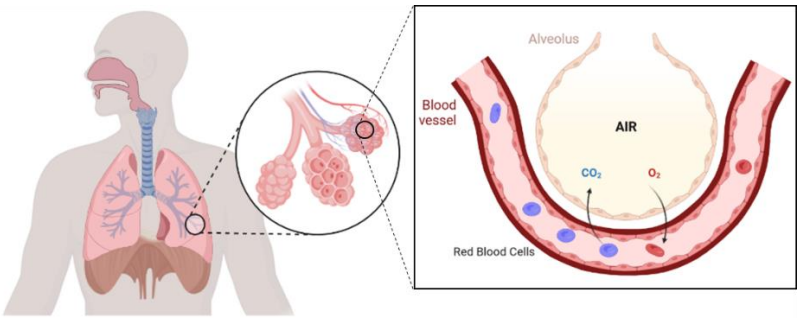

Figure 1.10 Schematic representation of the O_2/CO_2 transport pathway.

Pulmonary gas exchange is considered as a continuous process involving ventilation, diffusion (physical diffusion across the pulmonary barrier and subsequent chemical reactions (between O_2 and hemoglobin, a protein contained within red cells, and for carbon dioxide (CO_2) conversion to bicarbonate) and perfusion.[12] Hemoglobin is composed of four iron-containing ring structures (hemes) chemically bonded to a large protein (globin). Each iron atom can bind and then release an oxygen molecule. Hemoglobin binds not only to oxygen but to other substances as well, including hydrogen ions (which determine the pH of the blood), carbon dioxide, and 2,3-diphosphoglycerate (2,3-DPG; a salt in the red blood cells that plays a role in liberating oxygen from hemoglobin in the peripheral circulation). Transport of CO_2 in the blood is considerably more complex. A small portion of carbon dioxide, (about 5%), remains unchanged and is transported dissolved in blood. Some carbon dioxide binds to blood proteins, principally hemoglobin, to form a compound known as carbamate. About 88% of carbon dioxide in the blood is in the form of bicarbonate ion. Less than 10% of the total quantity of carbon dioxide carried in the blood is eliminated during passage through the lungs. Complete elimination would lead to large changes in acidity between arterial and venous blood. As carbon dioxide enters the blood, it combines with water to form carbonic acid (H_2CO_3), a relatively weak acid, which dissociates into hydrogen ions (H^+) and bicarbonate ions (HCO_3-). The change in molecular configuration of hemoglobin that accompanies the release of oxygen leads to increased binding of carbon dioxide to oxylabile amino groups. Thus, release of oxygen in body tissues enhances binding of

carbon dioxide as carbamate. Oxygenation of hemoglobin in the lungs has the reverse effect and leads to carbon dioxide elimination.[1]

1.1.2.4 Pulmonary epithelium

Cellular activity of viable tissue allows physiologic functioning of mammalian organ systems that are incredibly complex, responsive, interactive, and adaptable; collectively, multiple systems support a complex organism's life. To accomplish successful respiration, the respiratory tract uses approximately 40 different resident cell types and their products to make this occur.[13] The respiratory system in its totality is composed of multiple branched tissue systems, including the airways and blood vessels, and is lined with epithelial cells.

The larger airways of the respiratory system, including the trachea, are underlaid with bands of smooth muscle and in larger mammals, cartilaginous rings, both of which provide support and tone to airway flow. The branched structure of the airways is paralleled by the pulmonary vasculature, which eventually intersects with cells in the alveolus to form the gas diffusible interface.[14]

- **Airway Epithelium**

Airway epithelial cells line the conducting airways of the trachea and proximal airways (bronchi and bronchioles) in humans as well as in the mouse and consist of a pseudostratified respiratory epithelium, which contains multiple cell lineages, including multiciliated cells, secretory cells, goblet cells and basal stem/progenitor cells (BSCs). Each is functionally specialized to moisturize the air, clear inhaled particles, serve as progenitors in repair, or sense aerosolized signals creating a mucosal barrier to pathogens.[15]

Basal cells. Epithelial cells that underline luminal cells. They serves as progenitors for other airway epithelial cells in homeostasis and repair and are defined by the expression of transformation-related protein (TP63) and cytokeratins 5 and 14 (KRT5/14).[16] These cells reside in the basal layer of airway epithelium and aside from trachea and extrapulmonary bronchi, basal cells are also found in the intrapulmonary airways, with diminishing number toward respiratory bronchioles (in mouse are rare in

intrapulmonary airways that are without cartilage). These cells can be involved in chronic obstructive pulmonary disease (COPD) and can serve as precursors for non-small-cell lung cancer (NSCLC).[15]

 **Secretory Club cells (Clara cells).** Columnar or cuboidal luminal epithelial cells that contain secretory granules. They are located in the luminal layer of airway epithelium expressing SCGB1A1 as marker.[15] These cells have been shown to secrete surfactant apoprotein (secretoglobins) into airway lumen to decrease the surface tension in this area of the lung and prevent alveolar collapse. Club cells also serves as the reserve and reparatory cell in the small airways.[7] In diseases, such as asthma and COPD they can produce mucin.

 **Ciliated cells.** Multi-ciliated cells that display multiple motile cilia on the apical surface. They are located in the luminal layer of airway epithelium expressing FOXJ1 and acetylated tubulin as markers.[15] The main function is to reject and clear foreign particles via the mucociliary clearence mechanism.[7] Disruption of ciliated cell function is observed in primary ciliary dyskinesia, COPD, cystic fibrosis (CF) and asthma.

 **Goblet cells.** Most common non-ciliated cells that contain mucus granules in the apical region. They are located in the luminal layer of airway epithelium from the larger to the smaller bronchi but absent in the bronchioles (rare in mouse). The main protein markers are MUC5AC and AGR2.[15] These cells secrete mucus (acidic glycosaminoglycans) to the luminal surface by the fusion of the membranes of the granules and the cell to trap inhaled particles. Together with ciliated cells, they facilitate effective mucociliary clearence. Excessive goblet cells hyperplasia can disrupt the continuity of ciliary flow which is a key feature of many airway diseases (COPD, asthma and CF).[7]

 **Pulmonary neuroendocrine cells (PNECs).** Rare airway and tracheal epithelial cells with dense core vescicles that contain neuropeptides and neurotransmitters. Present either as solitary cells or in clusters in neuroepithelial bodies (NEBs), they express GRP^{H} and $CGRP^{M}$ as markers. Solitary cells are spindle-like in morphology while clustered cells are wedge-like in morphology with wider apical than basal surface. These cells act as airway sensor; when stimulated by signals such as allergen, nicotin and mechanical

stretch they secrete neuropeptides and neurotransmitters wich is a key feature of the allergen induced asthmatic response.[15]

In the airway epithelium, are also identified other rare cells: Tuft cells, spindle-shaped cells presenting microvilli on the apical surface that have a chemosensory function, Ionocytes, columnar epithelial cells involved in maintaining the airway fluid balance, and Bronchioalveolar stem cells, cuboidal epithelial cells that act as progenitor cells to both airway and alveolar cells during repair.[15]

- **Alveolar Epithelium**

Alveolar epithelial cells (AECs) line the alveoli of the distal airways. There are two types of alveolar lining cells: Alveolar type I cells, that constitute 95% of the surface area and 40% of the alveolar cells, and Alveolar type II cells that covers only 5% of the alveolar surface and constitute 60% of the cells. Together they perform the core function of gas exchange.[7,15]

 **Alveolar type I (AEC1) cells.** Large and squamous flattened epithelial cells localized in the alveoli and expressing AGER and HOPX as protein markers. These cells are essential for oxygen-carbon dioxide exchange by forming large and thin gas-diffusible interface in proximity to capillary endothelium. AEC1 cells are reduced in number and function in COPD and Bronchopulmonary dysplasia (BPD).[15]

 **Alveolar type II (AEC2) cells.** Cuboidal alveolar epithelial cells with lamellar bodies and specialized microvilli in the apical surface, localized in the alveoli and expressing SFTPC and ABCA3 as protein markers. AEC2 cells produce surfactant, a glycoproteins and phospholipids (dipalmitoyl lecithin) mixture that reduces surface tension to allow lung expansion during inhalation and promotes host defense by assisting the killing of pathogens.[15] These cells can act also as reserve cells, maturing into type I cells. Surfactant deficiencies leads to respiratory distress syndrome and AEC2 dysfunction and senescence are associated with pulmonary fibrosis[17] and NSCLC.[7]

In summary, the entire respiratory tract, which is lined with polarized airway epithelium (apical side facing air/lumen, basolateral side facing the internal milieu), is structurally

diverse and fulfills multiple functions, depending on the anatomical location. Pseudostratified ciliated columnar epithelium continues throughout the pharynx, larynx, trachea, all bronchi, and larger bronchioles. Moving further down the respiratory tree, the epithelium changes to simple cuboidal epithelium with an increased number of club cells. In contrast, goblet cells become increasingly less frequent until they can no longer be found in the alveoli, mainly composed of AEC1 and AEC2 cells. While the proximal conducting airways function as a gas transport system and barrier to pathogens, alveoli of the distal airway facilitate air exchange and respiration. Additionally, cells of the immune system (e.g., macrophages) are present to eliminate the intruding pathogen (Figure 1.11).[18,19]

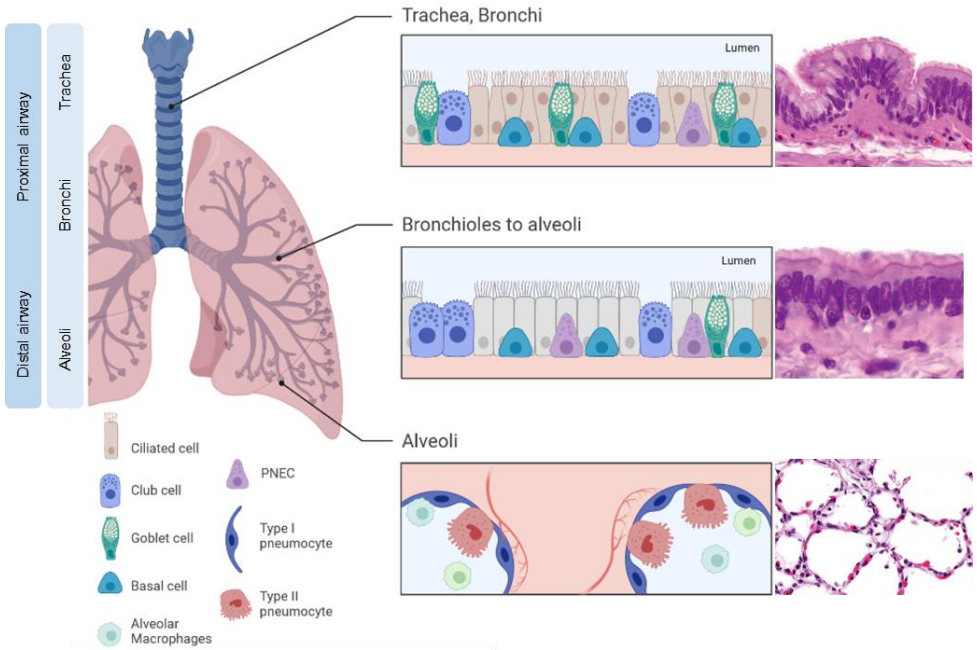

Figure 1.11 Organization and cellular characteristics of the human respiratory airway. Image source: Biorender - Human Histology - A Text and Atlas for Physicians and Scientists, 2023.

1.1.2.5 Other cell types in the lung microenvironment

In addition to epithelial cells, other important cell lineages are found in the lung parenchyma. In particular mesenchymal and immune cells play a fundamental role in physiological conditions but are often involved in important pulmonary diseases.

- **Mesenchyme**

Starting from early development, the lung mesenchyme provides instructive cues to the epithelium to control proliferation, differentiation, and patterning along the proximal-distal axis. Reciprocal paracrine signaling between the mesenchyme and epithelium coordinates the growth and differentiation of both cell populations. In the adult lung, several mesenchymal cell types serve as niches and provide signals and extracellular matrix (ECM) support for epithelial progenitors and their function in tissue regeneration.[15]

The main mesenchymal cells found in lung parenchyma: Airway smooth muscle cells (ASMCs), Vascular smooth muscle cells (VSMCs), Chondrocytes, Alveolar fibroblast 1 (AF1) cells, Alveolar fibroblast 2 (AF2) cells, Secondary Crest Myofibroblasts (SCMF), Pericytes and Mesothelial cells.[15]

Resident mesenchymal cells of the lung, including resident fibroblasts, pericytes, and resident mesenchymal stem cells, appear to be important sources of activated scar-forming cells called myofibroblasts in murine models of lung injury and fibrosis. Myofibroblasts contribute to tissue repair during wound healing, but that can severely impair organ function when contraction and ECM protein secretion become excessive.[20]

- **Immune Cells**

Cells of the immune system are also critical components of the lung with innate immune cell types taking up residence early in development. The lung constitutes the largest surface of the body that is exposed to the outside environment. Pathogens can enter the lung either with inhaled air through the epithelial layer or via bloodstream through the endothelium. The cells involved are both resident immune cell types in the lung interstitium and circulating immune cell types in the lung vasculature, ready to be recruited in response to infection or injury. Lung immune cells belong to either the innate or adaptive immune systems. In addition to defense against infection or injury, immune cells also play critical roles in tissue homeostasis.[15]

 **Alveolar macrophages (AMs).** Largest immune cells in lung, cytoplasm filled with lipid from surfactant localized in the luminal surface of alveoli in close proximity

to epithelial cells. They express CD45, CD11b, CD64, CD163, CD206, HLA-DR as protein markers.[15] These cells have important roles in surfactant turnover, phagocytosis of inhaled pathogens and particles. AMs inhabit a unique position at the interface between the pulmonary mucosa and the external environment, where they directly sense immunological stimuli and perform a crucial role in maintaining immune tolerance.[21] They participate in the onset of several lung diseases (infection, fibrosis, asthma, COPD and lung cancer) and are crucial for maintaining airway homeostasis.[22]

Interstitial macrophages (IMs). Smaller in size than AMs, with smoother surface, irregularly shaped nucleus and numerous cytoplasmic vacuoles, this cells are localized in the lung interstitium around airways, vessels, and nerves.[15] They express MerTK, CD11b, CD64, MHC II, and CD206 as protein markers.[21] IMs have a regulatory function. These cells have high levels of expression of genes related to the positive regulation of leukocyte chemotaxis, response to wounding and receptor-mediated endocytosis acting as key factors in presenting antigens and inducing adaptive immunity.[23]

AMs and IMs are tissue resident macrophages fulfilling the homeostatic, metabolic and repair functions while simultaneously acting as sentinel phagocytic immune cells. Since these cells have significant protective roles, they are involved in important lung disorders.

In the lung parenchyma, are also identified other important immune cells: Inflammatory monocytes (iMONs), Patrolling monocytes (pMONs), Dendritic Cells (DCs), Neutrophils, Basophils, Mast Cells, Innate lymphoid cells (ILCs), Natural Killer cells (NK cells), T cells and B cells.[15]

1.2 Macrophages role in immune system

Metchnikoff first described macrophages in 1892 on the basis of their ability to phagocytose microorganisms. These cells are a component of the primary innate immune

response playing a critical role against foreign pathogens and cellular debris.[22] They are found in various tissues throughout the body and are involved in a range of physiological processes, including tissue repair, regulation of immune responses, and maintenance of homeostasis. Macrophages are highly heterogeneous and can adopt a range of functional phenotypes depending on their local microenvironment.[24]

The origin and development of macrophages is complex, with different populations arising from different sources, including embryonic yolk sac, fetal liver, and bone marrow-derived precursors.[24] Circulating peripheral-blood mononuclear cells (PBMCs) that develop from a common myeloid progenitor cells in the bone marrow differentiate into monocytes that are released into the bloodstream. Monocytes are a heterogeneous population that continue to develop and mature in the blood and finally migrate into different tissues in the steady state or in response to inflammation where they can differentiate in tissue-specific macrophages (osteoclasts (bone), alveolar macrophages (lung), histiocytes (interstitial connective tissue) and Kupffer cells (liver)).[24,25]

Macrophages are characterized by their phagocytic activity, as well as their capacity to produce cytokines and chemokines in response to endogenous stimuli. Upon activation, macrophages can polarize into distinct functional phenotypes, which have distinct gene expression profiles and functions.

1.2.1 Polarization of macrophages

The current macrophage nomenclature is complex due to the macrophage functional plasticity mediated by microenvironment signals. The two main functionally polarized macrophage subsets, named according to external stimuli and cytokine profile that they deliver, are: classically activated macrophages (M1 macrophages) and alternatively activated macrophages (M2 macrophages). This paradigm oversimplify the pattern of macrophages because they can exhibit overlapping and mixed functional phenotypes depending on their local microenvironment.[25,26]

- **Classically activated macrophages (M1)**

M1 macrophages, also known as classically activated macrophages, are induced by the pro-inflammatory cytokines interferon-gamma (IFN-γ), tumor necrosis factor alpha

(TNF-α) and lipopolysaccharide (LPS), a component of the outer membrane of Gram-negative bacteria. These macrophages produce high levels of pro-inflammatory cytokines such as interleukin-1 beta (IL-1β), interleukin-6 (IL-6), TNF-α, and mediators such as reactive oxygen and nitrogen species.[25] They express high levels of main histocompatibility complex class II (MHC-II), CD68 marker, and CD80 and CD86 costimulatory molecules. M1 macrophages upregulate the expression of intracellular protein called suppressor of cytokine signalling 3 (SOCS3) and activate the inducible nitric oxide synthase (NOS2 or iNOS) generating nitric oxide (NO) (Figure 1.12).[26]

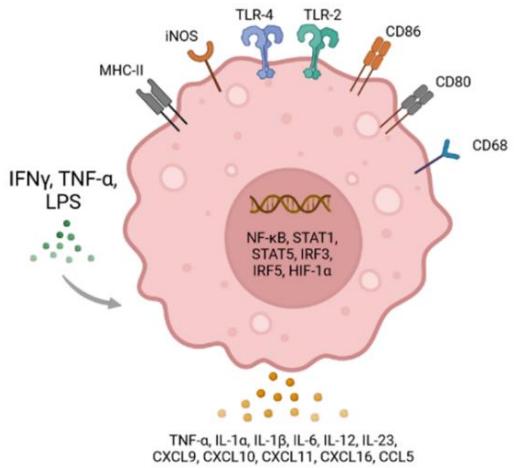

Figure 1.12 Classically activated macrophage (M1).

M1 macrophages are involved in cell-mediated immune responses, in particular in host defence against intracellular pathogens such as bacteria, viruses, and parasites.[25] These cells are able to phagocyte large numbers of pathogens and kill intracellular bacteria through microbicidal mechanisms by the synthesis of NO, the restriction of iron or nutrients for microorganisms and acidification of the phagosome.

IFN-γ is produced by both innate and adaptive immune cells. NK cells produce IFN-γ in response to stress and infections, activating macrophages with an increased killing ability to secrete pro-inflammatory cytokines. However, sustained production of IFN-γ by T helper 1 (Th1) cells, which are antigen-specific, is usually necessary to maintain

classically activated macrophages and confer stable host defence against many intracellular microorganisms.[25] LPS generates M1 macrophages through the interaction with toll-like receptor 4 (TLR-4), by inducing phosphorylation of both STAT1α and STAT1β.[26]

Classically activated macrophages play a crucial role in the host defence mechanisms, in the pro-inflammatory activity and in tissue damage. However, their activation needs to be regulated carefully as the cytokines and mediators they produce can cause host-tissue damage. In fact, these macrophages are key players in the immunopathology that occurs in various autoimmune diseases.[25]

- **Alternatively activated macrophages (M2)**

M2 macrophages, also known as alternatively activated macrophages, are induced by Th2 cytokines such as interleukin-4 (IL-4), interleukin-10 (IL-10), and interleukin-13 (IL-13), as well as by anti-inflammatory cytokines such as transforming growth factor-beta (TGF-β), fungi and helminth infections. These macrophages produce high levels of anti-inflammatory cytokines such as IL-10, and TGF-β, as well as growth factors involved in tissue repair and remodelling such as vascular endothelial growth factor (VEGF), insulin-like growth factor-1 (IGF-1), and platelet-derived growth factor (PDGF). M2 macrophages are characterized by the expression of the macrophage mannose receptor (CD206), CD200R and CD163 in combination with the transcription factor CMAF. Additionally, MGL1, MGL2, RGC-32, Arginase-1 (Arg1), FIZZ1, and chitinase 3-like 3 (Ym1) have also been suggested as potential M2 markers.[26]

M2 macrophages are involved in tissue repair and wound healing, as well as in the resolution of inflammation and immunoregulation. IL-4 is one of the first innate signals released during tissue injury by basophils, mast cells, and other granulocytes. IL-4 stimulates arginase activity in resident macrophages, allowing them to convert arginine to ornithine, contributing to the production of the ECM that leads to wound healing and tissue remodelling. They are also involved in the regulation of the Th2-type immune response and in the induction of immune tolerance.[25]

M2 macrophages are a heterogeneous population that can be subdivided into different subsets based on the stimuli that induce their activation and their functional characteristics. Four subsets have been described: M2a, M2b, M2c, and M2d (Figure 1.13).[27]

- **M2a**. induced by IL-4 and IL-13, which are produced by T helper 2 (Th2) cells and other immune cells. These macrophages are involved in tissue repair, angiogenesis, and extracellular matrix remodeling. They express high levels of CD206, Arg1, resistin-like molecule alpha (RELMα), and Ym1.[28]
- **M2b**. induced by immune complexes and TLR ligands, such as LPS and CG DNA. These macrophages are involved in immunoregulation and tissue repair. They express high levels of CD86, iNOS, IL-10, and TGF-β.[28]
- **M2c.** induced by IL-10, glucocorticoids, and TGF-β. They are involved in the resolution of inflammation and tissue repair. They express high levels of CD163, IL-10, TGF-β, and the scavenger receptor CD36.[28]
- **M2d**. induced by IL-6, TLR-ligands and adenosine, which is produced by tumors and damaged tissues. They promote tumor growth, angiogenesis, and immunosuppression. They express high levels of IL-10, VEGF, and C-C motif chemokine ligand 22 (CCL22).[24,25,27,28]

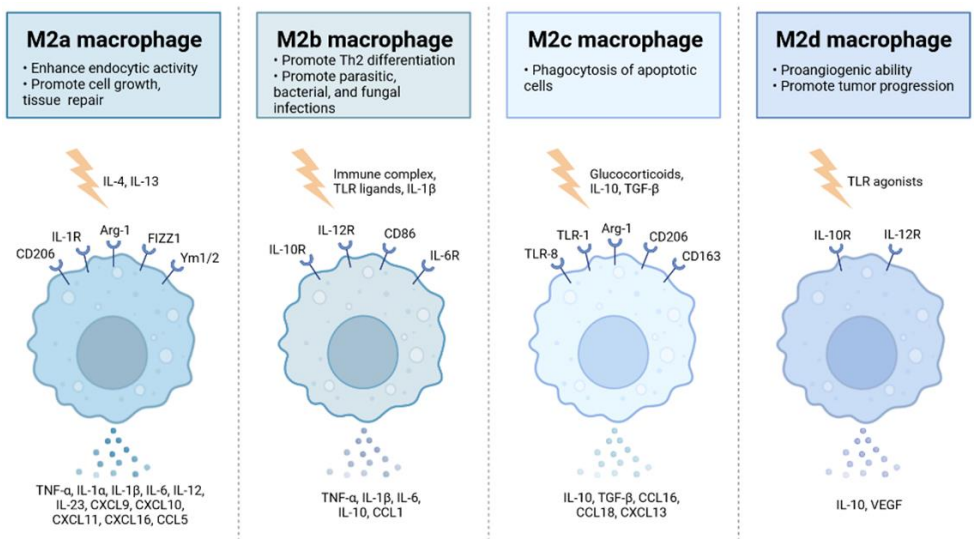

Figure 1.13 Different subsets of alternatively activated macrophages (M2). Image source: Biorender

These different subsets of M2 macrophages have distinct gene expression profiles and functional characteristics. The classification of M2 macrophages into different subsets has been useful to better understand their roles in different physiological and pathological conditions.

1.2.2 Macrophages role in lung pathologies

Macrophages, a key component of the innate immune system, play a pivotal role in maintaining lung homeostasis and immune defense. These immune cells reside in the lung tissue, where they actively participate in immune responses to protect against pathogens and respond to tissue damage. However, in the context of lung disorders, macrophages can exert both beneficial and detrimental effects, depending on their activation state and the microenvironment.[24]

In chronic lung disorders such as chronic obstructive pulmonary disease (COPD) and asthma, macrophages are involved in persistent inflammation. M1 macrophages contribute to the inflammatory response by releasing pro-inflammatory mediators, which exacerbate tissue damage and airway remodelling. In these conditions, an imbalance between M1 and M2 macrophages may lead to chronic inflammation and tissue destruction.[29]

In pulmonary fibrosis, macrophages play a crucial role in orchestrating fibrotic responses. Injured lung epithelial cells release chemokines and cytokines that recruit macrophages. M2-like macrophages are thought to contribute to fibrotic tissue remodelling by promoting ECM production and inhibiting matrix degradation. Their uncontrolled activation can lead to excessive collagen deposition, impairing lung function.[21]

In infectious lung diseases like tuberculosis and pneumonia, macrophages serve as a primary defense mechanism. They are responsible for phagocytosing and clearing invading pathogens. The activation of AM results in increased concentrations of pro-inflammatory cytokines and chemokines. However, the intracellular survival of pathogens, like Mycobacterium tuberculosis, is often linked to the ability of certain

strains to manipulate macrophage activation states, leading to granuloma formation and tissue damage.[30]

In the tumor microenvironment of lung cancer, tumor-associated macrophages (TAMs), play a multifaceted role. TAMs, often displaying an M2-like phenotype, support tumor progression by secreting growth factors, cytokines, and chemokines that enhance tumor cell proliferation, angiogenesis, and metastasis. Moreover, they foster an immunosuppressive microenvironment that shields tumor cells from immune surveillance, aiding tumor growth. These macrophages also hinder the activation of cytotoxic T cells and natural killer cells, leading to immune evasion. They can express immune checkpoint molecules like PD-L1, which binds to PD-1 on T cells, further suppressing the anti-tumor immune response.[31]

Given the pivotal role of macrophages in lung disorders, therapeutic strategies that target these cells are being explored. Modulating macrophage polarization and function offers potential approaches to control inflammation and promote tissue repair. Various preclinical and clinical studies are investigating the use of immunomodulatory agents, such as corticosteroids and immune checkpoint inhibitors, to influence macrophage activation and function in lung diseases.

Their functional plasticity and complex involvement in lung diseases make them attractive targets for therapeutic intervention. A better understanding of the mechanisms that regulate macrophage activation in specific lung disorders is essential for the development of effective treatments.

1.3 Pulmonary pathology

The lungs are vital organs responsible for exchanging oxygen and carbon dioxide between the air and the blood. Several diseases can affect the lungs, causing respiratory problems and impacting overall health. Lung diseases can be broadly categorized into four main groups: obstructive lung disease, restrictive lung disease, infectious disease and neoplastic disease.[32]

1.3.1 Obstructive lung diseases

Obstructive lung diseases are characterized by airflow limitation due to partial or complete obstruction of the airways. The key clinical aspects are the forced expiratory volume at one second (FEV1), the reduced forced vital capacity (FVC) ratio and the trapping of air in the parenchyma. The main obstructive lung diseases include COPD (emphysema, bronchiectasis and chronic bronchitis) and asthma.

1.3.1.1 Chronic obstructive pulmonary disease (COPD)

Chronic Obstructive Pulmonary Disease (COPD) is a chronic, multifactorial and progressive lung disease that affects millions of people worldwide.[33] It is primarily caused by the inhalation of noxious particles or gases, particularly cigarette smoke, and is characterized by persistent and progressive airflow limitation that is not fully reversible. COPD encompasses several respiratory conditions, including chronic bronchitis (small airway disease), emphysema (parenchymal and alveoli destruction, dilation of terminal airways) and narrowing of the airway. The underlying pathophysiology of COPD involves chronic inflammation, oxidative stress, and remodelling of the airways and lung parenchyma, leading to structural changes and functional impairments.[34] The inflammatory response is characterized by the infiltration of immune cells, such as neutrophils, macrophages and T lymphocytes, which release pro-inflammatory mediators and proteases that contribute to tissue damage and lung function decline. In COPD, there is an increase in the number of macrophages in various areas of the lungs, likely due to increased recruitment of monocytes from the circulation. These macrophages, particularly the pro-inflammatory M1 subset, release more inflammatory mediators and reactive oxygen species (ROS) than macrophages from non-smokers and smokers without COPD. The oxidative stress response results from an imbalance between oxidant and antioxidant agents, leading to the generation of ROS that cause cellular damage and trigger inflammation. The remodelling response involves changes in the airway and lung structure, including thickening of the airway wall, loss of alveolar attachments, and destruction of lung parenchyma, leading to airflow limitation and gas exchange impairment (Figure 1.14).[29]

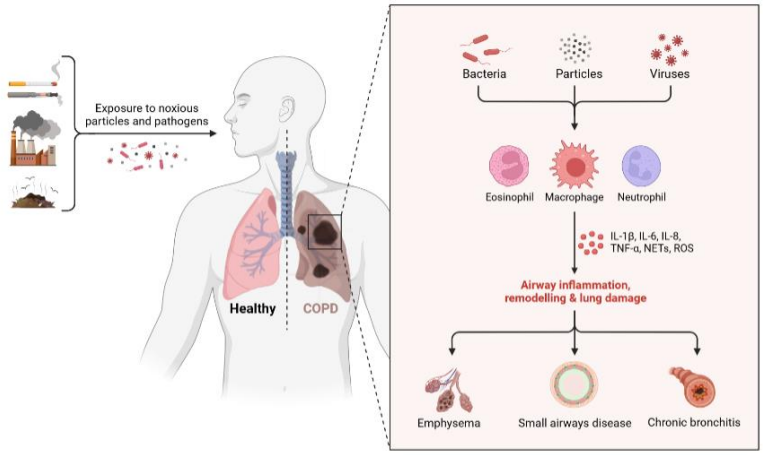

Figure 1.14 Development of chronic obstructive pulmonary disease. Image source: Biorender

The diagnosis of COPD is based on a combination of clinical symptoms, lung function tests, and imaging studies. The main symptoms include dyspnoea, cough, sputum production, and wheezing, which may vary in severity and frequency.[34]

Treatment options for COPD include pharmacotherapy, pulmonary rehabilitation, oxygen therapy, and surgery, depending on the severity and stage of the disease. The main goals of treatment are to relieve symptoms, improve lung function, prevent exacerbations, and enhance quality of life. Pharmacotherapy includes bronchodilators, such as beta-agonists and anticholinergics, and anti-inflammatory agents, such as corticosteroids and phosphodiesterase-4 inhibitors.[34]

1.3.1.2 Asthma

Asthma is a chronic inflammatory disease of the airways characterized by wheezing, shortness of breath, chest tightness and coughing.[35] It affects over 300 million people worldwide and is associated with significant morbidity and mortality. In asthma, there is infiltration of inflammatory cells, such as eosinophils, mast cells, and T cells, into the airway walls and surrounding tissues, resulting in airway hyper-responsiveness and airway remodeling.[29] Traditionally, two forms of asthma have been defined in the clinic, allergic and non-allergic. The inflammatory response is triggered by exposure to allergens or non-specific irritants, such as smoke or air pollution, which activate the

immune system and induce the release of cytokines and chemokines that recruit inflammatory cells to the lungs. The resulting inflammation leads to mucus overproduction, airway wall remodelling and narrowing, making it difficult to breathe.

Treatment options of asthma aims to reduce airway inflammation and improve airway function through the use of inhaled corticosteroids, bronchodilators, and other medications. A personalized approach to treatment, based on the underlying inflammatory phenotype, may improve outcomes for asthma patients.[36]

1.3.2 Restrictive lung diseases

Restrictive lung diseases are characterized by reduced lung volume and capacity due to damage to the lung tissue or chest wall. Restrictive lung disease is categorized into extrapulmonary and intrapulmonary forms. Extrapulmonary causes, such as obesity and kyphoscoliosis, lead to a restrictive lung disease by externally impairing lung filling. Intrapulmonary restrictive lung disease can be further divided into acute and chronic subcategories.[32]

Acute restrictive lung disease is predominantly associated with acute respiratory distress syndrome (ARDS). It is a rapid-onset condition occurring within minutes to days as a result of a severe systemic insult like sepsis or shock. It is characterized by hypoxemic respiratory failure with oxygen levels below 60 mm Hg and diffuse pulmonary infiltrates. The pathogenesis of ARDS involves diffuse alveolar damage, with damage to the alveolar epithelium and endothelium, leading to increased alveolocapillary permeability, loss of diffusion capacity, and protein leakage into the alveoli. The progression of diffuse alveolar damage occurs in three stages: exudative, proliferative, and fibrosis.[37]

Chronic forms can be subdivided by aetiology (i.e., work related, drug-related, autoimmune, and idiopathic). They are characterized by chronic diffuse lung injury with inflammation and fibrosis, impaired gas exchange (low diffusing capacity of lung for carbon monoxide), decreased FEV1 and FVC, and normal FEV1/FVC ratio. Examples of restrictive lung diseases include interstitial lung disease (ILD) and sarcoidosis.[32]

1.3.2.1 Interstitial Lung Disease (ILD)

Interstitial lung disease is a broad term that encompasses a group of lung disorders characterized by inflammation with infiltration of inflammatory cells and scarring (fibrosis) of the interstitial tissue that surrounds and supports the alveoli in the lung parenchyma. ILD is an umbrella term that includes various specific conditions, one of which is pulmonary fibrosis.[38] Pulmonary fibrosis refers specifically to the progressive and irreversible accumulation of scar tissue in the lungs, leading to decreased lung function and respiratory failure. It involves the abnormal accumulation of collagen and other fibrous proteins in the interstitial space, leading to thickening and stiffening of the lung tissue. Pulmonary fibrosis primarily affects the alveoli and the surrounding interstitial spaces, impairing lung function and gas exchange. Interstitial lung disease are classified on the basis of a known underlying disease, an inciting agent or the absence of a known cause and can be broadly sub-grouped into idiopathic, autoimmune-related, caused by external agents (hypersensitivity pneumonitis), sarcoidosis and others (Figure 1.15). Each of these conditions may have distinct clinical features, causes, and treatment approaches.[39]

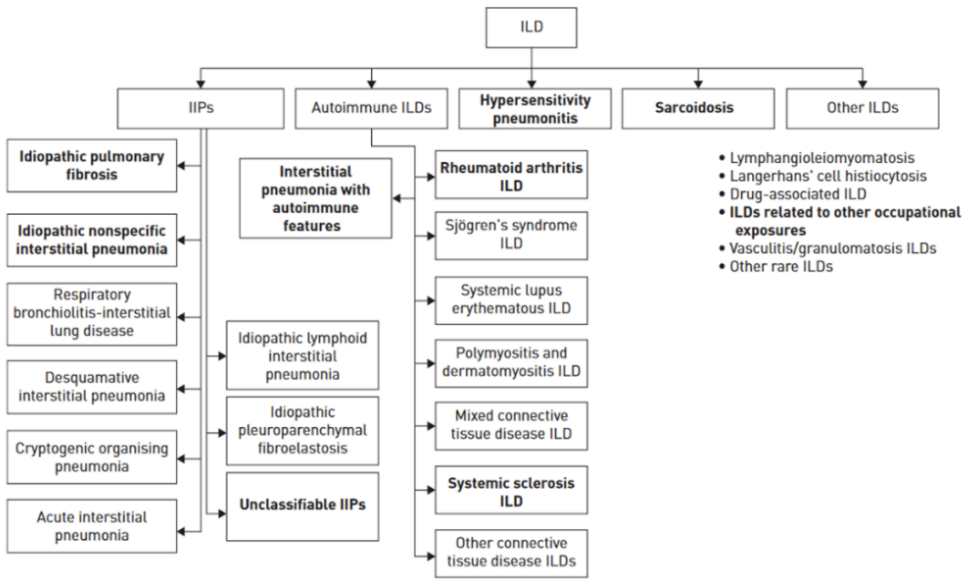

Figure 1.15 Classification of interstitial lung diseases. (IIPs: idiopathic interstitial pneumonias). Image source: V. Cottin et al, 2018

Idiopathic pulmonary fibrosis (IPF) is the most common chronic, progressive, fibrotic ILD. IPF is characterized by an imaging and pathological pattern of usual interstitial pneumonia (UIP) which includes fibroblastic foci, dense collagen deposition, and honeycombing without an identifiable cause or association with a disease known to be associated with pulmonary fibrosis. It occurs more commonly in men than in women (sex ratio, 7:3) and is more common in people older than 60 years of age than in younger people. IPF is a chronic and irreversible disease, usually progressing to respiratory failure and death.[40]

While each specific fibrosing ILD is considered rare, the combined impact of these conditions on patients is significant, representing a substantial burden of disease. The overall prevalence of ILDs is estimated to range from 76 cases per 100,000 individuals in Europe to 74.3 cases per 100,000 in the United States. Among the fibrotic ILDs, sarcoidosis, ILD associated with connective tissue diseases (CTD-ILD) and IPF are the most common.[40]

Pathogenesis Several risk factors contribute to the pathogenesis of IPF, including environmental exposures, particulate inhalation, smoking, chronic viral infections, and specific comorbidities. Increasing evidence indicates that also genetic factors play a significant role. Studies of familial interstitial pneumonia have identified rare genetic variants. Although these studies do not indicate a direct causal link, the potential importance of alterations in genes associated with surfactant dysfunction (SFTPC, SFTPA2), telomere biology (TERT, TERC, PARN, RTEL, OBFC1), in host defence (MUC5B, ATP11A, TOLLIP) and epithelial barrier function (DSP, DPP9) was identified. Age is the most influential demographic risk factor for IPF, suggesting that the lung aging process is a driving force in its development. Notably, IPF exhibits an exaggeration or premature occurrence of nearly all cellular and molecular hallmarks associated with aging.[41]

The lungs are constantly exposed to the external environment and possess remarkable regenerative abilities, coordinated by a precise sequence of biological processes, to counteract various injuries that can occur. With inhalation, the alveolar surface area interacts with various microparticles, including pollutants, microorganisms, and

oxidants. These elements have the potential to directly damage the delicate structure of the alveolar epithelium that acts as a physical barrier and possesses pathogen-sensing capabilities. To protect the lungs, both the innate and adaptive immune systems play crucial roles in the wound-healing response.[42]

The pathogenesis involves multiple cellular compartments, including the epithelium, lung fibroblasts, and the innate and adaptive immune system. However, the exact mechanisms underlying the interplay of these factors in disease pathogenesis remain unclear. Most ILDs are characterized by inflammation, fibrosis, or a combination of both, with initial inflammation often progressing to fibrosis. Additionally, some ultra-rare ILDs have distinct disease mechanisms and unique phenotypes.[43]

The alveoli in the lungs are lined by AEC1 and AEC2. AEC2 cells have the ability to differentiate into both AEC1 and AEC2. The interstitial space between these cells and the capillaries contains macrophages and fibroblasts. When there is an injury to the alveolar epithelium, AEC2 cells trigger the proliferation of fibroblasts, which differentiate into myofibroblasts. These cells secrete collagen fibres that maintain the structure and elasticity of the lungs. In normal conditions, myofibroblasts undergo apoptosis and restore normal lung function. However, the repetitive exposure of alveolar epithelium to micro-injuries in genetically susceptible individuals during the aging process can trigger pro-fibrotic epigenetic reprogramming. This, in turn, leads to premature and persistent senescence of epithelial cells, aberrant epithelial-fibroblast communication, excessive production of pro-fibrotic mediators, and ongoing activation of mesenchymal cells, resulting in a maladaptive response, considerable ECM accumulation and eventual development of a range of disorders. Dysfunctional AEC2 cells should regenerate damage cells, but their ability to re-establish normality is seriously impaired indicating the initiation of the maladaptive repair process with inflammation that contribute to cellular damage and tissue destruction. the apoptosis of myofibroblasts is disturbed, leading to abnormal wound healing and progressive fibrosis.[44] This results in ventilation issues and imbalances in oxygen supply to the body.

The wound-healing response in pulmonary fibrosis can be divided into three phases: injury, inflammation, and repair. While not all fibrotic conditions follow this pattern, it serves as a useful model to understand the mechanisms involved.

- **Phase I: Injury**. Various factors such as autoimmune reactions, allergies, environmental pollutants, infections, or mechanical damage can disrupt normal tissue architecture, triggering a healing response. Inflammation that occurs after the injury can further damage cells and tissues. Damaged epithelial and endothelial cells need to be replaced to maintain barrier function and prevent blood loss. Acute damage to endothelial cells leads to the release of inflammatory mediators and initiates a coagulation cascade, forming a temporary clot to plug the damaged vessel. Pulmonary fibrotic conditions show continuous activation of clot-forming responses, and the presence of thrombin confirms the activation of the clotting pathway. Thrombin can directly activate fibroblasts, leading to their proliferation and differentiation into collagen-producing myofibroblasts. Damage to the airway epithelium, particularly alveolar pneumocytes, triggers an anti-fibrinolytic cascade, causing interstitial edema, acute inflammation, and separation of the epithelium from the basement membrane.[45] For the crucial role that AECs play in the initiation and progression of the disease, IPF has been considered an "epithelium driver disease".[46]

Platelet recruitment and clot formation progress to vasodilation and increased permeability, allowing leukocytes to be recruited to the injured site. The basement membrane, which forms the ECM underlying the epithelium and endothelium, acts as a barrier to damaged tissue. Matrix metalloproteinases (MMPs), specifically MMP-2 and MMP-9, cleave ECM constituents, facilitating the extravasation of cells into and out of damaged sites. MMP-2 and MMP-9 are upregulated in fibrotic conditions, highlighting their role in tissue destruction and regeneration.[47] These MMPs are necessary for the successful clearance of inflammatory cells from inflamed tissue into the airspaces. The balance between MMPs and inhibitory mechanisms determines the level of inflammation and the amount of collagen deposited during the healing response.[48] These enzymes are upregulated in fibrotic conditions, contributing to tissue destruction and regeneration processes.[45]

The dysfunctional epithelium's inability to regenerate after repetitive injury plays a crucial role in disease progression. The damage to the epithelium disrupts the basement membrane, leading to the breakdown of the alveolar capillary barrier. This results in the leakage of proteins, including fibrin and fibronectin, into the interstitial and alveolar spaces. The activated epithelial and endothelial cells create an environment that promotes an abnormal communication between the epithelium and mesenchymal cells. This leads to the recruitment, migration, proliferation, and differentiation of fibrocytes and fibroblasts, primary source of collagen-producing cells in the lungs during fibrosis development. However, a small population of bone marrow-derived fibrocytes may also contribute to the cell population at the injury sites.[49]

- **Phase II: Inflammation**. Once access to the site of tissue damage is established, chemokine gradients attract inflammatory cells such as neutrophils, eosinophils, lymphocytes, and macrophages. These cells clear cell debris and areas of necrosis through phagocytosis. The role of specific inflammatory cells in downstream fibrosis, particularly in IPF, is still debated. Anti-inflammatory agents have shown limited efficacy in treating IPF and usual interstitial pneumonia patients, suggesting that inflammation may not be a significant contributing factor. However, this controversy originates from the incomplete understanding of the causative agents and mechanisms involved in IPF. The absence of inflammation observed in IPF patients and the interpretation that inflammation is not involved may be a matter of timing.[45]

The nature of the insult or causative agent determines the type of inflammatory response. Exogenous stimuli, such as pathogen-associated molecular patterns (PAMPs), are recognized by pathogen recognition receptors and influence the response of innate cells to invading pathogens. Endogenous danger signals also affect local innate cells and orchestrate the inflammatory cascade. The immune responses can be classified into Type 1 (pro-inflammatory), Type 2 (wound-healing), and Type 17 (associated with pro-inflammatory conditions) based on T helper cell-dominant cytokine responses.[45]

Various cytokines are involved throughout the wound-healing and fibrotic response, with specific groups of genes activated in different conditions. For example, chronic allergic airway disease in asthmatics is associated with elevated Type-2 cytokine

profiles, while IPF patients often exhibit pro-inflammatory cytokine profiles. Cytokines such as IL-4, IL-13, and TGF-β play significant roles in pulmonary fibrotic conditions by recruiting, activating, and proliferating fibroblasts, macrophages, and myofibroblasts.[45]

Moreover, epithelial-mesenchymal transition (EMT) is a process in which epithelial cells acquire characteristics of mesenchymal cells. It involves significant changes in transcriptional machinery and cellular reprogramming. While EMT is a normal process in embryological tissue, it is a rare occurrence in normal wound healing and is triggered by sustained inflammation and injury. TGF-β1 is considered a key cytokine involved in initiating this process. In IPF, there is evidence suggesting that epithelial cells acquire some mesenchymal features, but it is unclear whether a complete EMT occurs, as there are no definitive specific fibroblast cell markers. The most characteristic maker of these transitional cells is alpha smooth-muscle actin (αSMA).[49]

Inflammatory monocytes and tissue-resident macrophages are key regulators of tissue fibrosis, playing important roles in the initiation, maintenance and resolution of tissue injury. Monocytes and macrophages are recruited to areas of tissue injury. Pro-fibrotic macrophages play a significant role in coordinating scar formation by interacting with fibroblasts. Macrophages are in close proximity to contractile fibroblasts for effective communication. Contracting fibroblasts generate deformation fields in the fibrillar collagen matrix, which serve as physical cues for macrophages. Within these collagen deformation fields, macrophages migrate towards the source of force generated by fibroblasts and the presence of a dynamic force source is necessary to initiate and guide macrophage migration.[50] Macrophages play a crucial role in lung homeostasis and immune response following injury, making them potential targets for future therapeutic interventions.[45]

M1 macrophages are activated during the early inflammatory phase and are involved in clearing pathogens and promoting inflammation. They release MMPs and pro-inflammatory cytokines, contributing to tissue damage. On the other hand, M2 macrophages are associated with anti-inflammatory responses and are more prevalent in interstitial lung diseases, including IPF. M2 macrophages produce chemokines, TIMPs

and fibronectin, which regulate the development and progression of fibrotic lung diseases. They can also differentiate into fibrocyte-like cells that express collagen. The polarization of macrophages towards the M2 phenotype is believed to inhibit the inflammatory response and regulate fibrotic processes. M2 macrophages secrete cytokines that attract and stimulate the proliferation, survival, and migration of fibroblasts, which contribute to the development of fibrosis. Inhibition of M2 macrophage polarization has shown promise in reducing fibrosis in animal models.[45,51]

Several signaling pathways have been implicated in the involvement of macrophages in pulmonary fibrosis. These include TGFβ/Smad, Wnt/β-catenin, interleukin signaling, Lrp5/β-catenin, MAPK, Notch, PI3K-AKT-mTOR, STAT1, NFkB, IGF-1 receptor, 4-1BB, NRG-1/ErbB4, and M-CSF/M-CSFR pathways. These pathways regulate various aspects of macrophage activation and fibrotic processes.[51]

The interplay between M1 and M2 macrophage phenotypes is considered crucial in the development and progression of lung fibrosis. Understanding the molecular mechanisms underlying macrophage involvement in pulmonary fibrosis is essential for identifying potential therapeutic targets to mitigate the disease. Inhibiting specific signaling pathways or modulating macrophage polarization may hold promise for future interventions in fibrotic lung diseases.

The inflammatory response significantly affects tissue-resident and inflammatory cells and further propagates inflammation through the secretion of chemokines, cytokines, and growth factors. Various cytokines are involved in wound healing and fibrotic responses, with specific groups of genes activated in different conditions.

Cytokines such as IL-1α, IL-1β, TNF-α, TGF-β, and PDGF are frequently observed in PF patients. IL-1β plays a central role by stimulating collagen expression and promoting tissue destruction, inflammation, and collagen deposition. Uric acid and ATP released from injured lung cells activate the NALP3 inflammasome, leading to IL-1β production and lung fibrosis. IL-4, IL-13 and TGF-β are directly linked to the pathogenesis of PF through the mobilization, activation and proliferation of fibroblasts, macrophages and myofibroblast, respectively.[48]

The innate acute-phase pro-inflammatory cytokines IL-1, IL-6, and TNF-α, together with TGFβ, which are produced by macrophages, tissue fibroblasts and other local cell populations, promote the development of IL-17-secreting cells. IL-17A potentiates neutrophil responses that contribute to tissue injury through the production of ROS, induces inflammation while increasing the expression of TGF-β receptors on fibroblasts and thereby facilitating the production of ECM in response to TGF-β. Cytokines such as IL-17A and IL-22 have been identified as fibrosis triggers. IL-17A signaling contributes to fibrosis in multiple tissues, and it enhances fibroblast sensitivity to TGFβ. IL-22 also enhances TGF-β signaling in fibroblasts. The IL-17A-TGF-β axis is activated by upstream activators such as Caspase 1, NLRP3 inflammasome and Nuclear factor-kappa B (NFκB). Their sustained activation and signaling may involve stimulation of Toll-like receptors by microorganisms, leading to the production of pro-inflammatory cytokines and chemokines that exacerbate inflammation and fibrosis.[50]

Type 2-associated cytokines IL-4 and IL-13 are important inducers of fibrosis. In this case, eosinophils and M2 macrophages play a prominent role. Alarmin cytokines from epithelial cells and damaged tissues, such as thymic stromal lymphopoietin, IL-25, and IL-33, initiate type 2-dependent fibrosis by triggering the production of IL-4 and IL-13 in various immune cells. IL-4 receptors are present on lung fibroblasts increasing extra cellular matrix proteins and collagen deposition. Moreover, IL-4 promotes the alternative activation of macrophages that can produce TGF-β, PDGF and, through arginase upregulation, modulate polyamine and proline biosynthesis, cell growth, and collagen formation. IL-4 promote the differentiation of T cells into Th2 cells, providing a source of many type-2 cytokines in this inflammatory axis (IL-5, IL-9, IL-13, and IL-21) and propagating wound healing and potentially pro-fibrotic responses. IL-13 shares many properties with IL-4, due to common receptor subunits (IL-4Rα), signal transduction pathways and transcription factors (STAT-6). IL-13 has been identified as a key fibrogenic cytokine in many fibrotic conditions triggering the differentiation of fibroblasts into αSMA expressing myofibroblasts and PDGF-producing cells with significant mitogenic properties.[45,50]

Cross-regulation between IL-17A and IL-13 has been observed, suggesting that targeting one pathway may lead to upregulation of the other. Therefore, successful antifibrotic

strategies may need to target the dominant mechanism or reduce both pathways simultaneously (Figure 1.16).[50]

Furthermore, myofibroblasts produce the cytokine IL-11, stimulating the production of ECM in response to various pro-fibrotic mediators, including TGFβ and type 2 cytokines.[50]

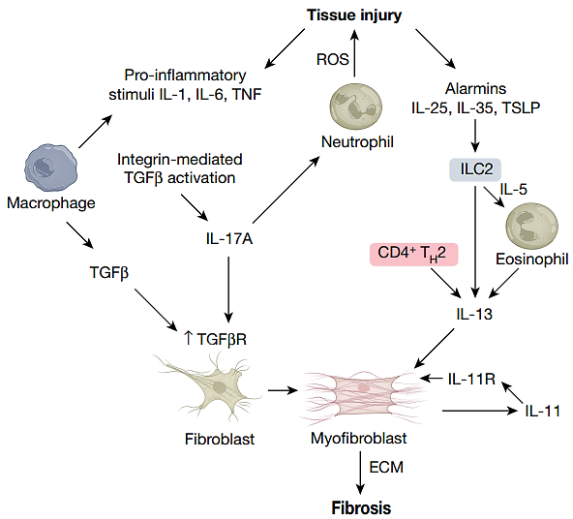

Figure 1.16 Cytokines-mediated regulation of fibrosis. Image source: C. Henderson et al, 2020

Growth factors like TGF-β, PDGF, VEGF, and fibroblast growth factor (FGF) are involved in the fibrotic changes. These growth factors act through various signalling pathways, such as TGFβ-SMAD, WNT-Catenin, sonic hedgehog, Notch, and FGF-FGFR, which play a role in the interaction between AECs and myofibroblasts.[45,51]

TGF-β is a key mediator in IPF and is involved in cellular activities such as proliferation, differentiation and programmed cell death. Fibronectin, VEGF, and PDGF are also involved in the activities of TGF-β. It is secreted in a latent form (latency-associated protein – LAP) and is activated by many agents commonly found in fibrotic conditions, including cathepsins, plasmin, calpain, thromombospondin, integrin αvβ6 and MMPs. Once active, it gains growth and chemotactic properties, stimulates fibroblast proliferation and the synthesis of ECM recruiting inflammatory cells through MCP-1 (CCL2) and suppressing T-cell responses. Interestingly, unlike IL-13 overexpression,

TGF-β did not recruit inflammatory cells or enhance mucus secretion in the lung, suggesting that this cytokine can directly induce fibrosis in the absence of significant inflammation.[45,52]

FGFs are proteins that regulate cell proliferation, survival, migration, and differentiation. Fibroblast growth factor receptor (FGFR) plays a role in the repair process. Nintedanib, a triple kinase inhibitor, blocks the activities of VEGF, FGF, and PDGF. It decreases the levels of ECM proteins and inhibits myofibroblast differentiation mediated by TGF-β1.

Another target for IPF treatment is WNT5A, a signalling protein of the WNT family. WNT5A induces the proliferation of lung fibroblasts and is elevated in IPF fibroblasts. WNT signalling is involved in epithelial cell proliferation, myofibroblast differentiation, and collagen synthesis (Figure 1.17).

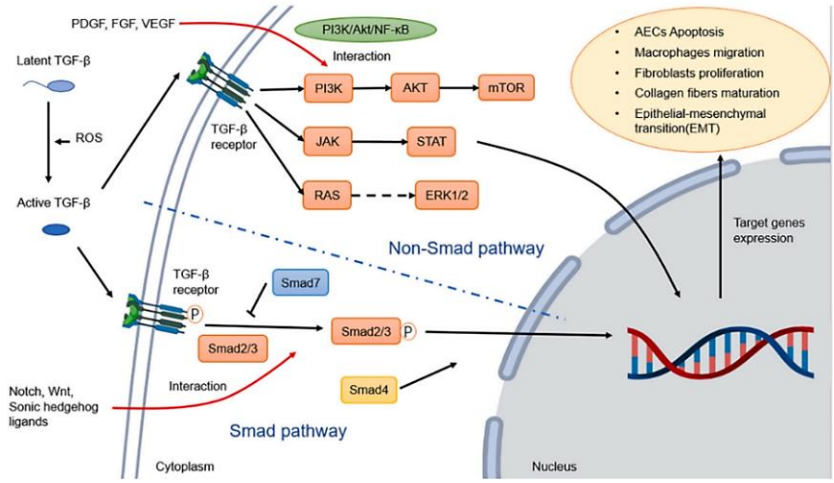

Figure 1.17 The roles of TGF-β in pathological pathways. Image source: R. Li et al, 2022

Understanding these signalling pathways and their manipulation can contribute to drug discovery for the treatment of PF. Several inhibitors of cytokines, chemokines, and growth factors are being tested in clinical trials for fibrosis treatment. These include inhibitors of IL-13, IL-4, TNF, CCR2, CCR5, IL-1, IL-6, CCL2, and follistatin.[50]

- **Phase III: Tissue repair and contraction**. It is the final phase of wound healing. Various cellular processes occur to reorganize the tissues, promote wound closure, and

restore normal function. The process of tissue repair and contraction involves the formation of a fibrin-rich scaffold, wound contraction, and re-epithelialization.

In this phase, myofibroblasts play a crucial role in producing collagen and contractile proteins. They contribute to the formation of a provisional extracellular matrix known as granulation tissue. Fibronectin, derived from macrophages, platelets, and fibroblasts, forms a key component of this matrix. Studies indicate that fibronectin production is elevated in patients with IPF, and it may be resistant to steroid treatment.[45] Activated fibroblasts and myofibroblasts form fibroblastic foci (FF), which are involved in excessive ECM deposition. This leads to progressive lung remodelling, architectural distortion, and fibrosis (Figure 1.16).[49]

Other components of the provisional extracellular matrix include glycoproteins, glycosaminoglycans, proteoglycans and elastin. Growth factors and TGF-β activate fibroblasts, promoting their migration along the extracellular matrix to repair the wound. TGF-β also induces a contractile response, regulating collagen fibre orientation.[48]

Myofibroblasts attach to the extracellular matrix at specialized sites called fibronexus or super mature focal adhesions. This attachment allows them to exert contractile forces, leading to wound contraction and reduction in the size of the wound. The balance between MMPs and tissue inhibitors of metalloproteinases (TIMPs), as well as collagens and collagenases, influences collagen deposition. The removal of inflammatory cells and myofibroblasts is crucial to terminate collagen deposition.[45,48]

Re-epithelialization involves the restoration of the epithelial layer at the wound site. Epithelial cells migrate, proliferate, and spread to cover the damaged area. Factors such as TGF-β and MMP-7 play important roles in regulating re-epithelialization. The degree of inflammation, angiogenesis, and extracellular matrix deposition determines the overall collagen deposition and the potential development of a fibrotic lesion. Therapeutic interventions targeting fibroblast activation, proliferation, or apoptosis require a comprehensive understanding of the wound repair phases.[45,48]

It is important to note that these three phases of wound healing often occur sequentially, but in chronic or repeated injury situations, they may function concurrently, posing

challenges for regulatory mechanisms (Figure 1.18). Understanding these diverse mechanisms is important as they can provide insights into prognosis and guide the selection of appropriate pharmacotherapy options.

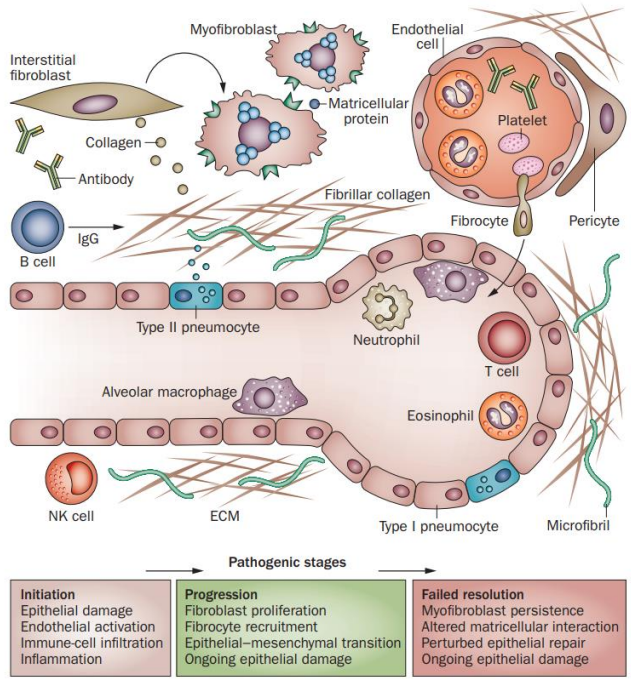

Figure 1.18 Cellular pathogenesis of fibrotic lung injury. Fibrosis develops in response to lung injury and cells in the epithelial, endothelial and interstitial compartments, together with components of the innate and adaptive immune system are implicated in pathogenesis. Image source: U. Wells et al, 2014

Diagnosis They are characterized by common clinical features such as dyspnoea, cough, fatigue and restrictive pulmonary function abnormalities. Diagnostic evaluation typically involves a combination of clinical assessment, pulmonary function tests, radiographic imaging (such as high-resolution computed tomography), and, in some cases, histopathological examination following surgical lung biopsy.[43] Histopathological findings show that the usual interstitial pneumonia pattern is characterised by interstitial fibrosis with spatial heterogeneity and patchy involvement of lung parenchyma, areas of marked fibrosis, architectural distortion, and microscopic honeycombing (cystic airspaces lined by bronchiolar epithelium, typically filled with mucin). At the interface

between fibrotic and normal lung tissue are aggregates of proliferating fibroblasts and myofibroblasts (fibroblastic foci) within a myxoid-appearing matrix. Fibroblast foci are a key histopathological feature of UIP pattern, which represent areas of active disease, and their absence excludes a definite histopathological usual interstitial pneumonia diagnosis (Figure 1.19).

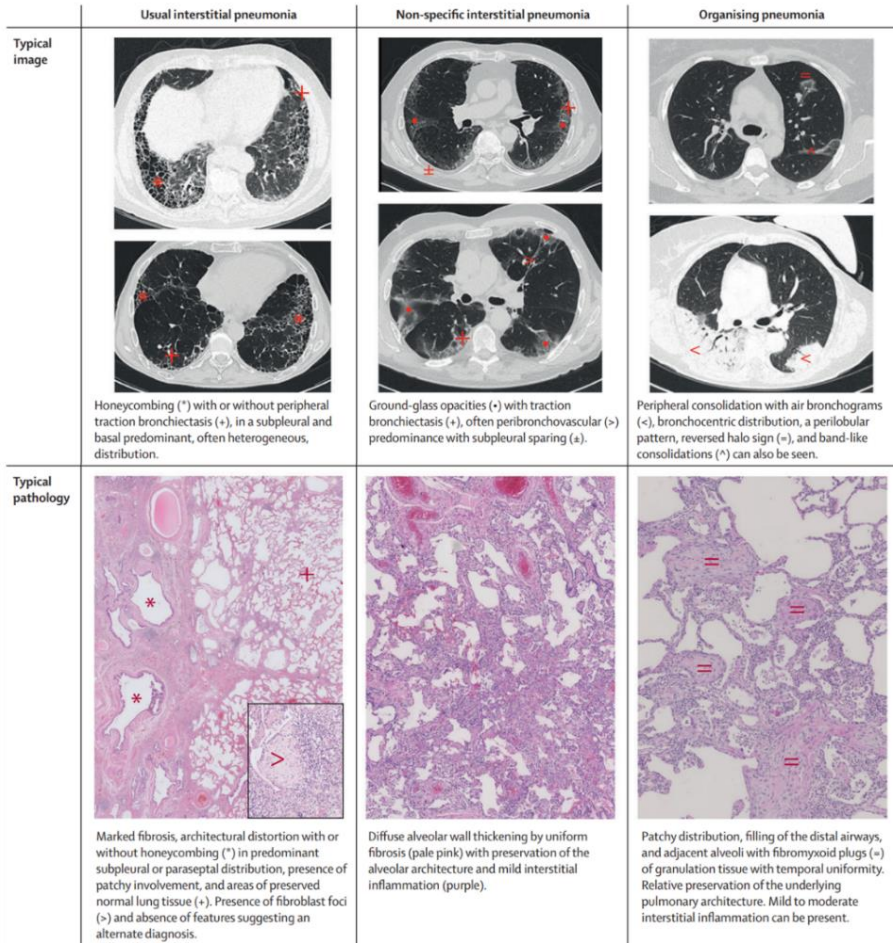

Figure 1.19 ILD histological and radiological patterns. Image source: M. Wijsenbeek, et al, 2022

Treatment options vary depending on the specific ILD subtype and may include immunosuppressive agents, anti-fibrotic drugs and lung transplantation.

Non pharmacologic management strategies are crucial for patients to lead healthier lives and are quitting smoking, administration of appropriate vaccines, including influenza

and pneumococcal vaccines and supplemental oxygen, that is strongly recommended for IPF patients, as it reduces breathlessness and improves exercise tolerance. Pulmonary rehabilitation, a structured exercise program, has shown to enhance exercise capacity and quality of life, while lung transplantation can be an option for selected candidates, but it is only available to a minority of IPF patients.[53]

Regarding pharmacologic management strategies, significant progress has been made in the treatment of ILDs in the past decade. Treatment strategies are divided in immunomodulatory or anti-fibrotic drugs. Most ILDs were presumed inflammatory, at least in their early phases, and thus likely to respond to corticosteroids and other immunosuppressives. Immunomodulatory drugs used in ILDs characterized by an inflammatory driver are connective tissue disease-associated ILD, hypersensitivity pneumonitis, and sarcoidosis, that often benefit from immunosuppressive therapy or disease-specific treatments.[54] In sarcoidosis, prednisone is generally recommended as first-line therapy, followed by other agents like methotrexate or azathioprine. Hypersensitivity pneumonitis may benefit from corticosteroids in non-fibrotic forms and mycophenolate mofetil or azathioprine in fibrotic forms. For drug-induced ILDs, corticosteroids are often used if discontinuing the causative agent is insufficient.[43]

Anti-fibrotic drugs are mainly used in IPF. Randomized controlled trials have led to the development of anti-fibrotic drugs for IPF and have shown that immunosuppressive therapy is detrimental for this condition. Anti-fibrotic therapy with Pirfenidone or Nintedanib is recommended, as they slow down lung function decline and provide a survival benefit.[43]

Nintedanib is a tyrosine kinase inhibitor that targets growth factor pathways involved in fibrosis. Diarrhea is a common side effect that can be managed with antidiarrheal agents. Nintedanib has also shown a positive effect on annual decline in FVC in systemic sclerosis-associated ILD. Liver function should be monitored regularly due to reported cases of drug-induced liver injury. Nintedanib is associated with a small increase in bleeding risk and should be used cautiously in patients on full-dose anticoagulant therapy or with cardiovascular risk factors. Atheroembolic events, including myocardial infarction, have been reported.[53]

Pirfenidone has anti-inflammatory and anti-fibrotic effects. It is prescribed in an escalating-dose manner over a 14-day period. Common side effects include anorexia, nausea, vomiting and photosensitive rash. These can be managed with antacids and antiemetic agents. Liver function should be monitored periodically.[53]

Regular monitoring for adverse events is necessary with these medications due to the strong gastro-intestinal side effects. Prompt initiation of treatment is essential for IPF, as the disease is irreversibly progressive from diagnosis.

Advances in understanding the pathogenesis and classification of ILDs have improved the management of these complex conditions. Further research is ongoing to enhance diagnostic accuracy and develop targeted therapies.

1.3.3 Infectious diseases

Infectious diseases are a significant cause of illness and death worldwide, with various factors contributing to their prevalence. These factors include the emergence of new pathogens, the resurgence of known infectious diseases, increasing microbial resistance to drugs, global environmental changes, ease of international travel, and a growing population with weakened immune systems. Lung biopsies often become the primary material for diagnosing infectious diseases. Once the infectious nature is established, identifying the causative agent becomes important for the treatment (antibiotics, antifungal and surgery). Routine staining techniques like Hematoxylin and Eosin (H&E) can reveal many organisms or their effects, but additional studies such as histochemical stains, immunohistochemistry, in situ hybridization, or molecular techniques may be necessary for organism identification and characterization.[55]

There are seven main categories of pulmonary infections, although they are not entirely distinct from each other. It is possible for one type of infection to increase the risk of developing another or for multiple types to coexist simultaneously. These seven categories include community-acquired typical pneumonia, community-acquired atypical pneumonia, nosocomial pneumonia (hospital-acquired), aspiration pneumonia, necrotizing pneumonia, chronic pneumonia, and pneumonia in immunocompromised patients.[32]

Infectious diseases (pneumonia) can also be divided by the causative agents in bacterial, parasitic, fungal and viral infections.

1.3.3.1 Bacterial Infections

Bacterial pneumonias are common infectious diseases caused by various microorganisms. Invasion and propagation of the bacteria into lung parenchyma at the alveolar level causes an inflammatory response, the clinical syndrome of pneumonia. They can range from mild to severe illness, with high mortality rates in some cases. The diagnosis of common bacterial pneumonias, such as those caused by Streptococcus pneumoniae, Haemophilus influenzae, and Klebsiella species, is typically based on a combination of clinical history, physical examination, radiographic imaging and microbiological cultures. Invasive surgical techniques are rarely needed for diagnosis in these cases. Among the bacterial agents, Mycobacteria are classically divided into two clinically important groups: Mycobacterium tuberculosis complex and non-tuberculous mycobacteria. However, there are a few bacterial pneumonias known as "pseudomycoses" that closely resemble fungal diseases clinically and radiologically. These pseudomycoses can raise suspicion of primary lung cancer, leading to surgical resection for definitive diagnosis. Among the pseudomycoses, actinomycosis, nocardiosis, and botryomycosis are bronchopulmonary infections that can be mistaken for bronchogenic carcinoma and are more commonly encountered by surgical pathologists.[55]

1.3.3.2 Fungal Infections

The incidence of pulmonary fungal infections has increased due to the growing number of immunocompromised patients, including those with malignancy, hematologic disease, HIV, and organ transplant recipients on immunosuppressive medication. While these infections can also occur in immunocompetent individuals, they are rare in this population. Advances in serologic and molecular testing have improved the diagnosis of pulmonary fungal infections, but culture and microscopic examination remain important diagnostic methods. New antifungal agents, such as potent azole compounds, lipid forms of amphotericin B, and echinocandins, have expanded treatment options for physicians,

replacing the previously used amphotericin B as the standard therapy. However, surgical intervention may still be necessary for certain fungal infections or complicated cases.[55]

The main types of fungal infections are Aspergillosis, Hstoplasmosis, Cryptococcosis, Coccidioidomycosis and Blastomycosis. Severe acute pulmonary infection can occur after inhalation of a large amount of fungus spores and lead to fever, chills, malaise, dyspnoea, chest pain, and cough and may culminate in acute respiratory distress syndrome.[55]

1.3.3.3 Parasitic Infections

Parasitic diseases continue to be a significant cause of illness and death worldwide. While most parasitic infections are endemic to tropical and subtropical regions, there has been an increased recognition of parasitic lung infections in other parts of the world in recent decades. Factors such as global climate change, population growth, immigration, travel practices, HIV/AIDS, immunosuppressive drug use, and organ transplantations have contributed to the spread of parasites to humans. The pulmonary system can be affected by various parasitic organisms, either during their migration phase or through embolic spread or direct invasion during generalized disease.[55] Parasitic pulmonary infections may be caused by a variety of organisms, which can be divided into three main categories: those caused by protozoa, helminths (worms), and arthropods. Parasitic infections can cause a variety of histopathologic patterns in the lung, including eosinophilic lung disease (eosinophilic pneumonia), eosinophilic abscess, granulomatous inflammation, vasculitis, pleuritis, empyema, and acute lung injury patterns (diffuse alveolar damage, organizing pneumonia, fibrinous pneumonia). Examples include pulmonary schistosomiasis, dirofilariasis, paragonimiasis, strongyloidiasis, and echinococcosis.[56]

1.3.3.4 Viral Infections

Viruses are responsible for a greater number of infections compared to other microorganisms and frequently affect the respiratory tract. The incidence of viral pneumonia has increased in the past decade, mainly due to improved diagnostic techniques such as sensitive nucleic acid amplification tests and the growing population

of immunocompromised patients.[57] Clinically, viral pneumonia in adults can be categorized into two groups: atypical pneumonia in individuals with normal immune function and viral pneumonia in immunocompromised individuals. In immunocompetent adults, influenza virus types A and B are the main causes of viral pneumonia, while cytomegalovirus, herpesviruses, measles virus, and adenovirus pose a risk for pneumonia in immunocompromised patients. Immunocompromised patients generally experience longer and more severe infections, with lung infection being the most common form of tissue-invasive infection in this population. Viral infections are typically mild and self-limiting in healthy individuals but can be life-threatening, especially in immunocompromised patients and infants.[55] Co-infections involving either bacterial and viral pathogens, or multiple viral infections, are common in adults and can exacerbate the severity of viral pneumonia. Viral pneumonias can exhibit various tissue reaction patterns, including bronchitis, bronchiolitis, interstitial pneumonia, diffuse alveolar damage, giant cell reaction, or minimal pathological changes. The detection of characteristic virus-induced cellular alterations, known as cytopathic effect (CPE), can provide useful clues in identifying the causative viral agent. Several methods are available for detecting respiratory viruses, including viral culture, rapid antigen detection, serology, and nucleic acid amplification methods (nasopharyngeal and throat swabs). Nucleic acid amplification tests, particularly polymerase chain reaction (PCR), offer improved sensitivity and specificity with rapid results and are often preferred for diagnosis.[58] While viral pneumonia in immunocompetent patients is often diagnosed based on clinical, radiological, and laboratory findings, more invasive techniques are commonly employed in the diagnostic workup of viral pneumonia in immunocompromised individuals due to atypical symptoms and the presence of characteristic CPE. The main types of viral infective agents are Adenovirus, Measles virus, Cytomegalovirus, Herpes simplex virus type I, Varicella zoster virus and Coronavirus.[55]

Severe Acute Respiratory Syndrome Coronavirus 2 (SARS-CoV-2), a novel coronavirus, has emerged as a global public health threat, causing the ongoing COVID-19 pandemic. This enveloped RNA virus belongs to the Betacoronavirus genus and is closely related to SARS-CoV and MERS-CoV.[59] It primarily spreads through respiratory droplets,

leading to a range of clinical manifestations, from mild respiratory illness to severe pneumonia and ARDS. SARS-CoV-2 exhibits high transmissibility, allowing for efficient human-to-human transmission. This enveloped RNA virus primarily targets the respiratory system and gains entry into host cells through the interaction between its spike (S) protein and the angiotensin-converting enzyme 2 (ACE2) receptor present on the surface of target cells. The S protein is composed of two functional subunits: S1, which contains the receptor-binding domain (RBD), and S2, responsible for membrane fusion. The binding of the RBD to ACE2 triggers a conformational change in the S protein, allowing the virus to fuse with the host cell membrane.[60] This fusion process is facilitated by host cell proteases, including transmembrane protease serine 2 (TMPRSS2) and cathepsin L, which cleave the S protein and activate its membrane fusion activity. Once inside the host cell, the viral RNA is released and serves as a template for the synthesis of viral proteins and replication of the viral genome. The virus hijacks the host cell machinery to produce viral proteins, including the replicase-transcriptase complex, which is responsible for viral RNA replication. The newly synthesized viral RNA and structural proteins are then assembled into new viral particles within the host cell. These viral particles are released either by budding from the host cell membrane or by cell lysis, leading to the spread of the virus to other cells and tissues (Figure 1.20).[61,62]

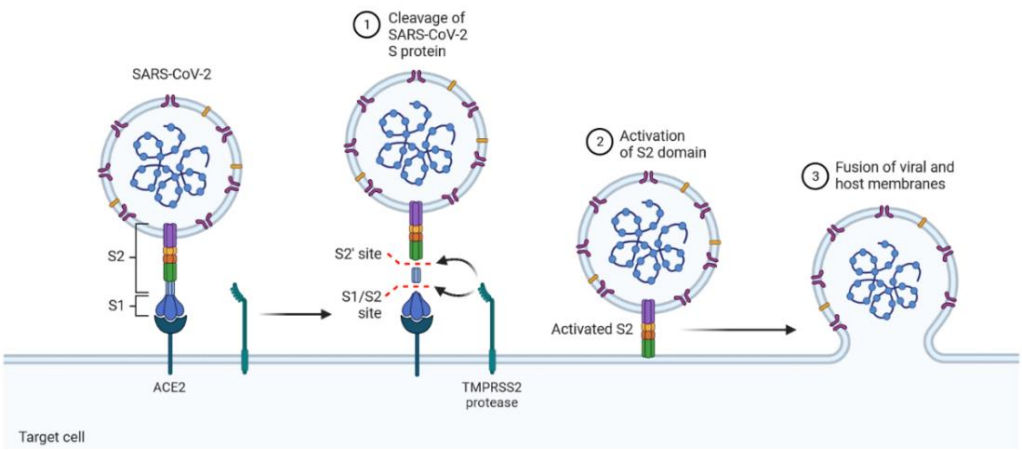

Figure 1.20 Mechanism of SARS-CoV-2 viral entry. Image source: Biorender

In addition to respiratory epithelial cells, SARS-CoV-2 can also infect other cell types expressing ACE2, including cells in the gastrointestinal tract, kidneys, heart, and blood vessels. The widespread expression of ACE2 in various tissues may contribute to the diverse clinical manifestations observed in COVID-19 patients.

In summary, COVID-19 infection within the lungs can be divided into three phases. The early infection phase involves viral replication and mild symptoms. The second phase, known as the pulmonary phase, is characterized by respiratory dysfunction due to lung injury and hypoxemia, as well as the activation of adaptive immunity. The most severe cases progress to a third phase called systemic hyper-inflammation, where a combination of direct viral injury, uncontrolled cytokine release, and microvascular inflammation can lead to multi-organ failure, ARDS, haemorrhage/coagulopathy, and secondary bacterial infections. Epithelial damage and vasculopathy are typical in the early infection phase, while fibrotic changes typically occur around three weeks after symptom onset. The presence of interstitial fibrosis has been observed in histological examinations of COVID-19 lung samples, suggesting ongoing fibrotic changes. Lung fibrosis can result in impaired lung function and long-term respiratory complications for individuals recovering from severe COVID-19.[63]

Efforts to understand the pathogenesis, epidemiology, and immune responses to SARS-CoV-2 are crucial for effective control and prevention strategies. Potential antivirals target the different steps of SARS-CoV-2 replication, ranging from receptor binding, entry and fusion to replication. Furthermore, immunoglobulin-based and immunomodulatory drugs (Dexamethasone - Dex) are potential therapeutics as well (Figure 1.21). Diagnostic methods, including RT-PCR-based assays targeting viral RNA, emerged to identify infected individuals. Vaccines have also been rapidly developed, such as mRNA-based vaccines and vector-based vaccines, to mitigate the impact of COVID-19. Ongoing research continues to explore potential therapeutics and antiviral agents to combat SARS-CoV-2. Targeting the viral entry process, such as blocking the interaction between the S protein and ACE2 or inhibiting host proteases involved in membrane fusion, represents potential strategies to prevent viral infection and spread.[64]

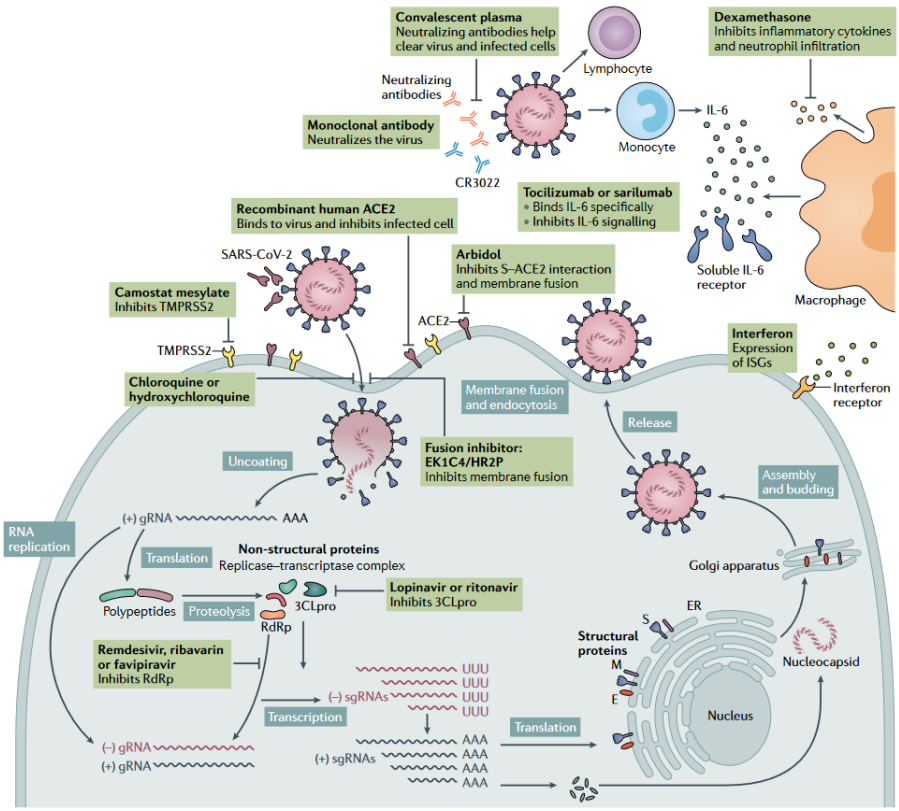

Figure 1.21 SARS-CoV-2 replication and potential therapeutic targets. Image source: B. Hu, et al, 2021

1.3.4 Neoplastic diseases

Lung cancers are traditionally divided into non–small cell carcinoma (NSCC) and small cell carcinoma (small cell lung carcinoma, SCLC), with the former accounting for 80% of the cases and the latter accounting for the remaining 20%. NSCC are divided in squamous cell carcinoma, adenocarcinoma and large cell carcinoma. SCLCs behave aggressively and are treated non-surgically in most cases with radiation and chemotherapy, whereas NSCCs are managed by a combination of surgery and adjuvant therapy.[65]

About 85–90% of lung tumors arise in active smokers or those who have recently stopped smoking, air pollution, occupational and radiation exposure, and the favoured sites of metastases for pulmonary neoplasms are liver, brain, and bone.[32]

Complications of pulmonary neoplasms are: partial obstruction of airway, predisposing to pneumonia, complete obstruction of airway, suppurative bronchitis that can lead to bronchiectasis, abscesses and local extension can also cause pleuritis and pericarditis.[32]

The main signs and symptoms are cough, haemoptysis, dyspnoea, obstructive pneumonia, wheezing and stridor due to airway obstruction, chest wall pain due to infiltration of chest wall and nerves, and hoarseness due to involvement of recurrent laryngeal nerve. Symptoms of metastases are seizures, bone pain, weight loss. Diagnosis methods are computed tomography (CT) scan and biopsy.[32]

Macrophages are critical players in a range of physiological and pathological processes, including inflammation, tissue repair, and cancer. Their role in these processes is highly context-dependent, and their dysregulation can lead to a range of diseases, including chronic inflammation, autoimmune disorders, and cancer.

Moreover, most drugs used in clinics have low solubility, their concentration in blood fluctuates widely, they are not easily eliminated from the organism and they distribute in other healthy tissues and cells, causing adverse effects. Any intervention needs to consider an optimal dose, time and specific targeting in relation to the stage of the disease.[66]

To address all this disadvantages, nanomedicine has offered promising strategies to overcome the current limitations in medicine, providing a more efficient platform. Nanocarriers can potentially be very sensitive and small changes in their size, shape and coating can significantly affect their properties with a greater chance to improve biostability and solubility of encapsulated drugs, promote transport across membranes and prolong circulation times to increase safety and efficacy.[67] Despite the progress in understanding the lung development, metabolism and repair, pulmonary disorders continue to have a significant global morbidity and mortality burdens. Understanding the complex biology of macrophages is therefore essential for the development of novel therapeutic strategies targeting these cells, including nanovectors systems. New

approaches to overcome the side effects of some current drugs can be pursued thanks to the advances in nanomedicine.

1.4 Nanoparticles for biomedical applications

Nanotechnology is the engineering and manufacturing of materials at the atomic and molecular scale. In its strictest definition from the National Nanotechnology Initiative (NNI) in 2000, nanotechnology refers to the intentional design, characterization, production, and applications of materials, structures, devices and systems by controlling their size and shape in the nanoscale range (1−100 nm size regime in at least one dimension). Despite this size restriction, nanotechnology commonly refers to structures that are up to several hundred nanometres in size and that are developed by top-down or bottom-up engineering of individual components.[68] Nanotechnology can be classified in two main categories: nanodevices, miniature devices at nanoscale including microarrays and some intelligent machines, and nanomaterials that contain particles in the nanoscale range.[69]

The term nanomaterial identifies particles that have a well-defined chemical composition, with their own organization and internal or external structures on the nanoscale dimension, making them comparable with sub-cellular entities.[70] Nanomaterials generally consist of metal atoms, non-metal atoms, or a mixture of both, commonly referred to as metallic, organic, or semi-conducting particles, respectively. The surface of nanomaterials is usually coated with polymers or bio-recognition molecules for improved biocompatibility and selective targeting of biologic molecules. The final size and structure of nanomaterials depend on the synthesis protocols (salt and surfactant additives, reactant concentrations, reaction temperatures and solvent conditions). A common feature of all nanomaterials is their large ratio of surface area to volume and in this dimensional range, the properties of matter change drastically.[71]

Nanomedicine is an interdisciplinary field, which combines technology, engineering, biomedical and pharmaceutical science for the improvement of diagnosis, treatment of diseases and for the evaluation of toxic effect played by many drugs.[71]

Nanotechnology could help overcome the limitations of conventional delivery (biodistribution and intracellular trafficking) through cell-specific targeting, molecular transport to specific organelles and other approaches. For that reason, due to their nanoscale level, nanoparticles (NPs) are a key component in nanomedicine. NPs used in biomedical research are highly diverse in structure, chemical composition, size, morphology, electrostatic charge, hydrophobicity, surface chemistry and other properties (Figure 1.22).[72]

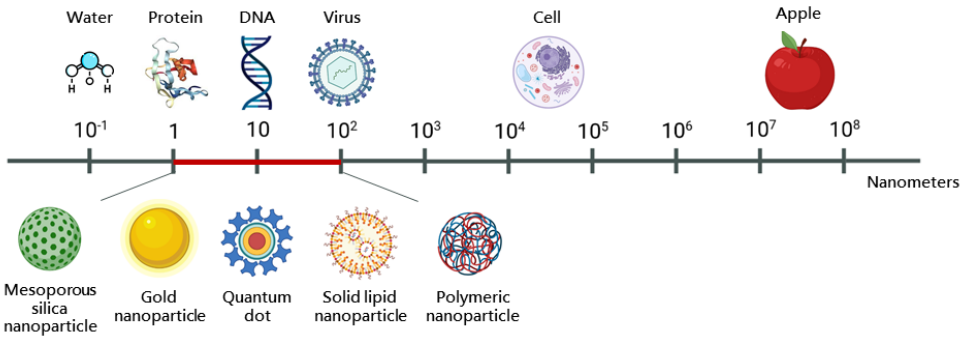

Figure 1.22 Nanoscale

1.4.1 Advantages of the use of nanoparticles

NPs are the essential component of nanotechnology and acquire a great potential in medical applications. Formation of stable interactions with ligands, variability in size and shape, high carrier capacity and the possibility of binding of both hydrophilic and hydrophobic substances make nanoparticles adaptable platforms for the specific and controlled delivery of micro- and macromolecules in disease therapy.[69] Moreover, the NPs larger ratio of surface area to volume, with dimension-related properties that differ from the bulk materials out of the nanoscale range, make them comparable and able to interact with sub-cellular entities. Modern medicine has recently started to take advantage of these unique properties concerning the availability of biomedical applications, from diagnostics to new therapies and biopharmaceuticals, leading to the development of nanomedicine.

One of the major obstacles in the treatment efficiency of various disease is the delivery of therapeutic agents to the target area. Conventional therapeutic agents often has

limitations such as non-selectivity, serious side effects, low efficiency, low solubility and poor biodistribution.[66,73] Drugs, to have a plasma therapeutic effect, must be absorbed in the targeting area and dissolved in an aqueous solution, independently of the route of administration. In the case of a low solubility, drugs are often poorly absorbed, leading to a lower bioavailability. Association of therapeutic agents with nanoparticles exhibiting unique physicochemical and biological properties and designing their pathways for suitable targeting is a promising approach in delivering a wide range of molecules to certain locations in the body increasing the **drug solubility**.[69] Therapeutics can be encapsulated within the NPs core, entrapped in the polymer matrix, chemically conjugated to the polymer or bound to the NPs surface. This enables delivery of various payloads including hydrophobic and hydrophilic compounds, as well as cargos with different molecular weights such as small molecules, biological macromolecules, proteins and vaccines (Figure 1.23).[74]

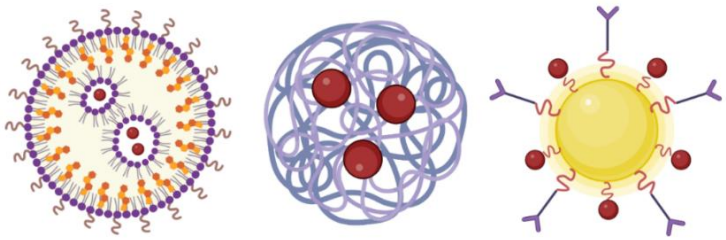

Figure 1.23 Strategy of drug association with NPs. In order to improve drug solubility and delivery, the active compounds can be encapsulated within the NPs core, entrapped in the matrix or chemically conjugated to the polymer or bound to the NPs surface.

The aforementioned association strategies improve the concentration of therapeutic agents within specific cells or tissues. This allows for the use of lower doses during therapy, especially when there is a conflict between the therapeutic activity and the agent's toxic effects. By increasing the concentration of therapeutic agents at the target site, their therapeutic index is enhanced, leading to improved effectiveness and/or increased tolerability within biological systems. The use of NPs as delivery systems can **improve drug pharmacokinetics**. Moreover, water-insoluble therapeutic agents can also be conjugate to nanoparticles, which can protect them from physiological barriers and improve their bioavailability.[69]

One of the main advantages in the use of NPs is the **targeted therapy** that allow the delivery of appropriate amounts of drug for a prolonged period to the specific affected site in the organism. By decorating the nanoparticles surface with polyethylene glycol (PEG), carbohydrates, acetyl groups and protein moieties (RGD peptide, albumin) it is possible to regulate the retention time in the blood circulation and in the body.[69] Surface modification of nanoparticles with long-chain polymers, for example PEG, was shown to minimize non-specific protein absorption onto the nanoparticle surface. Due to its intrinsic physicochemical properties, PEG is a favourable polymer for therapeutic nanoparticles, which decreases their phagocytic uptake and reduces their accumulation in non-target organs, enhancing their **biostability** and half-life circulation in the bloodstream giving more probabilities of reaching the targeting point. Factors such as length, shape, and density of PEG chains affect surface hydrophilicity and phagocytosis.[75] Designing a surface functionalization with the conjugation of targeting ligands (antibodies, sugars) able to interact with specific receptors expressed in biological barriers can improve the target-specific delivery of nanoparticles; however, surface modification can affects their biodistribution and recognition ability. This opportunity **enhance their efficacy**, as they increase the drug permeability by an active passage. Moreover, the association of therapeutic nanoparticles with contrast agents provides a way of tracking their pathway and imaging their delivery location in *in vivo* systems.[69]

The possibility of decorate and functionalize the NPs surface could favour the passage and accumulation of active compounds to their target, reducing off-targeting effects caused by the penetration into other organs. An example is doxorubicin, an antineoplastic agent for targeting a wide variety of cancers that cause cardiac toxicity, producing congestive heart failure. Its encapsulation into liposomal NPs, Doxil®, **reduced toxicity** and promote the **enrichment in the selected tissue.**[76]

NPs must contain a stabilizing agent (citrate or CTAB), to reduce the probabilities of aggregation and formation of clusters before administration, **increasing colloidal stability**[77].

The **size** of therapeutic nanoparticles plays a crucial role in their circulation and distribution within the body. Nanoparticles smaller than 10 nm can be easily eliminated through kidney filtration, while particles larger than 200 nm may be cleared by phagocytic cells in the reticuloendothelial system (RES).[67] The **shape** of nanoparticles also affects their biodistribution and cellular uptake. For example, rod-shaped cationic nanoparticles are more likely to be taken up by endosomes compared to cationic nanoparticles of other shapes, potentially due to their resemblance to rod-shaped bacteria.[69] The **surface charge** of therapeutic nanoparticles influences their clearance and targeted delivery. Positively charged nanoparticles generally induce a stronger immune response compared to neutral or negatively charged ones. Nanoparticles with a surface potential ranging from -10 to +10 mV are less prone to phagocytosis and non-specific interactions. However, the optimal range may vary depending on the nanoparticle material. Surface charge also relates to the pH sensitivity of nanoparticles, allowing them to be designed to recognize and locate in specific cellular compartments. For example, acidic nanoparticles can be targeted to endosomes or lysosomes, which have a pH below 6.0, for cargo release.[69,74] The modulation of these three important parameters give the opportunity to predict and control the biodistribution and the fate of the NPs within the body.

Moreover, the combination of more than two drugs with different physicochemical or pharmacological properties can be achieved in the nanomaterial surface, offering the **opportunity of a co-delivery**. An example of this strategy is the development of a cell-mediated lung-targeted delivery platform carrying dual combined therapies, an antioxidant agent and a kinase inhibitor that suppresses the activation of myofibroblast, in order to reverse IPF.[78]

NPs have the potential to improve the stability and solubility of encapsulated cargos, promote transport across membranes and prolong circulation times to increase safety and efficacy. For these reasons, NPs research has been widespread, generating promising results *in vitro* and in animal models.[74]

1.4.2 Types of therapeutic nanoparticles

Nanomaterials can be classified in two main categories: Nano-structured, sub-categorized into inorganic, lipid-based and polymeric nanoparticles, and nanocrystalline, particles formed by the combination of therapeutic agents in crystalline form.[69]

1.4.2.1 Inorganic nanoparticles

Inorganic materials such as gold, iron and silica have been used to synthesize nanostructured materials for various drug delivery, diagnostic and imaging applications, including carbon nanotubes, nanodiamonds, metallic nanoparticles, quantum dots, and silica-based nanoparticles. These inorganic NPs are precisely formulated and can be engineered to have a wide variety of sizes, structures and geometries. Moreover they possess unique physical, electrical, magnetic and optical properties from the base material itself.[69,74] Their small dimensions and well-established synthesis, allows the tuning of their size, shape and functionalization for specific targeting, making them very promising nanomaterials for theranostics (Figure 1.24). Gold NPs have been used in preclinical studies for photothermal therapies to kill cancer cells due their plasmonic properties[79]. Quantum dots and magnetic iron oxide (magnetite or maghemite) NPs possess superparamagnetic properties and are used in bioimaging as contrast agents for magnetic resonance imaging (MRI) as a diagnostic tool for tumour diagnosis, damaged tissues and neurological disorders, intensifying the contrast between tissues[80]. The main disadvantages in their clinical application is the low solubility and toxicity, especially with heavy metals.[74,81]

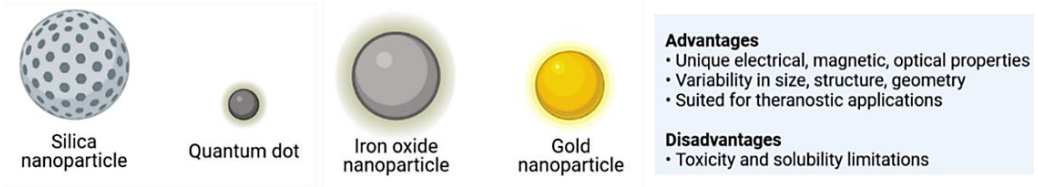

Figure 1.24 Most common types of inorganic nanoparticles with main advantages and disadvantages.

1.4.2.2 Lipid-based nanoparticles

Lipid-based NPs can be divided into liposomes and solid-lipid NPs.[69] These structures are most typically spherical comprising at least one lipid bilayer surrounding an internal aqueous compartment (Figure 1.25). Lipid-based NPs are characterized by formulation simplicity, self-assembly ability, biocompatibility, high bioavailability, ability to encapsulate big amount of drug molecules and a range of physicochemical properties that can be controlled to modulate their biological characteristics. For these reasons, lipid-based NPs are the most common class of Food and Drug Administration (FDA)-approved nanomedicines. Moreover, they give the opportunity of design surface modification (PEG) and decoration, thanks to the use of soft-materials like phospholipids, to extend their circulation and improve the drug delivery releasing the active molecules in the target site and reducing toxic effects in other healthy organs.[74,82] Liposomes are typically composed of phospholipids that arrange in unilamellar or multilamellar structures separated by aqueous spaces. This allows the liposome to carry and deliver hydrophilic, hydrophobic and lipophilic drugs and also combined in the same system.[83] One of the most important advantages of liposomes is their ability to fuse with cell membrane and release their contents into the cytoplasm, which makes them suitable intelligent carrier systems for targeted delivery.[69] Solid-Lipid NPS are aqueous colloidal dispersions comprised of a lipid matrix that is solid at room and body temperatures. Surfactants improve their stability, whereas the choice of lipid affects the drug delivery characteristics. The size of SLNs varies from 10 to 1000 nm. These NPs can be decorated or loaded with various moieties (antibodies, magnetic nanoparticles, pH sensitive lipids/polymers) to modulate targeted delivery and stimuli-responsive drug release. They are shown to be effective carriers for cancer, pulmonary and oral drug delivery purposes.[69,84] One of the most important lipid-based NPs, recently approved by the FDA, is the Pfizer/BioNTech and Moderna mRNA Covid-19 vaccine.[85]

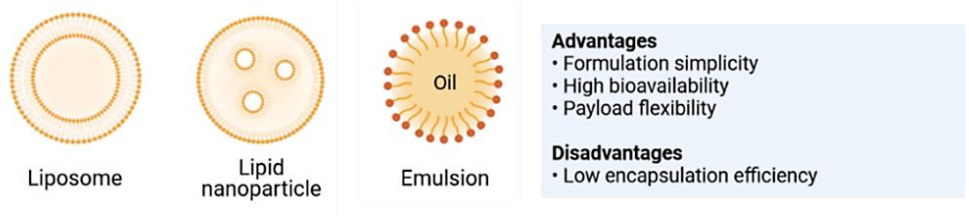

Figure 1.25 Most common types of lipid-based nanoparticles with main advantages and disadvantages.

1.4.2.3 Polymeric nanoparticles

Polymeric NPs include dendrimers, micelles, nanogels, nanospheres, protein nanoparticles and drug conjugates (Figure 1.26). They can be synthesized from synthetic (polycaprolactone, polylactic acid and their monomers) or natural (chitosan, albumin, gelatin and alginate) materials, providing NPs with therapeutic applications characterized by biocompatibility and biodegradability. Moreover, natural polymer-based materials seems to overcome toxicity issues with significant improvement in the therapeutic agents efficiency.[69] Polymeric NPs also have variable drug delivery capabilities. Therapeutics can be encapsulated within the NPs core, entrapped in the polymer matrix, chemically conjugated to the polymer or bound to the NPs surface. This enables delivery of various payloads including hydrophobic and hydrophilic compounds, making polymeric NPs ideal for co-delivery applications. By modulating properties such as composition, stability, responsivity and surface charge and functionalization, the loading efficacies and release kinetics of therapeutics can be precisely controlled.[74] They can be classified as nanocapsules, a unique polymer membrane that encloses therapeutic agents, or nanospheres, in which therapeutic agents are directly dispersed throughout or within the polymer matrix.[86] Existence of a multitude of preparation methods of polymeric nanoparticles can control the release characteristics of incorporated therapeutic agents, which allows the delivery of a higher concentration of agents to the target location.[69] Moreover, their surface could be easily modified and functionalized with a specific recognition ligand allowing them to deliver drugs, proteins and genetic material to targeted tissues, which makes them useful in cancer medicine, gene therapy

and diagnostics. There are also protein nanoparticles made of protein polymers, which are isolated from animal or plant origin (collagen, gelatin, silk, albumin, elastin, and soy), that are self-assembled into functional drug delivery carriers with advantages of polymer-based nanoparticles.[87] However, disadvantages of polymeric NPs include an increased risk of particle aggregation and toxicity.[74]

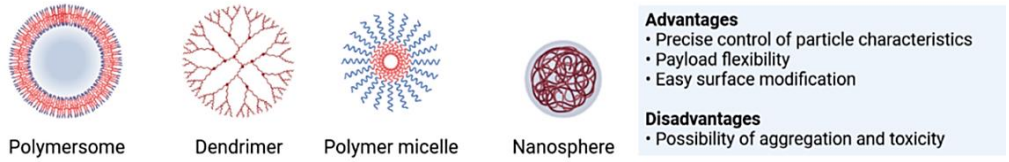

Figure 1.26 Most common types of polymeric nanoparticles with main advantages and disadvantages.

1.4.3 Delivery and biodistribution of nanoparticles

The biological barriers that NPs encounter depend on the route of administration as well as the patient's disease type and progression.[67] Although local delivery methods may allow NPs to bypass some of the obstacles faced by systemic delivery, they often involve more invasive procedures and complex techniques that present other limitations. Furthermore, local delivery may only be useful in diseases where the pathology is restricted to known, accessible sites (solid cancers, traumatic injuries) so systemic administration is more common.[74]

Circulation, stability and opsonisation - NPs in blood circulations have to face a complex series of biological barriers that limit site-specific bioavailability. Moreover, obstacles such as excretion, blood flow, opsonisation and subsequent interaction with the mononuclear phagocytic system (MPS - or reticuloendothelial system, RES) can influence their stability and delivery and these factors depend on the physicochemical properties of the nanomaterial itself. RES consists of a system of phagocytic cells, predominantly resident macrophages, in the spleen, lymph nodes and liver, that sequesters nanoparticles immediately after injection.[88] The process of sequestration begins with opsonization of nanoparticles with the adsorption of plasma proteins (serum

albumin, apolipoproteins, complement components and immunoglobulins) onto the surface of circulating nanoparticles, forming the protein corona and masking the functionalization of groups coated on the NPs surface.[89] The formation of protein corona can be divided in two different layers, an inner layer called hard corona, which is formed by high affinity binding proteins, with a very slow exchange rate and it is considered irreversible, and the upper layer, the soft corona. This soft corona has low affinity proteins with weak protein-protein interactions among them and between the proteins of the hard corona, which allows to a very fast exchanging and substitution of proteins depending on the biological environment. This process depends on several factors, including nanoparticle size, surface charge, hydrophobicity and surface chemistry.[90,91]

To prevent the protein absorption on the NP surface and rapid excretion, polymers such as PEG are widely used due its stealth effect. When NPs are PEGylated, the high level of hydration of the hydrophilic polyether backbone, prevents the protein adsorption on the hydrophobic polymer surface by steric repulsion.[92]

In the bloodstream, NPs are subjected to vary flow rates that induce shear stress and may damage the platforms or their cargo and prevent extravasation. These fluid forces can strip NPs of their surface coatings and can prevent NPs from localizing to vessel walls to extravasate to reach target tissues. Larger particles and ellipsoids, discoid shapes and nanorods with higher aspect ratios localize to blood vessels walls better than spheres, making them better internalized into epithelial cells. This is due to the flow-induced rolling in shapes with high ratios, which results in edge margination at a speed proportional to the NP aspect. Clearance of NPs from the circulation can be influenced by their physicochemical properties, but often results from interactions with the MPS. Phagocytes (predominantly macrophages), monocytes and dendritic cells take up NPs and accumulate in the spleen and liver. This clearance tends to happen more rapidly in stiffer NPs. In terms of surface charge, cationic NPs are generally rapidly cleared, followed by anionic NPs, whereas neutral and slightly negative NPs have the longest half-lives in circulation. Nanocarrier size also affects its *in vivo* fate, with larger particles (>200 nm) shown to accumulate in the liver and spleen while NPs with a diameter less than 10 nm are rapidly eliminated by the kidneys.[67,74]

Cross of biological barriers - To protect organs and tissues from physical, chemical and biological damage and maintain homeostasis in tissues, only small molecules with specific properties or ligands are able to cross some of the biological barriers in the organism using specific binding receptors. Extravasation is the first step for a NP in circulation to reach the target tissue, but this process leads to a non-specific distribution.[74] One of the first barriers that nanomaterials must be able to cross is the endothelium, which has a limited pore size.[93] The best way for the NPs to cross is through leaky blood vessels with an increase permeability, such as in tumours (enhanced permeation and retention effect- EPR), liver, spleen and bone marrow, where most of the administered NPs can be found. Other biological membranes are the intestinal tract or lung epithelium. However, optimizing the administration route and adding targeting moieties to the surface can improve biodistribution in the target site.[74] For example, intraperitoneally or intravenously injected NPs tend to accumulate in the liver and spleen, while NPs administrated by intratracheal or intranasal route are able to reach the lungs.[94,95]

- **Uptake from RES organs**

One of the main issues when NPs are administered into biological systems is their uptake by RES organs such as liver and spleen. Those organs express a high number of mononuclear phagocytic cells, which act as scavengers to eliminate cell debris, damaged cells and external materials from the bloodstream, as a clearance signal. The removal of NPs from the circulation is due to their phagocytic capacity that cause their accumulation in liver, spleen, bone marrow or lymph nodes[94,96].

Particles of >10 nm size, tend to accumulate inside the hepatobiliary system, with a little or no renal clearance[97] and particles over 200 nm tend to accumulate inside the spleen[98]. NPs that are smaller than 10 nm are eliminated by renal clearance[99,100].

PEGylation can increase the half-life circulation of NPs avoiding the RES organs uptake, due the reduction of the opsonisation of proteins in the NP surface. The higher is the number of proteins absorbed in the NP surface, the faster will be the uptake into liver and spleen[92,96].

- **Pulmonary administration and deposition**

Pulmonary drug delivery is an effective and efficient method for local and systemic effects but it is hindered by the fact that the respiratory tract has defense mechanisms to keep inhaled materials out of the lungs. [101] However, high vascularization, large epithelial surface area, high solute exchange capacity, and thin alveolar absorptive membranes are the factors that make the pulmonary system an ideal delivery target. Inhalation, intranasal and intratracheal treatments are therefore valid routes of administration for lung targeting. Once inhaled, NPs have to cross different types of barriers, namely, mechanical, chemical, immunological and behavioural barriers.[102]

- Mechanical barriers: The lungs are composed of a complex bronchial tree network through which NPs must pass without being deposited in order to reach and penetrate the alveolar region. This allows them to gain access to the target site, which is the large epithelial area. Drug absorption is regulated by a thin alveolar–vascular permeable barrier. This barrier gets more pronounced in pathological conditions because of the narrowing of the airway (bronchoconstriction, mucus hypersecretion, inflammation, or mucus plugs).[102]

The ideal aerosol size for delivering drugs to the entire lung is typically below 5 μm in aerodynamic diameter. To target the alveolar epithelium specifically, even smaller particles with an aerodynamic diameter in the range of 1 μm to 5 μm are deposited in the deep lungs, while particles >10 μm are generally deposited in the oropharyngeal region (Figure 1.27). However, the deposition of particles is a complex process that also relies on inhalation parameters, particularly the flow rate, lung volume, and breath-hold pause during inhalation.[103] Additionally, the presence of bifurcations in the airways creates a constantly changing flow field.

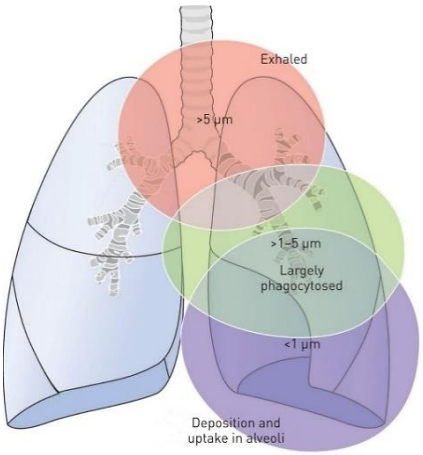

Figure 1.27 Schematic diagram showing the size-dependent deposition of particles at the different levels of the lungs. Image source: S.H. van Rijt, et al, 2014

Particle deposition (Figure 1.28) occurs through four main mechanisms, depending on particle size, airflow and location in the respiratory system:

1. Impaction: When the airflow changes at airway bifurcations, particles tend to continue along their original path due to inertia and may collide with an airway surface. This mechanism is more significant for larger particles near the first airway bifurcations, particularly in the bronchial region. Impaction accounts for the majority of particle deposition based on mass.[102,104]

2. Sedimentation: Sedimentation refers to the settling of particles in the smaller airways of the bronchioles and alveoli, where airflow is low and airway dimensions are small. The rate of sedimentation depends on the particles' terminal settling velocity, making it more relevant for particles with larger aerodynamic diameters. Hygroscopic particles, which increase in size in warm and humid air passages, are more likely to deposit through sedimentation.[102,104]

3. Interception: Interception occurs when a particle contacts an airway surface due to its physical size or shape. Unlike impaction, particles deposited by interception do not deviate from their airflow. Interception is most likely to happen in small airways or when the airflow is close to an airway wall. Fibrous

particles, especially, have a higher chance of intercepting due to their length and small aerodynamic diameters relative to their size.[102,104]

4. Diffusion: It is the primary mechanism for particles with diameters less than 0.5 μm and is determined by geometric size. It involves the net movement of particles from areas of high concentration to areas of lower concentration due to Brownian motion, random movement of particles caused by constant collisions with air molecules. Diffusional deposition is more prevalent when particles have just entered the nasopharynx and is also likely to occur in the smaller airways of the alveolar region with low airflow.[102,104]

The pulmonary membrane allows for the permeation of small molecule drugs, as well as certain peptides and proteins. The thickness of the lung epithelium varies throughout the respiratory system, being thicker in the trachea (50-70 μm) and thinner in the alveoli (0.2 μm). The lungs have greater permeability to macromolecules compared to other entry portals in the body and the effectiveness of absorption depends on various factors.[102] Certain endogenous molecules present in lung fluids, such as albumin, immunoglobulins, and transferrin, have specific receptor-mediated transport mechanisms in alveolar epithelial cells, resulting in higher absorption rates. Inhaled proteins can aggregate, stimulating opsonization and subsequent phagocytosis and enzymatic destruction by alveolar macrophages. Proteins, due to their structure and size, are generally resistant to peptidases, but can be hydrolyzed by proteases in specialized organelles. Small peptides and proteins are rapidly absorbed after inhalation, while lipophilic small molecules have extremely fast absorption rates. Inhalation allows for the control of absorption rates, with insoluble molecules remaining in the lungs for extended periods and encapsulation in slow-release particles aiding in absorption regulation.[101,104] The pulmonary route offers significantly higher bioavailability for peptides and proteins compared to other non-invasive routes. The lung's absorptive surface, small volume of fluid, and the presence of a capillary network near the air interface contribute to this high bioavailability.

The lungs contain also a gel layer of lung mucus above a periciliary liquid layer where cilia beat. Mucociliary clearance, a natural defence mechanism of the lungs, clears

deposited materials from the conducting airways and transports them to the oropharynx, where they are either swallowed or expectorated. In healthy lungs, the tracheobronchial airways are completely cleared of deposited material within 24 hours. Mucociliary clearance can have both negative and positive impacts on drug delivery, as it can either move drugs away from target sites or facilitate the movement of deposited drugs toward more favourable areas.[105]

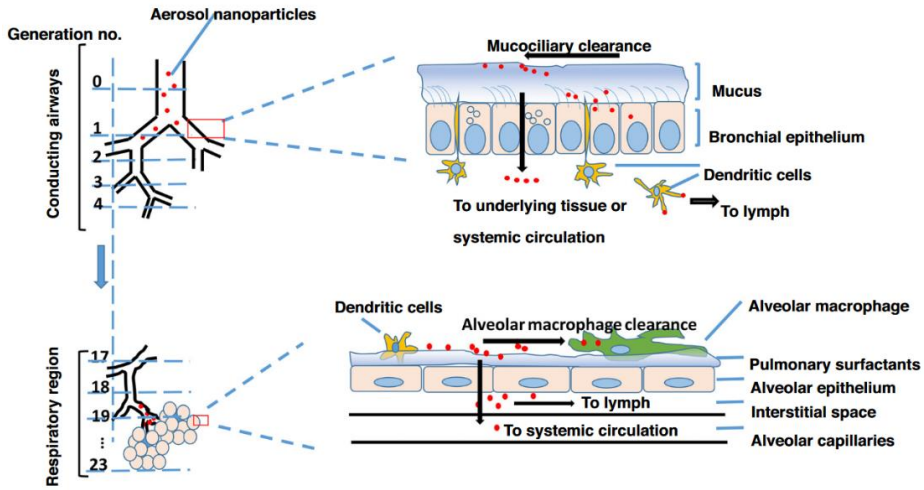

Figure 1.28 Different fate of nanoparticles after deposition in the lung. Human lung have 3 generations of branching airways, 16 generations of conducting airways and 7–23 generations of respiratory region. The main clearance mechanisms for NPs in the conducting airways and respiratory region is mucociliary clearance and alveolar macrophage clearance, respectively. Nanoparticles that cross epithelial cells to the interstitial space can translocate into the systemic circulation or lymph. Image source: Q. Liu, et al, 2020

- Chemical and immunological barriers: Particles deposited within the lungs are expected to dissolve in lung fluids, although the understanding of this process remains incomplete. If not removed by mucociliary clearance, the drug should be available to exert a local effect in the tissue or be absorbed into the systemic circulation. However, deposited drugs may face challenges from various factors, including proteolytic enzymes and surfactant. Proteolytic enzymes, such as neutral endopeptidase and cathepsin H, can hydrolyze peptides and proteins in the lungs, leading to their inactivation.[105] Undissolved drug particles may come into contact with alveolar macrophages, which are the primary phagocytic cells responsible for defending against inhaled particles. Alveolar

macrophages form an immunological barrier that can ingest drug particles and remove them from the lungs through the lymph system or by transferring them to the mucociliary system.[101] Nanoscale particles, measuring 200 nm or less, have the ability to penetrate cellular barriers without the need for energy and are only minimally engulfed by macrophages. On the other hand, particles in the micron scale range, between 1 and 5 μm, are effectively engulfed by macrophages. This suggests that when small particles are deposited in the deep lung, they can successfully evade macrophage clearance. Although these cells are generally regarded as a barrier for nanomedicine-mediated drug delivery in the lung, they constitute an important target for pulmonary pathologies with an inflammatory component. Consequently, nanoparticles possess favorable deposition characteristics, making them suitable for targeted delivery to the alveolar regions of the lung. However, in the deep lung, the monolayer of the alveolar epithelium is extremely thin and the surface liquid lining the alveoli is much thinner than in the bronchial tree and therefore represents less of a hindrance for particle uptake. The air side of the alveolar cells is patrolled by macrophages, which engulf and digest insoluble particles that are deposited there quite rapidly.[106]

Surfactant plays a crucial role in lung drug release by affecting the behaviour of drugs and their interaction with the pulmonary membrane. Surfactant is a mixture of lipids and proteins that lines the inner surface of the alveoli in the lungs. Its primary function is to reduce surface tension and maintain the stability of the alveoli during breathing.[107]

In the context of drug delivery, surfactant can impact the release and absorption of inhaled drugs through the formation of fine droplets or particles of inhaled drugs, the dissolution and solubilization of certain types of drugs, the penetration of drugs across the pulmonary membrane and the adherence to the mucus layer lining the airways, prolonging drug residence time and enhancing local drug concentration. This can be particularly advantageous for sustained drug release and localized therapy. Moreover, surfactant can protect drugs from enzymatic degradation and physical degradation caused by the lung environment. It forms a protective layer around the drug particles, shielding them from enzymatic reactions and maintaining drug integrity until absorption occurs.[107] Surfactant, on the other hand, may prevent the adhesion of inhaled particles to lung surfaces, making them more accessible to macrophages.[104,108] Due to this properties,

recently, bio-inspired pulmonary surfactant-modified nanocarrier have been formulated.[109]

- Behavioral barriers: In case of an inhalation therapy, the effectiveness of pulmonary drug delivery depends significantly on how patients use their inhaler devices. Adherence, which refers to the number of doses taken compared to the prescribed number, is a critical factor. Unfortunately, non-adherence to the prescribed regimen is common and can be intentional or unintentional, leading to a suboptimal and variable drug deposition in the lungs.[101,102]

NPs uptake and internalization - Once nanomaterials escape retention in RES organs or cross pulmonary barriers, they accumulate in the desired tissue and interact with the cell membranes and through which process will be internalized in the cytoplasm.

The corona formed around NPs can influence their interaction with cells and affect cellular uptake. The cellular membrane, consisting of a selectively permeable phospholipid bilayer, plays a crucial role in these interactions. NPs covered by the corona interact with the negatively charged cell surface, which contains various biomolecules in a fluid mosaic structure. The characteristics of NPs, such as hydrophilicity and charge, altered by the corona, can impact cellular uptake in different cell types.[110]

The charge of NPs also plays a significant role in their interaction with cells. Anionic NPs may struggle to make contact with the cell surface due to repulsive forces, while highly cationic NPs can damage the cell membrane and cause cytotoxicity. Regarding shape and size, spherical NPs have improved uptake over rod-shaped particles in non-phagocytic cells, while others show the opposite effect. The size of NPs also influences their uptake, with smaller NPs generally internalizing better, but possibly causing cytotoxicity.[111]

Cellular uptake can occur through passive and active mechanisms. Passive diffusion is limited to small, uncharged molecules, while NPs predominantly rely on active transport to cross the cell membrane. NPs commonly utilize endocytic pathways, where the plasma membrane engulfs NPs on the cell surface by invagination and releases them

intracellularly. The type of endocytosis a NP undergoes depends on factors such as cell type, NP size, and receptor interactions. Non-specific interactions lead to phagocytosis or macropinocytosis, while specific interactions, particularly with negatively charged NPs, may involve caveolin-mediated or clathrin-mediated endocytosis (Figure 1.29).[74,110]

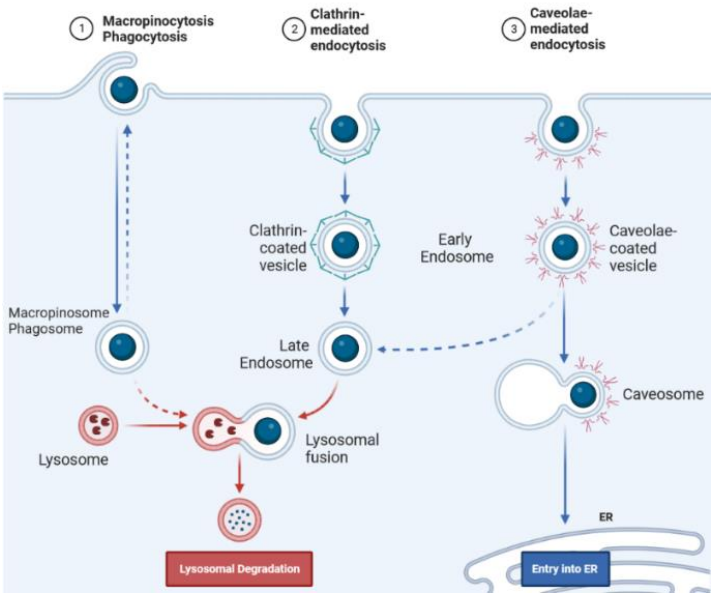

Figure 1.29 Routes of internalization of NPs: 1. Micropinocytosis/Phagocytosis, 2. clathrin-mediated endocytosis and 3. Caveolae-mediated endocytosis. Image source: Biorender

- Phagocytosis is a process primarily carried out by professional phagocytes (macrophages, monocytes, neutrophils, and dendritic cells), responsible for defense against pathogens and the removal of dead cells and debris. Other cell types, such as fibroblasts, epithelial cells, and endothelial cells, also have phagocytic activity but to a lesser extent and are called para-phagocytes.

The process is initiated by opsonization, where opsonins like antibodies, complement proteins, or other blood proteins are absorbed onto the surface of NPs. Opsonized NPs are recognized and attached to phagocytes through specific ligand-receptor interactions. This triggers a signalling cascade that leads to the engulfing and internalization of the particles, forming a structure called phagosome. Phagocyte receptors involved in this

process include Fc receptors, complement receptors, mannose/fructose receptors, and scavenger receptors.[110]

Larger particles (250 nm to 3 μm) are more efficiently taken up by phagocytes. Surface properties of NPs play a critical role in their uptake by phagocytes. NPs functionalized with hydrophilic polymers like PEG can repel opsonization and prevent protein adsorption, leading to increased circulation half-life and reduced uptake by phagocytes. On the other hand, NPs with charged or hydrophobic surfaces attract complement proteins and undergo greater uptake by phagocytes. The opsonization of NPs can lead to their accumulation in the liver and spleen, which can be advantageous for the selective treatment of diseases affecting these organs.[111]

- Clathrin-mediated endocytosis (CME) is another mechanism by which cells internalize substances. It involves the formation of clathrin-coated pits on the plasma membrane, which leads to the internalization of substances via specific receptors or non-specific interactions. CME is important for the uptake of nutrients and plasma membrane components. NP uptake through CME can be influenced by surface charge, with positively charged particles being more strictly subject to CME.[110]

- Caveolae-dependent endocytosis is a process mediated by caveolae, which are flask-shaped membrane invaginations present in various cell types. Caveolae play a role in cell signalling, transcytosis, and regulation of lipids.[110] NPs with the size range of 120–150 nm are internalized via clathrin- or caveolin-mediated endocytosis.[111]

- Clathrin/caveolae-independent endocytosis occurs in cells lacking clathrin and caveolae and involves other pathways for internalizing cargos.[110]

- Macropinocytosis is a unique form of pinocytosis where large membrane extensions or ruffles are formed, which then fuse back to the plasma membrane, creating large vesicles that engulf extracellular fluid. This process allows for non-specific bulk fluid uptake and can be important for the uptake of larger nanoparticles.[110]

During endocytic processes, the vesicles (endosomes) undergo changes in composition and pH, eventually becoming lysosomes. Lysosomes have low pH, high ionic strength, and proteolytic enzymes that can affect NP stability and cargo. For effective delivery,

NPs typically need to escape from these compartments before they become acidic. Responsive NPs, such as ionizable NPs that acquire a charge in low-pH environments, facilitate endosomal escape (proton sponge effect) and enable intracellular delivery. In contrast, unresponsive NPs often remain trapped within the endosomes and are eventually degraded by the acidic environment and proteolytic enzymes present in lysosomes. After endocytic escape, NPs may need to reach specific intracellular environments or organelles, which may require crossing additional intracellular membranes. On the other hand, pH-responsive NP systems and complex NP shapes have been explored to facilitate precise delivery to intracellular environments.[74,110,111]

NPs clearance and degradation – NPs clearance occurs through a combination of the renal and hepatobiliary systems. In the hepatobiliary pathway, NPs accumulated in the liver are processed by hepatocytes and eliminated through bile excretion in the feces. The renal pathway involves the filtration of small NPs through the kidneys, allowing their excretion in urine. Small NPs (less than 10 nm) are usually cleared through renal pathways, while NPs in the range of 10-200 nm may be eliminated through the hepatobiliary system. Larger NPs (more than 200 nm) might be filtered by the spleen's sinusoidal system. However, hepatobiliary elimination is a slower process because when NPs are taken up by macrophages in the liver, they are sequestered within lysosomes. Lysosomes have an acidic environment with a pH around 4.5 and contain enzymes called acid hydrolases that degrade exogenous substances.[92]

Another important consideration is the presence of PEGylation on the NP surface. PEG, a non-biodegradable polymer, has a tendency to accumulate in the body. If PEGylated NPs are used for treating chronic diseases and are systemically administered over a prolonged period, there may be unwanted side effects, such as the activation of the complement system. Therefore, careful attention must be given to the presence of PEGylation when designing NP-based therapies.[95]

Despite having a lower metabolic capacity compared to the liver, the lung possesses enzymes that play a role in maintaining its physiological function. Enzymes like antitrypsin, proteases, and trypsin can be found on the surface of bronchial and alveolar epithelial cells, as well as pulmonary smooth muscle cells. These enzymes contribute to

the breakdown of nanoparticles. However, there is limited research available on how the physicochemical properties of particles affect their degradation in the lung.[112]

1.4.4 From preclinical studies to clinical translation

Pulmonary lung diseases include asthma, COPD, cystic fibrosis, pulmonary tuberculosis, and IPF. These diseases often have fatal outcomes, and there is currently no effective treatment for fully restoring lung function. Traditional therapies are administered systemically or locally through inhalers. However, inhaling free drugs in aerosol form can lead to rapid release, resulting in potential lung toxicity. Additionally, the size of aerosol particles affects drug efficiency: particles larger than 5 μm cannot pass the upper respiratory tract, particles between 1–5 μm settle in the lower respiratory tract, and particles smaller than 1 μm remain suspended in the air and are exhaled.

To address these challenges, nanoparticle-based delivery systems offer advantages such as improved bioavailability, controlled release, and reduced dosage and application frequency. For the efficient targeted delivery, the NPs-loaded system should be retained in the physiological system for the necessary time, target specific cell/tissue and release the loaded therapeutic agent. The pulmonary route of drug administration holds significant importance as it allows for the direct delivery of drugs to the lungs for both regional and systemic therapeutic needs.[69,102]

Various lipid nanocarriers have been extensively studied. These carriers offer advantages such as sustained release, low toxicity and improved stability during nebulization compared to conventional drug delivery systems. These NPs showed and efficient delivery of anticancer drugs and siRNA directly to the lungs, resulting in preferential accumulation in lung cancer cells.[113] The possibilities for more effective utilization of aerosol-based therapies in the treatment of various pulmonary diseases have been expanded by the development of liposomal formulations that can be delivered through jet nebulizers. Liposomes used as aerosol delivery vehicles offer several potential advantages for clinical development. These include compatibility with aqueous solutions, enabling intracellular delivery, particularly to alveolar macrophages and lymphocytes. They also provide sustained release within the lungs to maintain

therapeutic drug levels. However, the effects of these factors on the human lung have not been extensively studied.[104]

Natural polymers like gelatin, chitosan, and alginate, as well as synthetic polymers such as poloxamer, PLGA, and PEG, are widely utilized for the development of nanomedicine inhalation formulations. Polymeric micelles have also gained attention for their ability to solubilize hydrophobic drugs, biocompatibility, and increased drug retention time in the lungs.[112] Polymer-drug conjugates have the potential to modify the pharmacokinetic profile of drugs delivered to the lungs and enable sustained release. Conjugation of paclitaxel (PTX) with PEG of different molecular weights prolonged PTX retention in the lungs and enhanced its antitumor efficacy. Intratracheal administration of these conjugates increased the maximum tolerated dose of PTX in mice.[114]

Inorganic nanoparticles, such as magnetic nanoparticles and mesoporous silica nanoparticles have also been investigated for lung delivery. Magnetic nanoparticles, in combination with a target-directed magnetic gradient field, can facilitate site-specific drug delivery to specific lung regions. Thanks to their large pore and surface area, it is possible to load a significant amount of drugs. However, safety remains a major concern when using these drug delivery systems.[113]

Regarding IPF, the current FDA-approved treatments only slow down its progression without providing a cure. Therefore, more effective treatments and strategies are needed.

One approach is the development of dual drug-containing nanoparticle formulations to achieve synergistic effects of anti-fibrotic agents. It was demonstrated the synergistic effect of liposomes containing Nintedanib and colchicine for IPF treatment. These liposomes, modified with a matrix metalloproteinase 2 (MMP-2) responsive peptide, exhibited stability, enhanced cellular uptake, and improved cell targeting.[115] Similarly, it was developed an inhalable nanostructured lipid carrier encapsulating siRNA and prostaglandin E, showing successful treatment of IPF.[116]

Inhalational delivery of drugs as aerosols has been explored to provide localized therapy for IPF. Nebulized Tacrolimus (Tac) possesses anti-fibrotic properties but has inflammatory side effects when taken orally. Nebulized Tac loaded-NPs demonstrated

improved survival rates and reduction in fibrotic lesions in the lungs compared to injected Tac.[117] Moreover, Tac-loaded chitosan-coated PLGA NPs, which were administered via direct inhalation and showed a reduction in inflammation and collagen deposition in lung tissue.[118]

Recent studies have demonstrated the versatility and potential of intranasal and intratracheal delivery of nano-formulations for the treatment of IPF. PLGA NPs containing pirfenidone, administered intratracheally to mice, effectively maintained higher levels of drug in the lungs compared to the free drug for up to one week, resulting in significantly reduced hydroxyproline levels and enhanced anti-fibrotic effects.[119]

In addition to pirfenidone and nintedanib, other novel therapeutics in various stages of preclinical and clinical development are also being explored for IPF therapy using nanoformulations. It was developed an intranasal hydrogel containing IL-10 trapped in a mixture of Hyaluronan, to retain moisture, and heparin, to bind IL-10. *In vivo* treatment with these hydrogels in a mouse model of bleomycin-induced fibrosis demonstrated significant preservation of lung architecture, as evidenced by minimal fibrosis, reduced collagen content, and decreased levels of α-SMA.[120]

Comparisons have also been made between inhalation delivery and other administration routes. It has been tested an endotracheal administration of Tetrandrine (TET) encapsulated in hydroxy propyl-β-cyclodextrin for IPF treatment. *In vivo* studies on a fibrotic rat model demonstrated the superior efficacy of inhaled TET complexes compared to intravenous administration of free TET, hydroxyproline content and histopathology analysis.[121]

These findings highlight the promising potential of intranasal and intratracheal delivery routes for IPF treatment using nanoformulations. Encapsulation of new therapeutic agents within NPs offers opportunities for targeted and sustained drug delivery, leading to improved efficacy and therapeutic outcomes. Further research and clinical studies are needed to explore the full capabilities and optimize these methods for PF therapy.[51]

Overall, these studies highlight the potential of NPs formulations for combination therapies in the site-specific and effective treatment of lung disorders. Inhalation

delivery appears to offer advantages in terms of localized therapy and improved outcomes compared to other routes of administration. However, further extensive studies are required to fully evaluate and validate these approaches.

1.5 Avidin-Nucleic Acid Nano-ASsembly (ANANAS)

Among protein-based NPs, a particular type of nanocarrier, exclusively made of soft biodegradable and biocompatible components, called Avidin-Nucleic Acid Nano-ASsembly has been developed in the last decade.[122–124] The term "ANANAS" refers to a "poly-avidin" nanoformulation originating from the high affinity interaction of avidin with the nucleic acids, leading to a spontaneous self-assembly.

1.5.1 Avidin and biotin

The avidin protein has been firstly isolated from chicken egg white in early 1940 by Eakin, and it is characterized by a high avidity for biotin.[125] It has been found in different vertebrate species (birds, amphibians and reptiles), while in humans and mammals in general, it is not present, but it is instead taken through the diet. Avidin is localized above all in the female reproductive tract and in the egg-white of many oviparous animals, suggesting a role in ovum survival and embryonic development. This may be due to three different mechanisms: an antimicrobial action against biotin requiring bacteria and yeasts, an immunomodulatory action during the ovum passage in the oviduct, and a metabolic effect by controlling the availability of biotin for enzymes dependent on it.[126] However, the role of avidin is not restricted to the reproductive system. Its function more widely regards the acute phase of host defence, caused by injurious factors such as microbes, viruses, toxic molecules or tissue trauma.

Avidin is a 76 kDa tetrameric glycoprotein, and the amino acid sequence of each subunit is reported in Figure 1.30 A. The avidin tetramer consists of four identical subunits, all bearing 128 amino acids and composed of eight antiparallel β-strands that form a β-barrel. The protein is basically charged (pI~10.5), and each of its monomers possesses 8 arginine and 9 lysine residues.[127] The polypeptide chain also contains a glycosylation

site at residue Asn-17. The carbohydrate moiety accounts for about 10 % of the molecular mass of avidin, and contains terminal N-acetyl glucosamine and mannose elements. The quaternary structure of avidin consists of a dimer of dimers (Figure 1.30 B).[128] The strong interaction at the 1-4 interface is a product of the cooperativity among more than two-dozen hydrogen bonds. In contrast, the dimer-dimer interface is less intricate and involves two types (i.e., the 1-2 and 1-3) of monomer-monomer interfaces.

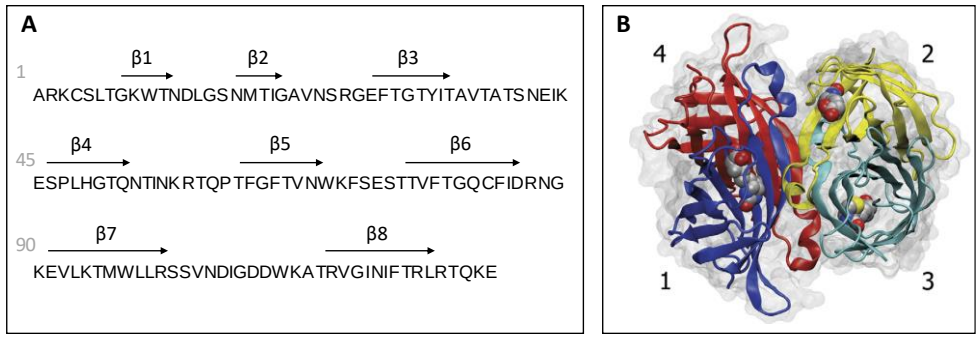

Figure 1.30 A) Avidin primary sequence. The secondary-structure elements are indicated by arrows. **B)** X-ray crystallography structures of avidin tetramers. The molecular surface is shown in transparent grey, the secondary-structure elements are indicated as cartoons and bound ligands. Four D-biotin molecules are shown in van der Waal's spheres.

Each subunit possesses one biotin binding site (BBS). Highly conserved tryptophan and lysine residues of avidin are implicated in the active site,[129,130] while the glycosidic component does not influence this process. In the absence of the ligand, five water molecules are situated in the biotin binding pocket and serve to emulate to some extent the shape and hydrogen-bonding capacity of biotin. The five water molecules abandon the pocket upon admission of the biotin ligand.

Biotin is a small molecule (244.31 Da) also known as vitamin H, vitamin B7 or co-enzyme R and it is composed of a tetrahydrothiophene ring fused to an ureido (tetrahydroimidizalone) ring. It plays a key role in cell signalling and acts as a cellular growth promoter.[131] One of the most interesting features of avidin is the high affinity for biotin. The complex ($K_d = 10^{-15}$M) is the most specific and stable non-covalent binding known in nature, about 10^3-10^6 times greater than an antigen-antibody interaction. The

high affinity ensures that, once formed, the complex is not disturbed by changes in pH, temperature, chaotropic agents, proteolytic enzymes or manipulations. When introduced into biologically active macromolecules, in most cases biotin does not affect their biological function, thus, biotinylation does not usually alter many properties of avidin. Interestingly, the binding of biotin by an isolated avidin monomer is characterized by a relatively low affinity constant ($K_d = 10^{-7}$M). This proves that the tetrameric assembly of avidin is essential to the establishment of the extremely high affinity towards biotin.[128] On the other hand, this strong interaction may pose a limitation in releasing the tagged biotinylated biomolecules from avidin. Reversibility or reduction of this affinity can be achieved by: 1) the addition of a highly concentrated biotin solution; 2) the use of biotin analogues with a slightly low affinity toward avidin;[132,133] 3) the insertion of a cleavable linker, such as a stimuli-responsive linker, between biomolecules and the biotin or avidin, but this chemical modification may compromise their activities. In conclusion, avidin can be used as "molecular bridge" to bring together different chemical entities (provided they have been biotinylated) for biomedical, nanotechnological, diagnostic and therapeutic applications. However, one limitation of the avidin-biotin technology is the "low" number of BBS per protein, so that only up to 4 biotinylated moieties can be linked together in one protein. A possibility to overcome this limit is to obtain polymerized forms of avidin (Figure 1.31).

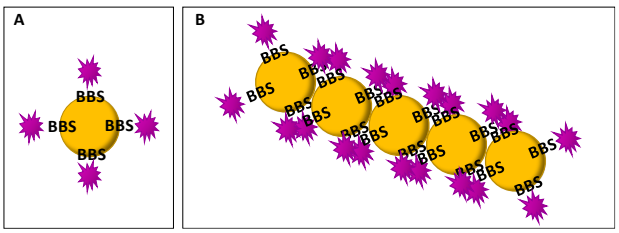

Figure 1.31 Simplified schematic representation describing **A)** the single avidin functionalized with only four biotinylated moieties compared to **B)** the poly-avidin system that allows an exponential signal amplification.

1.5.2 Avidin-nucleic acid interaction

An additional property of avidin has been recently brought to light, namely its ability to bind the nucleic acidic with high affinity ($K_d = 10^{-10}$M). Nucleic acids (DNA and RNA) are fundamental "molecules of life" as they play essential roles in gene heredity, regulation and expression. Beyond their biological functions, they also possess peculiar properties that make them versatile materials for nanoengineering. DNA double helix is indeed a nanoscale object. It has a diameter of approximately 2 nm, a helical repeat of 3.4 nm (10.5 base pairs) and a persistent length of approximately 50 nm.[134] For this reason, DNA can be exploited to build nanomaterials, thus avoiding the use of the more chemically labile RNA.

The high basicity of avidin is claimed to be the cause of the interaction with DNA. Crystallographic data reveals a region at the base of the avidin β-barrel where 11 residues of arginine and lysine are confined. Non-specific electrostatic interactions might be responsible for the initial docking of the DNA, while these basic regions may provide sites for further hydrogen bonding or van der Waals interactions. Avidin is able to bind both single (SS) and double (DS) strands, even if it shows a higher affinity for the last one. In SS DNA guanine and cytosine-rich sequences are probably involved in the interaction with avidin surface, while for DS DNA the main interactors with avidin are phosphate groups, since the bases pair up with each other. This binding is stable even at high dilutions and in physiological buffers and apparently does not directly involve the BBS. The avidin conformational change induced by biotin presence probably exposes a DNA binding motif thus improving the affinity between the protein and the nucleic acid.[122]

It is known that several poly-cations can induce DNA condensation neutralizing the phosphodiester negative charges and form small particles characterized by a size of approximately 50-100 nm with different morphology (spheres, rods, toroids).[135] Condensation occurs when the large volume occupied by a DNA molecule in its extended random coil conformation decreases dramatically, leading to compact structures with finite size and ordered morphology. Ultrastructural and light scattering studies showed that avidin assembles on the DNA molecule in an organized manner. The

Avidin-Nucleic Acid Nano-ASsemblies (ANANAS) lead to the formation of NPs that are about 100 nm in size (DNA~5 kb) and can have a rod-like or toroidal shape. In these particles, the DNA is highly condensed and one avidin is bound to 18±4 DNA base pairs, without recognizing a specific sequence. The ANANAS shape differs according to the type and length of the used DNA. With a circular plasmid, the formation of toroidal structures is favoured, while rods are obtained using linearized plasmids (Figure 1.32).[122]

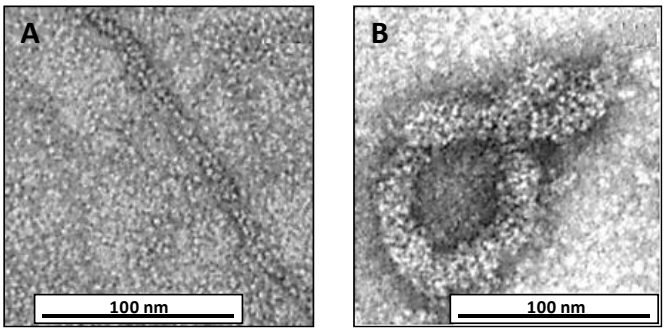

Figure 1.32 Transmission electron microscopy images of **A)** linear and **B)** circular plasmid DNA surrounded by rows of avidins.

In addition, it was shown that, in a salt-free environment and under specific concentration and ratio of the two elements, a single nucleic acid molecule is surrounded by several avidins. In this condition, ANANAS are well monodispersed and their size depends solely on the type and length of the nucleic acid used. However, in a buffered solution, the assembly process gives rise to agglomerates of large size (>1 μm), poorly soluble, highly polydispersed, with undefined geometry, and therefore unusable for practical purposes.[123] One possibility to prevent the aggregation in physiological buffer is to protect their surface with PEG (Figure 1.33). Interestingly, covalent PEGylation partially reduces the affinity for DNA, whereas PEG anchoring through the BBS does not. This strategy to modify the ANANAS surface allows to improve not only the solution properties, but also the pharmacokinetic and immunogenic profiles.

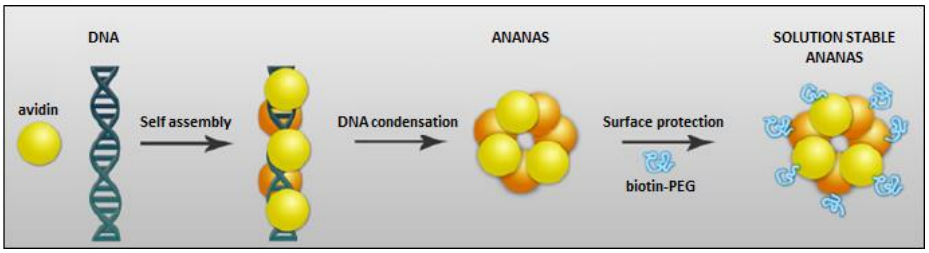

Figure 1.33 Nature-driven self-assembly mechanism. Initially, a nucleic acid molecule acts as a central element around which several avidins (1 each 14 base pairs) nucleate, leading to ANANAS toroidal assemblies. In a second step, a defined amount of biotinylated PEG is also added to permit buffer solubility and increase stability.

As compared to other poly-avidin systems described in the literature,[131] the ANANAS particles have the additional advantages of being stoichiometrically defined, having only biocompatible or biodegradable soft elements, and preserving the full biotin binding potentials. Moreover, they are poorly immunogenic. In fact, the avidin in the particles is highly shielded by the polymer layer and it is able to evade the immune system that recognizes only the degradation products, not the nanoassemblies. These are fundamental features that allow the potential application of ANANAS in further areas of investigation, among which drug delivery.

1.5.3. ANANAS-Dex synthesis and characterization

The synthesis and characterization of ANANAS were conducted by Dr. Margherita Morpurgo from the Department of Pharmaceutical and Pharmacological Sciences at the University of Padova. The *in vivo* fate and cellular internalization of ANANAS were then investigated at the Mario Negri Institute.

To achieve an effective therapeutic strategy, it has been developed a dexamethasone, a corticosteroid, -carrying nanoformulation based on ANANAS.

Corticosteroids, a class of steroid hormones, derived from cholesterol metabolism and produced by the adrenal cortex, exert their physiological effects through a complex mechanism of action involving intracellular receptor activation. Upon entering the target cell by diffusion through cell membranes, corticosteroids bind to cytoplasmic glucocorticoid receptors (GRs) and mineralocorticoid receptors (MRs), leading to the

formation of hormone-receptor complexes. These complexes then translocate to the cell nucleus, where they dimerize and modulate gene transcription by interacting with specific regulatory regions of the DNA, known as glucocorticoid response elements (GREs). This process results in altered gene expression, leading to various biological responses. In the case of glucocorticoids, their primary actions include the regulation of immune responses, inflammation and metabolism, while mineralocorticoids play a crucial role in electrolyte balance and blood pressure regulation. Corticosteroids inhibit genes responsible for expression of cyclooxygenase-2, inducible nitric oxide synthase, and pro-inflammatory cytokines, including tumor necrosis factor alpha and various interleukins. The overall impact of corticosteroids on cellular function has significant implications in various physiological and pathological conditions, making them essential therapeutic agents in the management of inflammatory, autoimmune, and allergic diseases. However, their systemic use warrants careful consideration due to potential side effects resulting from the broad range of affected cellular processes.[136]

The assembly process requires a biotinylated and PEGylated Dexamethasone with ANANAS core using an acid-reversible hydrazone bond (Hz), generating the ANANAS-Dex nanoassembly (Figure 1.34).[137-138]

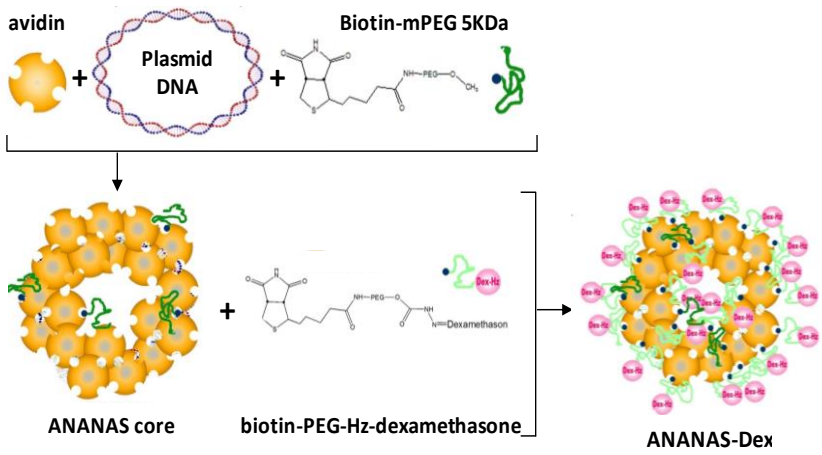

Figure 1.34 Process of ANANAS-PEG-Dex assembly.

Each NP contains about 350 avidins, which are available for docking any kind of biotinylated moiety. To maximize the PEG layer necessary for surface protection concomitantly with Dex loading, it has been introduced a 5KDa poly(ethylene glycol) spacer between the biotin and the drug hydrazo moiety (biotin-PEG-Hz-Dex). Dex carrying ANANAS were prepared by mixing biotin-PEG-Hz-Dex with empty NP previously obtained in freeze-dried form. These NPs contain also a small amount of a biotin-PEG-methoxy to guarantee colloidal stability during preparation. It has been evaluated in a preliminary experiment the maximum NP loading capacity for the Dex derivative. A mix of core NP and biotin-PEG-Hz-Dex have been generated and analyzed for their content of unbound PEG reagent by gel permeation chromatography. The results coming from this study indicate that a maximum of 410 units of biotin-PEG-Hz-Dex can be loaded in each ANANAS and that this amount corresponds to a BBS coverage of about 30%. Based on this result, all ANANAS-Dex have been later prepared following this procedure by mixing drug and NPs at 30% BBS coverage and without purification to do not saturate the BBS or the available surface area. Upon addition of the Dex-carrying reagent, the size of the NPs increased from 128± 1.2 nm to 132.9± 2.9 nm. Dynamic light scattering experiments also showed that the Dex-loaded formulations are colloidally stable for at least 48h after preparation.

1.5.4 ANANAS interaction with organ and cells in healthy mice

The biodistribution of both ANANAS and ANANAS-Dex after intraperitoneal administration was first investigated in healthy mice to assess their behavior in physiological conditions.[139] For this part of the analysis, the two formulations were fluorescently labeled with biotin-alexa633 covalently linked to ANANAS. Whole-body longitudinal tracking (30 min, 4 and 24h) showed a similar profile for the two formulations of NP regarding permanence and biodistribution in the body (Figure 1.35A). The signal associated with the two formulations remains in the abdominal cavity for a long time (about 40% of the signal recorded 30 min after injection is still present at 24 h). To exclude that the signal was related to the free circulation of dye detached from the ANANAS, they administered the same concentration of low molecular-weight biotin-alexa633, but the signal related to the free fluorophore rapidly disappeared over

time. Thus confirming the more lasting permanence of the NPs in the body compared to the dye. *Ex vivo* analysis showed that, 4h after administration, the fluorescent signal associated with ANANAS was well detectable in all selected organs, including the lungs and the brain. However, 1 day after treatment, the pattern of fluorescence showed almost selective tropism for the liver and the spleen and was much slower in other organs (Figure 1.35B).

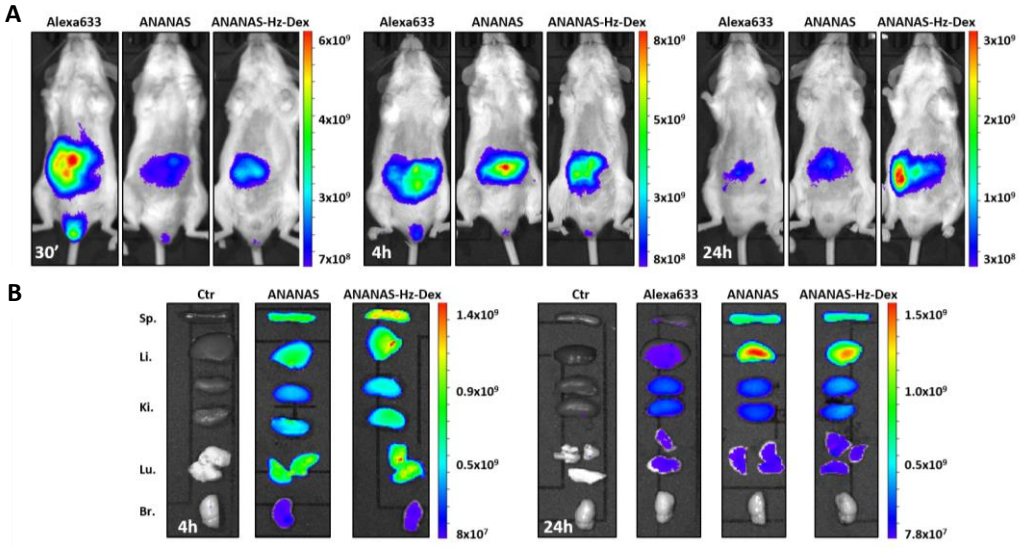

Figure 1.35 *In vivo* and *ex vivo* nanoformulation biodistribution **A)** *In vivo* optical imaging of mice treated with alexa633, ANANAS, or ANANAS-Dex and scanned 30', 4h, and 24h after treatment. **B)** *Ex vivo* optical imaging of excised organs from animals sacrificed 4 and 24h after vehicle, alexa633, ANANAS, and ANANAS-Dex administration. Li. = liver, Sp. = spleen, Ki. = kidneys, Lu. = lungs, Br. =brain.

To see whether the ANANAS formulations selectively interact with Kupffer cells in the liver, they used confocal laser to analyze the liver tissue of treated healthy mice and assessed the extent of NPs and KCs colocalization using a fluorescent marker for macrophages (anti-CD68) (Figure 1.36). Thirty minutes after injection, the red fluorescent signal associated with the drug-free ANANAS is mainly confined around the vessels and do not overlap with the CD68 marker (green) (Figure 1.36A). On the other hand, the Dex-carrying nanoformulation leads to a faster tropism for KCs at 30', because its signal almost overlaps with the CD68 signal in the liver parenchyma (Figure 1.36B).

24h after treatment the alexa633 signal related to both formulations was closely associated with that of KCs. The difference between the two formulations at the two time-points was quantified by measuring the percentage of NPs and CD68-associated signal colocalization, thus confirming the qualitative analysis (Figure 1.36C). These results indicate that CD68-positive cells play a key role in the sequestration of ANANAS, independently of the nature of the NPs cargo. The presence of Dex on the NP surface might facilitate the NPs interaction with the cell membrane, either because of its hydrophobic nature or by "hijacking" an interaction with steroid receptors.[139]

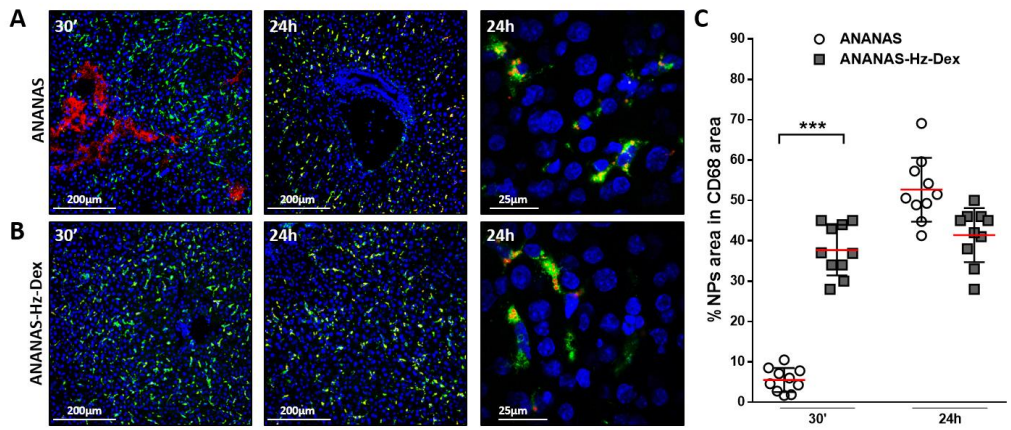

Figure 1.36 Localization of ANANAS and ANANAS-Dex in the liver of healthy mice. Confocal microscope images (**A** and **B**) from healthy mice sacrificed 30 min and 24h after ANANAS **(A)** and ANANAS-Dex **(B)**. The blue signal refers to the nuclei (Hoechst 33258 staining), green corresponds to the lysosomal compartment of macrophages (CD68 antibody), red is associated with the alexa633 dye linked to the NPs. **C)** Quantification of the area occupied by ANANAS overlapping the area of CD68 staining of liver sections from healthy mice. Data are reported as scatter plots. Statistical analysis is performed by one-way ANOVA followed by Tukey's post hoc test ***p<0,0001.

The ability of cells to internalize ANANAS was further demonstrated in an *in vitro* test in which NP accumulation in HeLa cells upon incubation for 2, 6, and 24h was monitored by confocal microscopy (Figure 1.37). The kinetics observed along this experiment suggest that ANANAS can be efficiently internalized in cells in a time-dependent manner. After 24h of incubation, NPs primarily localized within the cytoplasm where they appear as separate spots, resembling clusters of internalization vesicles.[140]

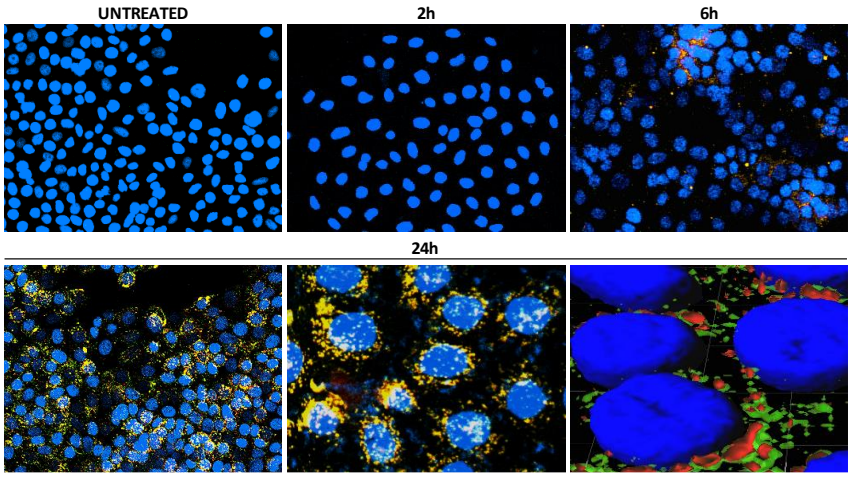

Figure 1.37 Representative confocal images of HeLa cells incubated with PEG-FITC-ANANAS-alexa633. In the upper panel, untreated and treated cells for 2 and 6h can be observed. In the lower panel, low and high magnification images and a 3D reconstruction of cells incubated with ANANAS for 24h are reported. The merge among the fluorescent channels associated with the NPs (red for alexa 633, green for FITC) is visible in yellow, with the nuclei are blue after staining with Hoechst 33258.

Treatment with chlorpromazine, a selective inhibitor of clathrin-dependent endocytosis, strongly reduces NPs entry, while incubation with amyloride, which selectively inhibits micropinocytosis, does not lead to significant alteration on NPs uptake. This strongly suggests that a vesicle-dependent process of endocytosis occurs, secondary to clathrin-dependent vesicle formation (Figure 1.38).[140]

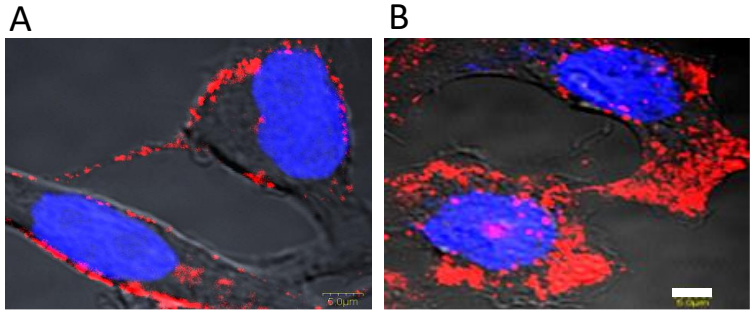

Figure 1.38 HeLa cells upon 24h incubation with ANANAS (in red) in the presence of chlorpromazine (**A**) or amyloride (**B**). Scale bar: (**A, B**) 5 µm

As shown above, when in close contact with cells, ANANAS were internalized through an endocytic pathway, and this also occurs in the liver parenchyma following systemic administration.[140] Therefore, is has been decided to exploit the low pH reversible hydrazone bond to promote the release of the drug only in the endosome/lysosome acidic compartment. The ability of ANANAS-Dex to release free drug selectively at acidic pH (Figure 1.39A) was demonstrated *in vitro* (Figure 1.39B). The formulation has been examined after incubation at three pH values (7.4, 5.0, and 4.0) at 37°C until 96 h. At neutral pH, the drug remains stably attached to the biotin linker, while at pH below 6.0, drug release occurs with a kinetics that increases in correlation with the decrease of pH.

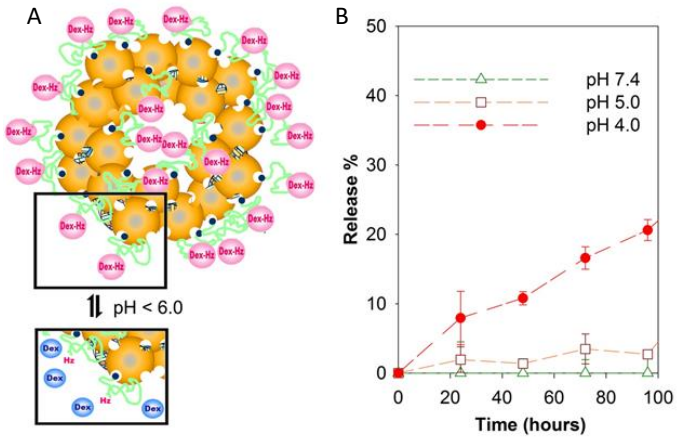

Figure 1.39 A) Scheme of pH-dependent release of Dex from ANANAS-Dex **B)** *In vitro* drug release at (△) pH 7.4, (□) pH 5.0, and (●) pH 4.0.

These previous studies suggest a promising therapeutic potential of this nanoformulation. Moreover, ANANAS-Dex have also been tested in a murine model of autoimmune hepatitis.[139] The specific organ targeting and the incorporation of the steroid to ANANAS-Dex make this nanoformulation extremely convincing also in terms of biosafety for future translational aims. Moreover this system can be also extended to other therapeutic targets, such as lungs, for the treatment of pulmonary disorders.

References

1. Rogers, K. *The respiratory system*. (Britannica Educational Pub., in association with Rosen Educational Services, 2011).
2. Moore, K. L., Dalley, A. F. & Agur, A. M. R. *Clinically oriented anatomy*. (Wolters Kluwer Health/Lippincott Williams & Wilkins, 2014).
3. Sahin-Yilmaz, A. & Naclerio, R. M. Anatomy and Physiology of the Upper Airway. *Proc. Am. Thorac. Soc.* **8**, 31–39 (2011).
4. Jafek, B. W. Ultrastructure of human nasal mucosa. *The Laryngoscope* **93**, 1576–1599 (1983).
5. McCullagh, K. L., Shah, R. N. & Huang, B. Y. Anatomy of the Larynx and Cervical Trachea. *Neuroimaging Clin. N. Am.* **32**, 809–829 (2022).
6. Drevet, G., Conti, M. & Deslauriers, J. Surgical anatomy of the tracheobronchial tree. *J. Thorac. Dis.* **8**, S121-129 (2016).
7. Tomashefski, J. F. & Farver, C. F. Anatomy and Histology of the Lung. in *Dail and Hammar's Pulmonary Pathology* (eds. Tomashefski, J. F., Cagle, P. T., Farver, C. F. & Fraire, A. E.) 20–48 (Springer New York, 2008). doi:10.1007/978-0-387-68792-6_2.
8. Yalcin, N. G., Choong, C. K. C. & Eizenberg, N. Anatomy and pathophysiology of the pleura and pleural space. *Thorac. Surg. Clin.* **23**, 1–10, v (2013).
9. Davies, A. & Moores, C. *The respiratory system: basic science and clinical conditions*. (Churchill Livingstone, 2010).
10. Suresh, K. & Shimoda, L. A. Lung Circulation. in *Comprehensive Physiology* (ed. Terjung, R.) 897–943 (Wiley, 2016). doi:10.1002/cphy.c140049.
11. Weibel, E. R. What makes a good lung? *Swiss Med. Wkly.* **139**, 375–386 (2009).
12. Wagner, P. D. The physiological basis of pulmonary gas exchange: implications for clinical interpretation of arterial blood gases. *Eur. Respir. J.* **45**, 227–243 (2015).
13. Franks, T. J. *et al.* Resident Cellular Components of the Human Lung: Current Knowledge and Goals for Research on Cell Phenotyping and Function. *Proc. Am. Thorac. Soc.* **5**, 763–766 (2008).
14. Zepp, J. A. & Morrisey, E. E. Cellular crosstalk in the development and regeneration of the respiratory system. *Nat. Rev. Mol. Cell Biol.* **20**, 551–566 (2019).
15. Sun, X. *et al.* A census of the lung: CellCards from LungMAP. *Dev. Cell* **57**, 112-145.e2 (2022).

16. Ruysseveldt, E., Martens, K. & Steelant, B. Airway Basal Cells, Protectors of Epithelial Walls in Health and Respiratory Diseases. *Front. Allergy* **2**, 787128 (2021).
17. Katzen, J. & Beers, M. F. Contributions of alveolar epithelial cell quality control to pulmonary fibrosis. *J. Clin. Invest.* **130**, 5088–5099 (2020).
18. Heinen, N., Klöhn, M., Steinmann, E. & Pfaender, S. In Vitro Lung Models and Their Application to Study SARS-CoV-2 Pathogenesis and Disease. *Viruses* **13**, 792 (2021).
19. Dudás, B. *Human histology: a text and atlas for physicians and scientists*. (Academic Press, 2023).
20. Hinz, B. *et al.* The Myofibroblast. *Am. J. Pathol.* **170**, 1807–1816 (2007).
21. Byrne, A. J., Maher, T. M. & Lloyd, C. M. Pulmonary Macrophages: A New Therapeutic Pathway in Fibrosing Lung Disease? *Trends Mol. Med.* **22**, 303–316 (2016).
22. Byrne, A. J., Mathie, S. A., Gregory, L. G. & Lloyd, C. M. Pulmonary macrophages: key players in the innate defence of the airways. *Thorax* **70**, 1189–1196 (2015).
23. Ogawa, T., Shichino, S., Ueha, S. & Matsushima, K. Macrophages in lung fibrosis. *Int. Immunol.* **33**, 665–671 (2021).
24. Murray, P. J. & Wynn, T. A. Protective and pathogenic functions of macrophage subsets. *Nat. Rev. Immunol.* **11**, 723–737 (2011).
25. Mosser, D. M. & Edwards, J. P. Exploring the full spectrum of macrophage activation. *Nat. Rev. Immunol.* **8**, 958–969 (2008).
26. Chávez-Galán, L. Much more than M1 and M2 macrophages, there are also CD169+ and TCR+ macrophages. *Front. Immunol.* **6**, 15 (2015).
27. Martinez, F. O. & Gordon, S. The M1 and M2 paradigm of macrophage activation: time for reassessment. *F1000Prime Rep.* **6**, (2014).
28. Italiani, P. & Boraschi, D. From Monocytes to M1/M2 Macrophages: Phenotypical vs. Functional Differentiation. *Front. Immunol.* **5**, (2014).
29. Barnes, P. J. Cellular and molecular mechanisms of asthma and COPD. *Clin. Sci.* **131**, 1541–1558 (2017).
30. Melo, E. M., Oliveira, V. L. S., Boff, D. & Galvão, I. Pulmonary macrophages and their different roles in health and disease. *Int. J. Biochem. Cell Biol.* **141**, 106095 (2021).

31. Noy, R. & Pollard, J. W. Tumor-associated macrophages: from mechanisms to therapy. *Immunity* **41**, 49–61 (2014).

32. Kemp, W. L., Brown, T. G. & Burns, D. K. *Pathology: the big picture*. (McGraw-Hill, 2013).

33. Barnes, P. J. *et al.* Chronic obstructive pulmonary disease. *Nat. Rev. Dis. Primer* **1**, 15076 (2015).

34. Vestbo, J. *et al.* Global Strategy for the Diagnosis, Management, and Prevention of Chronic Obstructive Pulmonary Disease: GOLD Executive Summary. *Am. J. Respir. Crit. Care Med.* **187**, 347–365 (2013).

35. Mims, J. W. Asthma: definitions and pathophysiology: Asthma: definitions and pathophysiology. *Int. Forum Allergy Rhinol.* **5**, S2–S6 (2015).

36. Lambrecht, B. N. & Hammad, H. The immunology of asthma. *Nat. Immunol.* **16**, 45–56 (2015).

37. Meyer, N. J., Gattinoni, L. & Calfee, C. S. Acute respiratory distress syndrome. *The Lancet* **398**, 622–637 (2021).

38. Longo, D. L. *et al. Harrison's principles of internal medicine*. (McGraw-Hill, 2012).

39. Cottin, V. *et al.* Presentation, diagnosis and clinical course of the spectrum of progressive-fibrosing interstitial lung diseases. *Eur. Respir. Rev.* **27**, 180076 (2018).

40. Wijsenbeek, M. & Cottin, V. Spectrum of Fibrotic Lung Diseases. *N. Engl. J. Med.* **383**, 958–968 (2020).

41. Richeldi, L., Collard, H. R. & Jones, M. G. Idiopathic pulmonary fibrosis. *The Lancet* **389**, 1941–1952 (2017).

42. Martinez, F. J. *et al.* Idiopathic pulmonary fibrosis. *Nat. Rev. Dis. Primer* **3**, 17074 (2017).

43. Wijsenbeek, M., Suzuki, A. & Maher, T. M. Interstitial lung diseases. *The Lancet* **400**, 769–786 (2022).

44. Sgalla, G. *et al.* Idiopathic pulmonary fibrosis: pathogenesis and management. *Respir. Res.* **19**, 32 (2018).

45. Wilson, M. S. & Wynn, T. A. Pulmonary fibrosis: pathogenesis, etiology and regulation. *Mucosal Immunol.* **2**, 103–121 (2009).

46. Samarelli, A. V. *et al.* Fibrotic Idiopathic Interstitial Lung Disease: The Molecular and Cellular Key Players. *Int. J. Mol. Sci.* **22**, 8952 (2021).

47. Craig, V. J., Zhang, L., Hagood, J. S. & Owen, C. A. Matrix Metalloproteinases as Therapeutic Targets for Idiopathic Pulmonary Fibrosis. *Am. J. Respir. Cell Mol. Biol.* **53**, 585–600 (2015).

48. Ishida, Y., Kuninaka, Y., Mukaida, N. & Kondo, T. Immune Mechanisms of Pulmonary Fibrosis with Bleomycin. *Int. J. Mol. Sci.* **24**, 3149 (2023).

49. Barratt, S., Creamer, A., Hayton, C. & Chaudhuri, N. Idiopathic Pulmonary Fibrosis (IPF): An Overview. *J. Clin. Med.* **7**, 201 (2018).

50. Henderson, N. C., Rieder, F. & Wynn, T. A. Fibrosis: from mechanisms to medicines. *Nature* **587**, 555–566 (2020).

51. Ghumman, M. *et al.* Emerging drug delivery strategies for idiopathic pulmonary fibrosis treatment. *Eur. J. Pharm. Biopharm.* **164**, 1–12 (2021).

52. Li, R. *et al.* Novel drug delivery systems and disease models for pulmonary fibrosis. *J. Controlled Release* **348**, 95–114 (2022).

53. Lederer, D. J. & Martinez, F. J. Idiopathic Pulmonary Fibrosis. *N. Engl. J. Med.* **378**, 1811–1823 (2018).

54. Johannson, K. A., Chaudhuri, N., Adegunsoye, A. & Wolters, P. J. Treatment of fibrotic interstitial lung disease: current approaches and future directions. *The Lancet* **398**, 1450–1460 (2021).

55. Weissferdt, A. Infectious Lung Disease. in *Diagnostic Thoracic Pathology* 3–71 (Springer International Publishing, 2020). doi:10.1007/978-3-030-36438-0_1.

56. Boland, J. M. & Pritt, B. S. Histopathology of parasitic infections of the lung. *Semin. Diagn. Pathol.* **34**, 550–559 (2017).

57. Febbo, J., Revels, J. & Ketai, L. Viral Pneumonias. *Radiol. Clin. North Am.* **60**, 383–397 (2022).

58. Ruuskanen, O., Lahti, E., Jennings, L. C. & Murdoch, D. R. Viral pneumonia. *The Lancet* **377**, 1264–1275 (2011).

59. Coronaviridae Study Group of the International Committee on Taxonomy of Viruses *et al.* The species Severe acute respiratory syndrome-related coronavirus: classifying 2019-nCoV and naming it SARS-CoV-2. *Nat. Microbiol.* **5**, 536–544 (2020).

60. V'kovski, P., Kratzel, A., Steiner, S., Stalder, H. & Thiel, V. Coronavirus biology and replication: implications for SARS-CoV-2. *Nat. Rev. Microbiol.* **19**, 155–170 (2021).

61. Hoffmann, M., Kleine-Weber, H. & Pöhlmann, S. A Multibasic Cleavage Site in the Spike Protein of SARS-CoV-2 Is Essential for Infection of Human Lung Cells. *Mol. Cell* **78**, 779-784.e5 (2020).

62. Jackson, C. B., Farzan, M., Chen, B. & Choe, H. Mechanisms of SARS-CoV-2 entry into cells. *Nat. Rev. Mol. Cell Biol.* **23**, 3–20 (2022).

63. John, A. E., Joseph, C., Jenkins, G. & Tatler, A. L. COVID-19 and pulmonary fibrosis: A potential role for lung epithelial cells and fibroblasts. *Immunol. Rev.* **302**, 228–240 (2021).

64. Tregoning, J. S., Flight, K. E., Higham, S. L., Wang, Z. & Pierce, B. F. Progress of the COVID-19 vaccine effort: viruses, vaccines and variants versus efficacy, effectiveness and escape. *Nat. Rev. Immunol.* **21**, 626–636 (2021).

65. Zheng, M. Classification and Pathology of Lung Cancer. *Surg. Oncol. Clin. N. Am.* **25**, 447–468 (2016).

66. Savjani, K. T., Gajjar, A. K. & Savjani, J. K. Drug Solubility: Importance and Enhancement Techniques. *ISRN Pharm.* **2012**, 1–10 (2012).

67. Blanco, E., Shen, H. & Ferrari, M. Principles of nanoparticle design for overcoming biological barriers to drug delivery. *Nat. Biotechnol.* **33**, 941–951 (2015).

68. Farokhzad, O. C. & Langer, R. Impact of Nanotechnology on Drug Delivery. *ACS Nano* **3**, 16–20 (2009).

69. Yetisgin, A. A., Cetinel, S., Zuvin, M., Kosar, A. & Kutlu, O. Therapeutic Nanoparticles and Their Targeted Delivery Applications. *Molecules* **25**, 2193 (2020).

70. Jeevanandam, J., Barhoum, A., Chan, Y. S., Dufresne, A. & Danquah, M. K. Review on nanoparticles and nanostructured materials: history, sources, toxicity and regulations. *Beilstein J. Nanotechnol.* **9**, 1050–1074 (2018).

71. Kim, B. Y. S., Rutka, J. T. & Chan, W. C. W. Nanomedicine. *N. Engl. J. Med.* **363**, 2434–2443 (2010).

72. Stater, E. P., Sonay, A. Y., Hart, C. & Grimm, J. The ancillary effects of nanoparticles and their implications for nanomedicine. *Nat. Nanotechnol.* **16**, 1180–1194 (2021).

73. Kadam, R. S., Bourne, D. W. A. & Kompella, U. B. Nano-Advantage in Enhanced Drug Delivery with Biodegradable Nanoparticles: Contribution of Reduced Clearance. *Drug Metab. Dispos.* **40**, 1380–1388 (2012).

74. Mitchell, M. J. *et al.* Engineering precision nanoparticles for drug delivery. *Nat. Rev. Drug Discov.* **20**, 101–124 (2021).

75. Shi, L. *et al.* Effects of polyethylene glycol on the surface of nanoparticles for targeted drug delivery. *Nanoscale* **13**, 10748–10764 (2021).

76. Barenholz, Y. (Chezy). Doxil® — The first FDA-approved nano-drug: Lessons learned. *J. Controlled Release* **160**, 117–134 (2012).

77. Soliman, M. G., Pelaz, B., Parak, W. J. & del Pino, P. Phase Transfer and Polymer Coating Methods toward Improving the Stability of Metallic Nanoparticles for Biological Applications. *Chem. Mater.* **27**, 990–997 (2015).

78. Chang, X. *et al.* Monocyte-derived multipotent cell delivered programmed therapeutics to reverse idiopathic pulmonary fibrosis. *Sci. Adv.* **6**, eaba3167 (2020).

79. Asadi, S. *et al.* Laser-induced optothermal response of gold nanoparticles: From a physical viewpoint to cancer treatment application. *J. Biophotonics* **14**, (2021).

80. Arias, L. *et al.* Iron Oxide Nanoparticles for Biomedical Applications: A Perspective on Synthesis, Drugs, Antimicrobial Activity, and Toxicity. *Antibiotics* **7**, 46 (2018).

81. Manshian, B. B., Jiménez, J., Himmelreich, U. & Soenen, S. J. Personalized medicine and follow-up of therapeutic delivery through exploitation of quantum dot toxicity. *Biomaterials* **127**, 1–12 (2017).

82. Sercombe, L. *et al.* Advances and Challenges of Liposome Assisted Drug Delivery. *Front. Pharmacol.* **6**, (2015).

83. Sarfraz, M. *et al.* Development of Dual Drug Loaded Nanosized Liposomal Formulation by A Reengineered Ethanolic Injection Method and Its Pre-Clinical Pharmacokinetic Studies. *Pharmaceutics* **10**, 151 (2018).

84. Weber, S., Zimmer, A. & Pardeike, J. Solid Lipid Nanoparticles (SLN) and Nanostructured Lipid Carriers (NLC) for pulmonary application: A review of the state of the art. *Eur. J. Pharm. Biopharm.* **86**, 7–22 (2014).

85. Schoenmaker, L. *et al.* mRNA-lipid nanoparticle COVID-19 vaccines: Structure and stability. *Int. J. Pharm.* **601**, 120586 (2021).

86. Zielińska, A. *et al.* Polymeric Nanoparticles: Production, Characterization, Toxicology and Ecotoxicology. *Molecules* **25**, 3731 (2020).

87. Tarhini, M., Greige-Gerges, H. & Elaissari, A. Protein-based nanoparticles: From preparation to encapsulation of active molecules. *Int. J. Pharm.* **522**, 172–197 (2017).

88. Moghimi, S. M. & Patel, H. M. Serum-mediated recognition of liposomes by phagocytic cells of the reticuloendothelial system – The concept of tissue specificity. *Adv. Drug Deliv. Rev.* **32**, 45–60 (1998).

89. Tenzer, S. *et al.* Rapid formation of plasma protein corona critically affects nanoparticle pathophysiology. *Nat. Nanotechnol.* **8**, 772–781 (2013).

90. Wolfram, J. *et al.* The nano-plasma interface: Implications of the protein corona. *Colloids Surf. B Biointerfaces* **124**, 17–24 (2014).

91. Monopoli, M. P., Åberg, C., Salvati, A. & Dawson, K. A. Biomolecular coronas provide the biological identity of nanosized materials. *Nat. Nanotechnol.* **7**, 779–786 (2012).

92. Schöttler, S. *et al.* Protein adsorption is required for stealth effect of poly(ethylene glycol)- and poly(phosphoester)-coated nanocarriers. *Nat. Nanotechnol.* **11**, 372–377 (2016).

93. Sørensen, K. K. *et al.* The scavenger endothelial cell: a new player in homeostasis and immunity. *Am. J. Physiol.-Regul. Integr. Comp. Physiol.* **303**, R1217–R1230 (2012).

94. Ngo, W. *et al.* Why nanoparticles prefer liver macrophage cell uptake in vivo. *Adv. Drug Deliv. Rev.* **185**, 114238 (2022).

95. Zhong, Q., Merkel, O. M., Reineke, J. J. & da Rocha, S. R. P. Effect of the Route of Administration and PEGylation of Poly(amidoamine) Dendrimers on Their Systemic and Lung Cellular Biodistribution. *Mol. Pharm.* **13**, 1866–1878 (2016).

96. Tsoi, K. M. *et al.* Mechanism of hard-nanomaterial clearance by the liver. *Nat. Mater.* **15**, 1212–1221 (2016).

97. Talamini, L. *et al.* Influence of Size and Shape on the Anatomical Distribution of Endotoxin-Free Gold Nanoparticles. *ACS Nano* **11**, 5519–5529 (2017).

98. Li, B. & Lane, L. A. Probing the biological obstacles of nanomedicine with gold nanoparticles. *WIREs Nanomedicine Nanobiotechnology* **11**, (2019).

99. Liang, X. *et al.* Short- and Long-Term Tracking of Anionic Ultrasmall Nanoparticles in Kidney. *ACS Nano* **10**, 387–395 (2016).

100. Choi, C. H. J., Zuckerman, J. E., Webster, P. & Davis, M. E. Targeting kidney mesangium by nanoparticles of defined size. *Proc. Natl. Acad. Sci.* **108**, 6656–6661 (2011).

101. Newman, S. P. Drug delivery to the lungs: challenges and opportunities. *Ther. Deliv.* **8**, 647–661 (2017).

102. Thakur, A. K. *et al.* Patented therapeutic drug delivery strategies for targeting pulmonary diseases. *Expert Opin. Ther. Pat.* **30**, 375–387 (2020).

103. Newman, S. P. Fine Particle Fraction: The Good and the Bad. *J. Aerosol Med. Pulm. Drug Deliv.* **35**, 2–10 (2022).

104. Smola, M., Vandamme, T. & Sokolowski, A. Nanocarriers as pulmonary drug delivery systems to treat and to diagnose respiratory and non respiratory diseases. *Int. J. Nanomedicine* **3**, 1–19 (2008).

105. Labiris, N. R. & Dolovich, M. B. Pulmonary drug delivery. Part I: Physiological factors affecting therapeutic effectiveness of aerosolized medications: Physiological factors affecting the effectiveness of inhaled drugs. *Br. J. Clin. Pharmacol.* **56**, 588–599 (2003).

106. van Rijt, S. H., Bein, T. & Meiners, S. Medical nanoparticles for next generation drug delivery to the lungs. *Eur. Respir. J.* **44**, 765–774 (2014).

107. Guagliardo, R., Pérez-Gil, J., De Smedt, S. & Raemdonck, K. Pulmonary surfactant and drug delivery: Focusing on the role of surfactant proteins. *J. Controlled Release* **291**, 116–126 (2018).

108. Patton, J. S. *et al.* The Particle has Landed—Characterizing the Fate of Inhaled Pharmaceuticals. *J. Aerosol Med. Pulm. Drug Deliv.* **23**, S-71-S-87 (2010).

109. Cañadas, O. *et al.* Characterization of Liposomal Tacrolimus in Lung Surfactant-like Phospholipids and Evaluation of Its Immunosuppressive Activity. *Biochemistry* **43**, 9926–9938 (2004).

110. Behzadi, S. *et al.* Cellular uptake of nanoparticles: journey inside the cell. *Chem. Soc. Rev.* **46**, 4218–4244 (2017).

111. Foroozandeh, P. & Aziz, A. A. Insight into Cellular Uptake and Intracellular Trafficking of Nanoparticles. *Nanoscale Res. Lett.* **13**, 339 (2018).

112. Liu, Q., Guan, J., Qin, L., Zhang, X. & Mao, S. Physicochemical properties affecting the fate of nanoparticles in pulmonary drug delivery. *Drug Discov. Today* **25**, 150–159 (2020).

113. Taratula, O., Kuzmov, A., Shah, M., Garbuzenko, O. B. & Minko, T. Nanostructured lipid carriers as multifunctional nanomedicine platform for pulmonary co-delivery of anticancer drugs and siRNA. *J. Controlled Release* **171**, 349–357 (2013).

114. Luo, T. *et al.* PEGylation of paclitaxel largely improves its safety and anti-tumor efficacy following pulmonary delivery in a mouse model of lung carcinoma. *J. Controlled Release* **239**, 62–71 (2016).

115. Chang, X. *et al.* Nanoengineered immunosuppressive therapeutics modulating M1/M2 macrophages into the balanced status for enhanced idiopathic pulmonary fibrosis therapy. *Nanoscale* **12**, 8664–8678 (2020).

116. Garbuzenko, Olga. B. *et al.* Combinatorial treatment of idiopathic pulmonary fibrosis using nanoparticles with prostaglandin E and siRNA(s). *Nanomedicine Nanotechnol. Biol. Med.* **13**, 1983–1992 (2017).

117. Shivshankar, P. *et al.* Inhaled tacrolimus modulates pulmonary fibrosis without promoting inflammation in bleomycin-injured mice. *J. Drug Deliv. Sci. Technol.* **24**, 469–477 (2014).

118. Lee, C. *et al.* Treatment of bleomycin-induced pulmonary fibrosis by inhaled tacrolimus-loaded chitosan-coated poly(lactic-co-glycolic acid) nanoparticles. *Biomed. Pharmacother.* **78**, 226–233 (2016).

119. Trivedi, R., Redente, E. F., Thakur, A., Riches, D. W. H. & Kompella, U. B. Local delivery of biodegradable pirfenidone nanoparticles ameliorates bleomycin-induced pulmonary fibrosis in mice. *Nanotechnology* **23**, 505101 (2012).

120. Shamskhou, E. A. *et al.* Hydrogel-based delivery of Il-10 improves treatment of bleomycin-induced lung fibrosis in mice. *Biomaterials* **203**, 52–62 (2019).

121. Su, W. *et al.* Inhalation of Tetrandrine-hydroxypropyl-β-cyclodextrin Inclusion Complexes for Pulmonary Fibrosis Treatment. *Mol. Pharm.* **17**, 1596–1607 (2020).

122. Morpurgo, M., Radu, A., Bayer, E. A. & Wilchek, M. DNA condensation by high-affinity interaction with avidin. *J. Mol. Recognit. JMR* **17**, 558–566 (2004).

123. Pignatto, M., Realdon, N. & Morpurgo, M. Optimized avidin nucleic acid nanoassemblies by a tailored PEGylation strategy and their application as molecular amplifiers in detection. *Bioconjug. Chem.* **21**, 1254–1263 (2010).

124. Morpurgo, M. *et al.* Characterization of multifunctional nanosystems based on the avidin-nucleic acid interaction as signal enhancers in immuno-detection. *Anal. Chem.* **84**, 3433–3439 (2012).

125. Eakin, R. E., McKINLEY, W. A. & Williams, R. J. Egg-white injury in chicks and its relationship to a deficiency of vitamin H (biotin). *Science* **92**, 224–225 (1940).

126. Pentti Tuohimaa, Timo Joensuu, Jorma Isola, Riitta Keinanen, Tarja Kunnas,Arja Niemela. Anu Pekki, Mika Wallen, Timo Ylikomi And Markku Kulomaa. Development of progestin-specific response in the chicken oviduct. *Int J Dev BioI* **33**, 125–134 (1989).

127. Pinn, E., Pähler, A., Saenger, W., Petsko, G. A. & Green, N. M. Crystallization and preliminary X-ray investigation of avidin. *Eur. J. Biochem.* **123**, 545–546 (1982).

128. Wilchek, M., Bayer, E. A. & Livnah, O. Essentials of biorecognition: The (strept)avidin–biotin system as a model for protein–protein and protein–ligand interaction. *Immunol. Lett.* **103**, 27–32 (2006).

129. Gitlin, G., Bayer, E. A. & Wilchek, M. Studies on the biotin-binding site of avidin. Lysine residues involved in the active site. *Biochem. J.* **242**, 923–926 (1987).

130. Gitlin, G., Bayer, E. A. & Wilchek, M. Studies on the biotin-binding site of avidin. Tryptophan residues involved in the active site. *Biochem. J.* **250**, 291–294 (1988).

131. Jain, A. & Cheng, K. The principles and applications of avidin-based nanoparticles in drug delivery and diagnosis. *J. Controlled Release* **245**, 27–40 (2017).

132. Hirsch, J. D. *et al.* Easily reversible desthiobiotin binding to streptavidin, avidin, and other biotin-binding proteins: uses for protein labeling, detection, and isolation. *Anal. Biochem.* **308**, 343–357 (2002).

133. Chivers, C. E. *et al.* A streptavidin variant with slower biotin dissociation and increased mechanostability. *Nat. Methods* **7**, 391–393 (2010).

134. Li, H., LaBean, T. H. & Leong, K. W. Nucleic acid-based nanoengineering: novel structures for biomedical applications. *Interface Focus* **1**, 702–724 (2011).

135. Bloomfield, V. A. DNA condensation by multivalent cations. *Biopolymers* **44**, 269–282 (1997).

136. Williams, D. M. Clinical Pharmacology of Corticosteroids. *Respir. Care* **63**, 655–670 (2018).

137. Pignatto, M., Realdon, N. & Morpurgo, M. Optimized avidin nucleic acid nanoassemblies by a tailored PEGylation strategy and their application as molecular amplifiers in detection. *Bioconjug. Chem.* **21**, 1254–1263 (2010).

138. Morpurgo, M. *et al.* Characterization of multifunctional nanosystems based on the avidin-nucleic acid interaction as signal enhancers in immuno-detection. *Anal. Chem.* **84**, 3433–3439 (2012).

139. Violatto, M. B. *et al.* Dexamethasone Conjugation to Biodegradable Avidin-Nucleic-Acid-Nano-Assemblies Promotes Selective Liver Targeting and Improves Therapeutic Efficacy in an Autoimmune Hepatitis Murine Model. *ACS Nano* **13**, 4410–4423 (2019).

140. Bigini, P. *et al.* In vivo fate of avidin-nucleic acid nanoassemblies as multifunctional diagnostic tools. *ACS Nano* **8**, 175–187 (2014).

AIM OF THE THESIS

Pulmonary fibrosis is a chronic disorder involving lung parenchyma. It is characterized by the deposition of extracellular matrix leading to lung remodelling. Although this alteration can be due to different factors (i.e. environmental exposure, viral infections, genetic factors), it always impairs respiratory function and, in idiopathic forms, is fatal. Activated macrophages play a key role in the initiation and perpetuation of fibrosis since they can secrete numerous factors leading to epithelial-mesenchymal transition. These cells are found in proximity to collagen-producing myofibroblasts, highly responsive to cytokines, indicating that inflammation and immune mechanisms contribute to fibrogenesis. The lack of efficient anti-fibrotic therapies prompted the scientific community to find alternative strategies to improve the lung tropism. My PhD project was aimed at investigating the targeting of intranasally-injected steroid-loaded (Dexamethasone) Avidin-Nucleic Acid-Nanoassemblies (ANANAS-Dex) in healthy mice and in a murine model of pulmonary fibrosis. The biodistribution of this nanoformulation towards the pulmonary system and specific internalization in lung macrophages has been assessed. To correlate the carrier biodistribution and the release of the drug by ANANAS-Dex, the levels of dexamethasone in lungs in off-target organs after a single administration were measured. Moreover, Avidin-Nucleic Acid Nanoassemblies are a versatile platform and can be functionalized with different compounds of interest in order to respond to various medical purposes, provided they are biotinylated with stoichiometric control, thanks to their intact biotin-binding capability and high affinity for biotin ligands. Indeed, Angiotensin converting enzyme 2 (ACE2) was attached to these NPs for the evaluation of a potential preventive activity against SARS-CoV-2 infection.

Thus, the following objectives were defined and pursued in Chapters 2-4, respectively:

1) Generation and characterization of a reliable murine model of pulmonary fibrosis.

2) Assessment of the impact of Avidin-Nucleic Acid-Nanoassemblies loaded with Dex in healthy and in pathological conditions such as in a pulmonary fibrosis murine model induced with bleomycin (BLM) and the effect in lung uptake.

3) Assessment of the impact of Avidin-Nucleic Acid-Nanoassemblies loaded with ACE2 as nanodecoy system for the prevention of COVID-19 infection and the effect in lung biodistribution and toxicity.

CHAPTER 2

Intranasal bleomycin instillation in anesthetized mice induces a process of pulmonary fibrosis: a comparative evaluation to reduce the animal distress

Annalisa Morelli*, Martina B. Violatto, Giulia Yuri Moscatiello, Anita Salmaso, Veronica Codullo, Patrizia Morbini, Federica Meloni and Paolo Bigini*

Manuscript submitted to The Journal of Pathology

Abstract

Pulmonary fibrosis is a chronic, progressive and deadly lung disease. Fibrogenesis is a dynamic process characterized by extracellular matrix production and myofibroblast activation, which leads to alveolar remodelling, disrupted gas exchange and ultimately respiratory failure and death. In humans is a consequence of intensive and repeated inflammatory or dis-immune injuries to alveolar and bronchiolar epithelium in a favourable genetic background. No current animal model recapitulates all of these cardinal manifestations of the human disease. However, investigations using experimental models such as the one that requires administration of bleomycin by intravenous or intratracheal route, have led to the identification of many pathological cells and mediators that are believed to be important in human disease as well. However, these models are often hardly reproducible, and the administration route of the injurious drug is invasive and does not resemble human exposure. Thus since animal models are crucial to understand pathogenic mechanisms and to preliminarily test new therapeutic strategies, this work was aimed at developing a reliable and feasible mouse model to study the evolution of fibrotic responses, which is based on bleomycin administration via intranasal route and to analyze whether its histological and biological features mirror human disease. A single dose of bleomycin with different routes of administration was tested in 10-week-old C57BL6/J male mice. Our results demonstrate that intranasal administration of bleomycin induced pulmonary injury, inflammation and subsequent fibrosis, resembling many features of the human disease. This preliminary result will be pivotal for the evaluation of the possible impact of new pharmacological treatments for lung disorders.

2.1 Introduction

Interstitial lung diseases (ILDs) represent a diverse spectrum of pathologies impacting the pulmonary parenchyma, characterized by extensive inflammation and diffuse fibrosis. Pulmonary fibrosis (PF) is distinguished by a persistent and progressive tissue repair response, resulting in irreversible scarring, lung remodelling, and compromised gas exchange. An overabundance of extracellular matrix (ECM) proteins leads to the accumulation of fibrotic tissue, alveolar destruction, and irreversible loss of pulmonary function.[1,2] Idiopathic pulmonary fibrosis (IPF) is the most prevalent ILD, with an estimated incidence ranging from 2-8 to 30 cases per 100,000 individuals annually in Europe and North America. Predominantly affecting individuals over 50, with a median age at diagnosis of approximately 65 years, IPF exhibits a variable and somewhat unpredictable disease course, with a median survival time of 3–5 years post-diagnosis.[3,4] Although ILDs differ for etiology, age of onset and clinical severity, they share many pathological and cellular hallmarks and, very often a poor prognosis. Currently, there is no effective treatment capable of arresting or reversing disease progression to improve clinical outcomes. The pathogenesis of ILDs, particularly IPF, involves complex interactions across various cellular compartments, including the epithelium, lung fibroblasts, and the innate and adaptive immune systems. Despite substantial research efforts, the precise mechanisms underlying the interplay of these factors in disease development remain elusive. This underscores the critical necessity for reliable experimental models that faithfully replicate the complex disease manifestations observed in humans.[5]

To gain insights into the pathogenesis of this complex disease and to explore potential therapeutic interventions, animal models are still indispensable. Among the various experimental models available (exposure to radiation, silica or asbestos, fluorescein isothiocyanate and transgenic mice or gene transfer employing fibrogenic cytokine), the bleomycin (BLM)-induced animal model represents one of the most widely employed due to its ability to mimic several aspects of human fibrotic lung disease.[6–9] The complexity deepens when considering IPF, given the uncertain origins and progression of the disease. No singular cause has been identified that definitively triggers this condition in animals. Various models of pulmonary fibrosis have emerged over time,

attempting to replicate certain aspects of human IPF. However, these models often fail due to the complex pathogenesis, particularly its severe and irreversible course and often the off-side accumulation.[8]

BLM, a glycopeptide antibiotic and antineoplastic agent, exerts its effects through the generation of reactive oxygen species (ROS), induction of single and double-strand DNA breaks and the inhibition of DNA metabolism, thereby disrupting the progression of the cell cycle. This process results in the chelation of metal ions, which in turn catalyzes the reaction of the resulting pseudo-enzyme with molecular oxygen. Consequently, this molecular interaction triggers the generation of DNA-cleaving superoxide and hydroxide free radicals.[10] BLM is primarily used in clinic for the treatment of various carcinomas and lymphomas.[11,12]

Notably, the enzymatic activity of BLM hydrolase, an enzyme responsible for its inactivation, plays a pivotal role in modulating the drug's effects across diverse tissues. Lungs, skin and mucous membranes exhibit relatively low levels of this enzyme, making them more susceptible to BLM exposure. The excessive accumulation of ROS in lungs can initiate an inflammatory cascade and fibroblast activation leading to pulmonary toxicity.[8] Among patients receiving BLM, approximately 10% may develop lung toxicity, which clinically presents as cough, dyspnoea, fever, cyanosis, and a decline in lung function metrics. This acute response may subsequently evolve into pulmonary fibrosis in approximately 1% of patients within a span of weeks to months.[6]

Although in preclinical settings the induction of fibrosis by BLM has been widely reported in literature[9,13], some controversies still remain. It is however important to pay attention on the phenotype generated by BLM induction comparing doses, posology and ways of administration. Therefore, the primary aim of this study was to establish and rigorously characterize a murine model of pulmonary fibrosis using BLM as the inducing agent, focusing on the optimization of the route of administration protocol. Through comprehensive histological and biochemical evaluations combined to an observational study, we assess the fidelity, suitability and reproducibility of this model. This research provides a crucial platform with a well-validated and reliable animal model for further elucidating the underlying mechanisms of pulmonary fibrosis pathogenesis and evaluating potential therapeutic targets for these debilitating lung disorders.

2.2 Materials and Methods

- **Animals**

The Mario Negri Institute for Pharmacological Research IRCCS adheres to the principles set forth in the following laws, regulations, and directives concerning the care and use of laboratory animals: Italian law (D.lgs 26/2014; Authorization No. 19/2008-A issued on March 6, 2008 by the Ministry of Health); the Mario Negri Institutional Regulations and Policies—which provide internal authorization for persons conducting animal experiments (Quality Management System Certificate, UNI EN ISO 9001:2015, Reg. No. 6121); the NIH Guide for the Care and Use of Laboratory Animals (2011 edition); and the EU Directives and Guidelines (EEC Council Directive 2010/63/UE). This work was reviewed by the IRCCS-IRFMN Animal Care and Use Committee (IACUC) and subsequently approved by the Italian "Istituto Superiore di Sanità" (Code: 558/2021-PR). Ten-week-old C57BL/6 male mice (Charles River) were used throughout the study. Mice were maintained under specific pathogen-free conditions in the Institute's Animal Care Facilities; they received food and water ad libitum and were regularly checked by a certified veterinarian who is responsible for animal welfare supervision and experimental protocol review.

- **Bleomycin-Induced Pulmonary Fibrosis in mice and treatment**

A total of 33 C57BL/6J animals were used for the routes of administration study and for the establishment and characterization of the animal model. For the intravenous administration (i.v.), mice were injected with 100 mg/kg of Bleomycin sulfate (TCI, Tokyo) in saline (0.9%) or vehicle (saline 0.9%) in a volume of 200 µl. The animals were allowed to recovery immediately afterwards and sacrificed 21 days post administration. For the low dose intranasal administration (i.n.), mice were short-term anesthetized with isoflurane (3–5%) and 1 mg/kg of Bleomycin sulfate (TCI, Tokyo) in saline (0.9%) or vehicle (saline 0.9%) was instilled with a micropipette (12,5 µl per nostril with a total volume of 25 µl). The animals were sacrificed at 7, 14, 21, and 28 days post administration. For the high dose i.n. administration, mice were anesthetized with medetomidine (Domitor®) at a dose of 0,4 mg/kg b.w. and ketamine (Lobotor®) at a dose of 36 mg/kg injected intraperitoneally and 5 mg/kg Bleomycin sulfate (TCI,

Tokyo) in saline (0.9%) or vehicle (saline 0.9%) was instilled with a micropipette (25 µl per nostril with a total volume of 50 µl). Animals were allowed to recover immediately afterwards (Antisedan® - 0,8 mg/kg injected intraperitoneally). The animals were sacrificed at 2, 7, 14, 21, and 28 days post administration.

- **Tissue Collection and Histological analysis**

Lungs were removed from BLM-treated animals at different timepoints (7-14-21-28 days) and fixed overnight in 10% formalin (BioOptica, Italy). Tissues were processed for paraffin embedding, cut with Leica RM55 microtome (Leica Microsystem, Italy) into 4 µm-thick sections and dried into the oven at 37°C overnight. Slices were deparaffinised in xylene and rehydrated through a series of alcohols to water. Hematoxylin-Eosin (BioOptica, Italy) staining method was used to investigate alveolitis and fibrosis. Picrosirius Red (0.5 g Sirius Red F3B (C.I. 35782) + 500 ml picric acid solution – Sigma Aldrich) and Masson's trichrome (Trichrome stain kit – Sigma Aldrich – HT15-KT) staining methods were performed to reveal collagen deposition following manufacturer's instructions. Samples were dehydrated through an alcohol scale, dried under the hood and mounted with xylene-based mounting medium (DPX, Sigma).

To achieve integrated detection of protein expression, sections obtained from paraffin-embedded samples were immunoassayed using Vectastain Elite ABC (Vector Laboratories, Burlingame, CA, USA). Antigen retrieval was performed in citrate buffer (pH 6) in a boiling pot for 15 minutes, followed by endogenous peroxidase inhibition with H_2O_2 3% for 10 min at RT and incubation with blocking solution (PBS-NGS 10%-Tween 20 0.05%) for 30 min at RT. For subcellular localization, Iba1 (clone 019-19741, Wako; 1:500) was used to label macrophage calcium binding protein and fibroblast activation was marked by α-SMA (thermoscientific, 1:100). Sections were stained with 3,3 - Diaminobenzidine (DAB, Sigma Aldrich) and counterstained with Mayer's hematoxylin (Bioptica, Italy). Samples were dehydrated through an alcohol scale, dried under the hood and mounted with xylene-based mounting medium (DPX, Sigma). For immunofluorescence analysis, at the moment of sacrifice, lungs from untreated and BLM-mice were collected, frozen in dry ice and stored at -80°C until immunofluorescence staining. Cryostat sections were cut at 20 µm and mounted on glass

slides. Slides were postfixed in 10% formalin (BioOptica, Italy) for 20 minutes, washed three times in phosphate-buffered saline (PBS) for 5 min and incubated for 1 h with a blocking solution (PBS-NGS 10%-Triton X-100 0.1%) then washed again with PBS. For subcellular localization, the antibody anti-CD68 (specific for lysosome and endosome membranes of macrophages) was used: primary rat anti-CD68 monoclonal antibody (1: 200, Serotec, Kidlington, UK) + Triton X -100 0.1% + NGS 3% in 1X PBS overnight at 4 ° C. After washing with 1X PBS, the slides were incubated with the Alexa488 conjugated secondary antibody (1: 500, Invitrogen) for 1 hour at room temperature in 1% 1X-NGS PBS solution. After this step, the slides were incubated with the Hoechst nuclear marker 33258 (2 µg / mL in 1X PBS, Sigma Aldrich) for 10 minutes. Fluoromount Aqueous Mounting Medium (Sigma Aldrich) was used for mounting with cover glass in order to preserve the tissue for long periods and prevent the decay of the fluorescence.

The slides were then observed at the Virtual Slide Microscopy VS120 (Olympus, Japan), a microscope that allows to obtain rapid scans of the organs in their entire volume, with high anatomical resolution.

- **Quantification of collagen deposition and lung damage**

For the determination of collagen fibers, Sirius Red stained whole sections were analysed in blind (3 mice per group). The percentage of collagen deposition area was determined using Image J software. For the determination of lung damage, Masson's trichrome stained whole sections were analysed in blind (3 mice per group). Fibrotic changes in each lung section were assessed as the mean score of severity from observed microscopic fields. 24 fields within each mid lung section were observed at a magnification of 20X. Scores from 0 (normal) to 8 (total fibrosis) were assigned according to the predetermined Ashcroft scale.[14,15] After examination of the whole section, the mean of the scores from all fields was taken as the fibrotic score.

- **Quantitative real-time polymerase chain reaction**

Total RNA was isolated with TRIzol Reagent (Thermo Fischer Scientific) according to the manufacturer's instructions, and 1 µg total RNA was reverse transcribed into cDNA using high-capacity cDNA reverse transcription kit (Applied Biosystems). cDNAs were

mixed with Quantifast SYBR Green Master Mix (BiotechRabbit) according to the manufacturer's instructions and both forward and reverse primers (0.5 μM) for detecting mRNA levels of mouse genes. qPCR was carried out using a QuantStudio 5 Systems (Applied Biosystems) and the amplification steps were 50 °C for 2 min, 95 °C for 10 min and followed by 40 cycles of 95 °C for 15 s and 60 °C for 1 min. Relative mRNA levels of the target genes were normalized to β-ACT mRNA expression and analyzed by the $2^{-\Delta\Delta Ct}$ method. Quantitative Rt-polymerase chain reaction primers:

	5'- 3' Forward	5'- 3' Reverse
β-ACT	GCCCTGAGGCTCTTTTCCAG	TGCCACAGGATTCCATACCC
TNF-α	AGACCCTCACACTCAGATCATCTTC	TTGCTACGACGTGGGCTACA
IL-6	TCTCTGGGAAATCGTGGAAA	TCTGCAAGTGCATCATCGTT
COL1a1	ACCTGTGTGTTCCCTACTCA	GACTGTTGCCTTCGCCTCTG
FIBRONECTIN	CACGGAGGCCACCATTACT	CTTCAGGGCAATGACGTAGAT

Table 2.1 Rt-PCR primers sequence.

- **Data calculation & statistical analysis**

All statistical analyses were done using GraphPad Prism version 7.00 for Windows (Graph-Pad Software, CA, USA). All data are expressed as mean ± standard error of the mean. The differences between groups were compared using one-way ANOVA analysis, followed by Dunnet's post hoc test analysis. P values <0.05 were considered statistically significant and reported on graphs. For *in vivo* experiments, the number of animals sacrificed at each data point was minimized according to the 3Rs principle.

2.3 Results and Discussion

Routes of administration, volume of injection and anaesthetic agent determination

The experimental conditions used to administer BLM can profoundly influence its biodistribution, pharmacokinetics and consequent systemic pathological and clinical outcomes. The protocol of administration is pivotal in determining the drug's therapeutic outcome and toxicity profile. In a first step, we compared the effects of diverse doses, anesthetic agents and routes of BLM administration in a murine model. We aim to provide critical insights into optimizing the use of BLM as inducing agent to obtain a

reliable mouse model of pulmonary fibrosis, combining *in vivo* and *ex vivo* studies during disease progression.

Ten-week-old C57BL6/J male mice were treated with a single i.v. administration of BLM at the dose of 100 mg/kg in 200µl.[13] Animals were monitored and sacrificed at different timepoints as reported in the experimental plan in figure 2.1A. Histopathology revealed at 21 days post treatment only a slight infiltration in lungs causing endothelial cell injuries (Fig 2.1B). Systemic administration is in fact thought to cause more diffuse disease with slower time course for fibrosis development and requires high doses. For this reasons, we investigated the i.n. administration as an alternative route for the induction of lung fibrosis in mice. BLM was administered intranasally (1 mg/kg in 25µl)[16–18] under light anaesthesia with 3-5% isoflurane and animals were monitored and sacrificed at different timepoints as reported in the experimental plan in figure 2.1A. In this case, no effect was seen after treatment (Figure 2.1B). This results is probably due to fact that reduced administration volumes facilitate enhanced brain accumulation. The nasal instillation of increasing volumes up to 50µl of fluid in mice facilitate a greater relative accumulation and persistence in lungs. Moreover, the presence of a deeper anaesthesia, could affect the relative distribution of intranasally instilled substances potentially facilitating their deposition within the more distal segments of the lungs when compared to the isoflurane exposition, that preserves a reflex related to the detection of fluid in the upper airways and restricts pulmonary aspiration.[19,20]

In light of these considerations and findings, we decided to optimize the protocol of induction and treat the animals with a single i.n. higher dose of BLM (5 mg/kg in 50µl) under ketamine/medetomidine anaesthesia. Animals were monitored and sacrificed at different timepoints as reported in the experimental plan in figure 2.1A. Histology revealed at 21 days post treatment a strong infiltration of inflammatory cells and a marked multifocal fibrosis as reported in figure 2.1B. With the use of this route of administration, the dose of BLM, and anaesthesia conditions, we were able to obtain a phenotype comparable to the one achieved with the most widely used protocols, avoiding the related limitations. For example, the intratracheal dosing approach includes the requirement for intubation and the use of a nose cone or additional ketamine sedation together with isoflurane anaesthesia. In addition, some procedures require surgical

intervention and post-surgery monitoring, making these protocols more invasive and stressful for the animals.[20] Conversely, the use of a systemic route of administration could be easier to perform but results in a more widespread BLM distribution with lower lung accumulation and slower time course for fibrosis development.[8,9] These findings highlight significant pulmonary impairment, suggesting that this protocol holds potential for establishing an animal model suitable for investigating pulmonary fibrosis. The i.n. instillation may also produce a more uniform distribution due to gravity and natural inhalation by the mouse resulting in an easy, efficient and reproducible approach.

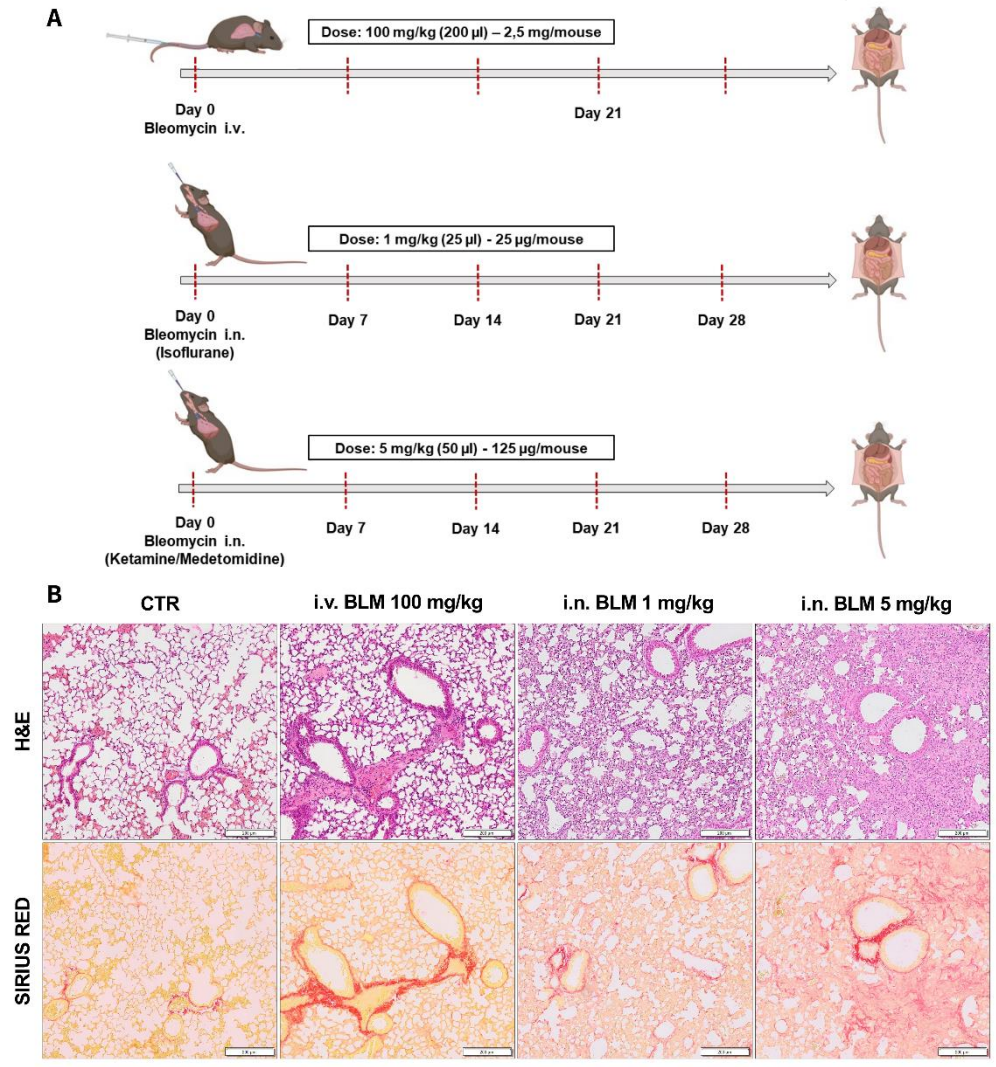

Figure 2.1 Bleomycin administration and histopathological evaluation. A) C57BL6/J mice, ten-week-old male were randomly distributed (3 animals/group) and treated via a single i.v. administration with BLM suspended in saline at a dose of 100 mg/Kg and sacrificed 21 days post administration, single i.n. administration or non-treated. I.n. treatment was performed at a low dose of 1 mg/Kg with isoflurane anesthetized animals or at a high dose of 5 mg/Kg with ketamine/medetomidine anesthetized animals. Mice were sacrificed at different time points (7, 14, 21 and 28 days) to study the lung injury and fibrosis progression. **B)** Histopathological evaluation by hematoxylin and eosin staining (H&E – upper panel) and Sirius Red staining (lower panel) of lungs of untreated mice (CTR) or treated with BLM after a single i.v. (100 mg/kg) or i.n. (1 or 5 mg/kg) administration. Representative images of lung sections of animals sacrificed at 21 days after the treatment are reported. Scale bar=200µm.

Histological characterization of the BLM animal model

Once established the protocol of administration, a deep histological characterization was performed. After BLM (5 mg/kg in 50 µl) i.n. administration, ten-week-old C57BL6/J male mice were monitored and sacrificed at different timepoints in order to follow the model disease progression. The treatment did not induce lethality with a maximum weight loss of 20% in the first two weeks followed by weight recovery (Figure 2.2A and B). Other signs of lung injury in BLM-treated mice included decreased activity, hunched posture and periods of dyspnoea.

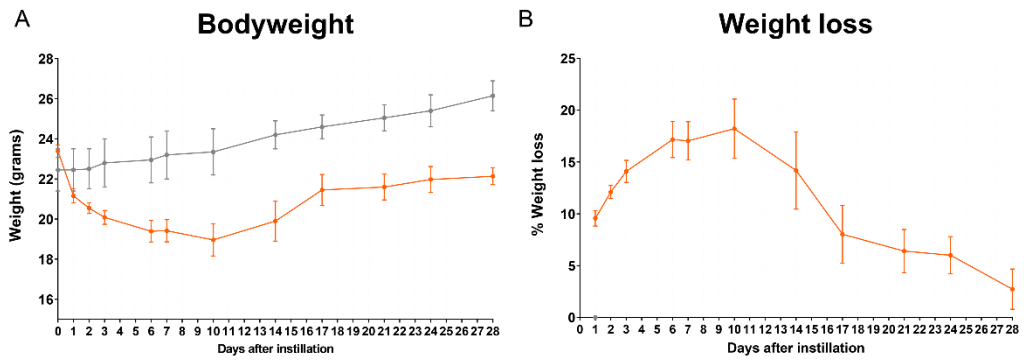

Figure 2.2 Health status in bleomycin mouse model of lung injury (i.n. - 5 mg/Kg). A) BLM instillation causes decreased bodyweight (orange line) when compared to the untreated animals (grey line) and **B)** an increase in weight loss with a maximum of 20% in treated mice.

The macroscopic examination of the lungs in BLM-treated mice revealed scattered lesions within regions that appeared normal. As the disease advanced, certain foci

merged, giving rise to larger, darker lesion areas. This pulmonary impact extended across multiple lobes and occurred bilaterally. Histologic evaluation from H&E staining showed at 7 days post instillation a slight to moderate infiltration of inflammatory cells, including macrophages and neutrophils, and disruption of alveoli, indicating an initial lung injury and acute inflammation. Between 7 and 14 days a transition phase characterized by a fibroproliferation process, in which mesenchymal, inflammatory and epithelial cells activate fibrotic repair pathways. Infiltration of inflammatory cells and moderate multifocal fibrosis was observed. Pulmonary fibrosis and disruption of normal lung architecture occurred at days 21 and 28. The presence of fibroblastic foci indicate sites of active fibrogenesis (Figure 2.3 – upper panel). Sirius Red staining showed expanded severe alveolar and interstitial fibrosis, abnormal collagen deposition and alveolar destruction. After day 28, the fibrotic changes tend to be resolved and normal situation restored (Figure 2.3 – middle panel). To confirm the fibrotic collagen deposition, Masson's trichrome staining was performed. It is highlighted in blue the presence of physiological collagen fibres, while in light blue the newly synthetized collagen, especially from day 14-21 post BLM administration, confirming the occurring of the pathological fibrotic process (Figure 2.3 – lower panel). Using this approach, the administration of a single i.n. dose of BLM induces a rapid development of injury and acute inflammation followed by a chronic inflammatory phase with the instauration of fibrosis over the subsequent weeks.

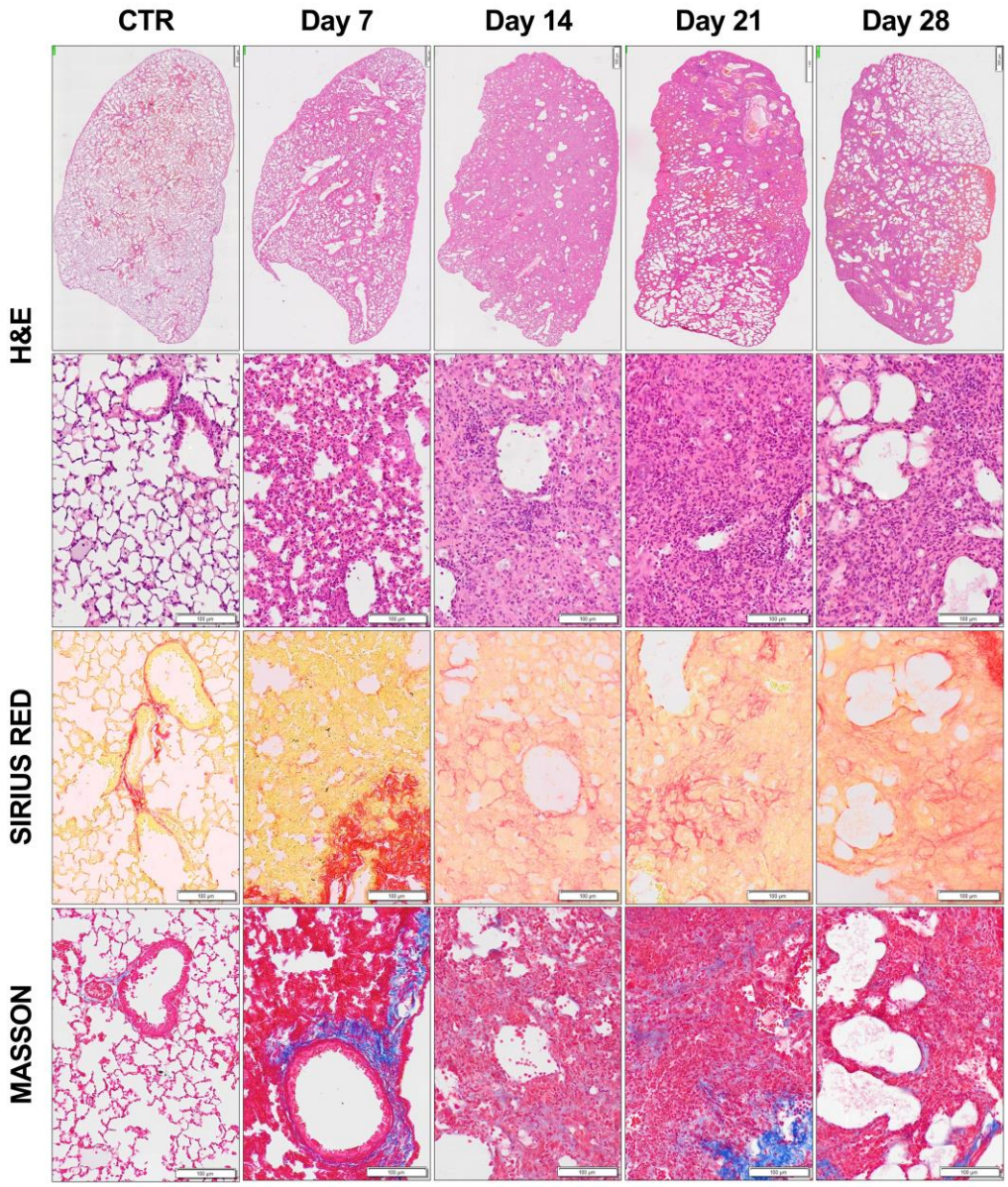

Figure 2.3 Histopathological characterization in bleomycin treated animals. Histopathological evaluation by H&E staining (upper panel), Sirius Red staining (medium panel) and Masson's trichrome (lower panel) of lungs of untreated mice (CTR) or treated with BLM after a single i.n. administration (5 mg/kg). Representative images of lung sections of animals sacrificed at 7, 14, 21 and 28 days after the treatment are reported. Scale bar=500 μm (upper panel) – 100 μm (lower panels).

To better determine the extent of fibrosis, two different quantitative parameters were evaluated. Regarding the collagen deposition, the percentage of positive Sirius Red staining was determined through ImageJ software. As reported in figure 2.4A, the quantification of collagen deposition revealed at 7 days no difference when compared to the untreated group, indicating that no significant accumulation is detected. This confirmed that the inflammatory phase occurs in the first week post BLM administration where ECM is not still highly produced. Opposite, from day 14 to 28 a strong significant accumulation is detected in lungs sections, with a peak of signal at 21 days after BLM administration. This result confirmed that there is a progression peaked by an established fibrosis at 3 weeks post induction. Since collagen deposition indicate enhanced stiffness in the ECM, remodelling of lung architecture and, as a consequence, impairment in lung functions[21], it is important to correlate these results with a lung damage parameter. The Ashcroft Scale assigns different score of fibrosis evaluating histological Masson's trichrome stained sections. The severity of lesions varied from one region to another, ranging from normal lung to complete fibrosis. As reported in figure 2.4B, lung sections from untreated animals showed predominately normal lung architecture. At 7 days a strong increase in the score is detected, were gentle fibrotic changes, alveolar septa with knot-like formations and single fibrotic masses are observed. Lung fibrosis, with confluent and large contiguous fibrotic masses, was most prominent between 14 and 21 days after BLM administration and less severe at 28 days. These observations are consistent with an acute inflammatory reaction with alveolitis in the first week. The following weeks are characterized by proliferation of fibroblasts and ECM proteins synthesis leading to perivascular, peri-bronchial and sub-pleural fibrosis. Moreover, in both parameters there is the tendency of a gradual decrease at day 28 post administration. It is known that BLM do not induce a progressive worsening of the symptoms and the induced damage tend to revert, representing a criticism in terms of resembling human IPF.[8] Conversely, a significant chronic inflammation is evident and appears to be important for the developing fibrosis, representing a fibrotic model after infection and acute inflammation, where it is not the end-stage. The exact quantification of the fibrotic lesions in histological section is therefore pivotal for the assessment of pathological markers and the determination of the efficacy of possible new therapeutic treatments.

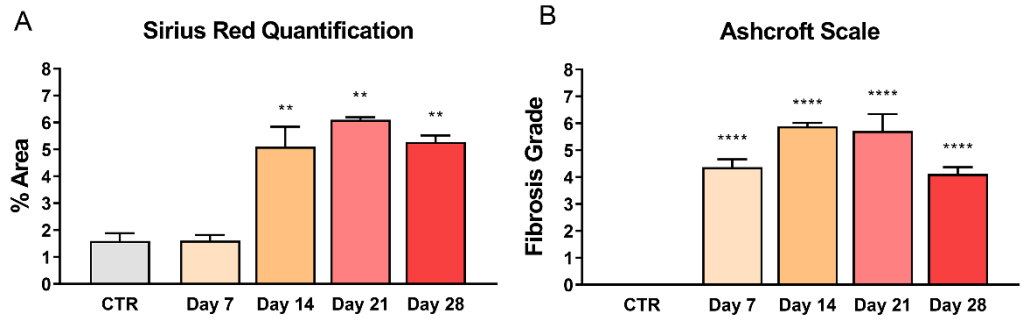

Figure 2.4 Histopathological quantification in bleomycin treated animals. Histopathological quantification of **A)** Sirius Red staining in lung section and **B)** representation of Ashcroft scale grade obtained by Masson's trichrome analysis of lungs of untreated mice (CTR) or treated with BLM after a single i.n. administration (5 mg/kg). Data are reported as mean ± SE. The data were analyzed by One-way ANOVA using Dunnet's test. **$p \leq 0.01$, ****$p \leq 0.001$.

Cellular characterization of the BLM animal model

The exact pathogenesis of IPF remains still not completely understood; however, existing evidence indicates a breakdown or imbalance within several pathways, ultimately culminating in the distinctive loss of alveolar epithelial cells and the accumulation of differentiated fibroblasts characteristic of this condition. To better understand the fibrotic process, the key factors involved in the pathogenesis and to assess histological disease status, immunohistochemical markers were explored.

Myofibroblasts, possessing contractile properties and expressing α-smooth muscle actin (α-SMA), play a pivotal role in the excessive collagen deposition and tissue remodelling observed in pulmonary fibrosis. Potential origins of myofibroblasts are identified: (1) the proliferation and differentiation of resident fibroblasts; (2) the recruitment of circulating fibrocytes to areas of lung injury; and (3) epithelial-mesenchymal transition.[5,22] Moreover, environmental exposure to toxicants or airway diseases like asthma, chronic obstructive pulmonary disease and cystic fibrosis can lead to remodelling of airway smooth muscle (e.g., hypertrophy) and decreased lung function.[23] Histology revealed extensive expression of α-SMA, particularly on days 14 and 21, suggesting a strong fibroproliferation and the presence of collagen-producing areas. In contrast, in control lungs the expression of α-SMA was found exclusively around blood vessel (Figure 2.5 – upper panel). To characterize the cellular composition and lung

infiltrates, immunohistochemical analysis for Iba1, marker of alveolar, interstitial and circulating macrophages, and CD68, marker of macrophage lysosomes, were performed. Iba1 is upregulated during the activation of these cells in inflammatory conditions. Macrophage infiltration into the lungs was significantly greater in the BLM group as compared to the control group, at 7, 14 and 21 days (Figure 2.5 – middle and lower panel). Notably, as highlighted with CD68 in green (Figure 2.5 – lower panel), macrophages showed a peculiar and irregular shape thus indicating their activated state when compared to the round and regular shape of the macrophages of the control group. Moreover, the high expression of lung infiltrates of the BLM group tend to persist in all timepoints, indicating that inflammation has a strong contribution in the progression of the pathology in the experimental model.

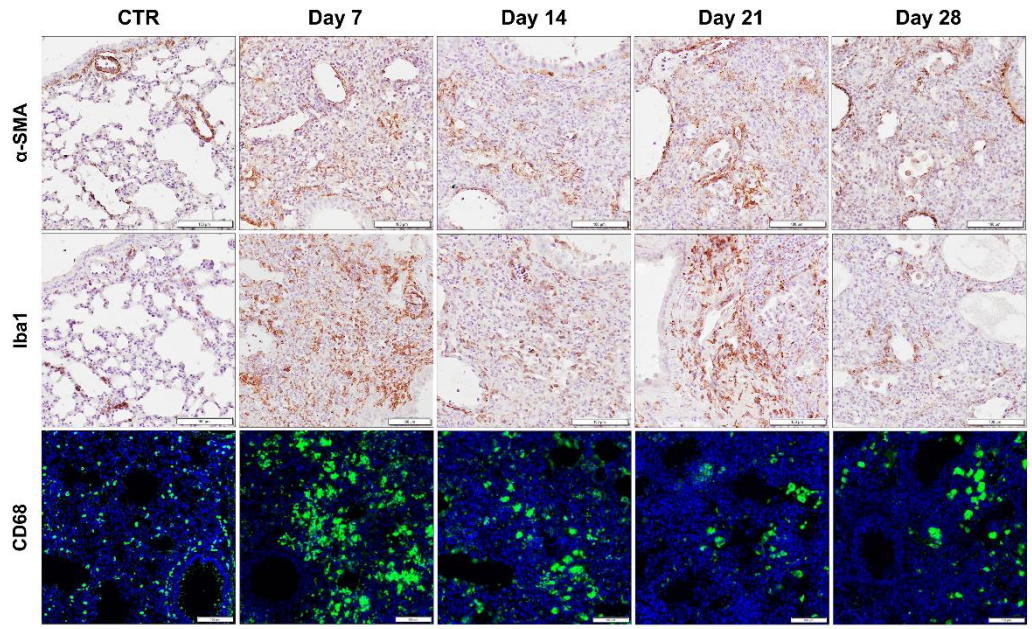

Figure 2.5 Histopathological evaluation of fibrotic and inflammatory markers. α-SMA (upper panel), Iba1 (middle panel) and CD68 staining (green - lower panel) obtained by immunohistochemistry protocol of lungs of untreated mice (CTR) or treated with BLM after a single i.n. administration (5 mg/kg). Representative images of lung sections of animals sacrificed at 7, 14, 21 and 28 days after the treatment are reported. Scale bar=100 μm.

Modulation of inflammatory and profibrotic markers after BLM treatment

To deepen the characterization of the BLM animal model in parallel to the histological evaluation, the gene expression analysis was assessed. Interleukin 6 (IL-6) and Tumor necrosis factor α (TNF-α), inflammatory cytokines also important in the instauration of fibrotic changes, have been tested. IL-6 is crucial for the inflammatory phase and the switch to a reparative environment during the resolution of wound healing.[24] TNF-α is a potent inflammatory cytokine that promote ROS generation from pulmonary and non-pulmonary tissues.[25] Since the effect of treatment on gene expression is an upstream event, we decided to also include in this study an early time point (day 2). As illustrated in the figure 2.6 (upper panel), from 2 days after administration of BLM, a notable upregulation of proinflammatory cytokines is evident. This high expression is maintained also at the latter timepoints, indicating that in this model the presence of inflammatory cells and pathway persist also in the fibrotic stage and this result is in accordance with what found in histological sections. Regarding the key fibrotic markers, collagen 1a1 and fibronectin[5,26], pivotal in ECM composition, were also assessed (Figure 2.6 – lower panel). In this context, a diverse pattern emerges regarding gene expression modulation. Specifically, the expression of both genes tend to increase at day 7 post administration when compared to the untreated group, indicating that the biological system is responding to the alveolar damage stimuli. Indeed, at 14 days post administration a significant peak is observed and correspond to the start of the fibrotic phase characterized by fibroproliferation and ECM synthesis. This signal tends to decrease in subsequent timepoints, and this is probably due to fact that the damage repair stimulus is important in this transition phase towards the established fibrotic phase and then a partial restoration to the physiological conditions occurs (21-28 days). It is widely known that key factors involved in pathogenesis are activated at the gene level during specific phases of disease progression, so it is extremely important the determination of their upregulation or downregulation for the experimental plan and, therefore, for clinical intervention. The possibility of intervening in a specific phase, targeting either inflammatory or fibrotic markers, can influence the success of a potential therapeutic strategy. Collectively, these results hold significance for investigating pathological markers and correlating them with histopathological evaluation.

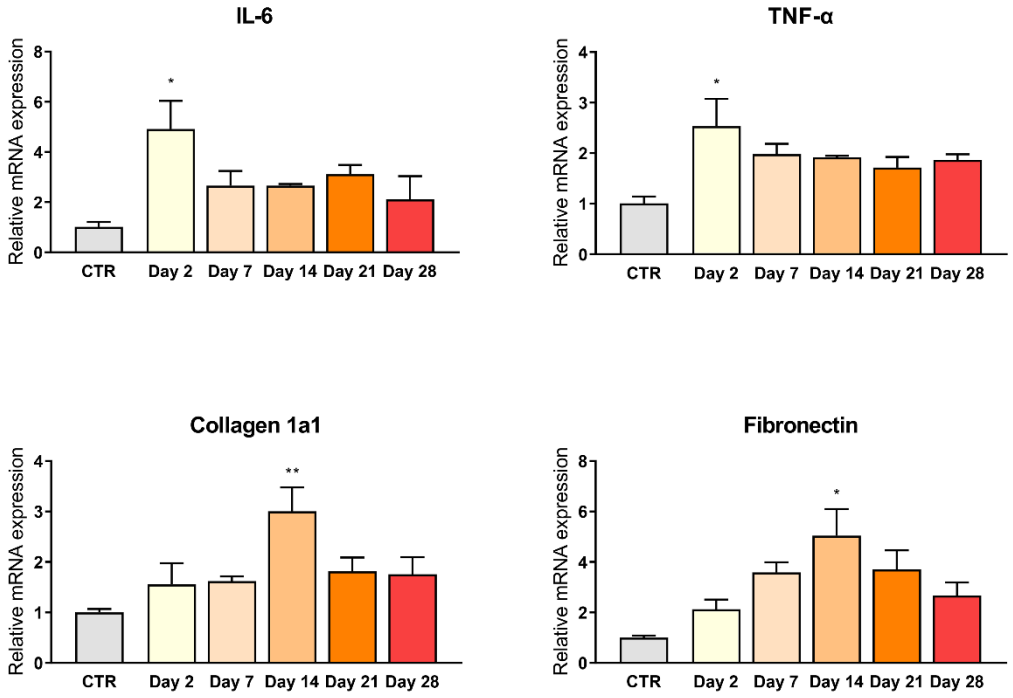

Figure 2.6 Modulation of inflammatory and profibrotic markers in lungs. A) mRNA expression of IL-6, TNF-α, collagen 1a1 and fibronectin was evaluated by RT-qPCR in lungs of mice (n =3 per group) treated with BLM and sacrificed at different timepoints. Genes were normalized on β-ACT and the $2^{-\Delta\Delta Ct}$ method was employed for relative quantification on an external calibrator. Data are reported as mean ± SE, and were analyzed with one-way ANOVA followed by Dunnets' post hoc test. Significant differences compared to the untreated group (CTR) are reported, *$p < 0.1$, **$p \leq 0.01$.

2.4 Concluding remarks

The generation of animal models capable of recapitulating as faithfully as possible the main pathological and clinical alterations of specific human pathologies is still of fundamental importance in the field of biomedical research for both diagnostics and therapy. Despite the enormous progress made in recent decades in alternative approaches to the use of vertebrates (increasingly advanced computational studies, analysis of increasingly sensitive biomarkers, use of organoids or invertebrates, high resolution non-invasive imaging) in translational preclinical studies, there are still many aspects that require its extensive use. However, it is the responsibility of researchers to adapt this need to the ever-increasing demands of the community regarding the reduction,

replacement and refinement of *in vivo* analysis techniques. The present study was born precisely from this need, that is, to refine the method and select the technique that can provide reliable and repeatable results and that can cause the least physical and psychological suffering to the experimental subject. Our model summarizes important characteristics of the evolution that various lung diseases have in common and which are characterized by a first phase of inflammation and a second phase of fibrosis. The combination of histological and molecular analysis is a useful tool for understanding the mechanisms and consequences on the anatomical target of interest. The i.n. instillation in anesthetized mice induces a reduction in handling stress, is less invasive and harmful than an intratracheal treatment and requires a lower sample size due to the extremely almost total percentage of survival. Additionally, it is also more suitable compared to the systemic administration. It is indeed widely reported that, although BLM has as preferential target the lungs, its effect is not limited to this organ but can also induce skin redness, blistering, tenderness.

Furthermore, the method we have selected has the advantage of inducing the pathology with a single treatment, further minimizing stress. The present study is limited to the characterization, but several endpoints could be easily exploitable in future studies to test the efficacy of therapeutic interventions or improving non-invasive methods of diagnosis and peripheral markers discovery.

References

1. Wijsenbeek, M., Suzuki, A. & Maher, T. M. Interstitial lung diseases. *The Lancet* **400**, 769–786 (2022).
2. Wijsenbeek, M. & Cottin, V. Spectrum of Fibrotic Lung Diseases. *N Engl J Med* **383**, 958–968 (2020).
3. Martinez, F. J. *et al.* Idiopathic pulmonary fibrosis. *Nat Rev Dis Primers* **3**, 17074 (2017).
4. Richeldi, L., Collard, H. R. & Jones, M. G. Idiopathic pulmonary fibrosis. *The Lancet* **389**, 1941–1952 (2017).

5. Wilson, M. S. & Wynn, T. A. Pulmonary fibrosis: pathogenesis, etiology and regulation. *Mucosal Immunology* **2**, 103–121 (2009).
6. Moeller, A., Ask, K., Warburton, D., Gauldie, J. & Kolb, M. The bleomycin animal model: A useful tool to investigate treatment options for idiopathic pulmonary fibrosis? *The International Journal of Biochemistry & Cell Biology* **40**, 362–382 (2008).
7. B. Moore, B. *et al.* Animal Models of Fibrotic Lung Disease. *Am J Respir Cell Mol Biol* **49**, 167–179 (2013).
8. Liu, T., De Los Santos, F. G. & Phan, S. H. The Bleomycin Model of Pulmonary Fibrosis. *Fibrosis* (ed. Rittié, L.) vol. 1627 27–42 (Springer New York, 2017).
9. Della Latta, V., Cecchettini, A., Del Ry, S. & Morales, M. A. Bleomycin in the setting of lung fibrosis induction: From biological mechanisms to counteractions. *Pharmacological Research* **97**, 122–130 (2015).
10. Li, S., Shi, J. & Tang, H. Animal models of drug-induced pulmonary fibrosis: an overview of molecular mechanisms and characteristics. *Cell Biol Toxicol* **38**, 699–723 (2022).
11. Froudarakis, M. *et al.* Revisiting bleomycin from pathophysiology to safe clinical use. *Critical Reviews in Oncology/Hematology* **87**, 90–100 (2013).
12. Bayer, R. A., Gaynor, E. R. & Fisher, R. I. Bleomycin in non-Hodgkin's lymphoma. *Semin Oncol* **19**, 46–52; discussion 52-53 (1992).
13. Wang, L., Wang, Y., Yang, T., Guo, Y. & Sun, T. Angiotensin-Converting Enzyme 2 Attenuates Bleomycin-Induced Lung Fibrosis in Mice. *Cell Physiol Biochem* **36**, 697–711 (2015).
14. Ashcroft, T., Simpson, J. M. & Timbrell, V. Simple method of estimating severity of pulmonary fibrosis on a numerical scale. *Journal of Clinical Pathology* **41**, 467–470 (1988).
15. Hübner, R.-H. *et al.* Standardized quantification of pulmonary fibrosis in histological samples. *BioTechniques* **44**, 507–517 (2008).
16. Lin, C. *et al.* Targeting protease activated receptor-1 with P1pal-12 limits bleomycin-induced pulmonary fibrosis. *Thorax* **69**, 152–160 (2014).
17. Babin, A. L. *et al.* Bleomycin-induced lung injury in mice investigated by MRI: Model assessment for target analysis: MRI Analysis of Bleomycin-Induced Lung Injury in Mice. *Magn. Reson. Med.* **67**, 499–509 (2012).

18. Egger, C. *et al.* Administration of Bleomycin via the Oropharyngeal Aspiration Route Leads to Sustained Lung Fibrosis in Mice and Rats as Quantified by UTE-MRI and Histology. *PLoS ONE* **8**, e63432 (2013).
19. Southam, D. S., Dolovich, M., O'Byrne, P. M. & Inman, M. D. Distribution of intranasal instillations in mice: effects of volume, time, body position, and anesthesia. *American Journal of Physiology-Lung Cellular and Molecular Physiology* **282**, L833–L839 (2002).
20. Seo, Y. *et al.* Optimizing anesthesia and delivery approaches for dosing into lungs of mice. *bioRxiv* 2023.02.01.526706 (2023) doi:10.1101/2023.02.01.526706.
21. Liu, L., Stephens, B., Bergman, M., May, A. & Chiang, T. Role of Collagen in Airway Mechanics. *Bioengineering* **8**, 13 (2021).
22. Barratt, S., Creamer, A., Hayton, C. & Chaudhuri, N. Idiopathic Pulmonary Fibrosis (IPF): An Overview. *JCM* **7**, 201 (2018).
23. McCuaig, S. & Martin, J. G. How the airway smooth muscle in cystic fibrosis reacts in proinflammatory conditions: implications for airway hyper-responsiveness and asthma in cystic fibrosis. *The Lancet Respiratory Medicine* **1**, 137–147 (2013).
24. Li, Y. *et al.* The Role of IL-6 in Fibrotic Diseases: Molecular and Cellular Mechanisms. *Int. J. Biol. Sci.* **18**, 5405–5414 (2022).
25. Mukhopadhyay, S., Hoidal, J. R. & Mukherjee, T. K. Role of TNFα in pulmonary pathophysiology. *Respir Res* **7**, 125 (2006).
26. Nho, R. S., Ballinger, M. N., Rojas, M. M., Ghadiali, S. N. & Horowitz, J. C. Biomechanical Force and Cellular Stiffness in Lung Fibrosis. *The American Journal of Pathology* **192**, 750–761 (2022).

CHAPTER 3

Intranasal administration of dexamethasone-loaded nanoparticles improves their lung tropism and reduces the off-targeting in both healthy and fibrotic mice

Annalisa Morelli*, Elisa Schiavon*, Martina Bruna Violatto, Alice Passoni, Alessia Lanno, Giulia Yuri Moscatiello, Anita Salmaso, Simone Bernardotto, Martina Stocco, Andrea Mattarei, Renzo Bagnati, Federica Meloni, Margherita Morpurgo and Paolo Bigini

*These authors contributed equally to this work

Manuscript in preparation for Journal of Controlled Release

Abstract

Pulmonary fibrosis is a chronic, progressive dynamic process characterized by extracellular matrix production and myofibroblast activation. Fibrogenesis can be activated by different stimuli but always leads to alveolar remodelling, gas exchange impairment that cause first respiratory failure and, ultimately, death. The lack of effective therapies has opened to new strategies including the use of targeted delivery systems by nanodrugs. Here, we optimized a nanocarrier based on the Avidin Nucleic Acid NanoASsembly (ANANAS) platform for the intracellular release of the anti-inflammatory steroid dexamethasone (ANANAS-Dex) and we investigated its fate following systemic or intranasally administration in mice. The nanoparticles biodistribution and the pharmacokinetics of free and NP-linked dexamethasone were investigated in both healthy and fibrotic mice. Intranasal administration showed a specific lung targeting particularly in fibrotic conditions. In particular, we found that by using this route of administration the NPs were able to penetrate in lungs rapidly and segregate inside the tissue resident macrophages. NP intranasal administration allowed to reduce drastically drug off-targeting compared to the administration of the free drug. These findings highlight the potentials of using intranasal delivery of nanodrugs as a promising approach for targeted and efficient treatment of lung disorders.

3.1 Introduction

Interstitial lung diseases (ILDs) are a heterogeneous group of pathologies that affect the lung parenchyma with wide inflammation and diffuse fibrosis. Pulmonary fibrosis (PF) is a condition characterized by a chronic and progressive tissue repair response, which leads to irreversible scarring, remodelling of the lung and impaired gas exchange. Excessive deposition of extracellular matrix (ECM) proteins results in fibrotic tissue accumulation, alveolar destruction and irreversible loss of lung function.[1,2] Idiopathic pulmonary fibrosis (IPF) is the most common ILD. Incidence of pulmonary fibrosis has risen over time, and in Europe and North America is estimated to range between 2-8 and 30 cases per 100 000 people per year. It is more common in men and is rare in people younger than 50 years (median age at diagnosis is about 65 years). Although disease course is variable and somewhat unpredictable, the median survival time from diagnosis is 3–5 years.[3,4] The pathogenesis involves multiple cellular compartments, including the epithelium, lung fibroblasts and the innate and adaptive immune system. However, despite extensive research efforts, the exact mechanisms underlying the interplay of these factors in disease development remain unclear. The current standard clinical treatment for lung fibrosis typically involves the administration of corticosteroids and immunosuppressive agents to mitigate inflammation and anti-fibrotic drugs (nintedanib and pirfenidone) to slow the progression of fibrotic tissue deposition.[2,5,6] There is no effective treatment able to halt or reverse disease progression and improve clinical outcome. Moreover, the widespread distribution of steroids, facilitated by their ability to readily cross biological barriers, presents a challenge for patients with PF, often compelling them to discontinue therapy due to the severe complications associated with prolonged steroid use (osteopenia leading to vertebral collapse, diminished bone density, diabetes, hypertension, mood and cognitive disorders, as well as obesity).[7,8] A potential solution to this issue lies in the strategic accumulation of active drug specifically within the lung, thereby reducing the total drug dosage and avoiding undesired systemic side effects.

Currently available therapeutic strategies are focused on achieving tissue-specific treatments through diverse approaches. For example, drug delivery systems, such as

nanoparticles (NPs), are engineered to transport drugs within specific anatomical locations. Notably, NPs possess the capacity to transport substantial drug quantities and can accommodate the simultaneous incorporation of therapeutic, diagnostic and targeting components when needed.[9–11] Most types of NPs show natural tropism for macrophages (both resident or recruited), which play a pivotal role in the initiation and progression of inflammatory diseases and possess a robust capacity to identify, internalize and degrade various types of NPs, making these systems the ideal drug carriers for inflammatory-related diseases.[12,13]

The present study aimed to develop an innovative therapeutic approach for lung disorders using a nanoformulation loaded with dexamethasone based on the Avidin-Nucleic-Acid-Nano-Assemblies (ANANAS) platform. ANANAS are biodegradable and biocompatible and non-immunogenic poly-avidin-based NPs obtained from the high-affinity interaction between the egg-white protein avidin and a non-coding nucleic acid filament.[14,15] Notably, thanks to the strong affinity (Kd ~10^-15 M) between avidin and biotin, these NPs can be readily loaded with biotin linked bioactive or contrast agents with stoichiometric control. In recent years, ANANAS-based formulations have shown potentials in different biomedical applications, among which diagnostics and drug delivery.[16] In this context, thanks to the strong tropism of these carriers for the liver upon parenteral administration, two dexamethasone-carrying ANANAS (ANANAS-Dex, first and second generation) formulations administered intravenously (i.v.) or intraperitoneally (i.p.) have been recently investigated for their potential in treating liver autoimmune diseases, showing efficacy and lack of off-target release of the drug.[17,18]

In this work, we extended the investigation on ANANAS-Dex to explore its potentials for the treatment of inflammatory lung disorders following a non-parenteral route, namely nasal instillation. In ANANAS-Dex formulations, in order to prevent release of the free drug in plasma and permit drug release within the acidic environment of target tissue endosomes/lysosomes, the drug is loaded onto the carrier by means of a biotin conjugate and an acid-reversible hydrazone linker. Along the investigation on first and second generation ANANAS-Dex[17,18], a number of linkers and spacers between biotin and the drug have been tested, showing that the chemistry of the hydrazone (Hz) bond and nature of the spacer between biotin the hydrazone impact on the NP behavior *in vitro*

and *in vivo*.[18] The data generated with first and second generation ANANAS-Dex allowed identifying composition/functionality relationships which were here used as guidelines for the design of third generation ANANAS(Hz)-Dex, which was aimed at maximizing loading capability, colloidal stability and tropism for tissue resident macrophages.

Following in vitro pre-formulation studies, the novel third generation ANANAS-Dex was evaluated on PF in the bleomycin (BLM) mouse model that reflects several key aspects of human PF, including histological hallmarks such as intra-alveolar buds, incorporation of collagen and obliteration of the alveolar space, as well as lung infiltration and fibrosis.[19] Before initiating the present study, we conducted an investigation using the systemic route in healthy animals to compare their behaviour with the first and second generations previously examined via the parenteral route. Subsequently, we moved to the inhalation route in the pathological model.[18] In this study, optical imaging and confocal microscopy were performed to localize fluorescently labelled ANANAS in the whole body and in lung sections. Additionally, high-performance liquid chromatography mass spectrometry (HPLC MS/MS) was employed to quantify free drug levels in plasma and various organs. Lastly, we assessed the clinical manifestations of PF in mice through molecular biology and histological assays. Overall, this study explores the therapeutic potential of ANANAS-Dex in the context of lung disorders, providing a promising approach for targeted treatment with controlled drug delivery and potential clinical translation.

3.2 Materials and Methods

Hexafluorophosphate Azabenzotriazole Tetramethyl Uronium (HATU), N,N-Diisopropylethylamine (DIPEA), triethylamine (TEA), Piperidine, and HCl 4M in dioxane sand all solvents were purchased from Merck Sigma-Aldrich. Biotin-NHS was purchased from Byosynth; dexamethasone was purchased from Metapharmaceutical. Biotin-Poly-(Ethylene Glycol) (PEG)5kDa-SVA and biotin-PEG5kDa-methoxy (biotin-mPEG) were purchased from Laysan Bio (Huntsville, AL, USA). Avidin was from

E.protein (Belgium). NMR experiments were performed on a Bruker Avance III 400 spectrometer (frequencies: 400.13 and 100.62 MHz for ^{1}H, and ^{13}C nuclei, respectively) equipped with a multinuclear inverse z-field gradient probe head (5 mm). For data processing, TopSpin 4.0.8 software was used and the spectra were calibrated using solvent signal (DMSO ^{1}H 2.50 ppm ^{13}C 39.52, MeOD ^{1}H 4.78ppm ^{13}C 49.15 ppm). Multiplicities are reported as follows: s, singlet; d, doublet; t, triplet; q, quartet; m, multiplet; b, broad; dd, doublet of doublets. Mass spectra were recorded by direct infusion ESI on a Thermo Fisher Scientific LCQ Fleet ion trap mass spectrometer. Dynamic light scattering measurements were performed with a Malvern Zetsizer Nano-ZS, UV-Vis spectra were recorded with an Agilent Cary 60 UV-Vis spectrophotometer. Gel permeation chromatography was carried out on a Cytiva Akta purifier Fast Protein liquid Chromatography (FPLC) system.

- **Synthesis**

The newly synthesized biotin hydrazone drug conjugates (compounds 6,7, Figure 3.1) were obtained through classic synthetic chemistry techniques (data not shown). All newly synthesized compounds were analyzed by High Resolution Mass Spectrometry (HR-MS), NMR, Reverse Phase Chromatography (RP-HPLC) and UV-Vis spectroscopy. The identity of Compound **7** was verified by a combination of assays, namely UV-Vis spectroscopy analysis to confirm the presence of the Dex C3-Hz bond which displays a typical chromophore at 300 nm, by quantification of biotin[20], PEG[21] and total dexamethasone. The latter was quantified by reverse phase chromatography (RP-HPLC, Phenomenex Kinetex C18 column, eluent A, H2O + TFA 0.1%; eluent B, 5% A in ACN; gradient from 10% to 95% B in 10 min) following acid-triggered (HCl 0.1M) release from the conjugate. Biotin-C6-Alexa633 was obtained as previously described.[16]

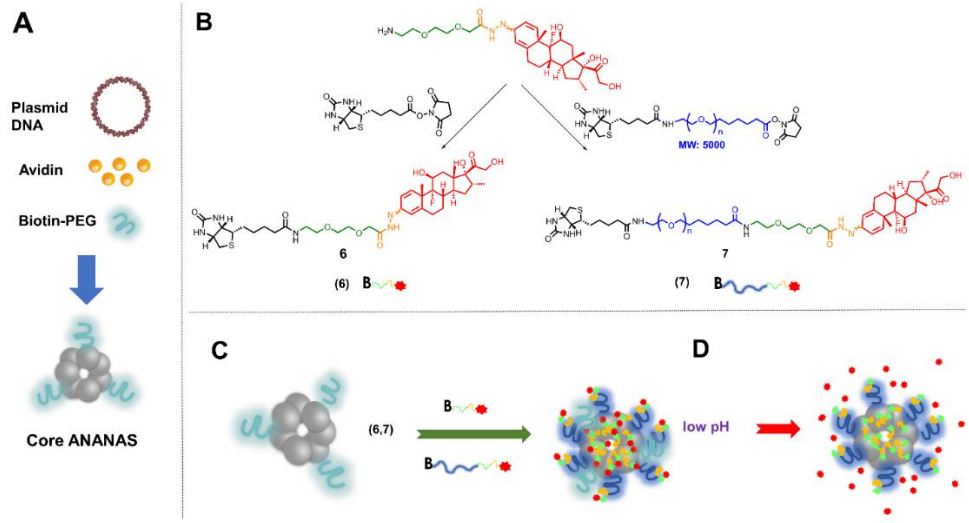

Figure 3.1 Schematic representation of the formulations tested and the assembly process. A) assembly of core nanoparticles; **B**) the biotin-dexamethasone synthesized for this work; **C)** functional assembly and generation of ANANAS-Dex; **D**) acid triggered release of the free drug.

- **Nanoparticle assembly**

Core ANANAS containing the minimum amount of 5kDa methoxy-PEG (12.5% of available biotin binding sites - BBS) to guarantee buffer solubility were prepared[15] and freeze-dried after purification. Core NPs were reconstituted in 10 mM phosphate, 150 mM NaCl, pH 7.4 (PBS) buffer and added of the biotinylated elements (compounds 6,7**,** or biotin-mPEG) to the desired biotin/BBS molar ratios. When needed, biotin-C6-alexa633 was also added at predefined biotin/BBS molar ratios (ANANAS-Dex-Alexa).[16]

- **Dexamethasone release *in vitro***

The release of dexamethasone from the novel PEO2-Hz- linker was measured using compound 6 (B-PEO2-Hz-Dex, low MW conjugate). Release of dexamethasone from this compound, as a free molecule and when linked to the NPs, was examined at three pH values (100 mM phosphate pH 7.4, 100 mM Na acetate, pH 5.0, and 100 mM Na acetate, pH 4.0). When tested as a free molecule, the release rate was assessed by UV-Vis spectrophotometry. Samples were incubated (at $3*10^{-5}$ M) in the selected buffer at the temperature of choice (50°C, 60°C and 70°C) and the disappearance of the Hz-related

chromophore was quantified from the intensity of its specific absorption band at 300 nm. The release rate at 37°C was then extrapolated from the Arrhenius plot generated with the kinetic constants (% Dex release/hour) obtained at the three temperatures. When tethered to the NPs, the release was monitored, at 37°C only, by measuring via RP-HPLC the concentration of the free drug liberated. Before HPLC analysis, the protein fraction was removed from the solution by cold acetone precipitation.

- **Animals**

The Mario Negri Institute for Pharmacological Research IRCCS adheres to the principles set forth in the following laws, regulations, and directives concerning the care and use of laboratory animals: Italian law (D.lgs 26/2014; Authorization No. 19/2008-A issued on March 6, 2008 by the Ministry of Health); the Mario Negri Institutional Regulations and Policies-which provide internal authorization for persons conducting animal experiments (Quality Management System Certificate, UNI EN ISO 9001:2015, Reg. No. 6121); the NIH Guide for the Care and Use of Laboratory Animals (2011 edition); and the EU Directives and Guidelines (EEC Council Directive 2010/63/UE). This work was reviewed by the IRCCS-IRFMN Animal Care and Use Committee (IACUC) and subsequently approved by the Italian "Istituto Superiore di Sanità" (Code: 558/2021-PR). Ten-week-old C57BL/6 male mice (Charles River) were used throughout the study. Mice were maintained under specific pathogen-free conditions in the Institute's Animal Care Facilities; they received food and water ad libitum and were regularly checked by a certified veterinarian who is responsible for animal welfare supervision and experimental protocol review.

- **Animal model generation**

Mice were anesthetized with medetomidine (Domitor®) at a dose of 0.4 mg/kg b.w. and ketamine (Lobotor®) at a dose of 36 mg/kg injected i.p. and Bleomycin sulfate (TCI, Tokyo), 5 mg/kg in saline (0.9%) or vehicle (saline 0.9%) was administered intranasally with a micropipette (25 µl per nostril with a total volume of 50 µl). Animals were allowed to recover immediately afterwards (Antisedan® - 0.8 mg/kg i.p.).

- ***Ex vivo* fluorescence imaging**

A total of 35 C57BL/6J male animals were used for the IV biodistribution study in healthy animals. Sixteen mice per group were injected intravenously with 0.167 mg/kg of Dex or linked to ANANAS (11.4 mg/kg - ANANAS-Dex) dissolved in 200 µl of saline. The remaining three were treated with PBS and were used as controls. A total of 43 C57BL/6J male animals were used for the i.n. biodistribution study in healthy animals. 20 mice per group were injected intranasally, with 0.167 mg/kg of Dex or linked to ANANAS (11.4 mg/kg - ANANAS-Dex) dissolved in 50 µl of saline with a micropipette (25 µl per nostril) after medetomidine (Domitor®) at a dose of 0.4 mg/kg b.w. and ketamine (Lobotor®) at a dose of 36 mg/kg intraperitoneal injection. Animals were allowed to recover immediately afterwards (Antisedan® - 0.8 mg/kg i.p.). The remaining three were treated with PBS and were used as controls. A total of 43 C57BL/6J male animals were used for the i.n. biodistribution study in fibrotic animals. 20 mice per group were injected intranasally 7 days post bleomycin induction, as reported above, with 0.167 mg/kg of Dex or linked to ANANAS (11.4 mg/kg - ANANAS-Dex) following the same procedure used for healthy animals. *Ex vivo* optical imaging was done 15 min, 30 min, 2 h, 24 h and 48 h after treatment. The remaining three were treated with PBS and were used as controls. Fluorescence images were acquired with an IVIS Lumina III imaging system (PerkinElmer). The following acquisition parameters were used: excitation filter range 680 to 740 nm, emission filter (790 nm, exposure time 2 s), binning factor 4, and f/Stop 2. At the end of the study mice were euthanized by decapitation. Liver, kidneys, spleen, lung and brain were removed and scanned for ex vivo imaging. Organs were collected without perfusing the animal so the signal also refers to their blood vessels. Spectral unmixing, image processing, and analysis were done using Living Image 4.3.1 software (PerkinElmer).

- **Tissue collection an Histological analysis**

At the moment of sacrifice, tissues from untreated and bleomycin (BLM) treated-mice were collected and directly frozen in dry ice. Cryostat sections were cut at 20 µm and mounted on glass slides. Slides were post-fixed in 10% formalin (BioOptica, Italy) for

20 minutes, washed three times in phosphate-buffered saline (PBS) for 5 min and incubated for 1 h with a blocking solution (PBS-NGS 10%-Triton X-100 0.1%) then washed again with PBS. For subcellular localization, the antibody anti-CD68 (specific for lysosome and endosome membranes of macrophages) was used: primary rat anti-CD68 monoclonal antibody (1: 200, Serotec, Kidlington, UK) + Triton X -100 0.1% + NGS 3% in 1X PBS overnight at 4 ° C. After washing with 1X PBS, the slides were incubated with the Alexa488 conjugated secondary antibody (1: 500, Invitrogen) for 1 hour at room temperature in 1% 1X-NGS PBS solution. After this step, the slides were incubated with the Hoechst nuclear marker 33258 (2 µg / mL in 1X PBS, Sigma Aldrich) for 10 minutes. Fluoromount Aqueous Mounting Medium (Sigma Aldrich) was used for mounting with cover glass. The slides were then observed at the Virtual Slide Microscopy (Olympus, Japan), a microscope that allows to obtain rapid scans of the organs in their entire volume, with high anatomical resolution. For confocal microscopy analysis, samples were acquired using Nikon A1 Confocal microscopes and pseudocolored (blue for Hoechst 33258, green for alexa488 and red for alexa633). For the histopathological evaluation, lungs were removed from BLM-treated animals at 7 days post administration and fixed overnight in 10% formalin (BioOptica, Italy). Tissues were processed for paraffin embedding, cut with Leica RM55 microtome (Leica Microsystem, Italy) into 4 µm-thick sections and dried into the oven at 37°C overnight. Slices were deparaffinised in xylene and rehydrated through a series of alcohols to water. Hematoxylin-Eosin (BioOptica, Italy) staining method was used to investigate alveolitis and fibrosis. Picrosirius Red (0.5 g Sirius Red F3B (C.I. 35782) + 500 ml picric acid solution – Sigma Aldrich) staining method was performed to reveal collagen deposition. To achieve integrated detection of protein expression, sections were immunoassayed using Vectastain Elite ABC (Vector Laboratories, Burlingame, CA, USA). Antigen retrieval was performed in citrate buffer (pH 6) in a boiling pot for 15 minutes, followed by endogenous peroxidase inhibition with H_2O_2 3% for 10 min at RT and incubation with blocking solution (PBS-NGS 10%-Tween 20 0.05%) for 30 min at RT. For subcellular localization, Iba1 (clone 019-19741, Wako; 1:500) was used to label macrophage calcium binding protein. Sections were stained with 3,3 - Diaminobenzidine (DAB, Sigma Aldrich) and counterstained with Mayer's hematoxylin (Bioptica, Italy).

Samples were dehydrate through an alcohol scale. Glasses were mounted with xylene-based mounting medium (DPX, Sigma). The slides were then observed at the Virtual Slide Microscopy (Olympus, Japan).

- **Pharmacokinetics**

To quantify the levels of Dex, lung, plasma and liver from the group of healthy and fibrotic C57BL/6J mice treated with free Dex (0.167 mg/kg) or ANANAS-linked were used. For this analysis, animals in both groups (ANANAS-Dex and Dex) were treated and sacrificed at different timepoints (15', 30', 2, 24 and 48 h) following the same procedure. As a first step of the analytical methods, the internal standard, fludrocortisone (10 ng) was added to the sample from treated mice, and Dex (0−100 ng) and fludrocortisone (20 ng) were included for the calibration curve. Lung and liver slices were digested with methanol (1:2 w/v) and acetonitrile (1:1 w/v), stirred and sonicated for 20 min. Then water (1:10 w/v) was added and stirring and sonication were repeated. The resulting samples were centrifuged at 7000g for 15 min at 4 °C. The supernatant was further cleaned up with solid-phase extraction using Sep-Pak C18 1 cc Vac Cartridges, conditioned before use with 1 mL of methanol, followed by 1 mL of water. Samples were loaded on the SPE columns and passed through dropwise. Then cartridges were rinsed with 1 mL of water/acetone (80:20) and then with 1 mL of water before drying the columns under vacuum for 5 min. Samples were eluted with 1.8 mL of acetonitrile into glass receiving tubes. Plasma aliquots were directly eluted with acetonitrile (1:4v/v) and centrifuged at 7000g for 15 min at 4 °C. All the samples were evaporated to remove the organic phase. Just before analysis, they were suspended in 100 µL of 0.05% acetic acid/ acetonitrile (80:20) in autosampler vials. Liquid Chromatography (HPLC) and Tandem Mass Spectrometry (MS/MS). All experiments were carried out on an Agilent 1200 series HPLC system interfaced to an Agilent 6410 triple-quadrupole mass spectrometer equipped with an electrospray ionization source (Agilent Corporation, MA, USA). All data were acquired and analyzed using Agilent MassHunter data processing software. Separation was performed with a Superspher 100 RP-18 (2.1 × 100 mm, Merck, Darmstadt, Germany) column, maintained at 30 °C. The elution solvents were 0.05% acetic acid in water (mobile phase A, MP-A) and

acetonitrile (mobile phase B, MP-B). The injection volume was 10 µL and the flow rate was 200 µL/min. The autosampler temperature was 6 °C. Elution started with 80% of MP-A and 20% MP-B for 2 min, followed by a 12 min linear gradient to 60% of MP-B, and a 2 min linear gradient to 99% of MP-B, held for 4 min and a 1 min linear gradient to 80% of MP-A, which was maintained for 6 min to equilibrate the column. Dex and fludrocortisone, were analyzed using electrospray in negative ionization mode, with the spray voltage set at 2000 V. Nitrogen was used as nebulizer gas at a pressure of 35 psi. Desolvation gas (nitrogen) was heated to 250 °C and delivered at a flow rate of 7.5 L/min. Analysis data were acquired in the multiple reaction monitoring (MRM) mode.

- **Quantitative real-time polymerase chain reaction**

For the gene expression experiment, a total of 24 C57BL/6J male animals were used. 6 mice per group were injected intranasally 7 days post BLM induction, as reported above, with 0.167 mg/kg of Dex or linked to ANANAS (11,4 mg/kg - ANANAS-Dex). Animals were sacrificed 24 h after treatment and lung for molecular biology analysis were collected. Total RNA was isolated with TRIzol Reagent (Thermo Fischer Scientific) according to the manufacturer's instructions, and 1 µg total RNA was reverse transcribed into cDNA using high-capacity cDNA reverse transcription kit (Applied Biosystems). cDNAs were mixed with Quantifast SYBR Green Master Mix (BiotechRabbit) according to the manufacturer's instructions and both forward and reverse primers (0.5 µM) for detecting mRNA levels of mouse genes. qPCR was carried out using a QuantStudio 5 Systems (Applied Biosystems) and the amplification steps were 50 °C for 2 min, 95 °C for 10 min and followed by 40 cycles of 95 °C for 15 s and 60 °C for 1 min. Relative mRNA levels of the target genes were normalized to β-ACT mRNA expression and analyzed by the $2^{-\Delta\Delta Ct}$ method. Quantitative Rt-PCR primers:

	5'- 3' Forward	5'- 3' Reverse
β-ACT	GCCCTGAGGCTCTTTTCCAG	TGCCACAGGATTCCATACCC
TNF-α	AGACCCTCACACTCAGATCATCTTC	TTGCTACGACGTGGGCTACA
IL-6	TCTCTGGGAAATCGTGGAAA	TCTGCAAGTGCATCATCGTT
COL1a1	ACCTGTGTGTTCCCTACTCA	GACTGTTGCCTTCGCCTCTG
FIBRONECTIN	CACGGAGGCCACCATTACT	CTTCAGGGCAATGACGTAGAT

Table 3.1 Rt-PCR primers sequence.

- **Data calculation & statistical analysis**

All statistical analyses were done using GraphPad Prism version 7.00 for Windows (Graph-Pad Software, CA, USA). All data are expressed as mean ± standard error of the mean. The differences between groups were compared using one-way ANOVA analysis, followed by Dunnet's post hoc test analysis. P values <0.05 were considered statistically significant and reported on graphs. For *in vivo* experiments, the number of animals sacrificed at each data point was minimized according to the 3Rs principle.

3.3 Results and Discussion

Design of the biotin dexamethasone conjugates for ANANAS decoration

Drug loading of ANANAS relies on the use of reversible biotinylated drug conjugates, which, upon binding to the avidin biotin binding sites (BBS), position the drug at the nanoparticle surface, at a distance from the protein core that will depend on the length of the spacer between the biotin and the drug moiety (Figure 3.1). If the drug is tethered using a short-spaced biotin linker, it will position in proximity to the particle protein surface (inner surface layer), whereas if a long-spaced linker (e.g. a 5kDa PEG) is used, it will locate at the outer surface layer. Results generated with first and second generation ANANAS-Hz-Dex formulations administered parenterally[17,18] showed that that a) only hydrazide-hydrazone (Hz-Hz) but not carbamate hydrazide-hydrazone (Cb-Hz) bonds allow acid-selective release of the drug; b) the chemical environment surrounding the dexamethasone-hydrazone link, which depends also on its distance from the NP protein core, affects the conjugate hydrolytic stability and shorter spacers display longer lasting drug release profiles; c) the presence of a 6-carbon atom spacer at the ω end of the 5kDa PEG reduces the conjugate solubility and has a negative impact on the polymer ability to colloid protection; d) the ratio between the number of methoxy- or dexamethasone ω-ending 5kDa biotin-PEGs at the NP surface affects the NP biodistribution pattern and the interaction with macrophages: a higher percentage of methoxy-ending PEGs make the NPs more stealth, while higher amounts of ω-dexamethasone-ending PEGs favor the interaction with tissue resident macrophages, positive for CD68 staining.

Keeping the above information in mind, a novel set of short- and long-spaced biotin-hydrazo-hydrazone (Hz-Hz)-Dex conjugates was designed and synthesized to generate third generation ANANAS-Dex (Figure 3.1) with optimized features. In the new conjugates the drug was linked selectively at the carbonyl C3 via a Hz-Hz linker to an amino-terminating PEO2 spacer (which is more water soluble than the 6-carbon atom as previously described[18]). The PEO2 conjugate was linked via an amide bond either directly to biotin (compound 6) or to a ω-carboxy, α-biotin-5kDa PEG (leading to compound 7). Selective linkage of the drug at the carbonyl C3 was confirmed by NMR ^{1}H-*d6*DMSO spectroscopy.[17] The identity and purity (94%) of the products was confirmed by ^{1}H-NMR and Mass Spectrometry (data not shown). The UV-Vis spectra show the formation of an absorption band with maximum at 300 nm (Figure 3.2), typical of the dex-Hz conjugates at the drug *C3 carbonyl*,[18] with a molar extinction value of about 20.000 M^{-1} cm^{-1} at neutral pH. When purified by flash chromatography (Silica gel F60), compound 6 elutes as two distinct products, which were initially isolated and identified as the hydrazone cis/trans isomers. Following characterization, it was demonstrated that the two isomers have superimposable behavior in aqueous media, therefore they were used in mixture in all experiments.

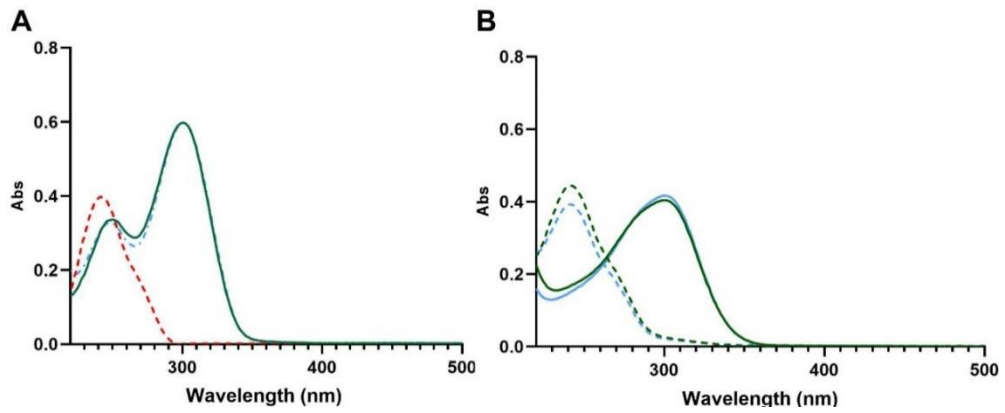

Figure 3.2 UV-Vis Characterization of the biotin-dexamethasone conjugates. **A)** UV-Vis spectra of compounds 6 (green full line), 7 (blue, dot-dashed line) and Dex (red, dashed line) at neutral pH (pH 7.4). **B)** UV-Vis spectra of compounds 6 (green) and 7 (blue) in acidic pH (HCl 0.1 M) immediately after solution preparation (full lines) and after 3h incubation at 50°C (dashed lines). Spectra were recorded from solutions at about $3x10^{-5}$ M concentration. The absorption band at 300 nm in both acidic and neutral solutions indicates the presence of the hydrazone bond; upon incubation in the acidic solution, the hydrazone-related band disappears yielding the typical spectrum of free Dex.

pH dependent release of dexamethasone

The pH-dependent hydrolytic stability of the PEO_2-Hz-Dex linker was verified by testing compound 6 at pH 7.4, 5.0 and 4.0 (Table 3.2). We observed high stability at neutral or slightly acidic pH (pH 5.0) and slow but sustained drug release at pH 4.0 (6% hydrolysis/hour), with no difference between the Cis and Trans isomers. Tethering the short-spaced biotin conjugate to the ANANAS core improved the hydrolytic stability (about 10 times higher with respect to the free molecule). The results are almost superimposable to those obtained with a biotin-Hz-Hz-dexamethasone conjugate having a 5-carbon atom aliphatic spacer instead of the PEO2.[18] It was also previously demonstrated that the presence of the 5kDaPEG between biotin and the C5-Hz-Hz-Dex bond does not affect the hydrolysis pattern and that the buffering effect exerted by attachment to core NPs occurs in short-spaced but not in PEG-spaced conjugates. Therefore, compound **7** was not tested here and it is expected to behave similar to compound 6 as a free compound, both when free in solution and when tethered to the NPs.

Compound 6 hydrolysis% /h

PH	free in solution (*)	NP-bound
7.4	n.d. (**)	0.12
5	1	0.26
4	6	0.59

Table 3.2 Hydrolysis of compound 6 at pH 4.0, 5.0 and 7.4 at 37°C, both as free molecule and tethered to the NPs. (*) Data for the free molecule are a prevision from an Arrhenius plot generated from experiments carried out at 50°C, 60°C and 70°C; data for the NP-linked compound were obtained directly at 37°C (Fig S.4.b); (**) For the duration of the experimentation (27h @ 50 and 70°C, 48h @ 60°C), the bond was stable at pH 7.4 at all temperatures tested.

Pre-formulation studies

The ideal formulation should guarantee a) high dexamethasone loading b) slow release of the active element, and c) colloidal stability. Considering these three requirements, we carried out a series of pre-formulation experiments to identify the most suitable composition for later in vivo testing. For maximal drug loading, all of the available BBS in the NPs should be tethered to a dexamethasone biotin conjugate. In core NPs, 12.5%

of the total BBS are occupied by biotin-PEG5kDa-methoxy to guarantee colloidal stability during preparation and freeze drying, and, in principle, the remaining 87.5% are potentially available for tethering other biotinylated elements. However, considering that steric factors may hamper the access of large MW biotin conjugates (as the PEG derivatives),[22] and the potential negative effects on colloidal stability exerted by hydrophobic moieties at the NP surface,[18] it is fundamental to experimentally assess both the loading capability for the different biotin conjugates and the colloidal stability of the functionalized NPs.

In order to optimize the NP Dex loading, we initially quantified the maximal capability of core NPs for each of the two biotin-Dex conjugates. To this end, core NPs were mixed with different amounts of either compounds 6 or **7** and the number of unbound conjugates was quantified by gel permeation chromatography (Figure 3.3). Concurrently, the colloidal stability of the mixtures was assessed by performing dynamic light scattering measurements one hour after mixing and 24 h and 48 h later (Figure 3.3D). The maximum capability for the high MW and low MW conjugate was reached at about 27% or 60% of the total BBS, respectively, confirming that steric hindrance plays a significant role in dictating NP loading when using bulky biotin conjugates. Addition of the large PEG conjugate did not affect colloidal stability, while the presence of the low MW conjugate alone made the system colloidally unstable.

A second set of experiments was carried out by mixing core NPs with both compounds 6 and 7 at 57.5% and 30% of total BBS, respectively. In these conditions, a fraction of both conjugates remained free in solution (data not shown). Notably, no aggregation was observed in the mixture indicating that the large PEG conjugate is capable of confer colloidal stabilization also in the presence of the partially destabilizing compound 6.

Finally, a formulation loaded at 25% BBS with compound **7** and 40% BBS with compound 6 was tested, showing both full retention of the two biotin conjugates (Figure 3.3C). This formulation was selected for the *in vivo* experiments. In this formulation, each NP carries about 870 molecules of dexamethasone which corresponds to 15.8 µg of dex/mg of carrier. A second formulation was also optimized for the biodistribution studies in which fluorescent biotin-C6-alexa633, necessary for tracking, was added at

5% BBS coverage to the detriment of compound 6, which was added at 35% BBS coverage. In this case each NP carries about 800 Dex moieties, corresponding to 14.6 µg dex/mg of carrier. Based on the composition and the hydrolytic stability of the two components, we calculated the drug release rate at pH 4.0 from these formulations to be approximately about 2.7% and 2.5% / h, respectively.

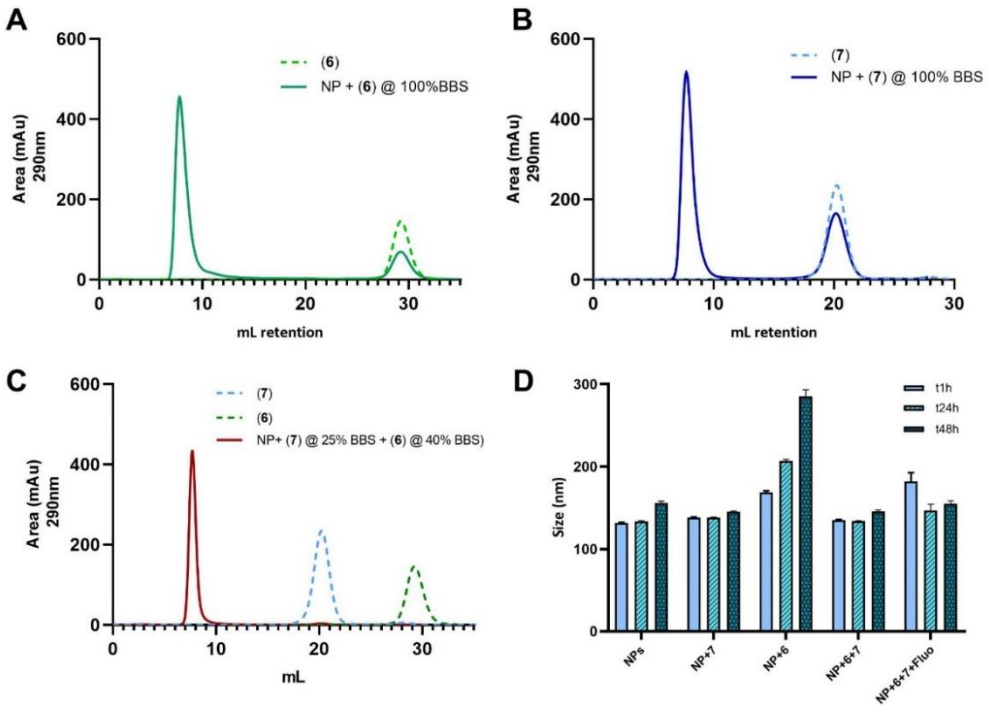

Figure 3.3 Nanoparticle pre-formulation studies. Gel permeation chromatograms of **A)** compound 6 and **B)** compound 7 as free molecules (dashed, blue or green) and when mixed with ANANAS at theoretical biotin:BBS ratio of 1:1 (solid, blue or green). The nanoparticles elute at about 8 mL; the peak eluting at 28 mL in panel A corresponds to the free compound 6; the peak eluting at 20mL in panel B corresponds to the long derivative; **C)** Gel permeation chromatogram of the final formulation mixture (full line, red) (25% BBS covered with compound 7 and 40% BBS covered with compound 6) and the free compounds 6 (dashed, green) and 7 (dashed, blue) analyzed at the same concentration as in the mixture; **D)** Summary of the colloidal stability studies: size of the assemblies (50µg/mL in PBS) measured 1h, 24h and 48h after mixing core NPs as such (NPs) or added of either compound 6 alone (B:BBS = 0.575:1) (NP+6) or compound 7 alone (B:BBS = 0.3:1) (NP+7) or a mixture of compounds 6 (B:BBS= 0.575:1) and 7 (B:BBS = 0.3:1) (NP+6+7), or a mixture of compounds 6 (B:BBS= 0.35:1) and 7 (B:BBS = 0.25:1) and B-C6-Alexa633 (B:BBS = 0.05:1) (NP-6+7+Fluo).

Routes of administration study in healthy animals

It is widely known how the treatment schedule can profoundly influence their biodistribution, pharmacokinetics and consequently the interaction between drugs and

hosts. In that context, the route of administration is a pivotal factor in determining the drug's therapeutic outcome and toxicity profile. Another important factor is represented by the presence of a carrier that can increase the stability of the drug, its permanence in the host and also improve the organ tropism. In a first step, we investigated and compared the fate of diverse routes of ANANAS-Dex administration in healthy animals in order to obtain a strong tropism towards lung. By evaluating variations in fluorescence signal localization and intensity in the *ex vivo* study, we aim to elucidate the effects of each administration route and provide critical insights into optimizing the use of intranasal administration as optimized protocol to obtain a reliable accumulation in pulmonary tissue.

For fluorescence visualization, a spaced biotin Alexa633 conjugate was added. Animals were monitored and sacrificed at different timepoints (30', 4h, 24h and 48h) for the *ex vivo* optical imaging analysis. Figure 3.4A shows the NPs' biodistribution in lungs after a single i.v. administration in ten-week-old C57BL6/J male mice of given freely Dex or linked to ANANAS at the dose of 0.167 mg/Kg. Histograms of the ANANAS-related signal measured by IVIS show a significant accumulation in the lungs at 30 minutes post treatment and a rapid decrease in the latter timepoints (Fig 3.4B). Figure 3.4C shows the quantification in off-target organs, indicating a transient signal in brain, spleen and kidney comparable to the lungs-related signal. Notably, it is observed a strong accumulation in liver, in particular at 30 minutes and at 4h after administration. NP-based carriers appear to be highly suitable for liver targeting. Indeed, most NPs display natural tropism for this filter organ in particular after systemic administration.

To assess the ability of the ANANAS−Dex to selectively release the steroid in the lung, we performed a pharmacokinetics study to monitor the levels of free drug in plasma and in the main target organs of healthy mice. It was previously demonstrated that the hydrazone linker is stable at neutral pH, but the passage and interaction with biological barriers in the body is more complex than an *in vitro* condition when exposed to the saline buffer.[17] Therefore, the quantification of the level of Dex is needed in order to evaluate the drug release in the target organ. Figure 3.4D shows the results of the pharmacokinetics study carried out in mice treated i.v. with either ANANAS−Dex or the free drug (0.167 mg/Kg). The free drug penetrates the bloodstream rapidly reaching all

major tissues, including liver and lungs, and being fully cleared 24 h after administration. However, when mice are treated with ANANAS−Dex, the free drug was found exclusively in the liver. Drug levels increased at 4 hours after administration and then slowly decreased, suggesting that the drug release occurs faster than NP degradation. One of the main issues when NPs are administered into biological systems is their uptake by reticuloendothelial system organs such as liver and spleen. Those organs express a high number of mononuclear phagocytic cells, which sequester NPs immediately after injection acting as scavengers to eliminate external materials from the bloodstream. The removal of NPs from the circulation, cause their accumulation in liver.[23,24] Taken together these results and considerations, the systemic route of administration is not optimal for lung targeting.

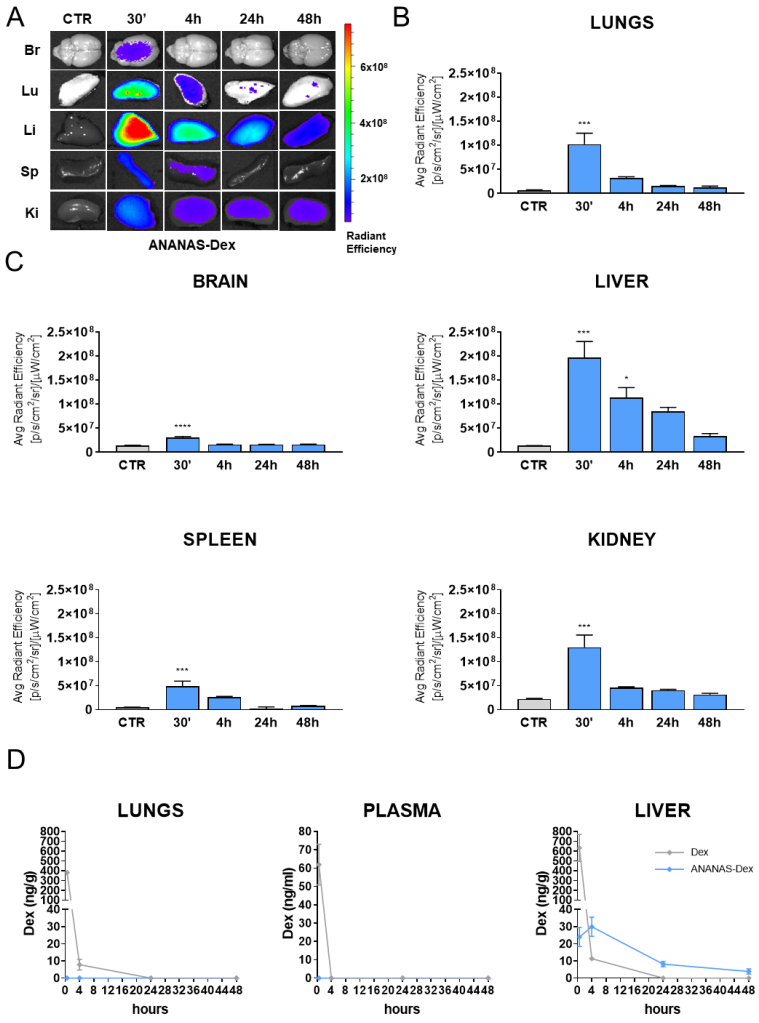

Figure 3.4 *Ex vivo* biodistribution after intravenous administration and pharmacokinetics: **A)** *Ex vivo* optical imaging of excised organs from healthy animals sacrificed 30', 4h, 24 h and 48 h after vehicle or ANANAS-Dex i.v. administration. Br. = brain, Lu. = lungs, Li. = liver, Sp. = spleen, Ki. = kidneys. **B-C)** Histograms related to the quantification of *ex vivo* optical imaging signal. Data are reported as mean ± SE. The data were analyzed by One-way ANOVA using Dunnet's test. *$p < 0.1$, ***$p \leq 0.001$, ****$p \leq 0.0001$. **D)** Levels of free Dex measured in lungs, plasma and liver from healthy mice. Mice were sacrificed at different time points after i.v. administration of Dex (grey line) or ANANAS−Dex (blue line) (0.4 mg/kg). Data are reported as mean ± SE. LoQ = Limit of quantitation of the HPLC MS/MS method: liver, 0.45 ng/g; brain, 0.8 ng/g; plasma, 1.2 ng/mL.

ANANAS-Dex biodistribution after intranasal administration

One of the main goals of NPs dependent drug delivery is to increase the tropism toward the target organ. Despite the lung is a filter organ[23], the systemic administration, as reported above, did not show a strong accumulation and persistent signal in the pulmonary tissue for the broader range of NPs with a mean diameter from 15 to 250 nm. In order to improve the tropism to the lung, we hypothesized a more specific and direct route of administration, exploiting the intranasal instillation (i.n.). The biodistribution of both Dex and ANANAS−Dex after i.n. administration was first investigated in healthy, immunocompetent, and specific pathogen-free mice to assess their behaviour in physiological conditions. Healthy mice after a single i.n. administration of Dex given freely or linked to ANANAS at the dose of 0.167 mg/Kg were sacrificed at different timepoints (15', 30', 2h, 24h and 48h respectively) for the *ex vivo* optical imaging analysis. Figure 3.5A shows the NPs' biodistribution in lungs after a single i.n. administration. Histograms of the ANANAS-related signal measured by IVIS show the ability of the NPs to penetrate the lungs rapidly reaching the maximum concentration at 30' after treatment where it persists for longer than 48h (Fig 3.5B). Figure 3.5C shows the quantification in off-target organs, indicating a transient signal in brain but much lower when compared to lungs-related signal.

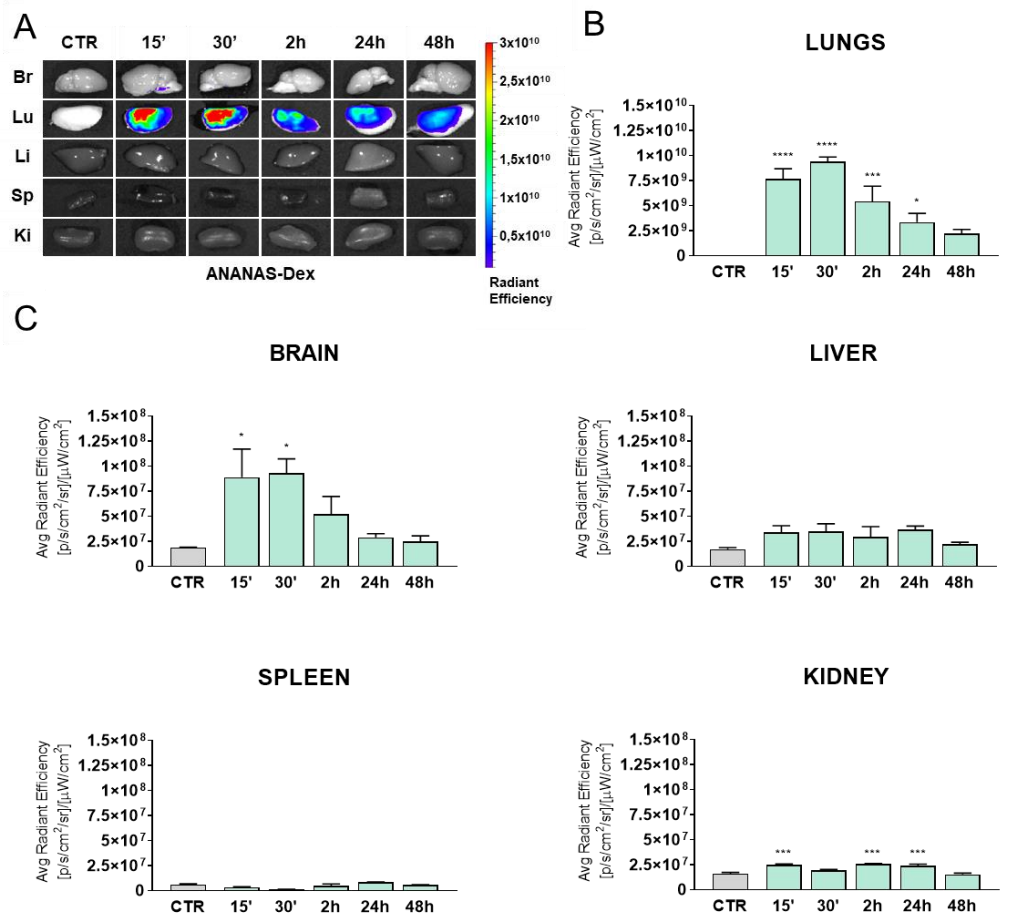

Figure 3.5 ***In vivo*** **biodistribution after intranasal administration**: **A)** *Ex vivo* optical imaging of excised organs from healthy animals sacrificed 15', 30', 2h, 24 h and 48 h after vehicle or ANANAS-Dex administration. Br. = brain, Lu. = lungs, Li. = liver, Sp. = spleen, Ki. = kidneys. **B-C)** Histograms represent the quantification of *ex vivo* optical imaging signal. Data are reported as mean ± SE. The data were analyzed by One-way ANOVA using Dunnet's test. *$p < 0.1$, ***$p \leq 0.001$, ****$p \leq 0.0001$.

These results suggest that direct nasal instillation, in this experimental condition, allow a strong accumulation in the pulmonary tissue avoiding spread in off-target organs and thus drug accumulation. Pulmonary drug delivery is an effective and efficient method for local effects; high vascularization, large epithelial surface area, high solute exchange capacity, and thin alveolar absorptive membranes are the factors that make the pulmonary system an ideal delivery target.[25,26] Inhalation, intranasal and intratracheal treatments are therefore valid routes of administration for lung targeting. Furthermore,

previous findings have indicated that the intranasal administration of progressively increasing fluid volumes in anesthetized mice led to a more significant relative accumulation within the lungs, as opposed to the brain. This suggests that an optimal delivery volume falls within the range of 35-50 µl.[27,28] Once optimized the nanoformulation instillation protocol and obtained a strong persistent signal in the target organ, we performed the same experimental plan in a murine model of pulmonary fibrosis. Since the inflammation process and fibrosis can dramatically affect the organ architecture, it is important to evaluate the nanoparticles' biodistribution also in the presence of a pathological condition. The biodistribution of both Dex and ANANAS−Dex after i.n. administration was investigated in fibrotic mice.

Fibrosis was induced in ten-week-old C57BL6/J male mice with a single i.n. administration of BLM at the dose of 5 mg/Kg. Seven days post induction, during the inflammatory phase, mice were treated with a single i.n. administration of Dex given freely or linked to ANANAS at the dose of 0.167 mg/Kg were treated. Animals were monitored and sacrificed at different timepoints (15', 30', 2h, 24h and 48h) for the *ex vivo* optical imaging analysis. The animal model of PF was obtained after i.n. administration of BLM, glycopeptide antibiotic and antineoplastic agent that exerts its effects through the generation of ROS, induction of single and double-strand DNA breaks and the inhibition of DNA metabolism, thereby disrupting the progression of the cell cycle and inducing alveolar damage. BLM treated mice show several features of human PF, including fibrotic lesions, alveolar remodeling and dysregulated lung function as well as lung infiltration and fibrosis.[19,29–31]

Figure 3.6A shows the NPs' biodistribution in lungs after a single i.n. administration. Histograms of the ANANAS-related signal measured by IVIS show the ability of the NPs to penetrate the lungs rapidly reaching the maximum concentration at 15' after treatment where it persists for longer than 48 h (Fig 3.6B). Figure 3.6C shows the quantification in off-target organs, indicating a transient signal in brain that rapidly decrease at 30 minutes. These data suggest that, despite the pathological condition, the nanoformulations are capable of reaching the lung parenchyma then follow the same fate after administration, without any accumulation in other filter organs, such as liver and

spleen. However, the fibrotic animals showed a similar but more rapid decrease in lung fluorescence signal, indicating that the presence of cellular infiltrates, especially macrophages, can influence the NPs biodistribution and thus their capture in phagocytic cells. This is extremely important because it enables ANANAS, and consequently Dex, to interact with macrophages' lysosomes where the acidic environment allows the drug release. Considering all these results, the i.n. administration route can be considered a valid protocol for the lung targeting also in fibrotic conditions.

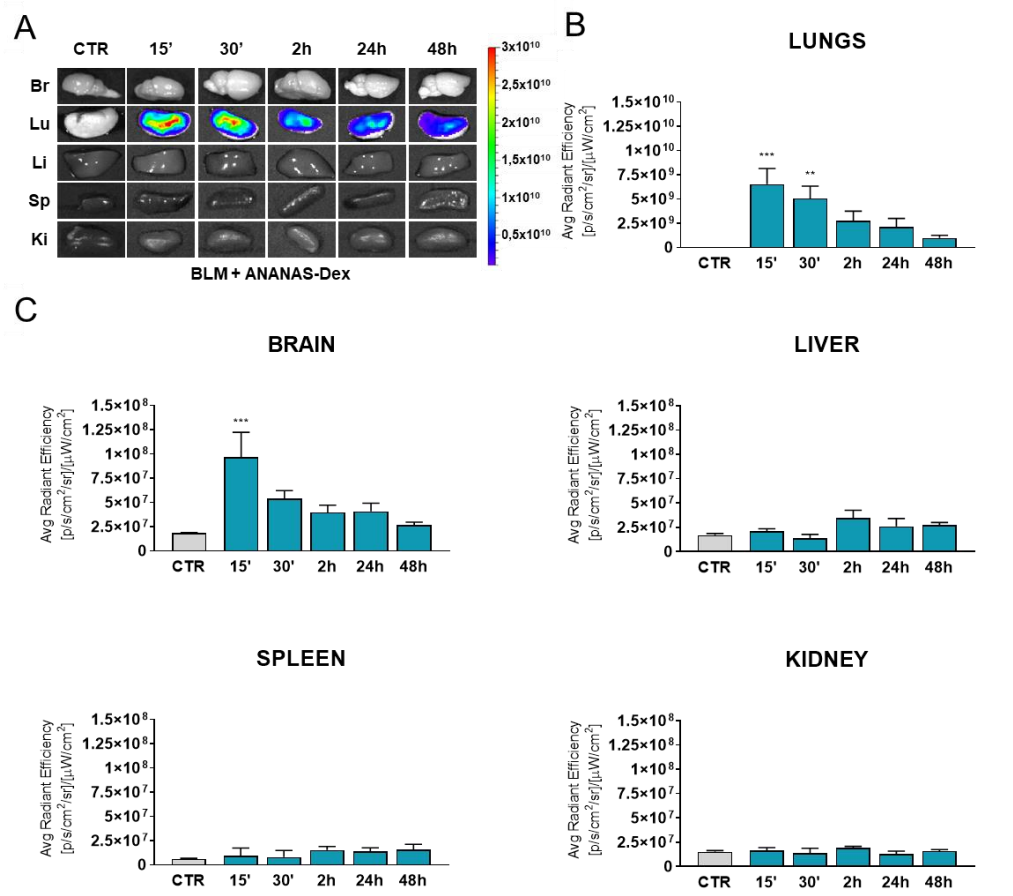

Figure 3.6 ***In vivo*** **biodistribution after intranasal administration in fibrotic conditions**: **A)** *Ex vivo* optical imaging of excised organs from animals sacrificed 15', 30', 2h, 24 h and 48 h after vehicle or ANANAS-Dex administration at 7 days post BLM instillation. Br. = brain, Lu. = lungs, Li. = liver, Sp. = spleen, Ki. = kidneys. **B-C)** Histograms represent the quantification of *ex vivo* optical imaging signal. Data are reported as mean ± SE. The data were analyzed by One-way ANOVA using Dunnet's test. **$p < 0.01$, ***$p \leq 0.001$.

Intrapulmonar localization of ANANAS−Dex in the lungs of healthy and fibrotic mice

The respiratory system in its totality is composed of multiple branched tissue systems, including the airways and blood vessels, and is lined with epithelial cells. In humans, at the end of a deep inspiration, over 80% of the total volume of the lung is air, and about 10% is blood. Thus, less than 10% is made of "real" tissue. The alveolar region (parenchyma) of the lung comprises about 90% of its total volume. The remaining non-parenchyma consists of conducting airways and larger vessels.[32] To accomplish successful respiration, the respiratory tract uses approximately 40 different resident cell types including epithelial, endothelial, stromal and immune population. In particular, tissue resident macrophages (alveolar and intestitial) and circulating immune cell types have important homeostatic, metabolic and repair functions while simultaneously acting as sentinel phagocytic immune cells, ready to be recruited in response to infection or injury. Since these cells have significant protective roles, they are involved in important lung disorders. Indeed, they can secrete several mediators of the inflammatory response and thus control the early phase of lung inflammation. An aberrant activation of macrophages can trigger inflammation contributing to both the start of disease and its progression.[13,33] To see whether the ANANAS formulations selectively interact with lung cell types, we used confocal laser microscopy to analyse the pulmonary tissue of NPs treated mice and evaluate the co-localization using a fluorescent marker for macrophages (anti-CD68). This experiment was carried out on both healthy and fibrotic mice models (Figure 3.7), to evaluate if the NPs fate changes in inflamed lungs. The nanoassemblies were effectively internalized by pulmonary macrophages, and this selective targeting of ANANAS-Dex remained consistent irrespective of the underlying pathology. Between 15 minutes and 2 hours post-administration, the red fluorescent signal associated with ANANAS predominantly diffused within the lung parenchyma, closely following the alveolar architecture and exhibiting no overlap with the macrophage marker CD68 (in green). However, between 24 and 48 hours after treatment, the Alexa633 signal closely coincided with that of macrophages (CD68). While we cannot entirely rule out the possibility of an initial, transient interaction between the nanoparticles and other cell populations (e.g., epithelial, endothelial cells), these findings

strongly suggest that CD68-positive cells play a pivotal role in the sequestration of ANANAS-Dex. Considering the pH-dependent stability of the hydrazone bond utilized to link Dex with ANANAS, this co-localization assumes fundamental significance as it allows the release of the drug from ANANAS. High-resolution images (Figure 3.7 – right panel) provide a closer view, revealing the localization of ANANAS within the mature acidic lysosomal compartments of macrophages in both healthy and fibrotic mice. This observation holds promise as it suggests the potential for drug release in an in vivo context.

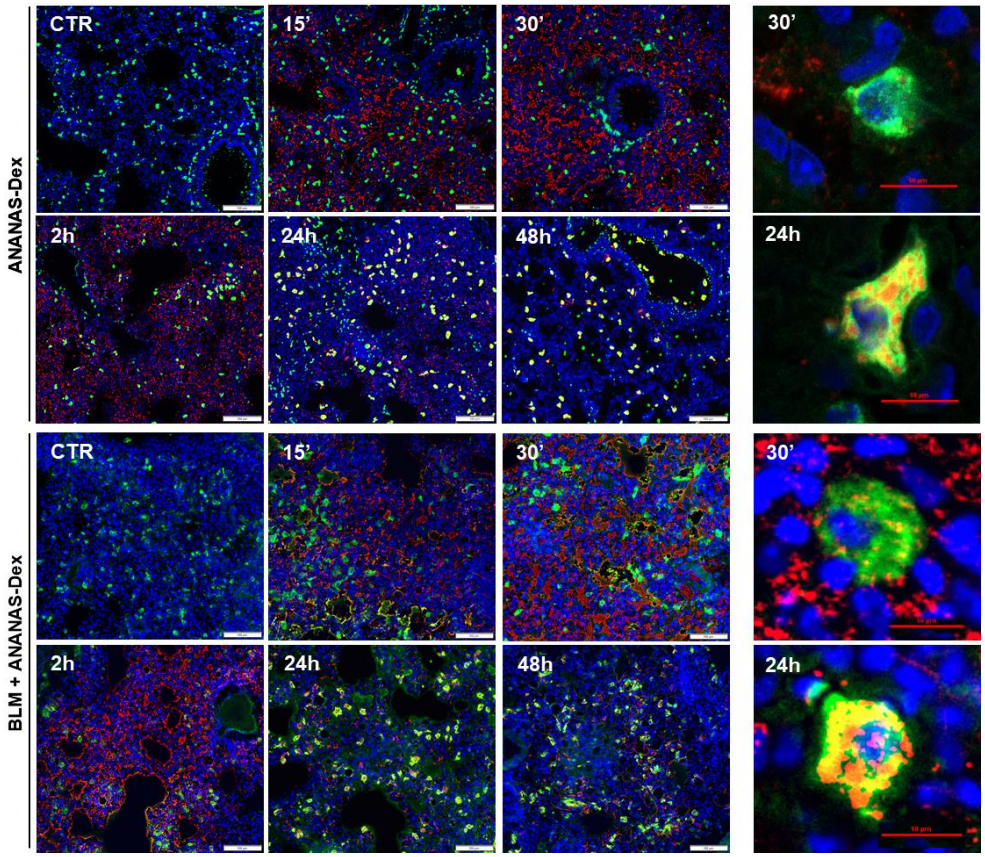

Figure 3.7 Localization of ANANAS−Dex in the lung of healthy and fibrotic mice. Representative images of the tissue distribution of ANANAS-Dex in lungs 15', 30', 2, 24 and 48 h after treatment in healthy (upper panel) and in BLM (lower panel) treated mice. The blue signal refers to the nuclei (Hoechst 33258 staining), green corresponds to the lysosomal component of macrophages (CD68 Antibody), red is associated with the alexa633 dye linked to the NPs, yellow corresponds to co-localized red and green signals. Scale bar=100µm. In the right panel, representative images of confocal microscopy of lungs at 30' and 24h after administration. Scale bar=10µm

Dexamethasone levels in Healthy and Fibrotic Models

To evaluate the corticosteroid pulmonary release characteristics of ANANAS-Dex, we conducted a pharmacokinetics study to monitor the concentrations of free Dex in both plasma and key target organs of both healthy and fibrotic mice. While the stability of the hydrazone linker at neutral pH had been established *in vitro*, the *in vivo* chemical environment within the body is considerably more intricate than a saline buffer, necessitating direct evidence regarding Dex levels within organs.

Figure 3.8 illustrates the outcomes of our pharmacokinetic study in mice, encompassing both healthy and fibrotic animals, following i.n. administration of ANANAS-Dex or the free drug (0.167 mg/Kg). The free drug exhibited rapid entry into the bloodstream, subsequently conforming to the conventional pharmacokinetic profile of Dex (with a half-life of 1.8−3.5 hours in humans, as per reference.medscape.com). It distributed throughout major tissues, including the liver and lung, and was entirely eliminated within 24 hours of administration. However, when mice received ANANAS-Dex treatment, free Dex was predominantly localized within the lung tissue. In healthy mice, drug release levels initially increase in the hours immediately following administration, followed by a gradual decline. Remarkably, in the lungs of fibrotic mice, both drug accumulation and elimination kinetics were notably higher compared to healthy counterparts. For instance, 24 hours post-administration, the levels of free drug were tenfold higher in fibrotic animals than in healthy mice. This difference is presumably attributed to altered metabolism or variations in bioavailability associated with pathological changes occurring during disease progression, particularly the strong cellular infiltration and lung architecture remodelling. Moreover, the levels of drug released by ANANAS nanoparticles persisted at 48 hours post-administration, in contrast to the free drug and the healthy condition. This sustained drug presence within the tissue could confer pharmacological advantages by potentially reducing the frequency of treatments required for patients.

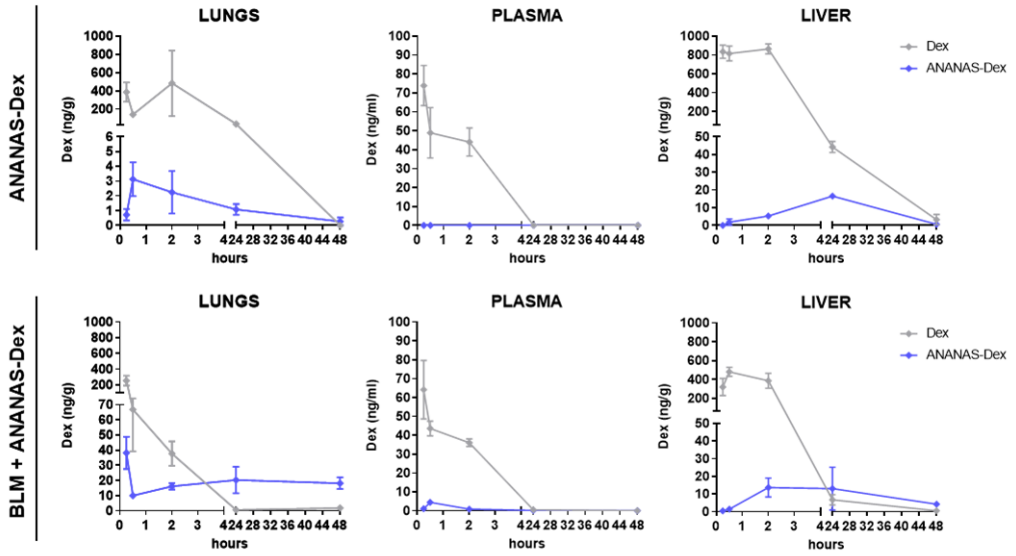

Figure 3.8 Pharmacokinetics study in filter organs. Levels of free dexamethasone measured in lung, plasma and liver, after administration of the drug (0.167 mg/kg) as free molecule (grey line), or formulated in ANANAS-Dex (blue line). Mice (n = 4 for each condition) were sacrificed at 15 min, 30 min and 2, 24 or 48 h after a single i.n. administration (upper panel) or in BLM treated mice (lower panel). Free Dex was measured by HPLC MS/MS with limit of quantitation (LoQ) equal to 0.01 ng/mg for lung and liver, and 0.1 ng/mL for plasma. Data are reported as mean ± SE.

Modulation of inflammatory and profibrotic markers after ANANAS-Dex treatment

Overall, the results shown above are promising regarding the potential efficacy for the treatment of lung disorders. However, to gain a proof of this potential effect, an acute treatment in affected mice has been carried out using the same doses as for biodistribution study and pharmacokinetics to detect in gene expression analysis any modifications in inflammatory and fibrotic markers 24 hours after treatment. It has been evaluated two main inflammatory cytokines, Interleukin 6 (IL-6) and Tumor necrosis factor α (TNF-α), both involved in the fibrotic process. IL-6 is crucial for the inflammatory phase and the switch to a reparative environment during the resolution of wound healing.[34] TNF-α is a potent inflammatory cytokine that promote ROS generation from pulmonary and non-pulmonary tissues.[35] As illustrated in the figure 3.9A (upper panel), 7 days after administration of BLM, a notable upregulation of proinflammatory

cytokines is evident. Treatment with free Dex effectively mitigates the expression of these cytokines, confirming its anti-inflammatory efficacy. Conversely, under these experimental conditions, treatment with ANANAS-Dex does not exert a significant influence on this cytokine expression. This differential behaviour can be attributed to the immediate availability of free drug to cellular targets, resulting in an anticipated anti-inflammatory response, in contrast to the slower yet persistent release observed with the NPs. The impact of these treatments on key fibrotic markers, notably collagen 1a1 and fibronectin[36,37] pivotal in ECM composition, was also assessed (Figure 3.9A – lower panel). In this context, an opposite pattern emerges regarding gene expression modulation. Specifically, free Dex does not exhibit a substantial effect, whereas treatment with ANANAS-Dex diminishes the expression of both genes. This peculiar outcome is challenging to elucidate. One hypothesis is the involvement of macrophages, highly active in wound healing processes, as well as in the clearance of exogenous materials and tissue surveillance. These diverse roles may potentially hijack macrophages from releasing profibrotic signals, thereby reducing their contribution to fibrosis. For a comprehensive assessment of the outcomes regarding the modulation of gene expression related to inflammation and fibrosis, representative histological lung sections of hematoxylin and eosin (H&E) and Sirius Red, respectively, are reported in Figure 3.9B. Collectively, these results hold significance for the evaluation of the potential therapeutic efficacy in the context of repeated treatments in a murine model of PF.

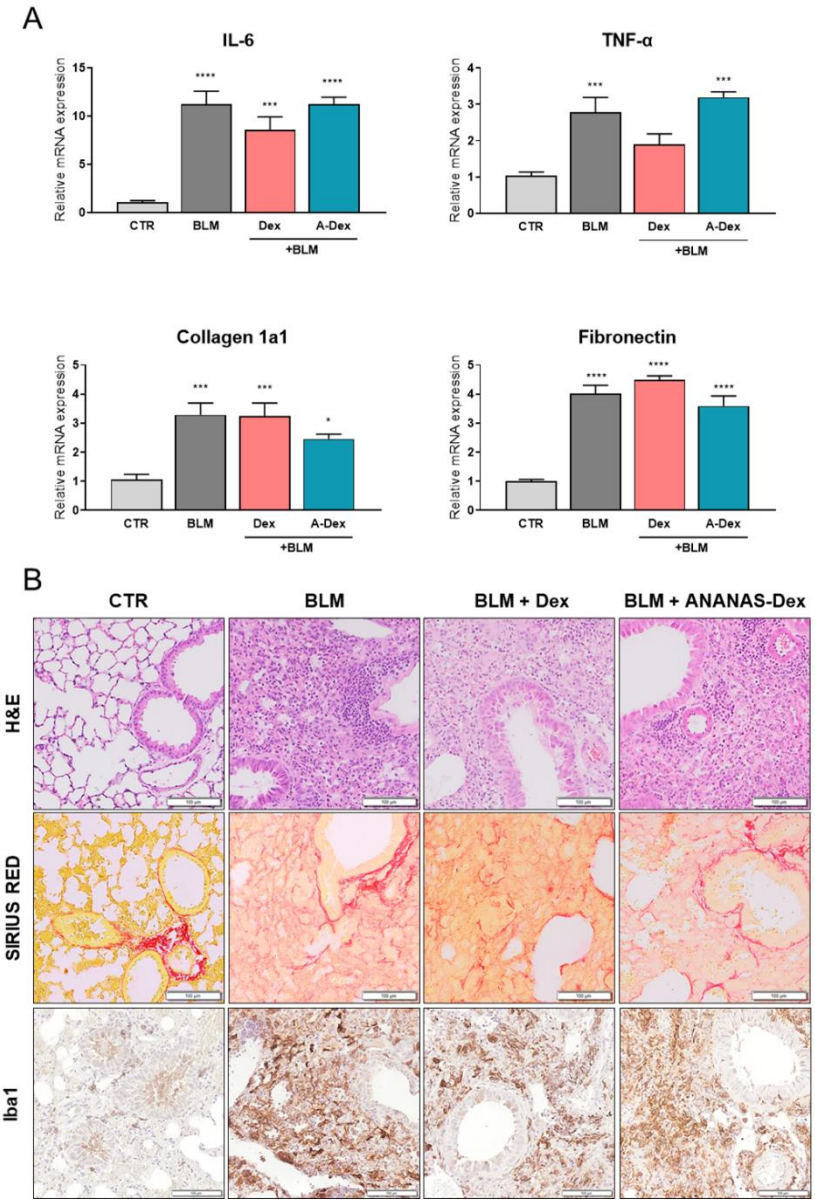

Figure 3.9 Modulation of inflammatory and profibrotic markers in lungs. A) mRNA expression was evaluated by RT-qPCR in lung of mice treated with dex (0.167 mg/kg) as free molecule or ANANAS-Dex at day 7 post BLM instillation. Mice (n = 6 for each condition) were sacrificed at 24 h after a single i.n. administration. Genes were normalized on β-ACT and the $2^{-\Delta\Delta Ct}$ method was employed for relative quantification on an external calibrator. Data are reported as mean ± SE, and were analyzed with one-way ANOVA followed by Dunnets' post hoc test. Significant differences compared to the untreated group (CTR) are reported, * P < 0.1, **P < 0.01, ***P < 0.001, ****P<0.0001. **B)** Representative images of H&E (upper panel), Sirius Red staining (middle panel) and Iba1 (lower panel) of lungs from untreated healthy animals (CTR) or treated with BLM alone (post 7 days), or with Dex or ANANAS-Dex and sacrificed 24 h after treatments. Scale bar= 100 µm.

3.4 Concluding remarks

Lung disorders represent a substantial burden for world human health. Respiratory diseases worldwide are among the leading causes of mortality. According to the World Health Organization (WHO), in the 28 European nations, they are responsible for approximately 660,000 deaths and lead to at least 6 million hospital admissions annually. Despite extensive research efforts, no effective treatment currently exists to arrest or reverse disease progression and improve clinical outcomes. This study emerged from the pressing need to explore alternative approaches for treating pulmonary fibrotic disorders, with a particular focus on determining the optimal administration route for lung dosing. In this context, the use of nanocarriers as delivery systems holds significant promise. The effectiveness of nanomedicine relies on the precise control of nanomaterials' chemical and physical properties, allowing the design of nanoparticles that respond to specific stimuli to enhance drug release, thereby improving therapeutic outcomes while minimizing off-target toxicity. Dexamethasone-loaded Avidin-Nucleic Acid Nanoassemblies (ANANAS-Dex) offer a promising drug delivery system for pulmonary fibrosis. These biodegradable, biocompatible nanoparticles exhibit low immunogenicity and possess unique attributes, offering potential applications in diagnostics and therapeutics. The choice of administration route plays a crucial role in determining how compounds, including nanoparticles, distribute throughout the body. To enhance lung targeting, we explored various routes for ANANAS-Dex administration in healthy mice. Systemic injection did not result in significant pulmonary accumulation due to phagocytic clearance. In contrast, intranasal instillation, a more direct route, showed excellent lung delivery in both healthy and fibrotic mice. In the presence of pathological conditions, such as inflammation and fibrosis, it's crucial to assess NPs' biodistribution. ANANAS-Dex effectively reached the lung parenchyma while avoiding off-target organs. Cellular infiltrates, particularly macrophages, played a crucial role in influencing the biodistribution and drug release profiles of the nanoparticles. Histological analysis confirmed efficient internalization of nanoparticles by pulmonary macrophages, enabling them to interact with lysosomes, facilitating drug release. Importantly, free Dex levels in fibrotic mice were tenfold higher, likely due to variations in bioavailability during disease progression. Notably, no dexamethasone signal was detected in mouse

plasma following nanoformulation administration, reducing the need for frequent treatments and off-target accumulation. Furthermore, a possible therapeutic effect was evaluated in a positive modulation in fibrotic markers. Although ANANAS-Dex did not significantly affect pro-inflammatory cytokine expression, it did reduce fibrotic gene expression, such as collagen 1a1 and fibronectin, in an acute treatment of affected mice. The exact reasons for these outcomes necessitate further investigation. However, these findings have significant implications for assessing the potential anti-fibrotic efficacy in a murine model of pulmonary fibrosis, suggesting a potential path toward clinical translation.

The present study is limited to an acute treatment, but several endpoints could be explored in future studies to test the efficacy of a chronic therapy. The precise control of physicochemical parameters achieved through high-affinity interactions that drive functional assembly formation holds promise for future translation from preclinical to clinical applications. These results can be translate into an inhaled nanoparticulate therapy that holds great potential for treating diseases that require direct lung delivery with reduced drug dosage and dosing frequency, leading to fewer systemic side effects and improved patient compliance.

References

1. Wijsenbeek, M. & Cottin, V. Spectrum of Fibrotic Lung Diseases. *N Engl J Med* **383**, 958–968 (2020).
2. Wijsenbeek, M., Suzuki, A. & Maher, T. M. Interstitial lung diseases. *The Lancet* **400**, 769–786 (2022).
3. Martinez, F. J. *et al.* Idiopathic pulmonary fibrosis. *Nat Rev Dis Primers* **3**, 17074 (2017).
4. Richeldi, L., Collard, H. R. & Jones, M. G. Idiopathic pulmonary fibrosis. *The Lancet* **389**, 1941–1952 (2017).
5. Johannson, K. A., Chaudhuri, N., Adegunsoye, A. & Wolters, P. J. Treatment of fibrotic interstitial lung disease: current approaches and future directions. *The Lancet* **398**, 1450–1460 (2021).

6. Lederer, D. J. & Martinez, F. J. Idiopathic Pulmonary Fibrosis. *N Engl J Med* **378**, 1811–1823 (2018).
7. Schacke, H. Mechanisms involved in the side effects of glucocorticoids. *Pharmacology & Therapeutics* **96**, 23–43 (2002).
8. Williams, D. M. Clinical Pharmacology of Corticosteroids. *Respir Care* **63**, 655–670 (2018).
9. Kim, B. Y. S., Rutka, J. T. & Chan, W. C. W. Nanomedicine. *N Engl J Med* **363**, 2434–2443 (2010).
10. Yetisgin, A. A., Cetinel, S., Zuvin, M., Kosar, A. & Kutlu, O. Therapeutic Nanoparticles and Their Targeted Delivery Applications. *Molecules* **25**, 2193 (2020).
11. Mitchell, M. J. *et al.* Engineering precision nanoparticles for drug delivery. *Nat Rev Drug Discov* **20**, 101–124 (2021).
12. Murray, P. J. & Wynn, T. A. Protective and pathogenic functions of macrophage subsets. *Nat Rev Immunol* **11**, 723–737 (2011).
13. Byrne, A. J., Maher, T. M. & Lloyd, C. M. Pulmonary Macrophages: A New Therapeutic Pathway in Fibrosing Lung Disease? *Trends in Molecular Medicine* **22**, 303–316 (2016).
14. Morpurgo, M., Radu, A., Bayer, E. A. & Wilchek, M. DNA condensation by high-affinity interaction with avidin. *J. Mol. Recognit.* **17**, 558–566 (2004).
15. Pignatto, M., Realdon, N. & Morpurgo, M. Optimized Avidin Nucleic Acid Nanoassemblies by a Tailored PEGylation Strategy and Their Application as Molecular Amplifiers in Detection. *Bioconjugate Chem.* **21**, 1254–1263 (2010).
16. Bigini, P. *et al. In Vivo* Fate of Avidin-Nucleic Acid Nanoassemblies as Multifunctional Diagnostic Tools. *ACS Nano* **8**, 175–187 (2014).
17. Violatto, M. B. *et al.* Dexamethasone Conjugation to Biodegradable Avidin-Nucleic-Acid-Nano-Assemblies Promotes Selective Liver Targeting and Improves Therapeutic Efficacy in an Autoimmune Hepatitis Murine Model. *ACS Nano* **13**, 4410–4423 (2019).
18. Ongaro, A. *et al.* The mode of dexamethasone decoration influences avidin-nucleic-acid-nano-assembly organ biodistribution and in vivo drug persistence. *Nanomedicine: Nanotechnology, Biology and Medicine* **40**, 102497 (2022).

19. Moeller, A., Ask, K., Warburton, D., Gauldie, J. & Kolb, M. The bleomycin animal model: A useful tool to investigate treatment options for idiopathic pulmonary fibrosis? *The International Journal of Biochemistry & Cell Biology* **40**, 362–382 (2008).
20. Green, N. M. Avidin. in *Advances in Protein Chemistry* vol. 29 85–133 (Elsevier, 1975).
21. Sims, G. E. C. & Snape, T. J. A method for the estimation of polyethylene glycol in plasma protein fractions. *Analytical Biochemistry* **107**, 60–63 (1980).
22. Morpurgo, M. *et al.* Characterization of Multifunctional Nanosystems Based on the Avidin-Nucleic Acid Interaction As Signal Enhancers in Immuno-Detection. *Anal. Chem.* **84**, 3433–3439 (2012).
23. Blanco, E., Shen, H. & Ferrari, M. Principles of nanoparticle design for overcoming biological barriers to drug delivery. *Nat Biotechnol* **33**, 941–951 (2015).
24. Ngo, W. *et al.* Why nanoparticles prefer liver macrophage cell uptake in vivo. *Advanced Drug Delivery Reviews* **185**, 114238 (2022).
25. Newman, S. P. Drug delivery to the lungs: challenges and opportunities. *Therapeutic Delivery* **8**, 647–661 (2017).
26. Thakur, A. K. *et al.* Patented therapeutic drug delivery strategies for targeting pulmonary diseases. *Expert Opinion on Therapeutic Patents* **30**, 375–387 (2020).
27. Southam, D. S., Dolovich, M., O'Byrne, P. M. & Inman, M. D. Distribution of intranasal instillations in mice: effects of volume, time, body position, and anesthesia. *American Journal of Physiology-Lung Cellular and Molecular Physiology* **282**, L833–L839 (2002).
28. Seo, Y. *et al.* Optimizing anesthesia and delivery approaches for dosing into lungs of mice. *bioRxiv* 2023.02.01.526706 (2023) doi:10.1101/2023.02.01.526706.
29. B. Moore, B. *et al.* Animal Models of Fibrotic Lung Disease. *Am J Respir Cell Mol Biol* **49**, 167–179 (2013).
30. Della Latta, V., Cecchettini, A., Del Ry, S. & Morales, M. A. Bleomycin in the setting of lung fibrosis induction: From biological mechanisms to counteractions. *Pharmacological Research* **97**, 122–130 (2015).
31. Li, S., Shi, J. & Tang, H. Animal models of drug-induced pulmonary fibrosis: an overview of molecular mechanisms and characteristics. *Cell Biol Toxicol* **38**, 699–723 (2022).

32. Knudsen, L. & Ochs, M. The micromechanics of lung alveoli: structure and function of surfactant and tissue components. *Histochem Cell Biol* **150**, 661–676 (2018).

33. Ogawa, T., Shichino, S., Ueha, S. & Matsushima, K. Macrophages in lung fibrosis. *International Immunology* **33**, 665–671 (2021).

34. Li, Y. *et al.* The Role of IL-6 in Fibrotic Diseases: Molecular and Cellular Mechanisms. *Int. J. Biol. Sci.* **18**, 5405–5414 (2022).

35. Mukhopadhyay, S., Hoidal, J. R. & Mukherjee, T. K. Role of TNFα in pulmonary pathophysiology. *Respir Res* **7**, 125 (2006).

36. Nho, R. S., Ballinger, M. N., Rojas, M. M., Ghadiali, S. N. & Horowitz, J. C. Biomechanical Force and Cellular Stiffness in Lung Fibrosis. *The American Journal of Pathology* **192**, 750–761 (2022).

37. Wilson, M. S. & Wynn, T. A. Pulmonary fibrosis: pathogenesis, etiology and regulation. *Mucosal Immunology* **2**, 103–121 (2009).

CHAPTER 4

Efficient SARS-CoV-2 infection antagonization by rhACE2 ectodomain multimerized onto the Avidin Nucleic-Acid-NanoASsembly

Simone Bernardotto, Ilaria Frasson, Silvia Faravelli, Annalisa Morelli, Elisa Schiavon, Giulia Yuri Moscatiello, Martina Bruna Violatto, Alberta Pinnola, Anselmo Canciani, Andrea Mattarei, Gianpaolo Rossi, Marisa Brini, Laura Pasetto, Valentina Bonetto, Paolo Bigini, Federico Forneris, Sara Richter and Margherita Morpurgo

Manuscript submitted to Biomaterials

Abstract

Nanodecoy systems based on analogues of viral cellular receptors assembled onto fluid lipid-based membranes of nano/extravescicles are potential new tools to complement classic therapeutic or preventive antiviral approaches. The need for lipid-based membranes for transmembrane receptor anchorage may pose technical challenges along industrial translation, calling for alternative geometries for receptor multimerization. Here we developed a semisynthetic self-assembling SARS-CoV-2 nanodecoy by multimerizing the biotin labelled virus cell receptor -ACE2-ectodomain onto a poly-avidin nanoparticle (NP) based on the Avidin-Nucleic-Acid-NanoASsembly-ANANAS. The ability of the assembly to prevent SARS-CoV-2 infection in human lung cells and the affinity of the ACE2:viral receptor-binding domain (RBD) interaction were measured at different ACE2:NP ratios. At ACE2:NP=30, 90% SARS-CoV-2 infection inhibition at ACE2 nanomolar concentration was registered on both Wuhan and Omicron variants, with ten-fold higher potency than the monomeric protein. Lower and higher ACE2 densities were less efficient suggesting that functional recognition between multi-ligand NPs and multi-receptor virus surfaces requires optimal geometrical relationships. In vivo studies in mice showed that the biodistribution and safety profiles of the nanodecoy are potentially suitable for preventing viral infection upon nasal instillation. Viral receptor multimerization using ANANAS is a convenient process which, in principle, could be rapidly adapted to counteract also other viral infections.

4.1 Introduction

In the context of the fight against viral infections, "decoy" systems based on the use of analogues of viral cellular receptors[1,2] as single molecules or assembled onto fluid lipid-based membrane nanoparticles represent new tools potentially capable of complementing classic therapeutic or preventive approaches based on antibodies, hyperimmune sera and vaccines. Decoy systems are designed to act as “baits” for the virus capable of diverting it from its target cells and blocking it before it infects them. Compared to the preventive/treatment options currently available in the clinic, major advantage of these systems stems from the fact that their efficacy is not affected by viral mutations.

During the recent COVID-19 pandemic, the decoy concept, whose efficacy has been initially demonstrated against the influenza virus[2] and HIV[1] has also been suggested to develop new tools against SARS-CoV-2.

SARS-CoV-2 infection is triggered by the binding of its envelope - Spike (S’) - protein to the cell target membrane angiotensin-converting enzyme 2 (ACE2).[3,4] S’ Protein–ACE2 binding allows viral attachment to cells, which is followed by viral S-protein priming by the TMRSS2 protease, membrane fusion, and viral entry.[3] The interaction with ACE2 is also responsible for increased angiotensin II levels and activation of the renin-angiotensin system, which further increases ACE-2 expression[5] and plays a critical role in the severe acute lung injury induced by SARS-CoV viruses.

Decoy strategies against SARS-CoV-2 infection tackle the S’-protein/ACE2 interaction using ACE2 analogues as baits for the virus. It was shown that a recombinant soluble version of the ACE2 receptor (rh-s-ACE2) is capable to inhibit SARS-CoV-2 infection in a concentration dependent manner[6] both in vitro and in clinical studies in a small number of patients.[7] Following these landmark results, other ACE2-based viral decoy systems have been proposed towards higher efficacy, either by inducing *in vivo* transient rh-s-ACE2 mucosal expression by means of mRNA lipid-based nanoparticles[8] or by engineering rh-s-ACE2 towards higher affinity for the S’ protein.[9–11] In addition, ACE2-based nanodecoy systems based on membrane-anchored ACE2 membrane vesicles have also been investigated[12–16] showing high efficacy, likely due to the synergistic effect of

multiple ACE2 units present at the vesicle membrane. However, despite the great potentials demonstrated by these ACE2-carrying nano/extra vesicles, their clinical translation may be hampered by the complexity in their production standardization. Therefore, alternative synthetic or semisynthetic tools for ACE2 nano-multimerization that reproduce the synergistic effect observed with the nano/extra vesicles, may markedly accelerate the clinical translation of this therapeutic strategy.

In this context a semisynthetic convenient tool for protein multimerization is the Avidin-Nucleic-Acid-Nano-ASsembly (ANANAS) platform. ANANAS are nanosized (Ø = 120 nm) colloidally stable poly-avidin toroids generated from the condensation of a non-coding nucleic acid (NA) filament by the high-affinity interaction with egg-white avidin.[17,18] ANANAS can be decorated at their surface, in one pot solution with up to 1000 functionalities (provided that these can be biotinylated) at stoichiometric control thanks to their intact biotin-binding capability and the high affinity for biotin ligands (Kd 10^{-15} M^{-1}).[19] Decoration occurs by simply mixing with biotinylated functional elements at desired biotin:biotin binding sites (BBS) molar ratios and if neither the BBS become saturated nor the surface area available is exceeded,[19,20] no purification is necessary. If these two requirements are fulfilled, an infinite number of surface composition combinations can be conveniently generated and screened so that, in principle, selection of the best performing composition is facilitated.

Successful application of this platform has been demonstrated in *in vitro* and *in vivo* diagnostics[21,22] and in drug delivery.[23,24] Thanks to the tolerogenic property of avidin,[25,26] these nanocarriers show no toxicity and poor immunogenicity even after multiple administration in mice for up to 30 days.[24] When administered parenterally they circulate freely in the bloodstream for more than 6 h and are later captured by scavenging organs such as liver and spleen, from which they are degraded within 48 h. An additional property that makes them suitable for pharmaceutical development is their highly defined composition which makes them suitable for scaling up studies.

In this work ANANAS were used as scaffold to generate multimerized ACE2 ectodomain to improve the avidity for the SARS-CoV-2 S' protein with the ultimate goal of preventing SARS-CoV-2 cell invasion. To this end, a monomeric biotin derivative of ACE2 ectodomain was optimized by recombinant DNA technologies. ACE2:NP

assemblies were generated at different ACE2-biotin:NP molar ratios and compared for size and affinity for the viral S' protein RBD of both the Wuhan and the new variant of concern Omicron (BA.1) which emerged later on and became dominant worldwide.[27,28] The ability to prevent SARS-Cov-2 infection of the two variants in human lung cells was also tested as a function of ACE2 density at nanoparticle surface and compared to that of the monomeric rh-sACE2-biotin. *In vivo* preliminary biodistribution and toxicity studies in healthy mice were then performed to assess the possibility of nasal administration.

4.2 Materials and Methods

ANANAS core nanoparticles were obtained in freeze dried form as described elsewhere using avidin from e.protein Belgium) and biotin-PEG5kDa (Laysan Bio) for colloidal protection[17]; Biotin-diaminohexanamido-Alexa633 (biotin-C6-Alexa633) was obtained in the lab according to published procedures;[22] biotin-HRP (code BH-0101) and ELISA Dilution buffer (DB) were from ANANAS nanotech (Padova, Italy). SARS-CoV-2 (COVID-19) Spike RBD (RBD) Wuhan-Hi-1 variant was produced recombinantly as described elsewhere;[29] RBD B.1.1.7 / Alpha (English), and B.1.617.1 / Kappa (Indian) variants were purchased from Genetex (Irvine, California, USA).

- **Cell culture and virus**

Vero E6 (ATCC® CRL-1586TM) were maintained in Dulbecco's modified Eagle's medium (DMEM; Thermo Fisher Scientific), Calu-3 cells (ATCC®, HB-55) were maintained in Dulbecco's Modified Eagle Medium: Nutrient Mixture F-12 (DMEM/F-12, Thermo Fisher Scientific). Media were supplemented with 10% (v/v) fetal bovine serum (FBS, Thermo Fisher Scientific) and penicillin/streptomicin (Thermo Fisher Scientific). Cell cultures were maintained at 37°C and 5% CO_2 in humidified atmosphere and routinely tested for mycoplasma contamination. For seeding and subcultivation, cells were first washed with phosphate buffered saline (PBS) and then incubated in the presence of trypsin/EDTA solution (Gibco, Thermo Fisher Scientific) until cells detached.

The SARS-CoV-2 Wuhan isolate SARS-CoV-2/human/ITA/CLIMVIB2/2020 was provided by the Virology Unit of Ospedale Luigi Sacco (GenBank accession ON062195 MW000351.1) (Milan, Italy). The SARS-CoV-2 UK and Delta isolates Human nCoV19 isolate/England/MIG457/2020 and hCoV-19/Netherlands/NH-RIVM-27142/2021_P2, respectively, were supplied by the European Virus Archive goes Global (EVAg) platform. The SARS-CoV-2 Omicron variant was provided by the Microbiology Unit of the University-Hospital of Padova (Padova, Italy), and previously described (GenBank accession ON062195). All viral stocks were prepared by propagation in Vero E6 cells in DMEM supplemented with 2% FBS. Viral titre was assessed by plaque reduction assay (PRA) and expressed as plaque forming units (PFU) per milliliter (ml). All experiments involving live SARS-CoV-2 were performed in compliance with the Italian Ministry of Health guidelines for Biosafety Level 3 (BSL-3) containment procedures in the approved laboratories of the Molecular Medicine Department of University of Padova.

- **Molecular cloning**

The sequence encoding for human ACE2 ectodomain (Uniprot Q9BYF1 residues 18-615) was amplified from a pCEP4-myc-ACE2 (Addgene plasmid # 141185)[30] using polymerase chain reaction with oligonucleotides BclI-ACE2-Fw (aaaatgatcaTCCACCATTGAGGAACAGGCC) and ACE2-NotI-Rv (aaaagcggccgcGTCTGCATATGGACTCCAGTC). The resulting sequence was processed with 5'-BclI and 3'-NotI restriction endonucleases for subsequent transfer into a modified pUPE.107.03-BAP (U-Protein Express BV) expression vector bearing a C-terminal 6xHis-tag followed by a Biotin Acceptor Peptide (BAP) sequence (GLNDIFEAQKIEWHE[31]). All sequences underwent checking for their correctness using Sanger sequencing (Microsynth). The plasmid used for *in vivo* biotinylation, encompassing the *E. coli* BirA sequence (UniProt P06709) followed by a KDEL sequence for retention in the endoplasmic reticulum (pUPE.107.03-BirA-KDEL) was a kind gift from U-Protein Express B.V.

- **Recombinant production of hACE2 ectodomain fragments**

Recombinant hACE2 ectodomain *(rh-s-ACE2)* was produced using HEK293-F cells (Invitrogen) cultivated in suspension using Freestyle medium (Invitrogen) as

described.[32] Briefly, cells were co-transfected at a cell density of 1 million mL^{-1} using 1.0 μg of pUPE.107.03-BAP-hACE2and 3 μg of polyethyleneimine (PEI; Polysciences). For in vivo biotinylation, a DNA mixture composed of 0.2 μg of pUPE.107.03-BAP-hACE2 and 0.2 μg of pUPE.107.03-BirA-KDEL was used. All cultures were supplemented with 0.6% Primatone RL (Merck) 4 h after transfection. The cell media containing secreted proteins were collected 6 days after transfection by centrifugation at 1000 × g for 15 min. The pH and ionic strength of the filtered medium were adjusted using concentrated phosphate buffer saline (PBS). Samples were loaded onto a 5 mL His-Trap Excel column (Cytiva) using a peristaltic pump and then eluted with a 0-250 mM imidazole gradient using a NGC fast protein liquid chromatography (FPLC) system (Bio-Rad). Iodoacetamide treatment to generate either rh-s-ACE2i or rh-s-ACE2i-biotin was performed on the eluted samples (rh-s-ACE2 or rh-s-ACE2-biotin, respectively) through incubation with 25 mM iodoacetamide (Merck) for 1 hour to block the reactivity of free cysteine residues, followed by concentration with concomitant buffer exchange with fresh PBS to remove imidazole using Amicon centrifugal filters (Merck). All samples were concentrated to 1 mg mL^{-1}, flash-frozen in liquid nitrogen and kept at -80 °C until usage.

- **Recombinant protein QC prior to usage**

Quality control during protein purification was carried out using reducing and non-reducing SDS-PAGE analysis and differential scanning fluorimetry (DSF) with a Tycho NT.6 instrument (Nanotemper). Evaluation of effective biotinylation was assessed through western blotting using HRP-conjugated streptavidin (Merck). For detection, the membranes were incubated with Clarity ECL substrate (Bio-Rad) and imaged in a ChemidocMP imaging system (Bio-Rad). Image processing and densitometry analyses were carried out using the Image Lab software (Bio-Rad).

- **rh-s-ACE2i-biotin:ANANAS assemblies**

Non-functionalized ANANAS "core" assemblies were obtained in freeze-dried form according to optimized procedures published elsewhere.[17] For ACE2 decoration, core nanoparticles were re-dissolved at 0.1-1 mg/mL in 10 mM phosphate, pH 7.4 + 0.0125% tween20, and mixed with rh-s-ACE2i-biotin or ANANAS Diluent Buffer (DB, ANANAS nanotech S.r.l., Padova,Italy) at predetermined molar ratios. Assembly size

was determined by dynamic light scattering (DLS) using a Malvern Ultrasizer apparatus. To quantify the nanoparticle loading capacity for rh-s-ACE2-biotin, assembly solutions generated at ACE2:NP molar ratios between 30 and 90 were analyzed by gel permeation chromatography using a fast protein liquid chromatography system (FPLC, Akta purifier, GE). Samples were eluted (1mL/min) using PBS in a Superose 6 prep® medium (Tricorn®10/300 column) which allows to separate NP-associated rh-s-ACE2-biotin from the one in solution.

- **Affinity of rh-s-ACE2i-biotin for SARS-CoV-2 RBD**

The affinity of *rh-s-ACE2i-biotin* (as free molecule or assembled onto ANANAS) for the different SARS-CoV-2 RBD variants was tested by Enzyme Linked ImmunoSorbed Assay (ELISA). Briefly, Nunc® Maxisorp 96-well plates were conditioned by overnight (4°C) incubation with the RBD (0.2 µg/ml) in 50 mM carbonate buffer pH 9.5. After blocking for 30 minutes with 3% BSA in 10 mM phosphate, 150 mM NaCl, pH 7.4 + 0.05% tween20 (PBST), wells were incubated for 2h at room temperature (RT) with serial dilutions of *rh-s-ACE2i-biotin* from 0.625 to $3.18x10^{-5}$ µg/mL (between $9x10^{-9}$ and $3.5x10^{-11}$M) in DB. When testing rh-s-ACE2-biotin as free molecule in solution, detection was carried out after incubation with avidin-HRP (Sigma-Aldrich, 1µg/mL in DB, 45 min, RT), followed by reaction with 100 µL of tetramethylbenzidine (TMB, SureBlue Reserve, KPL immunoassays Reagents, Gaithersburg, MD USA) and blocking with 100 µL of 1M H_2SO_4. When testing the protein assembled with ANANAS or mixed with avidin, detection was carried out after incubation with biotin-HRP (1µg/mL in DB, 45 min, RT) followed by TMB detection as above. To determine the experimental dissociation constants (Kds), the plots of absorbance at 450 nm *versus* rh-s-ACE2-biotin concentration were fitted by the *Graphpad-Prism*® software using the *One site - Specific binding* algorithm.

- **Transmission Electron microscopy (TEM)**

Solutions (in 10 mM HEPES buffer, pH 7.4) of ANANAS, ANANAS-ACE2-30, and SARS-CoV-2 (Wuhan variant) - as such, or preincubated (10' in ice) with ANANAS or ANANAS-ACE2-R30 - were fixed with 4% PFA (in ice) for 60 min, and one drop (50 µL) was placed on a 400-mesh holey-film grid for 10 min. After washing with PBS, samples were stained with 1% uranyl acetate for 2 min and washed with PBS. Finally,

biotin functionalized gold nanoparticles (5nm) (Thermofisher-AlphaAesar) (dilution 1:5000) in water were added for ANANAS staining. Samples were observed with a Tecnai G2 (FEI; Thermo Fisher Scientific, Waltham, MA, USA) transmission electron microscope operating at 100 kV. Images were captured with a Veleta (Olympus Soft Imaging System; Münster, Germany) digital camera. The initial viral titer in all spotted solutions was $2.8x10^6$ PFU/µl. Mixtures with ANANAS or ANANAS-ACE2-30 were generated a NP:PFU molar ratio = 100.

- **Antiviral assays**

Calu-3 cells ($2.75x10^4$ cells/well) were seeded in 96 well plates 24 h prior to infection. The cell culture medium was removed and replaced with virus inoculum (MOI of 0.1 PFU/cell), previously incubated with rh-s-ACE2i-biotin in solution or assembled onto ANANAS at ACE2:NP molar ratio equal to 0 (ANANAS), 15 (ACE2:NP-R15), 30 (ACE2:NP-R30) or 60 ACE2:NP-R60, or with vehicle (DB). Following 1 h adsorption at 37 °C, the virus inoculum was removed and replaced with fresh 10% FBS DMEM/F-12 media. Cells were incubated at 37 °C for 30 h before supernatants were harvested. The viral titer (expressed as PFU/ml) was calculated by PRA in Vero E6 cells.

- **SARS-CoV-2 titration by plaque reduction assay (PRA)**

Vero E6 cells were seeded in 24-well plates at a concentration of 9×10^4 cells/well. The following day, serial dilutions of the viral stocks or of the tested supernatants were performed in serum-free DMEM media. After 1 h absorption at 37 °C, 2× overlay media was added to the inoculum to give a final concentration of 2% (v/v) FBS/DMEM media and 0.6% (v/v) methylcellulose (Merck Life science, Cat: M0512) to achieve a semi-solid overlay. Samples were incubated at 37 °C for 48 h next fixed using 5% Formaldehyde in PBS (Merck Life Science, Cat: 252549). Plaques were visualized using Crystal Violet solution (20% Ethanol, Merck Life science, Cat: C6158).

- **Cytotoxicity**

The cytotoxicity of the tested ANANAS nanoparticles was assessed and expressed as cytotoxic concentration (CC_{50}). Calu-3 cells ($2.75x10^4$ cells/well) were seeded in 96 well plates and the tested nanoparticles or an equal volume of vehicle (Diluent Buffer, ANANAS Nanotech S.r.l., Padova, IT) were supplemented to the medium. ANANAS nanoparticles were incubated for 48 h and cell viability was determined by measuring

the adenosine triphosphate (ATP) content of the cells using the ATPlite kit (PerkinElmer, Waltham, MA, Cat: 6016941) according to the manufacturer's instructions. CC_{50} values were calculated using the Reed and Muench method.[33]

- **Animals**

The "Mario Negri" Institute for Pharmacological Research IRCCS adheres to the principles set out in the following laws, regulations, and policies governing the care and use of laboratory animals: Italian Governing Law (D.lgs 26/2014; Authorization no. 19/ 2008-A issued March 6, 2008 by Ministry of Health); Mario Negri Institutional Regulations and Policies providing internal authorization for persons conducting animal experiments (Quality Management System Certificate, UNI EN ISO 9001:2015, Reg. No. 6121); the NIH Guide for the Care and Use of Laboratory Animals (2011 edition), and EU directives and guidelines (EEC Council Directive 2010/63/UE). This work was reviewed by the IRCCS-IRFMN Animal Care and Use Committee (IACUC) and then approved by the Italian "Istituto Superiore di Sanità" (code: 49/2021-PR). Eight-week-old female CD1 mice were maintained under specific pathogen-free conditions in the Institute's Animal Care Facilities; they received food and water ad libitum and were regularly checked by a veterinarian who is responsible for animal welfare supervision and experimental protocol review.

- **Biodistribution in vivo**

Mice were anesthetized with medetomidine (Domitor®) at a dose of 0,4 mg/kg b.w. and ketamine (Lobotor®) at a dose of 36 mg/kg injected intraperitoneally. Nanoformulations (ACE2:NP-R30 or core ANANAS -ANANAS) or vehicle was administered intranasally with a micropipette (25 µl per nostril with a total volume of 50 µl). Animals were allowed to recover immediately afterwards (Antisedan® - 0,8 mg/kg intraperitoneally). A total of 27 CD1 animals were used. Twelve mice were treated with 51,6 µg of NPs/mouse (2 mg/kg) of ANANAS and twelve mice with ACE2:NP-R30 51,6 µg of NPs/mouse (2 mg/kg) loaded with 0.2 mg/kg of ACE2 (5 µg rh-s-ACE2i-biotin/dose). The remaining three mice were treated with PBS and were used as controls. At the end of the study, mice were euthanized 15 min, 2, 24, and 72 h after treatment with cervical dislocation. Liver, kidney, spleen and lungs were collected and scanned for *ex vivo*

imaging. Spectral unmixing, image processing and analysis were done using Living Image 4.3.1 software (PerkinElmer).

- **Tissue Collection and Histological Analysis**

For immunofluorescence analysis, at the moment of sacrifice, lungs were collected, frozen in dry ice and stored at -80°C until immunofluorescence staining. Cryostat sections were cut at 20 µm and mounted on glass slides. Slides postfixed in 10% formalin (Bioptica) for 20 minutes, washed three times in phosphate-buffered saline (PBS) for 5 min and incubated for 1 h with a blocking solution (PBS-NGS 10%-Triton X-100 0.1%) then washed again with PBS. For subcellular localization, the antibody anti-CD68 (specific for lysosome and endosome membranes of macrophages) was employed as follows: primary monoclonal rat antibody anti-CD68 (1:200, Serotec, Kidlington, UK) + Triton X-100 0.1% + NGS 3% in PBS O/N at 4 °C. For PEG staining: primary monoclonal rabbit antibody anti-Polyethylene glycol (PEG) (1:165, Abcam RabMab ab51257) + Triton X-100 0.1% + NGS 3% in PBS O/N at 4 °C. After washing with 1X PBS, the slides were incubated with the Alexa488 conjugated secondary antibody (1: 500, Invitrogen) for 1 hour at room temperature in 1% 1X-NGS PBS solution. After this step, the slides were incubated with the Hoechst nuclear marker 33258 (2 µg / mL in 1X PBS, Sigma Aldrich) for 10 minutes. Fluoromount Aqueous Mounting Medium (Sigma Aldrich) was used for mounting with cover glass in order to preserve the tissue for long periods and prevent the decay of the fluorescence. Sections were visualised through Olympus virtual slide microscope VS120 (Olympus, Japan). For confocal microscopy analysis, samples were acquired using Nikon A1 Confocal microscopes and pseudocolored (blue for Hoechst 33258, green for alexa488 and red for alexa633). For the histological evaluation, lungs were removed from treated animals at different timepoints (15 min, 2, 24 and 72 h) and fixed overnight in 10% formalin (Bioptica, Italy). Tissue were processed for paraffin embedding, cut with Leica RM55 microtome (Leica Microsystem, Italy) into 4 µm-thick sections and dried into the oven at 37°C overnight. Slices were deparaffinised in xylene and rehydrated through a series of alcohols to water. Hematoxylin-Eosin (BioOptica) staining method was used to investigate lung and kidney injury. Samples were dehydrated through an alcohol scale, dried under the hood

and mounted with xylene-based mounting medium (DPX, Sigma). Sections were visualised Olympus virtual slide microscope VS120 (Olympus, Japan).

- **Cytokines measurements**

Serum levels of IL-10, INF-γ and TNF-α were measured using commercially available AlphaLISA kits (#AL502C, #AL593C, #AL541C), as described by the manufacturer (Perkin Elmer). AlphaLISA signals were measured using an Ensight Multimode Plate Reader (PerkinElmer).

4.3 Results and Discussion

Optimizing biotinilation of rh-s-ACE2 ectodomain

The preparation of semi-synthetic multi-assemblies requires the use of components with defined and reproducible properties. In particular, multi-assembly using the poly-avidin ANANAS core necessitates the use of biotinylated ligands. Preliminary studies were carried out to identify the best strategy for obtaining a recombinant human soluble ACE2 (ACE2 ectodomain, rh-s-ACE2) biotin derivative with suitable properties for ANANAS tethering. SDS-PAGE and gel filtration chromatography analysis (Figure 4.1A and D) highlighted the tendency of the recombinant ACE2 ectodomain to multimerize/aggregate secondary to SS bond formation. In fact, while freshly prepared rh-s-ACE2 elutes in gel permeation chromatography as a single peak at about 17 mL retention volume, a second peak at lower retention appears after 24h storage at 4°C. SDS-PAGE electrophoresis of the same sample showed the presence of large MW aggregates, which reverted to the expected MW upon reductive treatment. *Rh-s-ACE2* not only had the tendency to aggregate but also was found difficult to biotinylate through classic bioconjugation tools. In fact, the product of reaction with 10 equivalents of a biotin-*N*-hydroxy succinimide ester derivative was not retained by the ANANAS core. A thiol-capped rh-s-ACE2 derivative was thus generated by S-iodoacetamide reaction of cysteines. The resulting protein (*rh-s-ACE2i*) lost the tendency to aggregate but, again, it was difficult to biotinylate by classic bioconjugation procedures, as less than 10 % of the product of biotin conjugation was retained by the nanoparticles (Figure 4.1B). Finally, a S-iodacetamide-capped biotin derivative (*rh-s-ACE2i-biotin*) was obtained by

inserting the biotin acceptor peptide (BAP) tag (also known as AVI tag) after the His-tag (AAAHHHHHH-MS-GLNDIFEAQKIEWHE)[34] at the protein C terminal using recombinant DNA technologies. Usage of BAP tagging for localized protein biotinylation is well established. This process typically relies on *in vitro* treatment of purified BAP-tagged proteins with soluble E. coli BirA enzyme, which specifically recognizes the BAP sequence attaching biotin to the free amino group found on the side chain of the lysine residue. To minimize sample handling and ensure homogeneity, we have relied on the possibility of applying the same strategy directly inside transfected cells[35], by co-transfecting HEK293-F cells with a plasmid encoding for rh-s-ACE2-BAP and a second plasmid containing *E. coli* BirA preceded by a Cystatin signal peptide and fused to a C-terminal retention signal for the endoplasmic reticulum. The resulting product was stable against aggregation and was efficiently biotinylated, as demonstrated by its ability to be completely retained by ANANAS (Figure 4.1C).

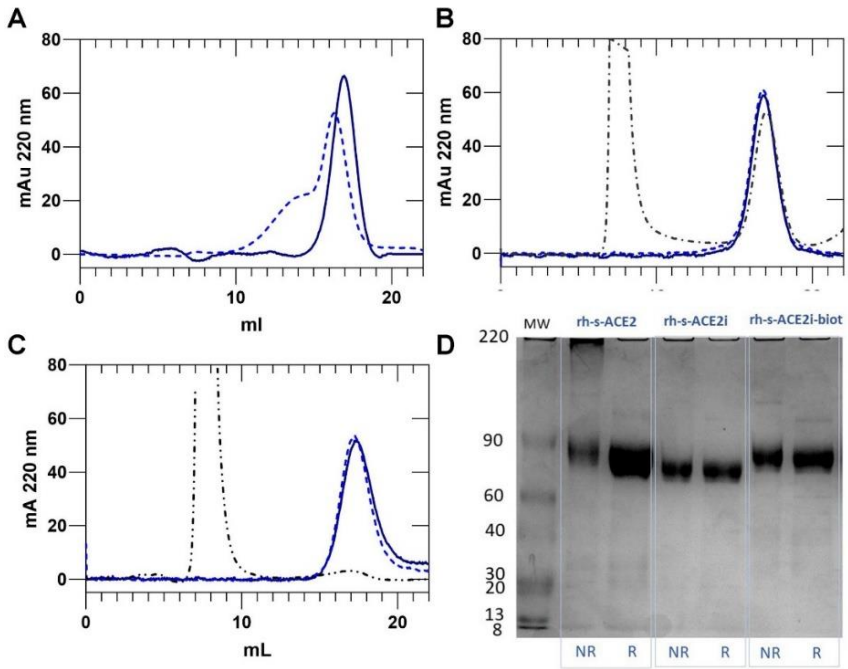

Figure 4.1 Gel permeation chromatograms and SDS-Page analysis of different rh-s-ACE2 products. A) rh-s-ACE2**, B)** rh-s-ACE2i and **C)** rh-s-ACE2i-biotin, as prepared (full line) and after 24 h storage at 4°C in PBS buffer (dashed lines). Rh-s-ACEi reacted with biotin-C6-NHS and rh-s-ACE2i-biotin were also analyzed after mixing with ANANAS (ACE2:NP = 30 mole:mole) (dash-dot lines). Only if biotinylated the protein binds to ANANAS and elutes

together with the nanoparticle fraction with a retention volume of about 8 mL; **D)** SDS-PAGE (4-15%) analysis of the different rh-s-ACE2 products after 24 h storage at 4°C, conducted in reducing (R) and non-reducing (NR) conditions. The expected protein (MW ~ 69500 Da) displays a band at around 70 kDa. The high MW smeared signal in the NR rh-s-ACE2 sample corresponds to protein multimers, which are reverted to the expected monomeric protein by the reducing (R) treatment.

ACE:ANANAS pre-formulation

Pre-formulation studies were carried out to quantify the loading capability of the NPs for *rh-s-ACE2i-biotin* and to assess the colloidal stability of the multimerized system as a function of ACE2 density at the NP surface. To assess the NP capability for *rh-s-ACE2i-biotin*, the protein was mixed with ANANAS at molar ratios varying between 15-120. Mixtures were analyzed by dynamic light scattering (DLS) and gel permeation chromatography to evaluate the size of the assemblies and the amount of NP-bound/unbound rh-s-ACE2-biotin, respectively. In addition, ʒ-potential measurements were carried to measure the effect of ACE2 loading onto the NP surface charge. Core nanoparticles displayed a size of about 114 nm and a rise in size up to about a maximum of 128 nm was observed by increasing the ACE2:NP in solution (Figure 4.2A). This increment is compatible with the build-up of a ~7 nm monolayer of rh-s-ACE2 around core nanoparticles, in line with the protein dimensions registered by X-ray crystallography.[36] NP size increase was proportional to the amount of rh-s-ACE2i-biotin in solution up to ACE2:NP ratio = 30; no further size increment was registered at higher molar ratios. On the other hand, ʒ-potential measurements and gel permeation chromatography (Figure 4.2B) collectively indicate that the NP capacity for *rh-s-ACE2i-biotin* is greater than 30. In fact, while NPs display (in PBS) a neutral to slightly negative surface charge (-15.43 mV), the ʒ-potential becomes systematically less negative as the ACE2:NP ratio increases, reaching a plateau at 60 ACE2:NP. In line with these data, gel permeation chromatograms of mixtures obtained at increasing ACE2:NP ratio reveal that the number of rh-s-ACE2i-biotin units bound/NP is 30, 53 and 71 at ACE2:NP ratios in solution of 30, 60, or 90, respectively (Fig. 4.2C and D). Overall, these data demonstrate that a maximum nanoparticle capacity for rh-s-ACE2i-biotin between 60 and 90, consistent with what previously found with biotin ligands of similar molecular weight.[19]

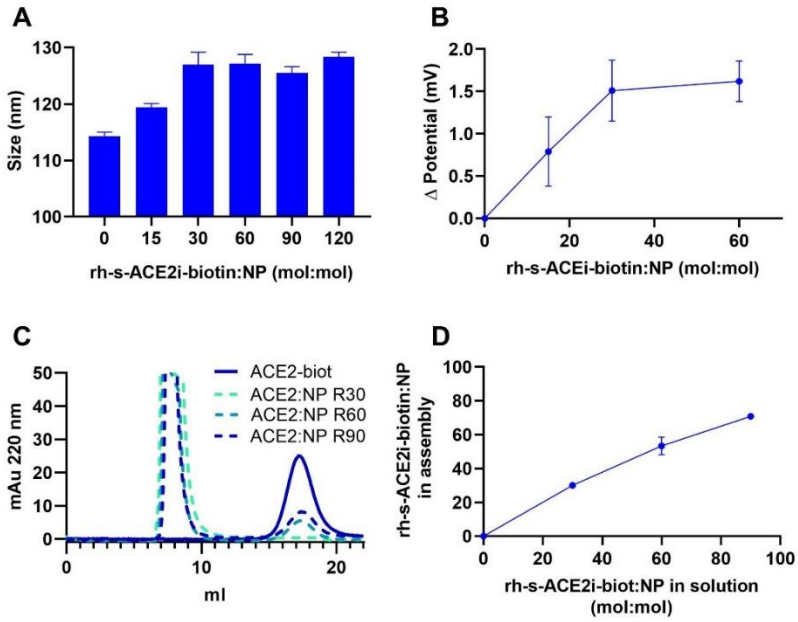

Figure 4.2 Pre-formulation studies. A) Size of rh-s-ACE2i-biotin:ANANAS assemblies at ACE2:NP molar ratio in solution between 15 and 120; **B)** Assemblies Z-potential as a function of rh-s-ACE2i-biotin:NP molar ratio in solution mixture. Values were measured in PBS buffer, where core ANANAS exhibit a slightly negative value of -15.43 mV; **C)** Gel permeation chromatograms of rh-s-ACE2i-biotin (5 µg/run) as such or when mixed with ANANAS at molar ratios ACE2:NP equal to 30, 60 and 90. The peak at retention volume of about 17 mL corresponds to the free protein, the peak at 8 mL corresponds to the nanoassembly; **D)** Number of rh-s-ACE2i-biotin molecules linked onto the NPs as a function of the ratio of ACE2i-biotin:NP in solution mixtures. Values were calculated from the chromatograms of panel C by comparing the areas of the rh-s-ACE2i-biotin peak in the assembly mixtures with that of the protein in the absence of the nanoparticles.

The affinity of rh-s-ACE2i-biotin for SARS-CoV-2 RBD is affected by its multimerization onto the ANANAS core

We investigated if and how the multimerization of ACE2 on the nanoparticles and the density of its packing affect its ability to recognize the Spike protein RBD. To this end, the interaction between rh-s-ACE2i-biotin and RBD was studied using an ELISA assay in which plate-immobilized RBD (Wuhan and Omicron: BA.1) was incubated with serial dilutions of rh-sACE2i-biotin in either monomeric form - as such or complexed with avidin (ACE2:avi =1:1 mole:mole) - or multimerized onto ANANAS at different surface densities. Assemblies were tested at up to a maximum of 60 molecules/NP (ACE2:NP = 15, 30 and 60 mole:mole – ACE2:NP-R15, ACE2:NP-R30, ACE2:NP-R60), namely the

highest molar ratio in solution which led to almost quantitative loading of the soluble protein onto the NP so that no need for purification to remove the unbound fraction was necessary prior to testing. The results (Figure 4.3) showed that, despite the presence of the C-terminal biotin tag and iodoacetamide thiol capping, rh-s-ACE2i-biotin maintains high affinity for RBD. The dissociation constants were in the nanomolar range (Wuhan: Kd = $1.34x10^{-9}M^{-1}$, Omicron Kd = $6.57\ x10^{-9}M^{-1}$) in agreement with the literature.[37] Despite the documented higher infectivity of the Omicron variant, the affinity recorded for its RBD variant (BA.1) was almost 5 times lower than the original variant, in agreement with what measured by other authors through a reverse ELISA assay (plate-immobilized RBD added of serial dilution of ACE2).[38]

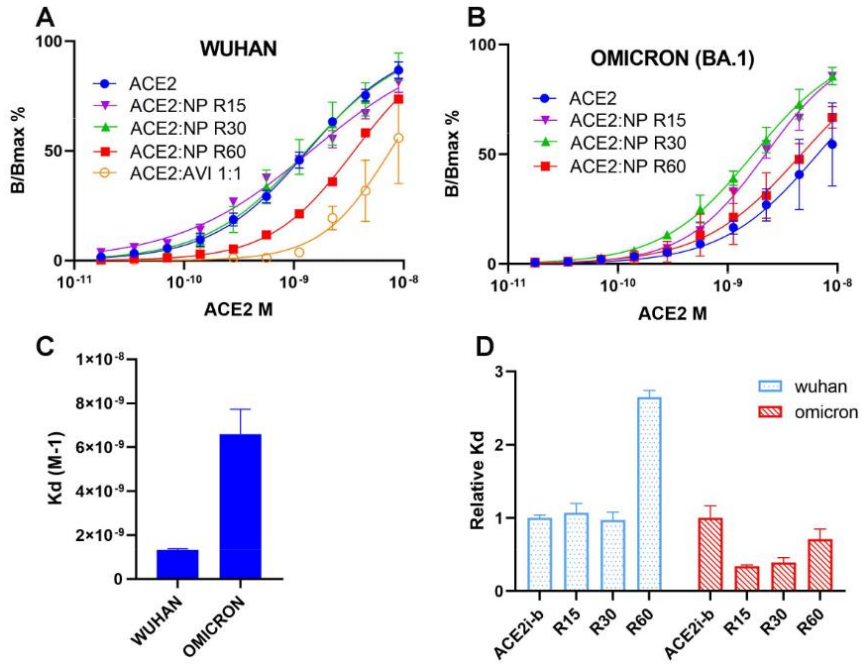

Figure 4.3 Affinity of rh-s-ACE2-biotin in solution or multimerized onto the NP surface. Representative curves of binding to RBD of rh-s-ACE2-biotin in free form, and multimerized onto the surface of nanoparticles at ACE2:NPs molar ratios between 15:1 and 60:1 measured by ELISA; **A)** Wuhan, **B)** Omicron variants, **C)** Dissociation constants calculated from the ELISA curves; **D)** dissociation constants of the rh-s-ACE2i-biotin:RBD interaction for ACE2i differently formulated relative to the protein in solution. An R value >1 indicates lower affinity. Kds were computed using the GraphPad-Prism® software and the one site specific binding equation. Data indicate mean ± SD of 2-4 independent experiments each performed in duplicate.

The rh-s-ACE2i-biotin: RBD interaction is negatively affected (Kd = $7.57x10^{-9}$M - Wuhan RBD only) by complexation of rh-s-ACE2i-biotin with monomeric avidin. This effect may be due to electrostatic repulsion, since both avidin[39] and RBD[40] are positively charged at neutral pH. Accordingly, this negative effect was not seen when rh-s-ACEi-biotin was complexed with the avidin in the nanoparticles, which have a net negative charge (in ANANAS the positive charge of avidin is neutralized by the nucleic acid of the nucleating plasmid).

More interestingly, the interaction is affected by the ACE2 packing density at the NP surface, with some differences and similarities amongst the two RBD variants. In the case of less densely packed ACE2:NP-R15 and ACE2:NP-R30 assemblies, the ACE2:RBD affinity was similar to that of the free molecule for the Wuhan variant, and higher for the BA.1 Omicron. Consistently for both RBDs, the highest ACE2 surface density tested (ACE2:NP-R60) showed the lowest affinity amongst the nanoassembled series.

rh-s-ACE2 inhibits SARS-CoV-2 infection more efficiently when multimerized onto the ANANAS core

To test if and how any of the different ACE2:NP formulations exerted antiviral activity against the SARS-CoV-2 virus, we used the Wuhan variant of the virus and studied its infection in Calu-3 cells. Calu-3 is a human lung epithelial cell line that expresses both the ACE2 receptor and the TMPRSS2 cofactor on the cell membrane and, thereby, is susceptible to SARS-CoV-2 infection.[3] We incubated the SARS-CoV-2 virus with the recombinant biotinylated ACE2 (*rh-s-ACE2i-biotin*) or different ACE2:NP formulations for 10 minutes prior to infection of Calu-3 cells. Thirty h post infection, which is the time required for the virus to complete the first round of replication,[41] we measured the amount of newly infectious viruses produced, using vehicle-treated virus as control. We used multiplicity of infection (MOI) of 0.1, which, in our assays corresponded to $2.75x10^{3}$ infectious particles. This assay allowed us to compare the viral progeny produced by a fixed number of infectious particles, treated or untreated with the soluble ACE2 or the ACE2:NP formulations, upon infection of Calu-3 cells. We measured to which level the soluble-ACE2- or the ACE2:NP-treated virus impaired infection of

human cells by measuring the amount of newly infectious virus produced after the first viral replication cycle, compared to vehicle-treated (control) virus.

First, we evaluated the inhibitory effect of increasing concentrations (0.025-2.5 µg/ml) of soluble *rh-s-ACE2i-biotin* on the SARS-CoV-2 infection of Calu-3 cells (Figure 4.4A). Under these conditions, *rh-s-ACE2i-biotin* reduced the SARS-CoV-2 infectious cycle in a dose-dependent manner, reducing the viral titre by up to 33% at the highest tested concentration (i.e. 2.5 µg/ml). These data are consistent with a recent report[6] and also in line with the ELISA results obtained when challenging the SARS-CoV-2 RBD with the *rh-s-ACE2i-biotin*. We further investigated the efficacy of the *rh-s-ACE2i-biotin* coupled to ANANAS nanoparticles in inhibiting the SARS-CoV-2 infectious cycle. We tested different ACE2:NP ratios (i.e. 15, 30 and 60) and obtained a very strong viral inhibition when using ACE2:NP-R30, which displayed the best antiviral activity (91.5 % of virus reduction). Also ACE2:NP-R60 displayed a good potency, albeit less (80 % of virus reduction) than ACE2:NP-R30 (Figure 4.4B).

Of note, rh-s-ACE2i multimerization on the ANANAS nanoparticles improved inhibition of the SARS-CoV-2 infection by about 10-fold, with respect to the use of the soluble monomeric protein. We observed no antiviral activity when we incubated core nanoparticles with the virus prior to viral infection, indicating that the antiviral effects depended on the presence of ACE2 on the surface of the ANANAS nanoparticles. We next measured the antiviral activity on both Wuhan and Omicron variants at increasing concentrations of ACE2:NP-R30 (Figure 4.4C) up to a maximum 5 µg/mL in ACE2 titer and obtained a dose-dependent reduction. In the case of the Wuhan variant, the maximum efficacy was reached at 2.5 µg/mL, with no additional effect at higher concentrations (about 80% inhibition at both 2.5 and 5.0 µg/mL). In case of the omicron Variant (Figure 4.4D) the efficacy was slightly superior: the Omicron infectious cycle was hampered up to 92% at the highest ACE2:NP-R30 dose tested, confirming the high antiviral potential of ANANAS coupled to the ACE2 receptor in the impairment of SARS-CoV-2 virus.

In parallel, we observed that the nanoparticles neither alone nor coupled to *rh-s-ACE2i-biotin* (at 30 and 60 ACE2:NP ratio) exhibited cytotoxic effects on human cells (data not

shown), indicating that the observed antiviral effect depends on the effect of ACE2:NP on the SARS-CoV-2 virus.

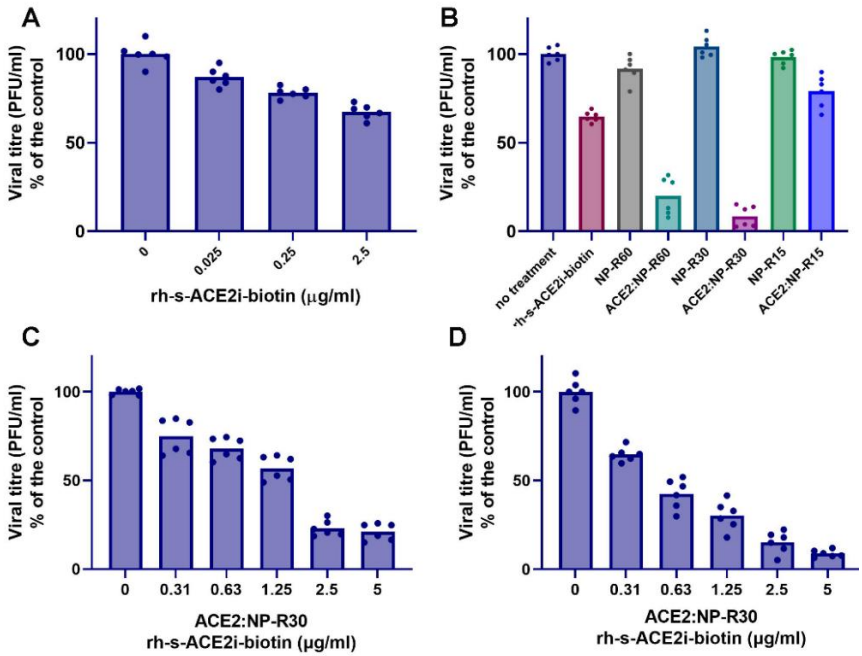

Figure 4.4 Inhibition of SARS-CoV-2 infectivity by monomeric and nanoassembled rh-s-ACE2i-biotin. A) Inhibition of SARS-CoV-2 infection in Calu-3 by rh-s-ACE2i-biotin in monomeric form as a function of its concentration. Infection (Wuhan variant) was performed at MOI (multiplicity of infection) of 0.1. The virus was pre-incubated for 10 minutes with rh-s-ACE2i-biotin prior to Calu-3 cells infection; **B)** Efficacy of inhibition of SARS-CoV-2 infection (Wuhan variant) by rh-s-ACE2i-biotin at 2.5 µg/mL in monomeric or multimerized form on the ANANAS core at different ACE2:NP molar ratios. To keep the concentration of ACE2 in the assay constant at 2.5 µg/mL, the concentration in nanoparticles was different in the different samples (12.9, 25.7 and 51.5 µg/mL for ACE2:NP-R60, ACE2:NP-R30 and ACE2:NP-R15, respectively). Non-functionalized nanoparticles were therefore tested as control at these three concentrations, together with rh-s-ACE2i-biotin at 2.5 µg/mL in monomeric form; **C/D)** Efficiency in viral (Wuhan/Omicron Variants) cycle inhibition of increasing ACE2:NP-R30 concentrations (0-5 µg/ml). Bars indicate the mean of n=2 biological replicates. Each condition was tested in triplicate per replicate. Individual data points are shown as dots.

We employed transmission electron microscopy (TEM) to directly visualize the effect exerted by the multimerized rh-s-ACE2i on the virus, (Figure 4.5). To this end, nanoassemblies and virus were mixed in buffer at the same ratio as for the infection inhibition experiments. Samples were then treated with PFA to inactivate the virus and

negatively stained with uranyl acetate. To confirm the identity of the poly-avidin based nanoparticles a second staining with biotinylated gold nanoparticles (5 nm) was performed. The virus alone shows the expected circular membrane structure, with a diameter of about 90 nm, surrounded by S' proteins. The ACE2:NP-R30 assemblies appear as toroids, in line with the shape of the 'core' NPs reported in the literature.[18] The addition of 30 rh-s-ACE2i-biotin molecules did not noticeably change the appearance of the NPs, in agreement with the colloidal stability demonstrated by the DLS data (Figure 4.2) The ACE2:NP-R30:virus mixture shows agglomerates in which several viral particles are "wrapped" within ANANAS-based multi-protein structures. Notably, the location of the NP:virus contact points are in line with the S' protein distribution at the viral surface.

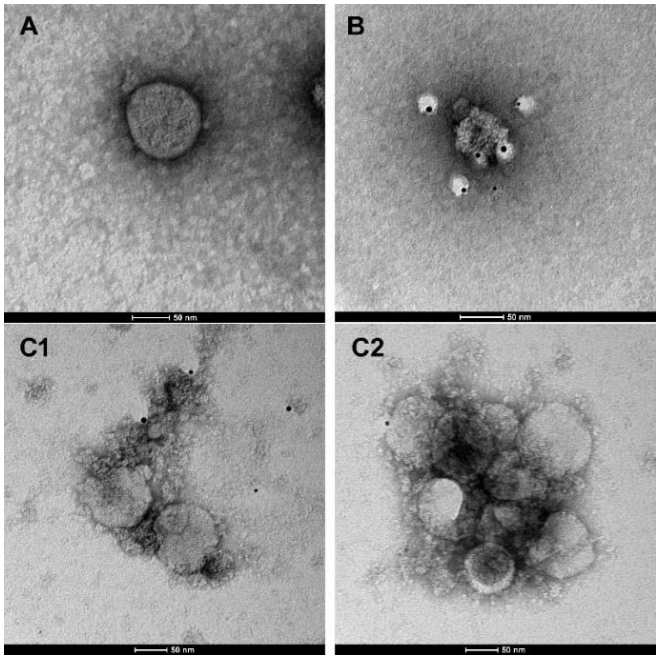

Figure 4.5 Transmission Electron Microscopy. Representative Images of **A)** SARS-CoV-2, **B)** the ANANAS:rh-s-ACEi2-30 (ACE2:NP-R30) nanoassembly and **C1/C2)** the mixture of SARS-CoV-2:ACE2:NP-R30 generated at PFU:NP molar ratio = 1:100. Samples were negatively stained with 1% uranyl acetate, followed by biotin-nanogold (5nm). The gold nanoparticles appear ad black dots.

Nasal instillation of the ACE2:ANANAS allows efficient and long lasting pulmonary localization

In humans, the SARS-CoV-2 has a peculiar tropism for the airway epithelial cells expressing the ACE2. Therefore, inhalation of the ACE2:NP nanodecoy could allow fast interaction with the virus and, therefore, reduce the symptoms due to the infection. The potentials of this approach depend on the ability of the nanoparticles to flow along the airways, trespass the surfactant barrier, penetrate in the lung parenchyma, and interact with resident macrophages without inducing acute toxicity. Based on these assumptions, we investigated the biodistribution of the nanoassemblies in healthy mice following nasal instillation by an *ex vivo* whole-organ measurement that furnishes a quantitative estimation of the ability of our formulations to reach the lungs. To this end, both ACE2:NP-R30 and non-functionalized ANANAS (ANANAS, used as controls) were fluorescently labelled by addition of biotin-C_6-alexa633 (10% of total BBS) as a tracking agent (data not shown). Their biodistribution was monitored for up to 72 h after a single nasal instillation by measuring the fluorescence from lungs collected from mice sacrificed at different timepoints after treatment with the two formulations.

Figure 4.6A shows the NPs' biodistribution in all selected organs after a single intranasal (i.n.) administration. The histograms of the NP-related fluorescent signal measured by IVIS (Figure 4.6B) reveal that signal associated with the nanoparticles rapidly reached the lungs with a peak of concentration at 15 minutes after administration and fades away very slowly, persisting for longer than 72 h. The fluorescence intensity registered in organs other than the lungs was about ten-fold lower, indicating that an almost selective tropism for this tissue can be obtained through this route of administration. No signal was detected in the spleen, while a small but detectable signal was observed in the kidneys of animals treated with ACE2:NP-R30. The measurement by IVIS confirmed this trend (Figure 4.6C and D). However, confocal microscopy did not reveal an accumulation of ACE2:NP-R30 in kidney parenchyma thus suggesting a transient flux due to their excretion (data not shown).

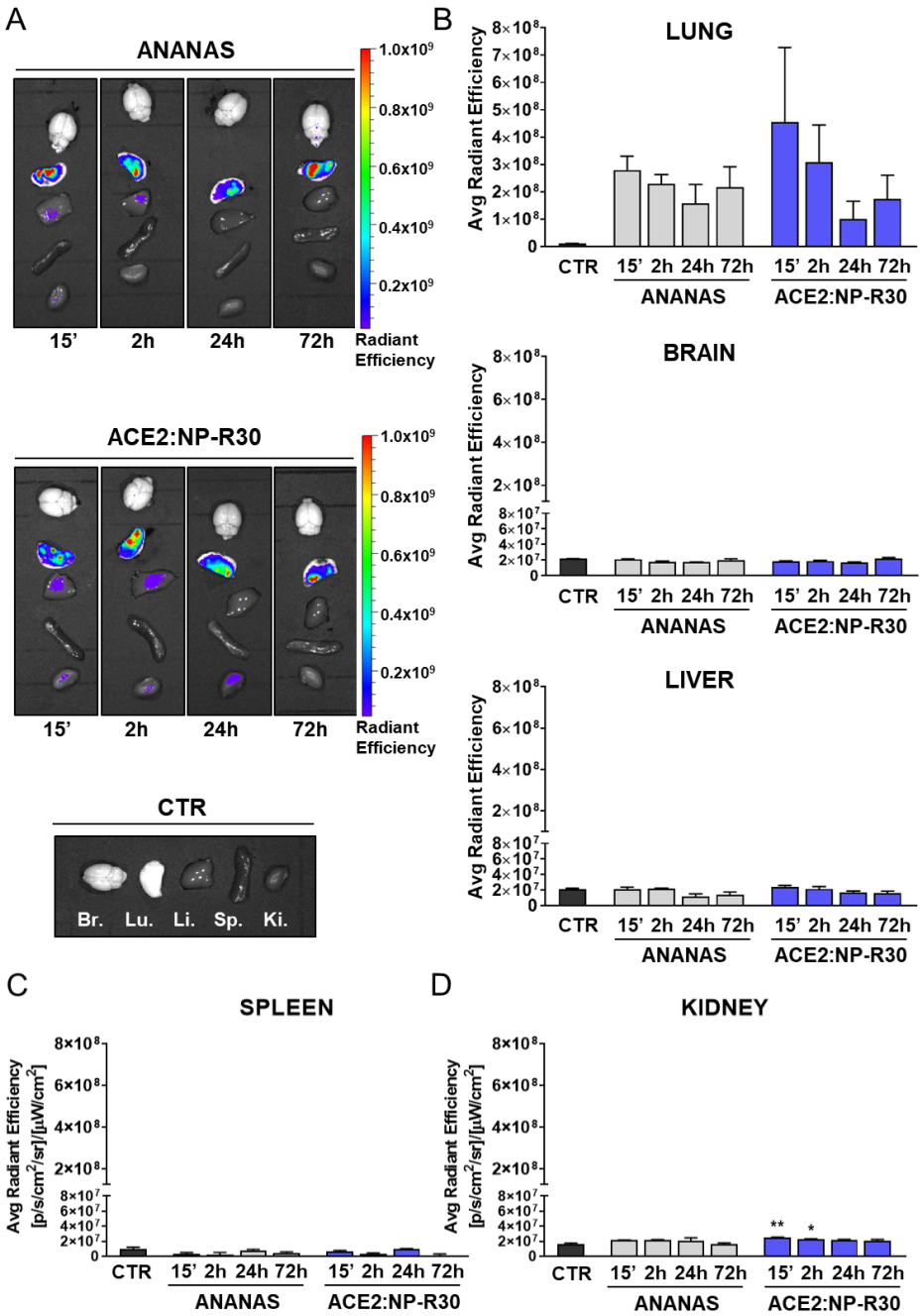

Figure 4.6 ***Ex vivo*** **imaging. (A)** Ex vivo optical imaging of excised organs from animals sacrificed 15', 2 h, 24 h and 72 h after vehicle, ANANAS, and ACE2:NP-R30 administration. Br. = brain, Lu. = lungs, Li. = liver, Sp. = spleen, Ki. = kidneys. **(B-C-D)** Quantification of ex vivo optical imaging signal. Data are reported as mean ± SE. The data were analyzed by One-way ANOVA using Dunnet's test. *$p < 0.1$, **$p \leq 0.01$. *= comparison between ANANAS or ACE2:NP-R30-treated and untreated (CTR) mice.

Confocal microscopy images (Figure 4.7) show that both formulations share the same pattern of penetration. The NP-associated signal (red) initially passes through the bronchioles, then spreads along the whole parenchyma, accumulates in the tissue macrophages (CD68 marker, green signal) and finally generates long lasting interaction with the alveolar vessels. A slight difference in the time-dependent pattern was observed between the groups. The ACE2 carrying nanoassemblies showed a faster and more extended distribution in the lung parenchyma, whereas the non-functionalized ones were up-taken from the macrophages more rapidly and had a more efficient passage in the endothelial cells. This could be due to the difference in the composition of the surfaces exposed by the two formulations. The higher magnified images (Figure 4.7, lower panel) show that the instilled nanoparticles localize in the bronchiolar area and rapidly penetrate the lung tissue. With time, a growing overlap of the NP related signal with that of the macrophages (yellow arrows) occurs, concurrent with progressive decrease of the NP-related signal in the lung parenchyma. Interestingly, at 72 h a particular localization of the Alexa633 (red) signal was found, which appears continuously distributed along the alveolar structures and at the periphery of the bronchioles, probably associated to NP degradation products. In fact, it is expected that once the protein-based ANANAS enter the lysosomes, they begin to lose their stability and to be proteolytically degraded. This process is likely to lead to progressive unravelling of the original NP structure and separation of the various NP components. The latter may be washed out of the tissue or captured by cell/tissue components, in any case changing their local environment. To investigate this phenomenon, we performed immunofluorescence staining of lung tissue samples from animals sacrificed 24h and 72h after inhalation with an anti-PEG antibody to visualize the biotin-PEG component of the core NPs (which is added for colloidal stabilization).[17]

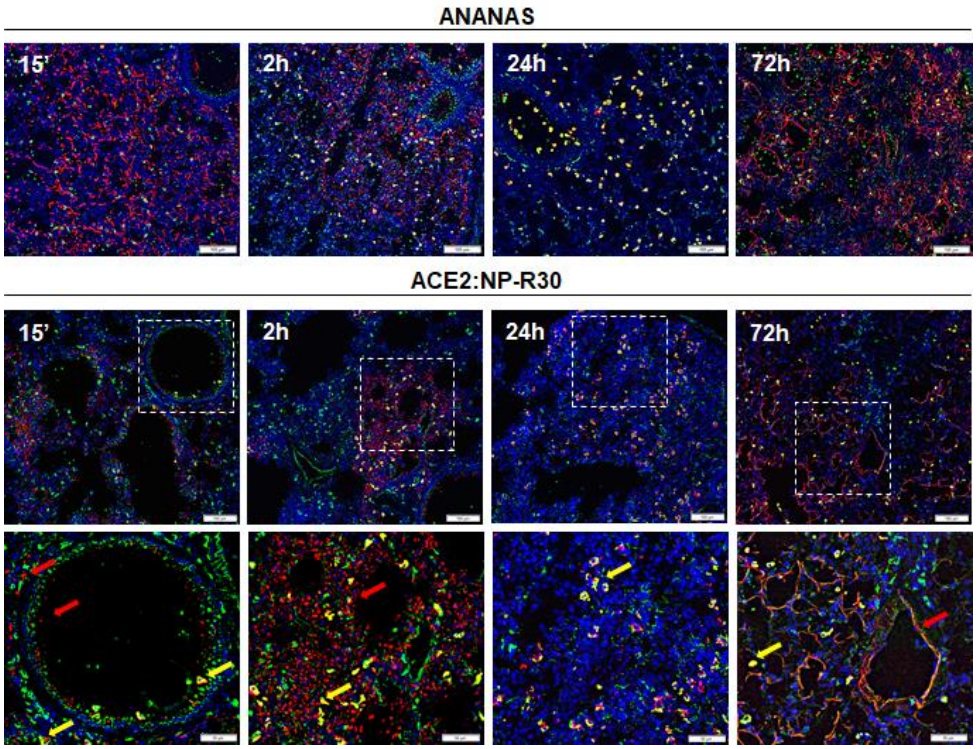

Figure 4.7 Nanoparticles localization in tissues. Representative images of the tissue distribution of ANANAS or ACE2:NP-R30 in lungs 15', 2, 24 and 72 h after treatment. The blue signal refers to the nuclei (Hoechst 33258 staining), green corresponds to the lysosomal component of macrophages (CD68 Antibody, Serotec 1:200), red is associated with the alexa633 dye linked to the NPs, yellow corresponds to co-localized red and green signals. Scale bar=100µm. In the lower panel, representative images of higher magnification (15X) of lungs for each timepoint (yellow arrows: nanoparticles co-localized with macrophages, red arrows: nanoparticles alone). Scale bar=50µm

The results (Figure 4.8) showed co-localization of biotin-C6-alexa633 and biotin-PEG at 24 h but not at 72 h post-administration, confirming that the NP structure was no longer preserved at the latest time point. Notably, the loss of NP integrity may be responsible for the slight increase in the biotin-C6-alexa633-related signal observed by IVIS in the lung at 72 h (Figure 4.6B), as it is known that the fluorescence of the dye is quenched when close to the ANANAS core[23] due to the presence of the aromatic amino acid residues within the avidin-biotin binding pocket.

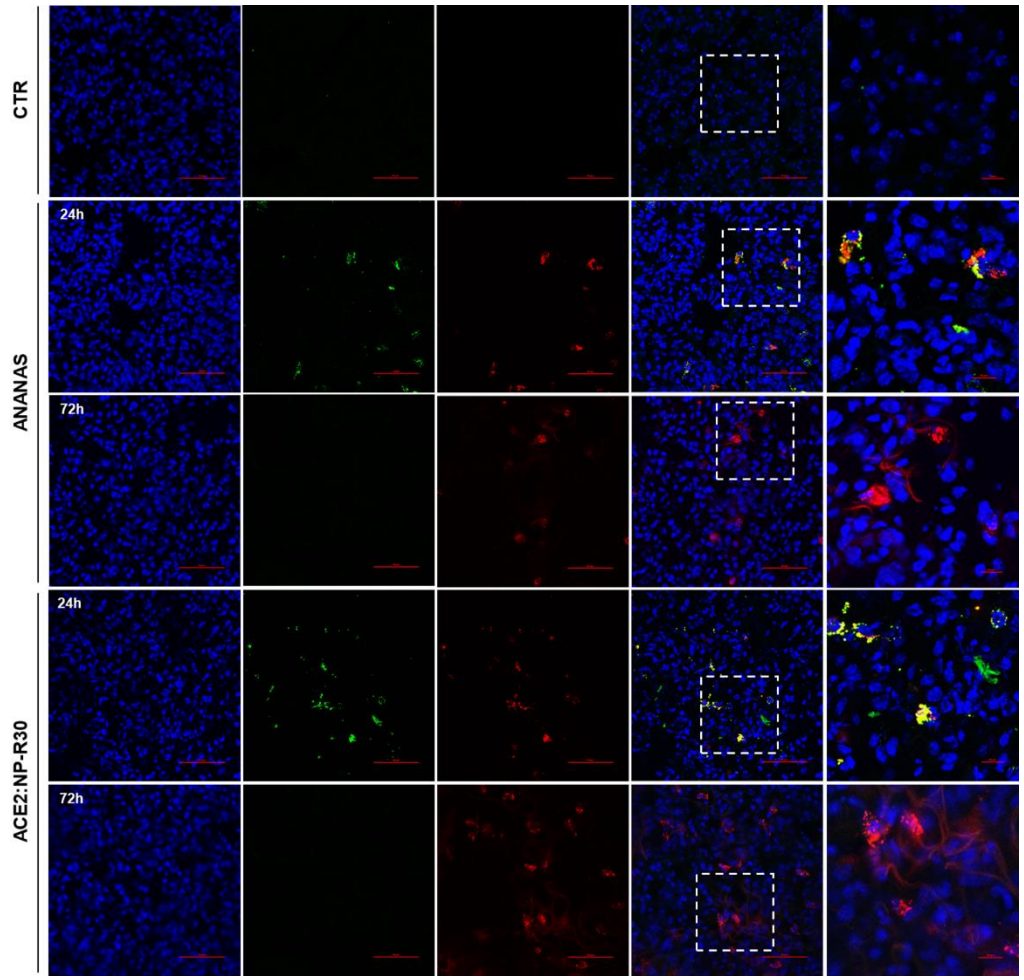

Figure 4.8 Nanoparticles degradation in lungs. Representative confocal images (60X) of the tissue distribution of vehicle (CTR), ANANAS or ACE2:NP-R30 in lungs 24 and 72 h after treatment. The blue signal refers to the nuclei (Hoechst 33258 staining), green corresponds to PEG (PEG Antibody, Abcam 1:165), red is associated with the Alexa633 dye linked to the NPs. Scale bar=50μm. Higher magnified pictures are reported in the far-right panels. Scale bar=10μm.

Nanodecoy Pulmonary Localization shows no hallmarks of inflammation or toxicity

Figure 4.9A shows representative images of the histopathological analysis of lung parenchyma processed with H&E from untreated mice or treated with ANANAS/ACE2:NP-R30 and sacrificed 15', and 2, 24, and 72 h after treatment. No relevant hallmarks of inflammation, alveolar damage or other tissue alterations were observed at all timepoints in the pathogen-free immunocompetent mice. No differences

between sections from vehicle- and ANANAS/ACE2:NP-R30- treated animals were detected, ruling out treatment-related pathological changes. The same profile of safety was observed in kidneys (Figure 4.9B).

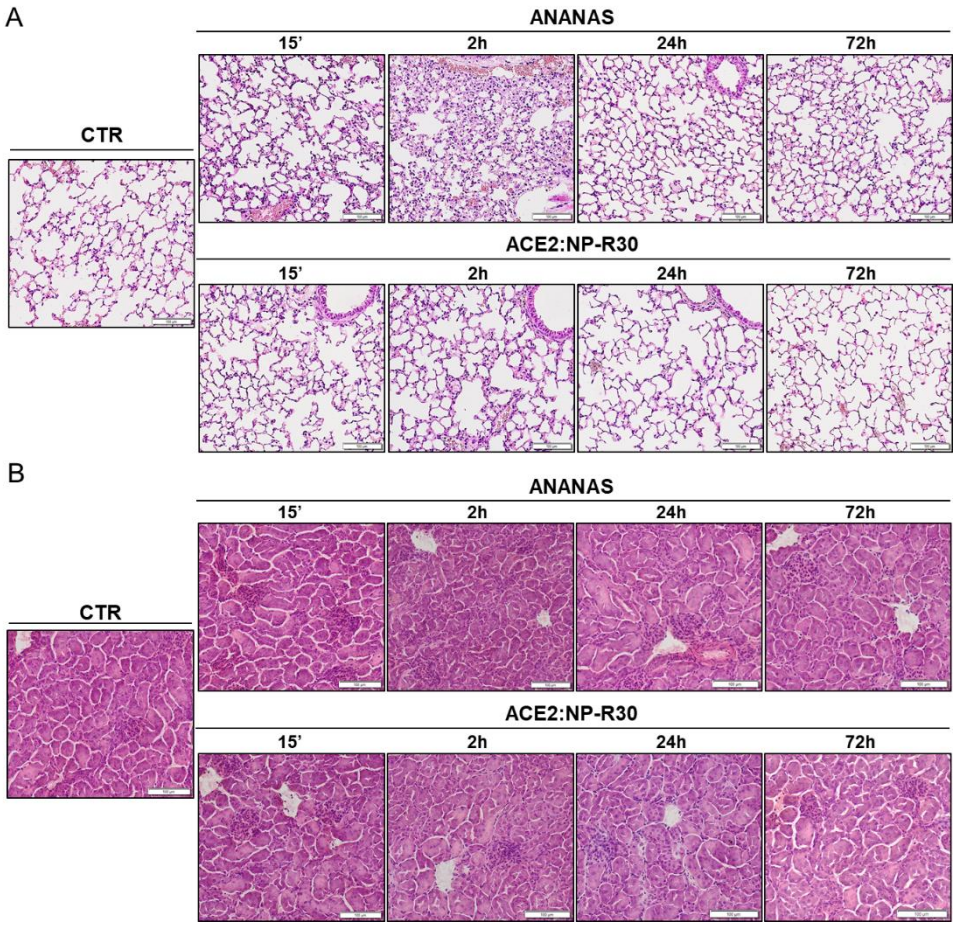

Figure 4.9 Histological evaluation. Hematoxylin and eosin staining of **A)** lungs and **B)** kidneys of mice treated with vehicle (CTR), ANANAS and ACE2:NP-R30 and sacrificed 15', 2, 24, and 72 h after the treatment. Scale bar=100μm.

ANANAS contain a non-coding plasmid DNA of bacterial origin, and therefore its unmethylated CpG sequences, even if masked by the avidin tightly bound to the nucleic acid, could potentially be recognized by TLR9 and activate the NF-κB mediated pro-inflammatory pathway.[42] To rule out this possibility, the levels of several pro-inflammatory cytokines (IFN-γ and TNF-α) and an anti-inflammatory cytokine (IL-10)

were measured using an AlphaLISA assay (Figure 4.10). Neither nanoformulations induced relevant changes in the cytokine levels compared to the untreated mice.

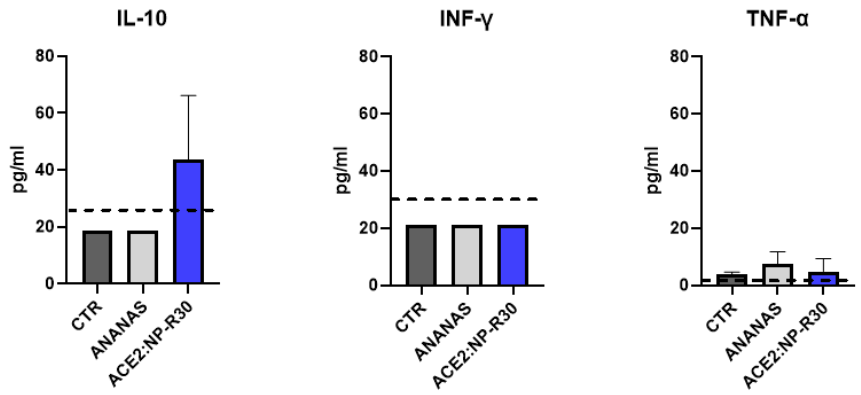

Figure 4.10 Cytokine analysis in serum of untreated and treated animals. **A)** IL-10, **B)** INF-γ, and **C)** TNF-α concentrations were measured in serum samples from treated animals and controls 72h after ANANAS or ACE2:NP-R30 administration. LDL = low detection limit (dotted line). Data are reported as mean +/- SD. Statistical analysis was performed by One-way ANOVA, followed by Tukey post-hoc test. No differences were found comparing ANANAS or ACE2:NP-R30 with CTR mice, or directly comparing the two nanoformulations.

Overall, these data indicate that the intranasal administration of these formulations to healthy mice does not stimulate an inflammatory response at least over the period of our analysis (72 h), confirming the evidence of lack of toxicity.

4.4 Concluding remarks

The possibility of using a protein-based nanoparticle system to generate an effective semisynthetic multimeric ACE2 nanodecoy capable of preventing SARS-CoV-2 infection was demonstrated. Efficacy was achieved without the use of a lipid membrane for receptor anchorage, as otherwise necessary in vesicle-based nanodecoys.

In our conditions, the optimized assembly was able to prevent 80-90% of infectivity within a few minutes of viral contact, at ACE2 nanomolar concentration and with more than 10-fold higher efficacy than the soluble protein. The fact that efficacy is maintained throughout both Wuhan and Omicron variants confirms that this approach can bypass virus mutations and suggests that this strategy could be a valid add-on to the use of monoclonal antibodies.

By taking advantage of the ease of composition modulation allowed by this nanotechnology platform we were able to screen composition/efficacy relationships. Indeed, while the use of ACE2 multimer-based nanodecoys and their effectiveness in inhibiting/preventing viral infections has already been demonstrated in the literature using a number of nanoparticle geometries,[43] as of today there was no indication as to if and to which extent receptor density at the nanoparticle surface affects efficacy. This is a fundamental information in case one seeks to bring the semisynthetic nanodecoy product towards clinical translation.

To study composition/function relationships using this polyavidin platform, it is necessary to use well-defined monomeric biotinylated building blocks. In our hands, the recombinant ACE2 ectodomain produced following established protocols[30,32] did not fulfill this requirement, both because it proved to be hard to biotinylate by chemical means and for its instability to disulfide – driven polymerization. Aggregation occurred even though this fragment does not to contain the ferredoxin-like fold domain (Neck-domain) that determines dimerization of the native receptor at the cell membrane.[44] However, the recombinant ACE2 ectodomain produced contains two free cysteine residues partially exposed to the protein surface (i.e., Cys261 and Cys498), which likely drive this process. Since information on rh-s-ACE2-biotin conjugates commercially available did not guarantee the absence of multimers, we decided to carry out enzymatic biotinylation and 'block' the recombinant product cysteines along the purification step by iodoacetamide. This strategy proved to be effective, as rh-s-ACE2i-biotin, besides being stable as a monomer, also maintained high affinity for the RBD.

Pre-formulation studies demonstrated that a) the rh-s-ACE2i-biotin can be tethered efficiently to ANANAS, b) the ACE2:NP assemblies are colloidally stable and c) each nanoparticle can accommodate more than 60 ACE2i-biotin units. However, the data also indicate that above the ACE2:NP molar ratio of 30 it is difficult for the biotin-protein to reach the nanoparticles surface, likely because of some crowding effect. In line with this interpretation, while the loading test performed at ACE2:NP ratio in solution = 90 revealed that at least 71 rh-s-ACE2i-biotin molecules can be linked to the NPs, at ACE2:NP ratio of 60, about 10% of the rh-s-ACEi-biotin molecules remained in solution. The fact that non-quantitative binding of biotin-rh-s-ACE2i occurs at

ACE2:NP > 30 but below the saturation limit suggests some difficulty in the avidin/biotin interaction at high rh-s-ACE2i packing densities. This is probably due to the relatively short BAP spacer between the protein and biotin moieties. Previous work describing the use of the ANANAS platform always showed quantitative binding of relatively bulky biotinylated moieties (e.g. proteins, polymers and peptides[19,21,22]) when added below their saturation limit. In these cases, the spacer between the biotin and the cargo was always a long (5kDa) PEG spacer, which is likely to allow efficient spacing of molecules around the NP core. It is possible that the short BAP spacer does not permit efficient spacing between the different rh-s-ACE2i-biotin units and therefore "forces" them to bind to the nanoparticle with a 'rigid' configuration. This would imply that above a certain surface density, ACE2 packing would occur without changing the thickness of the monolayer and, therefore, the hydrodynamic volume. This is consistent with the finding that no increase in size was registered by DLS between ACE2:NP 30 and 60, despite both gel permeation chromatography and zeta potential measurements indicated an increase in loading.

Even more importantly, our infectivity studies clearly showed that a) ACE2 density at the nanodecoy surface does make the difference and b) there is no univocal correlation between ligand surface packing and efficacy. In fact, in the antiviral tests ACE2:NP-R30 outperformed both the more and less densely packed R60 and R15 assemblies.

To understand whether affinity or avidity issues are responsible for these differences we compared the infectivity data with the affinity information gathered by ELISA. Both assays suggest that excessive ACE2 surface density has a negative impact on potency. In fact, the R60 assembly was less effective than the R30 in preventing viral infection and the affinity for RBD of the ACE2i assembled on it was less than when assembled at R30. This negative effect could be due to a distortion of the protein conformation due to excessive surface crowding, in agreement with the rigid conformation hypothesis derived from the pre-formulation studies. On the other hand, while the ACE2i:RBD affinity was similar when the ACE2i ligand was assembled at the R15 and R30 ratios, ACE2:NP-R15 proved to be much less effective than ACE2:NP-R30 from the point of view of the antiviral activity. This fact cannot be explained with affinity or crowding effects and suggests that there is a geometric/spatial requirement for optimal interaction

of the virus surface with the multimerized ACE2i nanodecoy. In this respect, the number of spikes/virion (Wuhan) is about 27, with a surface density of 1 molecule/1000 nm^2.[45] Earlier works have shown that the surface area onto the ANANAS nanoparticles available for binding biotinylated macromolecules is dictated by steric factors and is of about 6000 nm^2.[19] Therefore, 30ACE2i/assembly correspond to a surface density of about 1 molecule/200nm^2. Accordingly, a Spike:ACE2 surface ratio of 1:10 (corresponding to a 1:1 molar ratio) seems to guarantee the optimal geometry for efficacy.

It should be noted that the ANANAS nanoparticles primarily display a toroidal shape, which derives from the condensation of a circular plasmid DNA.[18] The coiling of this DNA promoted by the adsorption of avidin, is the most favored energetically; however, other more extended shapes are possible (see also S.I.), particularly if there is an energy gain. For example, this may occur when ligand-decorated (e.g. ACE2i) nanoparticles are exposed to surfaces covered with ligand baits (e.g. the S' protein on SARS-CoV-2 or the RBD decorated ELISA plate). Indeed, in the virus/ACE2:NP-R30 mixtures shown by the TEM images the nanoparticles appear as partially uncoiled filaments surrounding the virus. It is possible that in the presence of the virus the ACE2:toroidal nanoparticle disentangles and wraps around it with the ACE2 moieties interacting with the S' protein. Accordingly, the possibility to engulf all S' proteins (and therefore act as effective decoy) depends on the distance between the ACE2 moieties, justifying the spatial requirement observed experimentally.

While the overall data suggest that when both ligand and receptor are immobilized on solid surfaces, there is a relationship between the two elements spatial organization and recognition efficacy, the question remains as to *whether the relationship identified with the ACE2-ANANAS:SARS-CoV-2 system can be of general value* and can be transferred also to other multimeric nanodecoys. In fact, it is likely that the geometry (e.g. curvature radius) of the nanodecoy and its composition (e.g. lipid membrane vs polymer/protein interface) may play additional roles. Therefore, even if we could expect that ACE2 surface density may affect the potency of all ACE2 based nanodecoys, nanoparticles with geometries/compositions different than ANANAS may respond to different composition/efficacy rules.

The *in vivo* biodistribution and preliminary toxicology studies demonstrated that the ACE2:NP-R30 is safe and is capable of reaching the deep lung very rapidly by a simple inhalation. Its antiviral efficacy *in vivo* can depend on the ability of the nanoparticles to reach locations where the virus preferentially localizes, namely the lung parenchyma and its macrophages, which are at the forefront of the host immune-defense. Although *in vivo* efficacy studies are necessary, given the rapidity with which the assemblies reach the parenchyma and the slow remotion by the macrophages, it is reasonable to assume that they could provide protection against viral invasion, similar to other ACE2 multimer nanodecoys described in the literature that had shown similar efficacy *in vitro*. Another question is *how long this protection would* last after inhalation. The fluorescence signal associated with the assembly remains in the lungs for up to 72 h. However, while at 2 h and 24 h the histology data clearly show that the NPs are present in both the parenchyma and macrophages, at the late time point analyzed (72 h) the fluorescent signal is more likely due to NP degradation products, which may no longer be active. As a general methodological note, it is important to recognize that the sole organ fluorescent intensity data may not be sufficient to predict the duration of efficacy and should be complemented by sub-localization studies to ascertain the nanoparticles fate.

We herein showed that the optimized semisynthetic protein-based ACE2:ANANAS assembly is a potent tool capable to counteract SARS-CoV-2 infection. The combined in vitro, biodistribution and preliminary toxicity data suggest that ANANAS based nanodecoys can be administered by inhalation and may provide protection from infection for at least 2-24 h, without acute toxic effects. The poly-avidin platform used here is versatile and rapidly scalable. In principle, it could be easily adapted to generate nanodecoys against other viruses. With its safety profile demonstrated also in other contexts, its versatility and ease of preparation, this platform could become a useful tool to counteract pandemics and complement other preventive/pharmacological approaches.

From a more general perspective, the results demonstrate that semisynthetic nanoparticles lacking a fluid lipid-based membrane for receptor anchorage can be used as scaffolds to generate antiviral nanodecoys. In addition, we showed that the density of the recognition element at the decoy surface is important in defining its efficacy,

suggesting that this parameter should be monitored along the optimization of any decoy systems, independently of the scaffold employed for receptor multimerization.

References

1. Wei, X. *et al.* T-Cell-Mimicking Nanoparticles Can Neutralize HIV Infectivity. *Advanced Materials* **30**, 1802233 (2018).
2. Hendricks, G. L. *et al.* Sialylneolacto-N-tetraose c (LSTc)-bearing Liposomal Decoys Capture Influenza A Virus. *Journal of Biological Chemistry* **288**, 8061–8073 (2013).
3. Hoffmann, M. *et al.* SARS-CoV-2 Cell Entry Depends on ACE2 and TMPRSS2 and Is Blocked by a Clinically Proven Protease Inhibitor. *Cell* **181**, 271-280.e8 (2020).
4. Kuba, K. *et al.* A crucial role of angiotensin converting enzyme 2 (ACE2) in SARS coronavirus–induced lung injury. *Nat Med* **11**, 875–879 (2005).
5. Caputo, I. *et al.* Angiotensin II Promotes SARS-CoV-2 Infection via Upregulation of ACE2 in Human Bronchial Cells. *IJMS* **23**, 5125 (2022).
6. Monteil, V. *et al.* Inhibition of SARS-CoV-2 Infections in Engineered Human Tissues Using Clinical-Grade Soluble Human ACE2. *Cell* **181**, 905-913.e7 (2020).
7. Zoufaly, A. *et al.* Human recombinant soluble ACE2 in severe COVID-19. *The Lancet Respiratory Medicine* **8**, 1154–1158 (2020).
8. Kim, J. *et al.* Rapid Generation of Circulating and Mucosal Decoy Human ACE2 using mRNA Nanotherapeutics for the Potential Treatment of SARS-CoV-2. *Advanced Science* **9**, 2202556 (2022).
9. Higuchi, Y. *et al.* Engineered ACE2 receptor therapy overcomes mutational escape of SARS-CoV-2. *Nat Commun* **12**, 3802 (2021).
10. Zhang, L. *et al.* Engineered ACE2 decoy mitigates lung injury and death induced by SARS-CoV-2 variants. *Nat Chem Biol* **18**, 342–351 (2022).
11. Glasgow, A. *et al.* Engineered ACE2 receptor traps potently neutralize SARS-CoV-2. *Proc. Natl. Acad. Sci. U.S.A.* **117**, 28046–28055 (2020).
12. Xie, F. *et al.* Engineering Extracellular Vesicles Enriched with Palmitoylated ACE2 as COVID-19 Therapy. *Advanced Materials* **33**, 2103471 (2021).

13. Rao, L. *et al.* Decoy nanoparticles protect against COVID-19 by concurrently adsorbing viruses and inflammatory cytokines. *Proc. Natl. Acad. Sci. U.S.A.* **117**, 27141–27147 (2020).
14. Zhang, H. *et al.* Inhalable nanocatchers for SARS-CoV-2 inhibition. *Proc. Natl. Acad. Sci. U.S.A.* **118**, e2102957118 (2021).
15. El-Shennawy, L. *et al.* Circulating ACE2-expressing extracellular vesicles block broad strains of SARS-CoV-2. *Nat Commun* **13**, 405 (2022).
16. Wang, C. *et al.* Membrane Nanoparticles Derived from ACE2-Rich Cells Block SARS-CoV-2 Infection. *ACS Nano* **15**, 6340–6351 (2021).
17. Pignatto, M., Realdon, N. & Morpurgo, M. Optimized Avidin Nucleic Acid Nanoassemblies by a Tailored PEGylation Strategy and Their Application as Molecular Amplifiers in Detection. *Bioconjugate Chem.* **21**, 1254–1263 (2010).
18. Morpurgo, M., Radu, A., Bayer, E. A. & Wilchek, M. DNA condensation by high-affinity interaction with avidin. *J. Mol. Recognit.* **17**, 558–566 (2004).
19. Morpurgo, M. *et al.* Characterization of Multifunctional Nanosystems Based on the Avidin-Nucleic Acid Interaction As Signal Enhancers in Immuno-Detection. *Anal. Chem.* **84**, 3433–3439 (2012).
20. Morpurgo, M. *et al.* Detection of a fluorescent-labeled avidin-nucleic acid nanoassembly by confocal laser endomicroscopy in the microvasculature of chronically inflamed intestinal mucosa. *IJN* 399 (2015) doi:10.2147/IJN.S70153.
21. Facchin, S. *et al.* Discrimination between ulcerative colitis and Crohn's disease using phage display identified peptides and virus-mimicking synthetic nanoparticles. *Nanomedicine: Nanotechnology, Biology and Medicine* **13**, 2027–2036 (2017).
22. Bigini, P. *et al. In Vivo* Fate of Avidin-Nucleic Acid Nanoassemblies as Multifunctional Diagnostic Tools. *ACS Nano* **8**, 175–187 (2014).
23. Roncato, F. *et al.* Improvement and extension of anti-EGFR targeting in breast cancer therapy by integration with the Avidin-Nucleic-Acid-Nano-Assemblies. *Nat Commun* **9**, 4070 (2018).
24. Violatto, M. B. *et al.* Dexamethasone Conjugation to Biodegradable Avidin-Nucleic-Acid-Nano-Assemblies Promotes Selective Liver Targeting and Improves Therapeutic Efficacy in an Autoimmune Hepatitis Murine Model. *ACS Nano* **13**, 4410–4423 (2019).

25. Bubb, M. O. *et al.* Natural antibodies to avidin in human serum. *Immunology Letters* **35**, 277–280 (1993).

26. Petronzelli, F. *et al.* Therapeutic Use of Avidin Is Not Hampered by Antiavidin Antibodies in Humans. *Cancer Biotherapy and Radiopharmaceuticals* **25**, 563–570 (2010).

27. Fan, Y. *et al.* SARS-CoV-2 Omicron variant: recent progress and future perspectives. *Sig Transduct Target Ther* **7**, 141 (2022).

28. Chen, D.-Y. *et al.* Spike and nsp6 are key determinants of SARS-CoV-2 Omicron BA.1 attenuation. *Nature* **615**, 143–150 (2023).

29. Bruni, M. *et al.* Persistence of Anti-SARS-CoV-2 Antibodies in Non-Hospitalized COVID-19 Convalescent Health Care Workers. *JCM* **9**, 3188 (2020).

30. Chan, K. K. *et al.* Engineering human ACE2 to optimize binding to the spike protein of SARS coronavirus 2. *Science* **369**, 1261–1265 (2020).

31. Verma, V., Kaur, C., Grover, P., Gupta, A. & Chaudhary, V. K. Biotin-tagged proteins: Reagents for efficient ELISA-based serodiagnosis and phage display-based affinity selection. *PLoS ONE* **13**, e0191315 (2018).

32. Faravelli, S. *et al.* Optimized Recombinant Production of Secreted Proteins Using Human Embryonic Kidney (HEK293) Cells Grown in Suspension. *BIO-PROTOCOL* **11**, (2021).

33. Ramakrishnan, M. A. Determination of 50% endpoint titer using a simple formula. *WJV* **5**, 85 (2016).

34. Beckett, D., Kovaleva, E. & Schatz, P. J. A minimal peptide substrate in biotin holoenzyme synthetase-catalyzed biotinylation. *Protein Science* **8**, 921–929 (2008).

35. O'Callaghan, C. A. *et al.* BirA Enzyme: Production and Application in the Study of Membrane Receptor–Ligand Interactions by Site-Specific Biotinylation. *Analytical Biochemistry* **266**, 9–15 (1999).

36. Han, P. *et al.* Molecular insights into receptor binding of recent emerging SARS-CoV-2 variants. *Nat Commun* **12**, 6103 (2021).

37. Kumar, S., Karuppanan, K. & Subramaniam, G. Omicron (BA.1) and sub-variants (BA.1.1, BA.2, and BA.3) of SARS-CoV-2 spike infectivity and pathogenicity: A comparative sequence and structural-based computational assessment. *Journal of Medical Virology* **94**, 4780–4791 (2022).

38. Wu, L. *et al.* SARS-CoV-2 Omicron RBD shows weaker binding affinity than the currently dominant Delta variant to human ACE2. *Sig Transduct Target Ther* **7**, 8 (2022).
39. Livnah, O., Bayer, E. A., Wilchek, M. & Sussman, J. L. Three-dimensional structures of avidin and the avidin-biotin complex. *Proc. Natl. Acad. Sci. U.S.A.* **90**, 5076–5080 (1993).
40. Zhang, Z., Zhang, J. & Wang, J. Surface charge changes in spike RBD mutations of SARS-CoV-2 and its variant strains alter the virus evasiveness via HSPGs: A review and mechanistic hypothesis. *Front. Public Health* **10**, 952916 (2022).
41. Mautner, L. *et al.* Replication kinetics and infectivity of SARS-CoV-2 variants of concern in common cell culture models. *Virol J* **19**, 76 (2022).
42. Cornélie, S. *et al.* Direct Evidence that Toll-like Receptor 9 (TLR9) Functionally Binds Plasmid DNA by Specific Cytosine-phosphate-guanine Motif Recognition. *Journal of Biological Chemistry* **279**, 15124–15129 (2004).
43. Huang, X. *et al.* Nanotechnology-based strategies against SARS-CoV-2 variants. *Nat. Nanotechnol.* **17**, 1027–1037 (2022).
44. Zhu, J., Su, Y. & Tang, Y. Disrupting ACE2 Dimerization Mitigates the Infection by SARS-CoV-2 Pseudovirus. *Front. Virol.* **2**, 916700 (2022).
45. Ke, Z. *et al.* Structures and distributions of SARS-CoV-2 spike proteins on intact virions. *Nature* **588**, 498–502 (2020).

CHAPTER 5

Conclusions and future perspectives

5.1 Global impact of respiratory diseases: A call for innovative solutions

Lung disorders represent a huge burden for world human health. Respiratory diseases worldwide are among the leading causes of mortality. According to the World Health Organization (WHO), in the 28 European nations, they cause approximately 660,000 deaths and lead to at least 6 million hospital admissions annually. Furthermore, they are responsible for more than 43 million hospitalization days. Four respiratory diseases, including pulmonary infections such as primarily pneumonia and tuberculosis, lung cancer, and chronic obstructive pulmonary disease, are among the top 10 leading causes of mortality together with cardiovascular diseases. These conditions constitute one-sixth of all deaths and one-tenth of the life expectancy lost due to disability. Among respiratory diseases, ILDs include a broad spectrum of pathologies affecting the lung parenchyma, characterized by extensive inflammation and diffuse fibrosis. Pulmonary fibrosis is a common condition that is distinguished by a persistent and progressive tissue repair response, resulting in irreversible scarring, lung remodelling, and compromised gas exchange. IPF is the most prevalent ILD, with an estimated annual incidence ranging from 2 to 30 cases per 100,000 individuals in western countries. Despite extensive research efforts, no effective treatment currently exists to arrest or reverse disease progression and enhance clinical outcomes. Smoking and respiratory infections serve as primary contributors to the issue of respiratory diseases in Europe and are potentially preventable. In addition, the COVID-19 pandemic has had a profound impact on human health, leading to considerable difficulties for the healthcare systems worldwide. This crisis has emphasized the importance of early detection, treatment, and prevention measures, highlighting the importance of pandemic preparedness, but has also accelerated the advancement of medical science. Researchers and healthcare professionals worldwide have been working intensively to better understand the virus, its transmission, and the development of effective treatments and vaccines. The urgency and scale of this situation have prompted a convergence of resources and knowledge, leading to the rapid development and testing of new therapies and vaccines. It is an example to what can be achieved when scientific communities, pharmaceutical industries, and governments worldwide collaborate. The investment in medical research and the development of novel pharmaceutical strategies are pivotal for safeguarding

global public health. Taking together these considerations and assessing the magnitude of the impact on the global population, the importance of combining prevention with new, effective pharmacological therapies and strategies becomes strikingly evident.

It is from this scenario that my PhD thesis originates. Its first aim was to gain insights into the pathogenesis of pulmonary fibrosis and to explore potential therapeutic interventions. This involved the generation and characterization of a reliable animal model that resemble key features of the human disease. With this study, it was possible to obtain the model through the intranasal delivery of the bleomycin inducing alveolar damage and inflammation, followed by a significant fibrotic phase characterized by a strong accumulation of collagen in 21-28 days post administration, thus providing an alternative reliable protocol. Furthermore, it was possible to optimize this route of administration and the methodology to obtain an efficient delivery of compounds into the lungs. The obtainment of this model could allow to better understand the fibrotic process, the key factors involved in the pathogenesis and to standardize technical progression through histological analysis. This is not ancillary, because the optimization of pathological and clinical endpoints represent the starting point of a robust and reliable translational study of new therapeutic strategies.

5.2 Lung fibrosis treatment: Nanoparticles as advanced drug carriers

Nanotechnology is one of the main field where technological innovation comes to life, with a remarkable impact in the field of medicine. The use of nanocarriers as delivery systems is in the first line of this healthcare revolution, offering important results. The efficacy of nanomedicine is based on the precise control of the chemical and physical properties of nanomaterials. This control allows the design of nanoparticles responsive to precise stimuli that can effectively promote drug release, enhancing therapeutic outcomes and minimizing off-target toxicity. One valid strategy within this concept is the encapsulation or the chemical link of cytotoxic, insoluble, and non-selective drugs. These drugs accumulate selectively within diseased tissues, effectively reducing the risk of off-targeting healthy tissues and the associated toxicity. NPs also hold potential for overcoming critical challenges in healthcare. Their small size, compared to bulk materials, results in a significantly higher surface area. This property enables the surface

decoration of NPs with targeting biomolecules, such as antibodies or specific ligands, for precise and active targeting. Therefore, nanoparticles are small to interact with biological matrices and elements, but highly functionalizable and able to load and transport a relevant amount of compounds of interest. Furthermore, nanomaterials offer the possibility of co-delivering multiple drugs or functionalization with linkers. Traditional drugs often suffer from poor biodistribution and a lack of selectivity, whereas drug delivery systems differ from conventional pharmacokinetics and biodistribution patterns, effectively transporting drugs to target organs, shielding them from degradation, and increasing their accumulation in specific tissues. The exploitation of nanomedicine to lung disorders is therefore clear, and local administration of nanodrugs by nasal instillation may constitute a promising therapeutic approach for treating lung diseases, such as pulmonary fibrosis, offering an alternative to common treatments.

For this reason, the second step of my PhD thesis was to explore the applicability of Dexamethasone-carrying Avidin-Nucleic Acid Nanoassemblies as an effective drug delivery system for treating pulmonary fibrosis. These biodegradable and biocompatible nanoparticles, characterized by their low immunogenicity, possess distinctive features, opening doors to potential diagnostic and therapeutic applications. The way of administration significantly influences the biodistribution, pharmacokinetics, and subsequent systemic and local effects of various compounds, including nanoparticles. To achieve a strong lung-targeting effect, we initially investigated and compared various routes of ANANAS-Dex administration in healthy subjects. Systemic injection, which often results in nanoparticle clearance by phagocytic cells from the mononuclear phagocytic system, did not show significant pulmonary accumulation. To overcome this limitation, we tested intranasal instillation as a more direct and specific route in both healthy and fibrotic mice. In light of the profound effect of inflammation and fibrosis on organ architecture, it is essential to assess the nanoparticles' biodistribution in the presence of pathological conditions. ANANAS-Dex showed a great capability to reach the lung parenchyma and to avoid a spread in off-target organs. Fibrotic animals displayed a quicker decrease in lung fluorescence signal, suggesting the influence of cellular infiltrates, particularly macrophages, on NPs biodistribution and profile of distribution of the drug release. Histological analysis confirmed that the nanoparticles

were effectively internalized by pulmonary macrophages within 24-48 hours post-administration, a crucial aspect of pharmacokinetics, allowing ANANAS, and thus Dex, to interact with CD68 positive lysosomes, facilitating drug release. Indeed, free dexamethasone was detected in the lungs of both healthy and fibrotic mice. Remarkably, the levels of free drug in fibrotic animals were tenfold higher than those in healthy mice, likely due to variations in bioavailability associated with pathological changes during disease progression. Moreover, the levels of drug released by ANANAS nanoparticles persisted for 48 hours post-administration, unlike the drug given freely. Interestingly, no dexamethasone signal was detected in the plasma of mice receiving the nanoformulation. This offers potential pharmacological advantages by likely reducing the frequency of treatments required for patients and off-target accumulation. In summary, these results are promising in the context of treating lung disorders. However, to investigate the potential therapeutic effect, it was conducted an acute treatment in affected mice, aiming to detect any alterations in the expression of inflammatory and fibrotic markers 24 hours after treatment. In these experimental conditions, ANANAS-Dex did not significantly affect pro-inflammatory cytokine expression but reduced the expression of fibrotic genes, including collagen 1a1 and fibronectin. While the precise reasons for this outcome remain to be elucidated and warrant further investigation, these findings have significant implications for evaluating the potential anti-fibrotic efficacy in the context of repeated treatments in a murine model of pulmonary fibrosis and for potential clinical translation.

5.3 Nanomedicine revolution: Nanoassemblies for preventing viral invasion and beyond

The ability to adjust the shape, composition, and functionalization of nanoparticle surfaces while maintaining interactions with biological targets represents one of the greatest advantages of these innovative nanosystems. Moreover, these properties allow the extension of the application of specific types of NPs for various purposes, ranging from drug carriers, imaging devices and vaccines. As proof of this concept, ANANAS can be functionalized with different compounds, provided they are biotinylated with stoichiometric control, thanks to their intact biotin-binding capability and high affinity for biotin ligands. In the previous chapter of the thesis it was investigated the use of this nanoparticles as drug delivery system for the treatment of lung fibrosis. Herein, it was

hypothesized the use of this platform as ‘nanodecoy’ for a preventive strategy against SARS-CoV-2 infection. Given the demonstrated ability of these NPs to efficiently flow through the respiratory system and penetrate lung parenchyma after intranasal administration, ANANAS were used as a scaffold to generate a multimerized ACE2 ectodomain to enhance the avidity for the SARS-CoV-2 S protein with the ultimate goal of preventing viral cell invasion.

First, a monomeric biotin derivative of ACE2 ectodomain was optimized using recombinant DNA technologies. ACE2:NP assemblies were generated at different ACE2-biotin:NP molar ratios and compared for size and affinity for the viral S’ protein RBD of both the Wuhan and the new Omicron (BA.1) variant, which later emerged as the dominant strain worldwide. Pre-formulation studies demonstrated that a) the rh-s-ACE2i-biotin can be tethered efficiently to ANANAS, b) the ACE2:NP assemblies are colloidally stable and c) each nanoparticle can accommodate more than 60 ACE2i-biotin units. However, the data also indicate that above the ACE2:NP molar ratio of 30 it is difficult for the biotin-protein to reach the nanoparticles surface, likely due to some crowding effect.

Second, the ability to prevent SARS-Cov-2 infection of the two variants in human lung cells was also tested as a function of ACE2 density at nanoparticle surface and compared to that of the monomeric rh-sACE2-biotin. In vitro testing demonstrated that excessive ACE2 surface density had a negative impact on potency. The R60 assembly was less effective than the R30 in preventing viral infection, and the affinity for RBD of the ACE2i assembled on it was lower than when assembled at R30. This negative effect could be due to a distortion of the protein conformation due to excessive surface crowding, in line with the rigid conformation hypothesis derived from pre-formulation studies, suggesting a geometric/spatial requirement for optimal interaction of the virus surface with the multimerized ACE2i nanodecoy. Therefore, while it can be expected that ACE2 surface density may affect the potency of all ACE2-based nanodecoys, nanoparticles with different geometries and compositions than ANANAS may respond to different composition/efficacy rules.

Lastly, *in vivo* preliminary biodistribution and toxicity studies in healthy mice were performed to assess the possibility of nasal administration. The biological evaluation demonstrated that ACE2:NP-R30 is safe and can reach the deep lung very rapidly through simple inhalation. Its *in vivo* antiviral efficacy may depend on the ability of the nanoparticles to reach locations where the virus primarily localizes, namely the lung parenchyma and its macrophages, which are at the forefront of the host's immune defense. Given the rapidity with which the assemblies reach the parenchyma and their slow removal by macrophages, it is reasonable to assume that they could provide protection against viral invasion. However, this is a proof-of-concept study, and *in vivo* efficacy studies are necessary in SARS-CoV-2 infected mice to determine how long this protection would last after inhalation.

NPs are fascinating platforms for specific targeting strategies, and for the transition from preclinical studies to clinical translation, these nanodevices must be biodegradable, non-toxic and non-immunogenic. Moreover, to exclude potential toxicity, an evaluation of prolonged exposure to nanomaterials is needed to observe any resistance after chronic treatment or secondary effects.

5.4 Exploring the potential of Nanocarriers in healthcare: A promising beginning

As a concluding remark of my PhD thesis work, I conducted a detailed investigation of a murine model of pulmonary fibrosis that was used to assess Avidin-Nucleic Acid Nanoassemblies as an innovative therapeutic strategy for pulmonary fibrosis. Moreover, the same NPs were repurposed to explore their potential activity in preventing SARS-CoV-2 infection, highlighting not only their versatility but also that of NPs in general. It was evaluated the critical interaction between NPs and biological targets across various anatomical levels, encompassing organism, organs, cells, subcellular compartments, while considering diverse parameters like biodistribution, toxicity, and cellular behaviour. The main outcome emerging from my research is that these nanocarriers hold promise not only for the main purpose of this project but also for a wide range of lung pathologies, spanning from inflammatory and chronic disorders to infectious diseases. Moreover, the murine model of pulmonary fibrosis induced through bleomycin

intranasal administration has been optimized for the study of other types of nanoparticles carrying compounds of interest. In addition, the intranasal route of administration also has been optimized in detail and can be taken into consideration for lung dosing and accumulation when pulmonary tropism is required. These results could be useful in case of an inhalation therapy and so think about a formulation and devices that can be easily used by patients. While I acknowledge that my work did not fully achieve my initial aim, which was the chronic treatment of ANANAS for evaluating its positive effects on disease progression and treatment, it is clear to me that this marks a promising beginning to define the potential of these nanodevices and beyond.

While scientific progress is characterized by leaps forward, it is important to recognize the significance of the smaller steps. These gradual achievements pave the way for more substantial breakthroughs. It is evident that scientific research is a perpetual journey with no final destination. The path itself is lined with knowledge, perspective, and personal growth and with the profound awareness that our efforts, whether marked by success or challenged by adversity, contribute to the advance of human understanding, thus offering a brighter and more enlightened future for all.

The ability to persist even when experiments do not yield the expected outcomes, define a researcher.

CHAPTER 6

Communication of results

Journal publications

Morelli, A., Violatto, MB., Moscatiello, GY., Salmaso, A., Codullo, V., Morbini, P., Meloni, F., and Bigini, P. Intranasal bleomycin instillation in anesthetized mice induces a process of pulmonary fibrosis: a comparative evaluation to reduce the animal distress. Manuscript submitted to *The Journal of Pathology*. **2023**.

Morelli, A., Schiavon, E., Violatto, MB., Passoni, A., Lanno, A., Moscatiello, GY., Salmaso, A., Bernardotto, S., Stocco, M., Mattarei, A., Bagnati, R., Meloni, F., Morpurgo, M., and Bigini, P. Intranasal administration of dexamethasone-loaded nanoparticles improves their lung tropism and reduces the off-targeting in both healthy and fibrotic mice. Manuscript in preparation for *Journal of controlled release.* **2023**.

Bernardotto, S., Frasson, I., Faravelli, S., Morelli, A., Schiavon, E., Moscatiello, GY., Violatto, MB., Pinnola, A., Canciani, A., Mattarei, A., Rossi, G., Brini, M., Pasetto, L., Bonetto, V., Bigini P., Forneris, F., Richter S., and Morpurgo. M. Efficient SARS-CoV-2 infection antagonization by rhACE2 ectodomain multimerized onto the Avidin Nucleic-Acid –NanoASsembly. Manuscript submitted to *Biomaterials*. **2023**.

Journal publications outside the thesis topic

Violatto, MB., Pasetto, L., Casarin, E., Tondello, .C, Schiavon, E., Talamini, L., Marchini, G., Cagnotto, A., Morelli, A., Lanno, A., Passoni, A., Bigini, P., Morpurgo, M., Bonetto, V. Development of a Nanoparticle-Based Approach for the Blood-Brain Barrier Passage in a Murine Model of Amyotrophic Lateral Sclerosis. *Cells*. **2022**, 11(24):4003.

Violatto, MB., Sitia, G., Talamini, L., Morelli, A., Tran, NL., Zhang, Q., Masood, A., Pelaz, B., Chakraborty, I., Cui, D., Parak, WJ., Salmona, M., Bastús, NG., Puntes, V., Bigini, P*. Variations in Biodistribution and Acute Response of Differently Shaped Titania Nanoparticles in Healthy Rodents. *Nanomaterials*. **2023**, 13(7):1174

Moscatiello, GY., Natale, C., Inserra, M., Morelli, A., Russo, L., Battajini, N., Sironi, L., Panzeri, D., Candiani, G., Bigini, P., Diomede, L. The surface charge dramatically impacts the penetration and safety of polystyrene nanoparticles *in vitro* and *in vivo.* Manuscript submitted to *International Journal of Molecular Science*, **2023.**

Presentation in scientific meeting

Poster presentation. Morelli A, Violatto MB, Ndembe G, Recordati C, Moscatiello GY, Corti M, and Bigini P. 'Platform standardization for the detection of histopathological features in murine models of hepatic and pulmonary disorders'. 13th TeCSBi PhD meeting. **September 2021**, Milan, Italy.

Poster presentation. Morelli A, Violatto MB, Passoni A, Lanno A, Moscatiello GY, Corti M, Schiavon E, Morpurgo M and Bigini P. 'Intranasal administration of dexamethasone-loaded nanoparticles improves lung tropism and reduces steroid off-target accumulation in healthy and in pulmonary fibrosis-affected mice'. Nanomed 2022. **October 2022**, Athens, Greece. Best Poster Award.

Poster presentation. Morelli A, Violatto MB, Passoni A, Lanno A, Moscatiello GY, Corti M, Schiavon E, Morpurgo M and Bigini P. 'Intranasal administration of dexamethasone-loaded nanoparticles improves lung tropism and reduces steroid off-target accumulation in a model of pulmonary fibrosis'. 8th PhD students meeting. **June 2023**, Istituto di Ricerche Farmacologiche Mario Negri, Milan, Italy.

Oral presentation. Morelli A, Violatto MB, Passoni A, Lanno A, Moscatiello GY, Corti M, Schiavon E, Morpurgo M and Bigini P. 'Intranasal administration of dexamethasone-loaded nanoparticles improves lung tropism and reduces steroid off-target accumulation in healthy and in pulmonary fibrosis-affected mice'. 14th TeCSBi PhD meeting – THE One Health. **September 2022**, Avigliana, Italy

Oral Presentation. Morelli A, Violatto MB, Passoni A, Lanno A, Moscatiello GY, Schiavon E, Morpurgo M and Bigini P. 'Lung disorders treatment: Investigating the impact of inhalable nanoformulations in a murine model of pulmonary fibrosis'. 15th TeCSBi PhD meeting – THE One Health 2.0 – Beyond the boundaries. **September 2023**, Istituto di Ricerche Farmacologiche Mario Negri, Milan, Italy.

Appendix

cells

MDPI

Article

Development of a Nanoparticle-Based Approach for the Blood–Brain Barrier Passage in a Murine Model of Amyotrophic Lateral Sclerosis

Martina Bruna Violatto [1,†], Laura Pasetto [1,†], Elisabetta Casarin [2], Camilla Tondello [3,4], Elisa Schiavon [3], Laura Talamini [1], Gloria Marchini [1], Alfredo Cagnotto [1], Annalisa Morelli [1], Alessia Lanno [5], Alice Passoni [5], Paolo Bigini [1], Margherita Morpurgo [3,*] and Valentina Bonetto [1,*]

[1] Department of Biochemistry and Molecular Pharmacology, Istituto di Ricerche Farmacologiche "Mario Negri" IRCCS, 20133 Milan, Italy
[2] Ananas Nanotech S.r.l., 35131 Padua, Italy
[3] Department of Pharmaceutical and Pharmacological Sciences, University of Padova, 35122 Padua, Italy
[4] Pharmazentrum Frankfurt/ZAFES, Goethe University Hospital Frankfurt, 60596 Frankfurt am Main, Germany
[5] Department of Environmental Health Sciences, Istituto di Ricerche Farmacologiche "Mario Negri" IRCCS, 20133 Milan, Italy
* Correspondence: margherita.morpurgo@unipd.it (M.M.); valentina.bonetto@marionegri.it (V.B.); Tel.: +39-049-8275330 (M.M.); +39-02-39014548 (V.B.)
† These authors contributed equally to this work.

check for updates

Citation: Violatto, M.B.; Pasetto, L.; Casarin, E.; Tondello, C.; Schiavon, E.; Talamini, L.; Marchini, G.; Cagnotto, A.; Morelli, A.; Lanno, A.; et al. Development of a Nanoparticle-Based Approach for the Blood–Brain Barrier Passage in a Murine Model of Amyotrophic Lateral Sclerosis. *Cells* **2022**, *11*, 4003. https://doi.org/10.3390/cells11244003

Academic Editor: Alessandra Pacini

Received: 7 November 2022
Accepted: 8 December 2022
Published: 10 December 2022

Publisher's Note: MDPI stays neutral with regard to jurisdictional claims in published maps and institutional affiliations.

Copyright: © 2022 by the authors. Licensee MDPI, Basel, Switzerland. This article is an open access article distributed under the terms and conditions of the Creative Commons Attribution (CC BY) license (https://creativecommons.org/licenses/by/4.0/).

Abstract: The development of nanoparticles (NPs) to enable the passage of drugs across blood–brain barrier (BBB) represents one of the main challenges in neuropharmacology. In recent years, NPs that are able to transport drugs and interact with brain endothelial cells have been tested. Here, we investigated whether the functionalization of avidin-nucleic-acid-nanoassembly (ANANAS) with apolipoprotein E (ApoE) would allow BBB passage in the SOD1^{G93A} mouse model of amyotrophic lateral sclerosis. Our results demonstrated that ANANAS was able to transiently cross BBB to reach the central nervous system (CNS), and ApoE did not enhance this property. Next, we investigated if ANANAS could improve CNS drug delivery. To this aim, the steroid dexamethasone was covalently linked to ANANAS through an acid-reversible hydrazone bond. Our data showed that the steroid levels in CNS tissues of SOD1^{G93A} mice treated with nanoformulation were below the detection limit. This result demonstrates that the passage of BBB is not sufficient to guarantee the release of the cargo in CNS and that a different strategy for drug tethering should be devised. The present study furthermore highlights that NPs can be useful in improving the passage through biological barriers but may limit the interaction of the therapeutic compound with the specific target.

Keywords: amyotrophic lateral sclerosis; Nanomedicine; pharmacology; blood–brain barrier

1. Introduction

In the field of neurology, a relevant number of encouraging results have been described from in vitro studies, generating a number of new potential drug candidates. Nevertheless, translating the results from in vitro to in vivo or from preclinical studies to clinical trials remains very challenging. One of the main hurdles is the limited passage of drugs from the circulatory system to the central nervous system (CNS). To prevent the risks deriving from an uncontrolled passage of potentially hazardous substances, the blood–brain barrier (BBB), formed by brain endothelial cells, strictly segregates blood components, drastically reducing the entry of circulating compounds inside the CNS. By this mechanism, the BBB also limits the cerebral uptake of therapeutic molecules. The main factors that influence BBB permeability include molecular weight, charge, lipid solubility, surface activity, and the relative size of the compounds [1]. Over the years, great efforts have been taken to

deliver drugs and diagnostic agents to the brain. A series of technical approaches have been tested, among which are the use of viral vectors, nanoparticles (NPs), extracellular vesicles, and/or by trying to exploit active transporters, brain permeability enhancers, or non-invasive techniques (ultrasounds, magnetic stimulations). Unfortunately, the results are often controversial and lack the robustness to further proceed to clinical application. In some pathological conditions, the BBB has a higher permeability, making the passage of therapeutic compounds easier. In particular, neuroimaging studies have demonstrated BBB dysfunction in many neurodegenerative diseases, including amyotrophic lateral sclerosis (ALS) [2,3].

Nanotechnology could play a pivotal role in the development of strategies for drug delivery in ALS [4,5]. In this context, different types of materials (such as lipid-based, polymeric, and inorganic NPs) have been engineered to deliver therapeutics to the brain. NPs can be engineered to display specific physicochemical features to favor drug delivery, for example, by increasing bloodstream stability, reducing drug clearance, or improving affinity to the cellular target [6].

In order to increase the affinity of NPs to brain capillaries, surface modification is greatly exploited. Brain capillary endothelial cells express a large number of blood-to-brain transport systems that, in principle, could facilitate the entry of compounds into the brain. Peptides and proteins, such as insulin, transferrin, or lipoproteins, are indeed transported across the BBB via receptor-mediated transcytosis. Apolipoprotein E (ApoE) associates with lipids to form lipoproteins and plays a key role in the transport and uptake of cholesterol to the brain [7]. Lipoprotein-associated receptors are highly expressed by brain endothelial cells, and ApoE has been extensively investigated as a major ligand candidate for NP-based drug delivery targeting the brain [8]. In fact, it was shown that ApoE guided the NP's display and increased endocytosis and transcytosis, especially in vitro.

An attractive alternative NP platform combining advanced surface chemistry to a safe interaction with biological targets is represented by the nanoassembly ANANAS. ANANAS are poly-avidin NPs that form upon the high affinity-driven nucleation of avidin units around a non-coding plasmid DNA [9,10]. Each nanoparticle, which is protected by a PEG layer for colloidal stability (Figure 1), possesses a large number of biotin binding sites (BBS), which are available for docking about 1000 functional elements (drugs, fluorophores for tracking and/or targeting elements), provided these are linked to a biotin moiety. The high affinity of biotin for avidin (Kd~10^{-15} M) permits the exploitation of the available BBS to obtain functional NPs with stoichiometric control of composition by simply mixing core NPs (which are obtained and freeze-dried in a separate process) with the desired biotinylated moieties. Functional NPs are thus obtained in a "one pot" solution, and as long as the number of available BBS or the available NP surface (about 6000 nm^2) is not exceeded, they can be used without the need for purification.

In the past few years, these protein-based assemblies have been proposed as platforms for drug delivery, showing great potential for the treatment of cancer [11] and liver disease [12]. ANANAS are extremely promising because of their safety, multifunctionality, stoichiometric drug encapsulation, defined composition, and scalability but also for their high biocompatibility, biodegradability, and low immunogenicity [13].

In the present study, we exploited the ANANAS platform to investigate NP delivery to the CNS in wild-type (WT) and $SOD1^{G93A}$ mice, which develop a motor neuron disease and display morphological damages to BBB and the blood-spinal cord barrier (BSCB) as the disease progresses [14]. To evaluate the ability of intravenously injected ANANAS and ANANAS-ApoE to reach CNS tissues, we developed an experimental platform combining biochemical and imaging approaches. Finally, to evaluate if the BBB passage could be accompanied by a local release of a therapeutic payload, we treated the $SOD1^{G93A}$ mice with an ANANAS-based nanodrug [12,15] carrying the steroid dexamethasone (Dex), and we evaluated the amount of Dex released in the brain and spinal cord. Dex was selected as a potential drug candidate to control the neuroinflammatory response associated with motor neuron diseases [16,17]. Targeting steroids in the CNS by means of nanocarriers may

be a way to maximize their therapeutic effect. In the ANANAS-Dex here used, the drug was tethered through an acid-reversible hydrazone bond [12,15], which should be capable to release the free drug upon reaching an acidic compartment, such as an inflamed tissue or a target cell endosomal/lysosomal compartment.

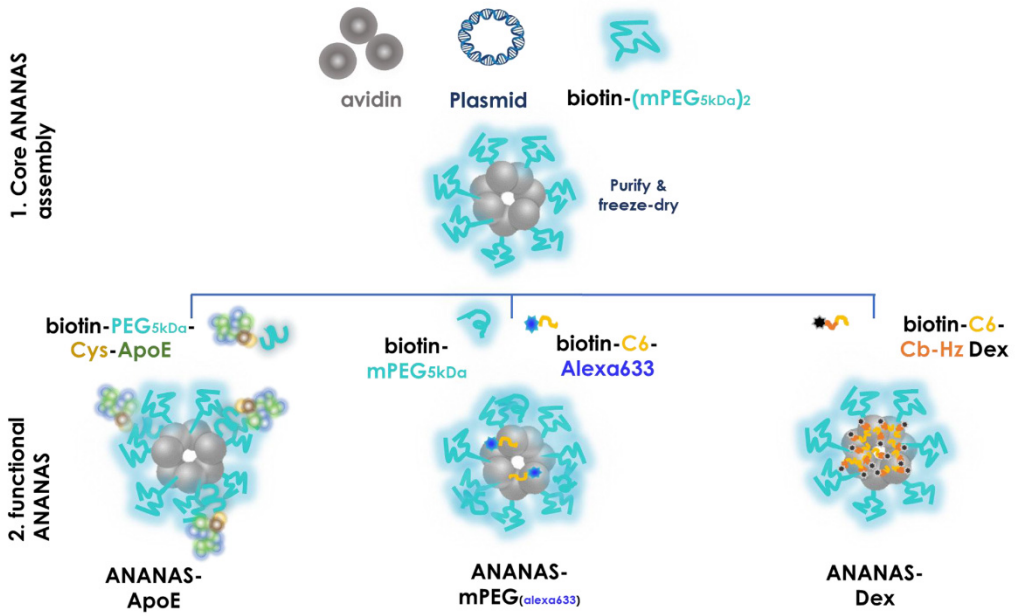

Figure 1. Schematic representation (not in scale of the formulations selected for the in vivo studies). Upper panel: components of the core ANANAS; lower panel: functional assemblies are generated by mixing core ANANAS with the different biotin components at predefined biotin:ANANAS BBS molar ratios.

2. Materials and Methods

2.1. Materials

Avidin was purchased from e.protein (Belgium), biotin-methoxy-PEG5kDa (B-mPEG-5kDa), and biotin-PEG5kDa-NH_2 were purchased from Laysan bio (Arab, AL, USA). Atto488-NHS was purchased from Attotech Gmbh (Siegen, Germany, code # 11U26). Biotin-C6-Alexa633, Biotin-L-lys-(methyl-PEG5kDa)$_2$, and biotin-C6-Cb-Hz-Dexamethasone (B-C6-Cb-Hz-Dex) were synthesized according to published procedures [10,13,15]. Maleimido-succinimidyl propionate (MSP) and all other reagents were purchased from Sigma Aldrich. Biotin-PEG5kDa-propylamido-maleimide was obtained by mixing biotin-PEG5kDa-NH_2(LaysanBio lot #127-123) with 3 equivalents of MSP in 10 mM phosphate, 150 mM NaCl, pH 7.4 (PBS buffer). The product was purified by gel filtration on a G25 resin (NAP10, Cytiva Life Sciences, Karnataka, India) using water as an eluent.

2.2. Biotin-PEG5kDa-Cys-ApoE Synthesis

The peptide, corresponding to residues 141–150 of human ApoE CWG-(LRKLRKRLLR), was synthesized on an automated Alstra synthesizer (Biotage, Uppsala, Sweden) at a 0.1 mM scale with NOVASYN-TGA resin (Novabiochem, San Diego, CA, USA) using Fmoc-protected L-amino acids (Sigma Aldrich, St. Louis, MO, USA). The peptide was bearing in the N-term position a glycine residue as a spacer, a tryptofan residue for fluorescence monitoring, and ended with cysteine for covalent coupling with ANANAS. Amino acids were activated by a reaction with O-(Benzotriazol-1-yl)-N,N,N′,N′-tetramethyluronium tetrafluoroborate and N,N-diisopropylethylamine. A capping step with acetic anhydride after the last coupling cycle of each amino acid was included. The peptide was cleaved from the resin with trifluoroacetic acid/thioanisole/water/phenol/ethanedithiol (82.5:5:5:5:2.5 *v*/*v*), precipitated, and washed with diethyl ether. The precipitate was then purified by reverse-

phase high-performance liquid chromatography on a semi-preparative C4 column (Waters Corporation, Milford, MA, USA). The correct peak fraction corresponding to the peptide molecular weight was identified using a MALD-TOF spectrometer (Applied Biosystems, Waltham, MA, USA) before being freeze-dried and stored at −20 °C until use. The peptide purity was higher than 95%. Biotin-PEG5kDa-Cys-ApoE was obtained by mixing Biotin-PEG5kDa-propylamido-maleimide with 1 equivalent of ApoE CWG-(LRKLRKRLLR). The product was purified by gel filtration. Peptide coupling to the biotin-PEG-linker was confirmed by a combination of analytical techniques: UV-Vis spectrophotometry was used to measure the ApoE concentration, HABA assay was used to measure biotin content [18], and iodine assays [19] measured the PEG content.

2.3. ANANAS Formulations

Core ANANAS carrying the surface protective biotin-L-lys-(methyl-PEG5kDa)$_2$ to guarantee colloidal stability were prepared according to Pignatto [10] and were freeze-dried. For functional assembly preparation, core NPs were reconstituted in the buffer, and biotinylated elements were added (Biotin-PEG5kDa-ApoE, biotin-mPEG, biotin-C6-Cb-Hz-Dex, SI for chemical structures) to the desired biotin/biotin binding site (BBS) molar ratios. When needed, biotin-C6-Alexa633 was also added at 15% BBS coverage [13]. NPs were characterized by size by the Zetaseizer nano ZS (Malvern instruments) instrument. The NP loading capability for different biotin elements was measured by a combination of tools, including gel permeation chromatography, dot blot analysis, and DLS (see also Supplementary Material).

2.4. Animals

The "Mario Negri" Institute for Pharmacological Research IRCCS adheres to the principles set out in the following laws, regulations, and policies governing the care and use of laboratory animals: Italian Governing Law (D.lgs 26/2014; Authorization no. 19/2008-A issued March 6, 2008, by Ministry of Health); Mario Negri Institutional Regulations and Policies providing internal authorization for persons conducting animal experiments (Quality Management System Certificate, UNI EN ISO 9001:2015, Reg. No. 6121), the NIH Guide for the Care and Use of Laboratory Animals (2011 edition), and EU directives and guidelines (EEC Council Directive 2010/63/UE). This work was reviewed by the internal Animal Care and Use Committee (IACUC) and approved by the Italian "Istituto Superiore di Sanità" (code: 722/2017-PR). Animals were maintained under specific pathogen-free conditions and regularly checked by a veterinarian responsible for animal welfare supervision and experimental protocol review. Mice were bred in standard conditions: temperature 21 ± 1 °C, relative humidity 55 ± 10%, 12 h light schedule, and food and water ad libitum. Both in vivo and ex vivo analyses were performed on CD1 and SOD1^{G93A} mice. The CD1 mouse (WT mice), acquired from Charles Rivers, is a multipurpose model. It is an albino outbred strain of mouse model that has frequently been used in toxicology (safety and efficacy study) and pharmacological research. The SOD1^{G93A} mouse is an established mouse model of ALS. The SOD1^{G93A} line on a homogeneous 129S2/SvHsd background derives from the B6SJL-TgNSOD-1-SOD1G93A-1Gur line that was originally obtained from The Jackson Laboratory (Bar Harbor, ME, USA), which expresses about 20 copies of mutant human SOD1^{G93A} [20,21]. This transgenic SOD1^{G93A} mouse strain develops the first signs of motor neuron pathology at about 4 weeks of age. Mice start to show muscle strength and motor function impairment at 14 weeks of age and survive for up to 18 weeks of age. Genotyping for SOD1^{G93A} was performed by a standard PCR using primer sets designed by The Jackson Laboratory. The number of animals was calculated on the basis of experiments designed to reach a power of 0.8, with a minimum difference of 20% (α = 0.05).

2.5. In Vivo Treatments

The experimental groups enrolled for in vivo and ex vivo analyses are summarized in Table 1. SOD1^{G93A} mice were treated at the onset of symptoms (14 weeks of age), and

the same age was maintained for the treatment of WT mice. In detail, WT and SOD1^{G93A} mice were intravenously treated with ANANAS-mPEG (ANANAS) 0.54 mg NPs/mouse (21.6 mg/kg) or ANANAS 0.54 mg NPs/mouse (21.6 mg/kg) loaded with 10% ApoE (ANANAS-ApoE) or PBS as a vehicle. In addition, another group of SOD1^{G93A} mice received intravenously ANANAS 1 mg NPs/mouse (40 mg/kg) loaded with dexamethasone 17.1 µg, Dex/mouse (0.68 mg/kg) (ANANAS-Dex), or free Dex 17.1 µg Dex/mouse (0.68 mg/kg). Mice were sacrificed at different time points (Table 1) and were analysed for pharmacokinetics measurements through biochemical (dot blot, HPLC/MS) and imaging approaches (ex vivo imaging).

Table 1. Animals, treatment schemes, and type of analysis.

Mice	Intravenous Treatment	Time of Sacrifice	Perfusion	Analyses
4 WT	ANANAS	30′	Yes	Dot blot
4 WT	ANANAS	30′	No	Dot blot
4 WT	Vehicle	24 h	Yes	Dot blot
4 WT	ANANAS	30′	Yes	Dot blot
4 WT	ANANAS	4 h	Yes	Dot blot
4 WT	ANANAS	24 h	Yes	Dot blot
4 WT	ANANAS-ApoE	30′	Yes	Dot blot
4 WT	ANANAS-ApoE	4 h	Yes	Dot blot
4 WT	ANANAS-ApoE	24 h	Yes	Dot blot
4 SOD1^{G93A}	Vehicle	24 h	Yes	ex vivo imaging, Dot blot
4 SOD1^{G93A}	ANANAS	30′	Yes	ex vivo imaging, Dot blot
4 SOD1^{G93A}	ANANAS	4 h	Yes	ex vivo imaging, Dot blot
4 SOD1^{G93A}	ANANAS	24 h	Yes	ex vivo imaging, Dot blot
4 SOD1^{G93A}	ANANAS-ApoE	30′	Yes	Dot blot
4 SOD1^{G93A}	ANANAS-ApoE	4 h	Yes	Dot blot
4 SOD1^{G93A}	ANANAS-ApoE	24 h	Yes	Dot blot
4 SOD1^{G93A}	ANANAS-Dex	15′	Yes	HPLC/MS, Dot blot
4 SOD1^{G93A}	ANANAS-Dex	30′	Yes	HPLC/MS, Dot blot
4 SOD1^{G93A}	ANANAS-Dex	60′	Yes	HPLC/MS, Dot blot
4 SOD1^{G93A}	Dex	15′	Yes	HPLC/MS, Dot blot
4 SOD1^{G93A}	Dex	30′	Yes	HPLC/MS, Dot blot
4 SOD1^{G93A}	Dex	60′	Yes	HPLC/MS, Dot blot

2.6. Tissue Dissection and Plasma Isolation

Mice were deeply anesthetized with an overdose of ketamine hydrochloride (IMALGENE, 150 mg/kg; Alcyon Italia) and medetomidine hydrochloride (DOMITOR, 2 mg/kg; Alcyon Italia) by intraperitoneal injection. Before sacrifice, all groups except one in a preliminary experiment were perfused transcardially with 50 mL of phosphate-buffered saline (PBS). The liver, brain, and spinal cords were rapidly removed, collected, and frozen at −80 °C for subsequent analysis. Blood samples were collected in EDTA pre-coated vials and centrifuged at 13,400× *g* for 2 min. Mouse plasma samples were stored at −80 °C until used.

2.7. Dot Blot Analysis

Tissues were homogenized by sonication in 1% boiling SDS. Protein homogenates were further boiled for 10 min and centrifuged at 13,500× *g* for 5 min. In order to quantify the

proteins, supernatants were analysed by the BCA protein assay (Pierce) and subsequently boiled for 1 h immediately before dot blot analyses. The treatment was carried out on tissues before dot blot analysis so as to denature and thus disassemble the ANANAS. This permitted the detection/quantification of their presence in the tissues by titering avidin: their major component. For dot blot, proteins (3 µg) were loaded directly onto nitrocellulose Trans-blot transfer membranes (0.45 µm; Bio-Rad, Hercules, CA, USA) by vacuum filtration, as described previously [22]. Dot blot membranes were blocked with 3% (*w*/*v*) BSA (Sigma-Aldrich, St. Louis, MO, USA) and 0.1% (*v*/*v*) Tween 20 in Tris-buffered saline, pH 7.5, were incubated with primary antibodies and then with peroxidase-conjugated secondary antibodies (GE Healthcare, Chicago, IL, USA). Antibodies used for immunoblotting included: rabbit polyclonal anti-Avidin antibody (1:5000, Abcam, Cambridge, UK; RRID: AB_305644); goat anti-rabbit peroxidase-conjugated secondary antibodies (1:10000, GE Healthcare). Blots were developed with the Luminata Forte Western Chemiluminescent HRP Substrate (Millipore, Burlington, MA, USA) on the ChemiDoc™ Imaging System (Bio-Rad). Densitometry was conducted with Image Lab 6.0 software (BioRad). The relative immune reactivity of the different proteins was normalized to the total protein loading by Ponceau Red staining (Fluka, Vancouver, BC, Canada).

2.8. Ex Vivo Fluorescence Imaging

Ex vivo optical imaging was performed on the excised brain and spinal cord after fluorescent NP administration. Fluorescence images were acquired with an IVIS Lumina III imaging system (PerkinElmer, Waltham, MA, USA). The following acquisition parameters were used: excitation filter range from 680 to 740 nm, emission filter (790 nm, exposure time 2 s), binning factor 4, and f/Stop 2. Spectral unmixing, image processing, and analysis were performed using Living Image 4.3.1 software (PerkinElmer).

2.9. Pharmacokinetics

2.9.1. Sample Preparation and Extraction

The analytical method was revised in accordance with other protocols found in the literature [23,24]. As a first step, the internal standard (IS) fludrocortisone (10 ng) was added to the samples from treated mice, and Dex (0–300 ng) and fludrocortisone (10 ng) was included for the calibration curve. The liver, brain, and spinal cord tissue samples were treated with methanol (1:4 *w*/*v*) and acetonitrile (1:1 *w*/*v*), stirred, and sonicated for 20′. Then, water (1:10 *w*/*v*) was added, and the stirring and sonication steps were repeated. The resulting samples were centrifuged at 7000× *g* for 15 min at 4 °C. The supernatant was further purified with solid-phase extraction using Sep-Pak C18 1 cc Vac Cartridges (Waters, Milford, MA, USA) and was conditioned before use with 1 mL methanol, followed by 1 mL water. Samples were loaded on the SPE columns and passed through dropwise. Finally, the cartridges were rinsed with 1 mL water:acetone (80:20) and then with 1 mL of water before drying the columns under a vacuum for 5′. Samples were eluted with 1.8 mL acetonitrile into glass receiving tubes. Plasma aliquots were directly eluted with acetonitrile (1:4 *v*/*v*) and centrifuged at 7000× *g* for 15 min at 4 °C. All samples were evaporated to remove the organic phase. Just before analysis, they were suspended in 100 µL of 0.05% acetic acid:acetonitrile (80:20).

2.9.2. Liquid Chromatography (HPLC) and Tandem Mass Spectrometry (MS/MS)

The LC–MS/MS system was a Nexera ultra-high-pressure liquid chromatography (UHPLC) system interfaced with a triple quadrupole LCMS-8060 (Shimadzu, Japan). The mass spectrometer (MS) operated in negative electrospray ionization (ESI) mode, with the following conditions: nebulizing gas flow rate 3 L/min, drying gas flow rate 10 L/min, heating gas flow rate 10 L/min, interface temperature 300 °C, and heating block temperature 400 °C. In a preliminary phase, standard solutions of Dex and the IS (100 ng/mL in water/acetonitrile) were directly injected into the mass spectrometer to identify and optimize the best ion transitions for MRM acquisition. The selected transitions and their

collision energies (CE) were: m/z 361.2 > 292 (quantification transition, CE = 26) and m/z 361.2 > 325 (qualification transition, CE = 21) for Dex; m/z 349.1 > 295.2 (quantification transition, CE = 22) for IS. The chromatographic separation was obtained on an Ascentis C18 column (150 × 2.1 mm; 2.7-µm particle size, Sigma-Aldrich, St. Louis, MO) using an elution mixture composed of solvent A (0.05% acetic acid in water) and solvent B (acetonitrile) at 35 °C. The elution gradient was from 20 to 60% of solvent B in 12.5 min, from 60% to 99% of solvent B in 1.5 min (hold at 99% for 2 min), and re-equilibration in 4 min to 20% of solvent B. The injection volume was 5 µL, and the flow rate was 180 µL/min. Shimadzu's LabSolutions software was used for instrument control, data handling, and analysis.

2.10. Statistical Analysis

Prism 7.0 (GraphPad Software Inc., San Diego, CA, USA) was used. For each variable, the differences between the experimental groups were analysed by one-way ANOVA followed by Tukey's post hoc test. *p*-values below 0.05 were considered significant.

3. Results

3.1. ANANAS Formulations

The composition administered is shown in a schematic representation in Figure 1 and is summarized in Table 2.

Table 2. Composition and size of the formulations used in the in vivo studies.

Formulation Name	Biotin Reagent Added to Core NPs	(% BBS)	Z-Average (nm) 1 h	PDI (1 h)	Z-Average (nm) 24 h	PDI 24 h	ζ Potenzial
ANANAS-ApoE	B-PEG5kDaCys-ApoE	10	138.9 ± 0.3	0.26	142.4 ± 7.0	0.36	−3.76 ± 0.903
ANANAS-mPEG	mPEG5kDa (*)	10	136.9 ± 1.5	0.17	137.3 ± 2.5	0.23	−6.50 ± 0.310
ANANAS-Hz-Dex	BC6-Cb-Hz-Dex	57.5	141.1 ± 1.1	0.31	142.5 ± 2.1	0.33	−5.8 ± 1.711

(*) for in vivo fluorescent tracking, biotin-C6-Alexa633 was added to cover 15% BBS.

The functional assemblies were generated starting from core ANANAS which had 25% of the available BBS covered with biotin-L-lys-(methyl-PEG5kDa) (biotin-$(mPEG5kDa)_2$ [10]. This highly ω-methoxy-PEGylated core NP was selected based on recent results [15], which showed that a high number of ω-5 kDa PEG units at the outer NP surface gave them more stealth, favouring reaching out to tissues that were different than the liver, as for example the brain.

For ANANAS-ApoE-related investigations, following pre-formulation studies (Supplementary Information, S.I.), we selected the NP composition with the maximum ApoE loading among the colloidally stable ones (10% BBS coverage). In the non-functionalized ANANAS, the surface of the core NPs was capped with biotin-methoxy-PEG5kDa (ANANAS-mPEG) to cover the same number of BBS (10%) as in ANANAS-ApoE. This formulation is also colloidally stable in the presence of biotin-C6-Alexa633, [13] which was added to cover 15% BBS for in vivo NP tracking with the IVIS instrumentation. On the contrary, alexa633 labelling of ANANAS-ApoE could not be performed due to an interference of the fully negatively charged dye with the positively charged ApoE component, which negatively affected the NP solubility.

The ANANAS-Dex assembly was generated by mixing core NPs with sub-saturating (57.5% of BBS) amounts of acid-sensitive short-spaced (C6) biotin-carbonate-hydrazone-dexamethasone conjugate (B-C6-Cb-Hz-Dex). The conjugate sub-saturating amount was selected so that no unbound conjugate remained in the assembly solution (see also Supplementary Material). Therefore, the latter could be administered as such without the need for further purification [10,11,13,15]. The biotin-C6-Cb-Hz-Dex conjugate used for dexamethasone loading was investigated in vitro in previous work [15] and was selected for the in vivo experiments of this work based on two main properties: (a) it is a low MW short-link spaced conjugate which permits high NP drug loading; (b) it is the least hydrolytically stable among the short-spaced Hz-dexamethasone conjugates investigated:

a property which should favour fast drug release once it is internalized by target cells. The final formulation displayed in vitro a pH-dependent release of Dex, with no release at a neutral pH (as in serum) and 5.69% release/24 h at pH 4.0 [15].

3.2. In Vivo Studies

The experimental design developed for this study is reported in Figure 2.

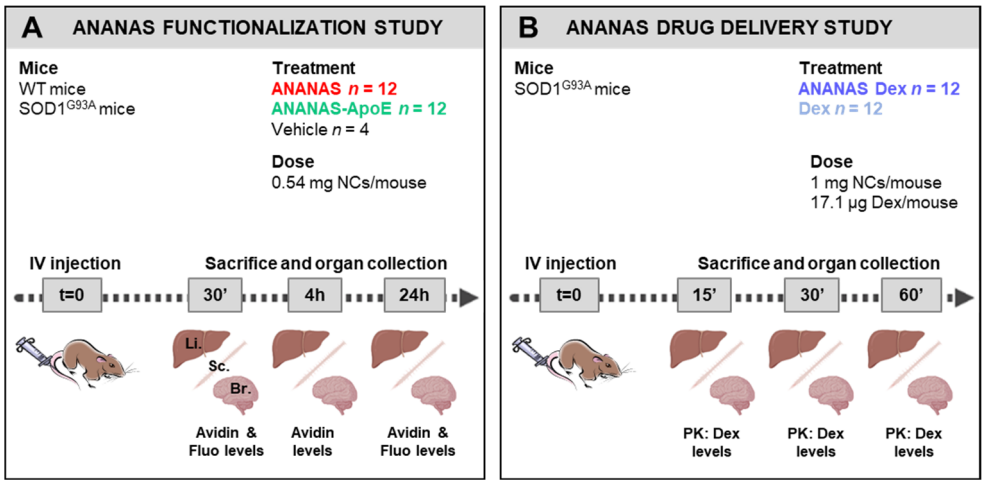

Figure 2. Experimental plan for NP functionalization and delivery study (**A**) WT and SOD1^{G93A} mice (n = 12 mice per group) were intravenously (IV) treated with ANANAS, ANANAS-ApoE, or vehicle for ANANAS functionalization study. Liver (Li.), spinal cord (Sc.), and brain (Br.) were collected 30 min, 4 h and 24 h post treatment for biochemical and imaging analysis. (**B**) SOD1^{G93A} mice (n = 12 mice per group) were intravenously (IV) treated with ANANAS-Dex or Dex for ANANAS drug delivery study. Organs were collected for PK measurements 15-, 30-, and 60-min post treatment.

To understand the impact of NP functionalization, a biodistribution study was performed in WT and SOD1^{G93A} mice, which were treated with ANANAS, ANANAS-ApoE or the vehicle and then sacrificed 30′, 4 h, and 24 h after administration (Figure 2A). As a proof of concept, SOD1^{G93A} mice were intravenously treated with Dex as a free molecule or linked to ANANAS (ANANAS-Dex) to evaluate the possible drug release from NPs. In this case, Dex was covalently linked to the ANANAS surface through an acid pH-sensitive linker [12,15] and should be released from the carrier upon reaching an acidic environment (cell internalization via endosome or an inflamed tissue). A pharmacokinetics study was performed by analysing tissue dex levels 15′, 30′, and 60′ after NP administration (Figure 2B). In addition to the brain and spinal cord, we analysed NP and drug levels at the liver as a control tissue since NPs introduced in the bloodstream are normally cleared by it and other organs of the reticuloendothelial system.

A methodological setting-up experiment was carried out in WT mice to evaluate the possible artefactual estimation of ANANAS accumulation inside the tissues due to blood contamination (Figure 3A). To this end, WT mice were injected intravenously with ANANAS. After 30 min of treatment, the first group was sacrificed and perfused with PBS to remove the blood, and the second one was sacrificed without perfusion. The liver, brain, and spinal cord were analysed for avidin levels. The liver showed the highest levels of NP-related avidin with no differences between the perfused and not perfused conditions. Probably, since the majority of NPs accumulate in the liver, the contribution of blood contamination is negligible. On the contrary, in the brain and spinal cord, where avidin levels are low, it is possible to appreciate a significant difference between perfused and non-perfused tissues. Therefore, we introduced the perfusion procedure in all further analyses.

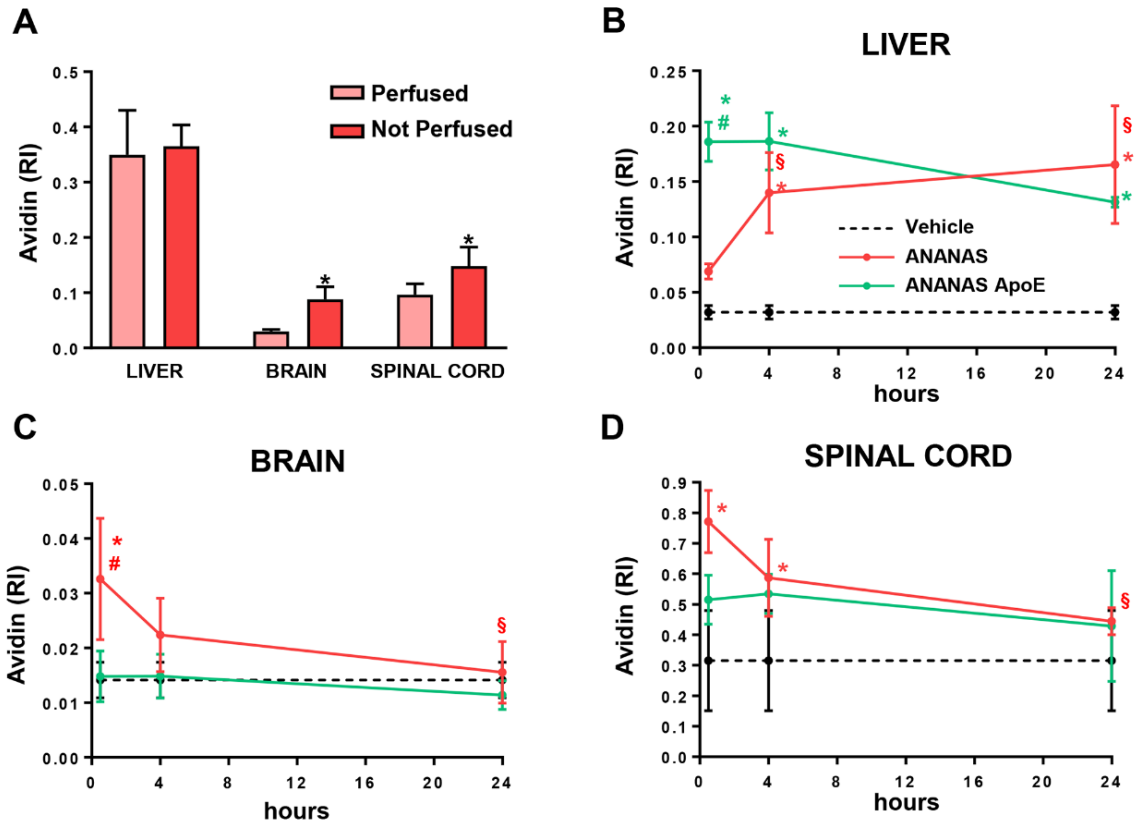

Figure 3. NP biodistribution in WT mice. (**A**) Avidin quantification from liver, brain, and spinal cord of WT mice intravenously treated with ANANAS and sacrificed 30 min after injection, with (pink bars) or (red bars) without intracardial perfusion. Data are mean ± SEM (n = three in each experimental group) and indicates the relative immunoreactivity (RI) normalized to total protein loading; * $p < 0.05$ versus the respective perfused tissue by Student's t-test. (**B**–**D**) Dot blot analysis for avidin quantification in liver (**B**), brain (**C**), and spinal cord (**D**) of WT mice treated with vehicle (dotted line), ANANAS (red line), and ANANAS-ApoE (green line) and sacrificed with intracardial perfusion 30 min, 4 h, and 24 h after the injection. (**B**–**D**) Data are mean ± SD (n = three or four in each experimental group) and indicates the relative immunoreactivity (RI) normalized to total protein loading; * $p < 0.05$ versus vehicle; # $p < 0.05$ versus ANANAS-ApoE and § $p < 0.05$ versus ANANAS 30 min, by one-way ANOVA, Tukey's post hoc test.

We next moved to evaluate the presence and evolution over time of ANANAS and ANANAS-ApoE in the liver, brain, and spinal cord (Figure 3B–D).

In WT mice, ANANAS, both with and without ApoE, accumulated in the liver but with different kinetics. The non-functionalized ANANAS signal reached a significantly higher level versus the vehicle only 4 h after administration and further increased along the following hours. On the contrary, the level of ANANAS-ApoE was high already after 30 min, comparable to that of non-functionalized ANANAS at 24 h, and decreased along the following hours (Figure 3B). This indicates that the accumulation of ANANAS in the liver is favoured by the ApoE functionalization.

In the brain, the NP-related avidin signal was higher than the vehicle only in the ApoE-free ANANAS group. The levels were the highest at 30 min, then significantly decreased over 24 h. On the other hand, levels of NP in ANANAS-ApoE-treated mice were similar to those of the vehicle group, indicating that the functionalized NP was unable to penetrate the brain (Figure 3C).

In the spinal cord mice treated with both ANANAS and ANANAS, ApoE showed NP-related avidin levels above the vehicle but with a different trend. In particular, only non-functionalized ANANAS reached significant levels in the tissue 30 min after administration

and then decreased in the next hours. ANANAS-ApoE levels were slightly higher than the controls; however, this was without reaching significance (Figure 3D), and this did not change over time. These results show that ANANAS can reach the spinal cord, but the presence of ApoE has a negative impact on this property.

Overall, biodistribution data in WT mice indicate that, in the early phase, the unmodified ANANAS can reach both the spinal cord and brain with similar kinetics and accumulates in the liver over the next 24 h. The presence of ApoE prevents ANANAS accumulation in CNS tissues and favours NP accumulation in the liver already from the early time points.

Tissue biodistribution analysis of NPs over time was also performed in the ALS disease animal model (Figure 4).

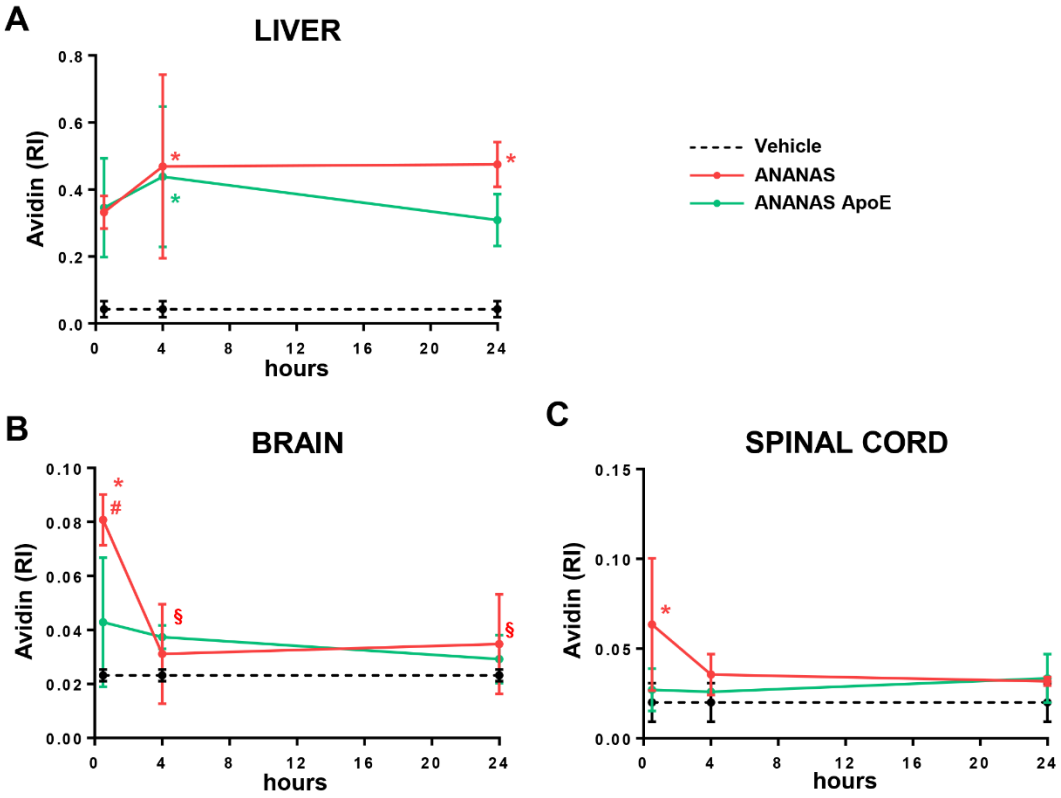

Figure 4. NP biodistribution in SOD1^{G93A} mice. (**A**–**C**) Dot blot analysis for avidin quantification in the liver (**A**), brain (**B**), and spinal cord (**C**) of SOD1^{G93A} mice treated with a vehicle (dotted line), ANANAS (red line), and ANANAS-ApoE (green line) and sacrificed with intracardial perfusion 30 min, 4 h, and 24 h after the injection. (**A**–**C**) Data are mean ± SD (n = three or four in each experimental group) and indicates the relative immunoreactivity (RI) normalized to total protein loading; * $p < 0.05$ versus vehicle; # $p < 0.05$ versus ANANAS-ApoE and § $p < 0.05$ versus 30 min, by one-way ANOVA, Tukey's post hoc test.

SOD1^{G93A} mice were treated with ANANAS and ANANAS-ApoE at the onset of symptoms (14 weeks of age): a stage at which treatments are usually started in preclinical drug testing and when BBB and BSCB damage is normally observed [14,25].

In the liver, NP levels were already high 4 h after administration and independently of the presence of ApoE at the NP surface, confirming the strong tropism of the ANANAS carrier for this tissue. Similar to what was observed in WT time, the presence of ApoE was correlated with a faster NP signal decay from this tissue. The levels of untargeted ANANAS remained stable between 4 and 24 h and decreased by about 30% in the case of the ApoE-linked formulations (Figure 4A).

Thirty min after administration, NP-related avidin levels in the brain were just above the controls in ANANAS-ApoE-treated mice. On the other hand, levels were significantly higher in animals treated with untargeted ANANAS, whose signal slowly decreased over time, reaching that of the ANANAS-ApoE group (Figure 4B) 4 h after administration.

In the spinal cord, NP-related avidin was already detectable 30 min after administration in ANANAS-treated animals, and again, the levels gradually decreased over time, reaching untreated control levels 4 h after administration. In the case of the ANANAS-ApoE-treated mice, the avidin-related signal was barely detectable (without significance) at all time points. The results also confirmed in the SOD1^{G93A} mouse (Figure 4C) the ability of non-functionalized NPs to reach the spinal cord earlier and with greater amounts than ApoE-NPs.

Since functionalization with ApoE did not induce an improvement in ANANAS penetration inside the brain and spinal cord in either healthy or ALS mice, we focused our attention on non-functionalized ANANAS in SOD1^{G93A} mice. A biodistribution study 30′ and 24 h after ANANAS intravenous administration was carried out using ex vivo optical imaging (IVIS Lumina XRMS) (Figure 5).

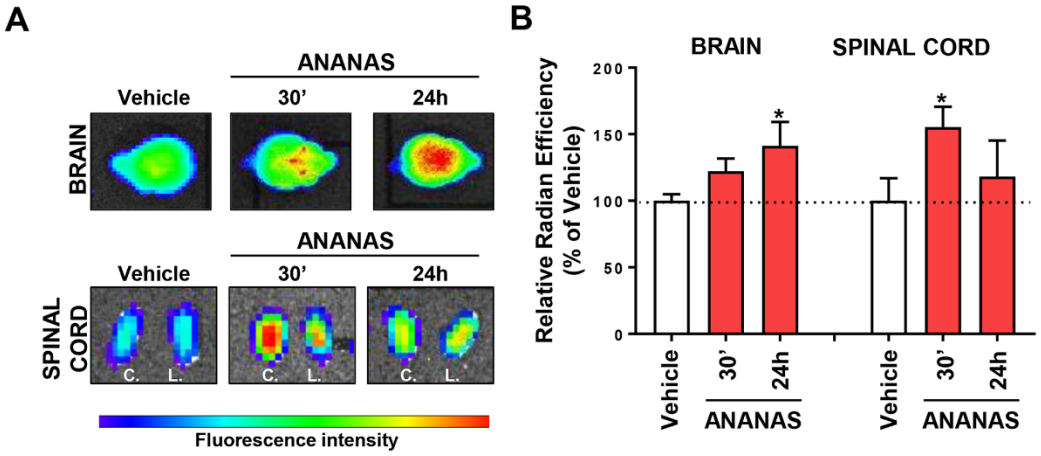

Figure 5. Ex vivo biodistribution in SOD1^{G93A} mice. (**A**,**B**) Ex vivo optical analysis of brain and spinal cord from SOD1^{G93A} mice treated with saline (Vehicle) or with ANANAS and sacrificed with intracardial perfusion 30 min and 24 h after the treatment. (**A**) Representative images of brain and cervical (C.), lumbar (L.), spinal cord. (**B**) Quantification of ex vivo optical imaging signal in brain and spinal cord. Dotted lines indicate the mean of vehicle. Data (mean ± SD; n = three or four in each experimental group) indicates the relative radian efficiency and are expressed as percentages of the respective vehicle. * $p < 0.05$ versus vehicle, by one-way ANOVA, Tukey's post hoc test.

For longitudinal tracking, ANANAS were labelled with the fluorophore biotin-alexa633, which was added to cover 5% of the total biotin binding sites available. The ex vivo analysis showed that at both 30 and 24 h after administration, the fluorescent signal associated with ANANAS was detectable in both the brain and spinal cord, with significant differences with respect to the vehicle group at 30′ and 24 h in the spinal cord and the brain, respectively. Figure 5A shows a rapid increase in the signal associated with the administration of ANANAS compared to the control mouse. In the SOD1^{G93A} mouse model, motor neuron degeneration affects mostly the lumbar spinal cord. For this reason, we measured the lumbar and cervical regions separately in case degeneration affected CNS penetration. However, our data indicate no anatomical differences and, therefore, a homogeneous distribution of the nanoformulation throughout the spinal cord. Thus, in the histogram, we reported the fluorescent signal to be associated with the entire cord.

In recent decades, several drugs have been tested in preclinical ALS models targeting different molecular mechanisms with very limited results. One of the possible explanations for this failure is that the majority of the available compounds have poor BBB permeability.

On the other hand, a proof-of-concept study provided encouraging results through the invasive intracranial delivery of a promising anti-inflammatory compound [25]. It is, therefore, pivotal to investigate innovative methods for the release of compounds with therapeutic potential. Therefore, we evaluated the combination of the CNS-permeable ANANAS with an established anti-inflammatory drug, such as dexamethasone.

Figure 6 shows the results of the pharmacokinetics study carried out in SOD1^{G93A} mice treated intravenously with ANANAS-Dex at the onset of symptoms.

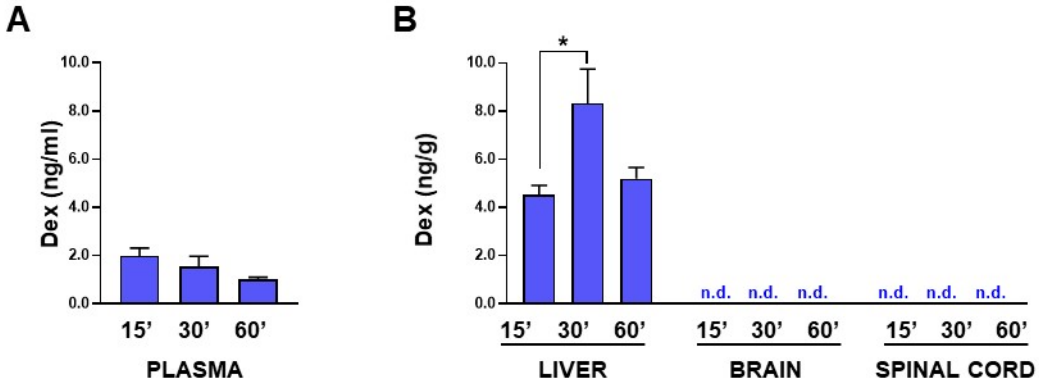

Figure 6. Pharmacokinetics study of free Dex in SOD1^{G93A} mice. Levels of free Dex measured in plasma (**A**) and liver, brain, and spinal cord (**B**) from SOD1^{G93A} mice at different time points (15, 30, 60 min) after intravenous administration of ANANAS-Dex. Dex released from the NP was measured by HPLC MS/MS with limit of quantitation (LoQ) equal to 0.01 ng/g for the brain and spinal cord, and 0.1 ng/mL for plasma. Data are mean ± SEM (n = four in each experimental group); * $p < 0.05$ by one-way ANOVA, Tukey's post hoc test. n.d.: not detected.

Similar to what was reported in healthy mice treated with ANANAS-Dex formulations, in the SOD1^{G93A} model, the majority of the free Dex was detected in the liver, whereas only low levels were found in the plasma (from 2 to 1 ng/mL over time, Figure 6A). This is explainable by the fact that, in these formulations, the drug is linked through an acid reversible linker to be released after the localization of the ANANAS in an acidic compartment (e.g., the liver macrophage endo/lysosomes or an inflamed tissue). Unfortunately, no free Dex was detected in the brain and spinal cord homogenates (Figure 6B) of the SOD1^{G93A} mice. This probably indicates that in these tissues, the conditions favouring the release of the drug from the linker were not met.

4. Discussion

The BBB is considered the major obstacle to the pharmacological treatment of CNS disorders. The tight junctions, together with the activity of several transporters at the barrier tissues, hinder penetration in CNS and the persistence of a very large amount of substances and drugs. More than 98% of small molecule candidate drugs and the majority of novel proteins and peptides are unable to reach the brain tissue due to poor permeability across the BBB [26]. Nanotechnologies through engineered and functionalized NPs may represent a suitable strategy to overcome this challenge. In this study, we detected the presence of ANANAS in the brain and spinal cord of healthy and SOD1^{G93A} mice, especially in the first interval of time after administration (30′ and 4 h), since an active process of clearance occurs 24 h after NP injection. Surprisingly, we found no signal related to the NPs in the brain and spinal cord of mice treated with ANANAS-ApoE. Such a paradoxical behaviour is not in agreement with what has been previously reported, especially in vitro, and supported the exploitation of the lipoprotein-associated receptor transport as an attractive strategy to shuttle drug molecules across the BBB. In particular, the low-density lipoprotein receptors (LDLR), characterized by a high affinity for ApoE, seemed functional to this aim. On the other hand, more recent in vivo data clearly demonstrated that, once in the bloodstream,

NPs underwent a series of events that dramatically hamper the brain endothelial targeting and the possibility to cross the BBB. In addition to the uptake by organ filters and renal clearance, circulating NPs are functionalized to enhance specific targeting and tend to lose their affinity over time. This reduced ability to bind the appropriate ligands or receptors is due to the coverage of the NP surface by circulating plasma proteins through a process widely known as "protein corona" [27]. The effect of plasma protein interaction with NPs is still a matter of debate. If there are much data confirming the shielding effect played by protein corona [28], on the other hand, a pre-formed, homogeneous protein corona around NPs using only ApoE increased the uptake by cancer cells overexpressing LDLR [29]. However, the efficacy of the BBB passage of this naturally functionalized complex is not known. A possible explanation for the poor BBB passage of our ANANAS-ApoE can be related to endogenous ApoE expression and its interaction with LDLR. LDLR is expressed in the liver, peripheral vasculature, brain, and other tissues [30,31], and in the brain is the most abundantly expressed neuron. Endogenous ApoE is primarily produced by glial cells [32]; therefore, we can hypothesize that astroglial ApoE can compete and interfere with the ligand exposed to the ANANAS surface and limit its CNS penetration.

Disease condition and progression have to be considered in NP design and CNS penetration. BBB/BSCB functional and structural impairments in neurological disorders have been reported in several studies [2]. In both patient and animal ALS models, damage in BBB/BSCB integrity and function, the downregulation of tight junction proteins, endothelial cell degeneration, and impairments in the micro vessels [3,33] have been observed. This suggests that in the pathological condition, BBB/BSCB may be more permeable to drugs. However, our results show the same kinetics of ANANAS for brain and spinal cord tissue in healthy and $SOD1^{G93A}$ mice. Non-functionalized ANANAS in both animal models shows the major penetrance in the brain and spinal cord immediately after NP injection, suggesting an equal CNS penetrance of NP in healthy and diseased mice. It has been reported that in ALS patients and in $SOD1^{G93A}$ mice, the P-glycoprotein and breast cancer resistance protein, two drug efflux transporters at the brain endothelium with remarkably broad specificity, increase their expression and function at the BBB and BSCB as the disease progresses [34]. Therefore, it is possible to hypothesize that despite the potential breakage of BBB, a disease-driven process of pharmaco-resistance limits the ability of the NPs to pass the BBB.

When using NPs for brain drug delivery, the first question that has to be answered is whether, after their passage through the BBB, they can reach the pathological target and selectively release the cargo. However, increased NP concentration in the brain (as in the case of ANANAS) does not necessarily imply that a selected drug load can be released in the affected areas. To better investigate the relationship between the carrier and cargo, we tested a Dex carrying an ANANAS formulation, in which the steroid was linked to the NPs by means of a pH-sensitive reversible linker. In previous work by our group, an ANANAS-Dex formulation with a strong tropism for the liver showed therapeutic efficacy in a murine model of autoimmune hepatitis [12,15]. A remarkable characteristic of ALS patients and animal models is the neuroinflammatory reaction consisting of activated glial cells and T cells which have been largely explored as a potential therapeutic target. In particular, free Dex and other corticosteroids have shown encouraging neuroprotective and anti-inflammatory effects in the mouse models of motor neuron diseases [16,17]. However, none have translated to an effective therapy in patients, probably because of their side effects [35–37]. Targeting steroids into the CNS by NPs may be a way to maximize the therapeutic effect while reducing unwanted side effects [38]. In the case of ANANAS, the strong tropism for CD68-positive phagocytic cells, in particular for those carrying Dex [12], was considered attractive for ALS and aimed to reduce microglial cell activation. Unfortunately, Dex levels that were released from NPs in the brain and spinal cord were under the detection limit. There are several possible reasons why the ANANAS penetration did not correspond to a detectable amount of Dex. The more probable is that the conditions that allowed the release of the steroid from the acid pH-sensitive linker were not met as it

otherwise occurred in the lysosomes of the liver macrophages reached by the ANANAS-Dex formulation investigated in our previous studies [12,15].

In conclusion, in the present study, we demonstrated that NP penetrance in CNS is not sufficient to enable efficient drug brain- and spinal cord-targeting. Specifically, the hydrazone bond used here for dexamethasone tethering to ANANAS was clearly not suitable for the release of the drug to the brain tissue. Therefore, in order to fully take advantage of the NP's ability to penetrate the CNS, a different strategy for drug tethering should be devised, which does not require the NP cell internalization for drug release but rather exploits brain parenchyma-specific enzymatic activities. On the other hand, this study demonstrates that drug measurement studies in vivo are a necessary step in the development of a nano-drug. Moreover, it highlights that NPs can be useful for improving the passage through biological barriers but may limit the interaction of the therapeutic compound with the specific target.

Supplementary Materials: The following supporting information can be downloaded at: https://www.mdpi.com/article/10.3390/cells11244003/s1.

Author Contributions: Conceptualization, M.M., V.B. and P.B.; Methodology, M.B.V., L.P., E.C., C.T., E.S., L.T., G.M., A.C., A.M., A.L. and A.P.; Formal Analysis, M.B.V., L.P. and L.T.; Investigation, M.B.V., L.P., E.C., C.T., L.T., G.M., A.C., A.L. and A.P.; Writing—Original Draft Preparation, M.B.V., L.P., M.M., V.B. and P.B.; Writing—Review and Editing, M.B.V., L.P., M.M., V.B. and P.B.; Supervision, M.M., V.B. and P.B.; Funding Acquisition, M.M., V.B. and P.B. All authors have read and agreed to the published version of the manuscript.

Funding: This research was funded by the Italian Ministry of Health, Ricerca Finalizzata 2013 project 02356221427 (RF-2013-02356221) (to P.B. and M.M.).

Institutional Review Board Statement: The "Mario Negri" Institute for Pharmacological Research IRCCS adheres to the principles set out in the following laws, regulations, and policies governing the care and use of laboratory animals: Italian Governing Law (D.lgs 26/2014; Authorisation n.19/2008-A issued March 6, 2008 by Ministry of Health); Mario Negri Institutional Regulations and Policies providing internal authorisation for persons conducting animal experiments (Quality Management System Certificate—UNI EN ISO 9001:2015—Reg. N° 6121); the NIH Guide for the Care and Use of Laboratory Animals (2011 edition), and EU directives and guidelines (EEC Council Directive 2010/63/UE). This work was reviewed by the internal Animal Care and Use Committee (IACUC) and then approved by the Italian "Istituto Superiore di Sanità" (code: 722/2017-PR).

Informed Consent Statement: Not applicable.

Data Availability Statement: The datasets presented in this study can be found in online repositories. The names of the repository/repositories and accession number(s) can be found below: 10.5281/zenodo.6504947.

Acknowledgments: We warmly thank Ilona Barker for editorial assistance and English revision.

Conflicts of Interest: The authors declare no conflict of interest. The funders had no role in the design of the study; in the collection, analyses, or interpretation of data; in the writing of the manuscript; or in the decision to publish the results.

References

1. Islam, Y.; Leach, A.G.; Smith, J.; Pluchino, S.; Coxon, C.R.; Sivakumaran, M.; Downing, J.; Fatokun, A.A.; Teixidò, M.; Ehtezazi, T. Physiological and Pathological Factors Affecting Drug Delivery to the Brain by Nanoparticles. *Adv. Sci.* **2021**, *8*, 2002085. [CrossRef] [PubMed]
2. De Vries, H.E.; Kooij, G.; Frenkel, D.; Georgopoulos, S.; Monsonego, A.; Janigro, D. Inflammatory Events at Blood-Brain Barrier in Neuroinflammatory and Neurodegenerative Disorders: Implications for Clinical Disease. *Epilepsia* **2012**, *53* (Suppl. 6), 45–52. [CrossRef] [PubMed]
3. Garbuzova-Davis, S.; Sanberg, P.R. Blood-CNS Barrier Impairment in ALS Patients versus an Animal Model. *Front. Cell. Neurosci.* **2014**, *8*, 21. [CrossRef] [PubMed]
4. Zhu, F.-D.; Hu, Y.-J.; Yu, L.; Zhou, X.-G.; Wu, J.-M.; Tang, Y.; Qin, D.-L.; Fan, Q.-Z.; Wu, A.-G. Nanoparticles: A Hope for the Treatment of Inflammation in CNS. *Front. Pharmacol.* **2021**, *12*, 683935. [CrossRef] [PubMed]

5. Wang, G.Y.; Rayner, S.L.; Chung, R.; Shi, B.Y.; Liang, X.J. Advances in Nanotechnology-Based Strategies for the Treatments of Amyotrophic Lateral Sclerosis. *Mater. Today Bio* **2020**, *6*, 100055. [CrossRef]
6. Duan, X.; Li, Y. Physicochemical Characteristics of Nanoparticles Affect Circulation, Biodistribution, Cellular Internalization, and Trafficking. *Small* **2013**, *9*, 1521–1532. [CrossRef]
7. Mahley, R.W. Central Nervous System Lipoproteins: ApoE and Regulation of Cholesterol Metabolism. *Arterioscler. Thromb. Vasc. Biol.* **2016**, *36*, 1305–1315. [CrossRef]
8. Re, F.; Cambianica, I.; Zona, C.; Sesana, S.; Gregori, M.; Rigolio, R.; La Ferla, B.; Nicotra, F.; Forloni, G.; Cagnotto, A.; et al. Functionalization of Liposomes with ApoE-Derived Peptides at Different Density Affects Cellular Uptake and Drug Transport across a Blood-Brain Barrier Model. *Nanomedicine* **2011**, *7*, 551–559. [CrossRef]
9. Morpurgo, M.; Radu, A.; Bayer, E.A.; Wilchek, M. DNA Condensation by High-Affinity Interaction with Avidin. *J. Mol. Recognit.* **2004**, *17*, 558–566. [CrossRef]
10. Pignatto, M.; Realdon, N.; Morpurgo, M. Optimized Avidin Nucleic Acid Nanoassemblies by a Tailored PEGylation Strategy and Their Application as Molecular Amplifiers in Detection. *Bioconjug. Chem.* **2010**, *21*, 1254–1263. [CrossRef]
11. Roncato, F.; Rruga, F.; Porcù, E.; Casarin, E.; Ronca, R.; Maccarinelli, F.; Realdon, N.; Basso, G.; Alon, R.; Viola, G.; et al. Improvement and Extension of Anti-EGFR Targeting in Breast Cancer Therapy by Integration with the Avidin-Nucleic-Acid-Nano-Assemblies. *Nat. Commun.* **2018**, *9*, 4070. [CrossRef] [PubMed]
12. Violatto, M.B.; Casarin, E.; Talamini, L.; Russo, L.; Baldan, S.; Tondello, C.; Messmer, M.; Hintermann, E.; Rossi, A.; Passoni, A.; et al. Dexamethasone Conjugation to Biodegradable Avidin-Nucleic-Acid-Nano-Assemblies Promotes Selective Liver Targeting and Improves Therapeutic Efficacy in an Autoimmune Hepatitis Murine Model. *ACS Nano* **2019**, *13*, 4410–4423. [CrossRef] [PubMed]
13. Bigini, P.; Previdi, S.; Casarin, E.; Silvestri, D.; Violatto, M.B.; Facchin, S.; Sitia, L.; Rosato, A.; Zuccolotto, G.; Realdon, N.; et al. In Vivo Fate of Avidin-Nucleic Acid Nanoassemblies as Multifunctional Diagnostic Tools. *ACS Nano* **2014**, *8*, 175–187. [CrossRef]
14. Garbuzova-Davis, S.; Saporta, S.; Haller, E.; Kolomey, I.; Bennett, S.P.; Potter, H.; Sanberg, P.R. Evidence of Compromised Blood-Spinal Cord Barrier in Early and Late Symptomatic SOD1 Mice Modeling ALS. *PLoS ONE* **2007**, *2*, e1205. [CrossRef] [PubMed]
15. Ongaro, A.; Violatto, M.B.; Casarin, E.; Pellerani, I.; Marchini, G.; Ribaudo, G.; Salmona, M.; Carbone, M.; Passoni, A.; Gnodi, E.; et al. The Mode of Dexamethasone Decoration Influences Avidin-Nucleic-Acid-Nano-Assembly Organ Biodistribution and in Vivo Drug Persistence. *Nanomedicine* **2022**, *40*, 102497. [CrossRef] [PubMed]
16. González Deniselle, M.C.; González, S.L.; De Nicola, A.F. Cellular Basis of Steroid Neuroprotection in the Wobbler Mouse, a Genetic Model of Motoneuron Disease. *Cell. Mol. Neurobiol.* **2001**, *21*, 237–254. [CrossRef]
17. Tokuda, E.; Watanabe, S.; Okawa, E.; Ono, S. Regulation of Intracellular Copper by Induction of Endogenous Metallothioneins Improves the Disease Course in a Mouse Model of Amyotrophic Lateral Sclerosis. *Neurotherapeutics* **2015**, *12*, 461–476. [CrossRef] [PubMed]
18. Green, N.M. Avidin. In *Advances in Protein Chemistry*; Elsevier: Amsterdam, The Netherlands, 1975; Volume 29, pp. 85–133, ISBN 978-0-12-034229-7.
19. Sims, G.E.C.; Snape, T.J. A Method for the Estimation of Polyethylene Glycol in Plasma Protein Fractions. *Anal. Biochem.* **1980**, *107*, 60–63. [CrossRef]
20. Lauranzano, E.; Pozzi, S.; Pasetto, L.; Stucchi, R.; Massignan, T.; Paolella, K.; Mombrini, M.; Nardo, G.; Lunetta, C.; Corbo, M.; et al. Peptidylprolyl Isomerase A Governs TARDBP Function and Assembly in Heterogeneous Nuclear Ribonucleoprotein Complexes. *Brain* **2015**, *138*, 974–991. [CrossRef]
21. Filareti, M.; Luotti, S.; Pasetto, L.; Pignataro, M.; Paolella, K.; Messina, P.; Pupillo, E.; Filosto, M.; Lunetta, C.; Mandrioli, J.; et al. Decreased Levels of Foldase and Chaperone Proteins Are Associated with an Early-Onset Amyotrophic Lateral Sclerosis. *Front. Mol. Neurosci.* **2017**, *10*, 99. [CrossRef]
22. Luotti, S.; Pasetto, L.; Porcu, L.; Torri, V.; Elezgarai, S.R.; Pantalone, S.; Filareti, M.; Corbo, M.; Lunetta, C.; Mora, G.; et al. Diagnostic and Prognostic Values of PBMC Proteins in Amyotrophic Lateral Sclerosis. *Neurobiol. Dis.* **2020**, *139*, 104815. [CrossRef] [PubMed]
23. Damonte, G.; Salis, A.; Rossi, L.; Magnani, M.; Benatti, U. High Throughput HPLC-ESI-MS Method for the Quantitation of Dexamethasone in Blood Plasma. *J. Pharm. Biomed. Anal.* **2007**, *43*, 376–380. [CrossRef] [PubMed]
24. Yuan, Y.; Zhou, X.; Li, J.; Ye, S.; Ji, X.; Li, L.; Zhou, T.; Lu, W. Development and Validation of a Highly Sensitive LC-MS/MS Method for the Determination of Dexamethasone in Nude Mice Plasma and Its Application to a Pharmacokinetic Study: Quantitative Determination of Dexamethasone in Nude Mouse Plasma. *Biomed. Chromatogr.* **2015**, *29*, 578–583. [CrossRef] [PubMed]
25. Pasetto, L.; Pozzi, S.; Castelnovo, M.; Basso, M.; Estevez, A.G.; Fumagalli, S.; De Simoni, M.G.; Castellaneta, V.; Bigini, P.; Restelli, E.; et al. Targeting Extracellular Cyclophilin A Reduces Neuroinflammation and Extends Survival in a Mouse Model of Amyotrophic Lateral Sclerosis. *J. Neurosci.* **2017**, *37*, 1413–1427. [CrossRef] [PubMed]
26. Pardridge, W.M. The Blood-Brain Barrier: Bottleneck in Brain Drug Development. *Neurotherapeutics* **2005**, *2*, 3–14. [CrossRef] [PubMed]
27. Salvati, A.; Pitek, A.S.; Monopoli, M.P.; Prapainop, K.; Bombelli, F.B.; Hristov, D.R.; Kelly, P.M.; Åberg, C.; Mahon, E.; Dawson, K.A. Transferrin-Functionalized Nanoparticles Lose Their Targeting Capabilities When a Biomolecule Corona Adsorbs on the Surface. *Nat. Nanotechnol.* **2013**, *8*, 137–143. [CrossRef]

28. Cox, A.; Andreozzi, P.; Dal Magro, R.; Fiordaliso, F.; Corbelli, A.; Talamini, L.; Chinello, C.; Raimondo, F.; Magni, F.; Tringali, M.; et al. Evolution of Nanoparticle Protein Corona across the Blood–Brain Barrier. *ACS Nano* **2018**, *12*, 7292–7300. [CrossRef]
29. Yeo, E.L.L.; Cheah, J.U.-J.; Thong, P.S.P.; Soo, K.C.; Kah, J.C.Y. Gold Nanorods Coated with Apolipoprotein E Protein Corona for Drug Delivery. *ACS Appl. Nano Mater.* **2019**, *2*, 6220–6229. [CrossRef]
30. Kong, W.-J.; Liu, J.; Jiang, J.-D. Human Low-Density Lipoprotein Receptor Gene and Its Regulation. *J. Mol. Med.* **2006**, *84*, 29–36. [CrossRef]
31. Zhang, B.; Sun, X.; Mei, H.; Wang, Y.; Liao, Z.; Chen, J.; Zhang, Q.; Hu, Y.; Pang, Z.; Jiang, X. LDLR-Mediated Peptide-22-Conjugated Nanoparticles for Dual-Targeting Therapy of Brain Glioma. *Biomaterials* **2013**, *34*, 9171–9182. [CrossRef]
32. Kim, J.; Basak, J.M.; Holtzman, D.M. The Role of Apolipoprotein E in Alzheimer's Disease. *Neuron* **2009**, *63*, 287–303. [CrossRef] [PubMed]
33. Zhong, Z.; Deane, R.; Ali, Z.; Parisi, M.; Shapovalov, Y.; O'Banion, M.K.; Stojanovic, K.; Sagare, A.; Boillee, S.; Cleveland, D.W.; et al. ALS-Causing SOD1 Mutants Generate Vascular Changes Prior to Motor Neuron Degeneration. *Nat. Neurosci.* **2008**, *11*, 420–422. [CrossRef] [PubMed]
34. Jablonski, M.R.; Jacob, D.A.; Campos, C.; Miller, D.S.; Maragakis, N.J.; Pasinelli, P.; Trotti, D. Selective Increase of Two ABC Drug Efflux Transporters at the Blood–Spinal Cord Barrier Suggests Induced Pharmacoresistance in ALS. *Neurobiol. Dis.* **2012**, *47*, 194–200. [CrossRef] [PubMed]
35. Werdelin, L.; Boysen, G.; Jensen, T.S.; Mogensen, P. Immunosuppressive Treatment of Patients with Amyotrophic Lateral Sclerosis. *Acta Neurol. Scand.* **1990**, *82*, 132–134. [CrossRef]
36. Fournier, C.N.; Schoenfeld, D.; Berry, J.D.; Cudkowicz, M.E.; Chan, J.; Quinn, C.; Brown, R.H.; Salameh, J.S.; Tansey, M.G.; Beers, D.R.; et al. An Open Label Study of a Novel Immunosuppression Intervention for the Treatment of Amyotrophic Lateral Sclerosis. *Amyotroph. Lateral Scler. Frontotemporal Degener.* **2018**, *19*, 242–249. [CrossRef]
37. Van Es, M.A.; Van Eijk, R.P.A.; Bunte, T.M.; Van Den Berg, L.H. A Placebo-Controlled Trial to Investigate the Safety and Efficacy of Penicillin G/Hydrocortisone in Patients with ALS (PHALS Trial). *Amyotroph. Lateral Scler. Frontotemporal Degener.* **2020**, *21*, 584–592. [CrossRef]
38. Evans, M.C.; Gaillard, P.J.; de Boer, M.; Appeldoorn, C.; Dorland, R.; Sibson, N.R.; Turner, M.R.; Anthony, D.C.; Stolp, H.B. CNS-Targeted Glucocorticoid Reduces Pathology in Mouse Model of Amyotrophic Lateral Sclerosis. *Acta Neuropathol. Commun.* **2014**, *2*, 66. [CrossRef]

nanomaterials

MDPI

Article

Variations in Biodistribution and Acute Response of Differently Shaped Titania Nanoparticles in Healthy Rodents

Martina B. Violatto [1], Giovanni Sitia [2], Laura Talamini [1], Annalisa Morelli [1], Ngoc Lan Tran [2], Qian Zhang [3], Atif Masood [4], Beatriz Pelaz [5], Indranath Chakraborty [6], Daxiang Cui [3], Wolfgang J. Parak [7], Mario Salmona [1], Neus G. Bastús [8,9], Victor Puntes [8,9,10,11] and Paolo Bigini [1,*]

1 Department of Molecular Biochemistry and Pharmacology, Istituto di Ricerche Farmacologiche Mario Negri IRCCS, Via Mario Negri 2, 20156 Milano, Italy; martina.violatto@marionegri.it (M.B.V.); laura.talamini@marionegri.it (L.T.); annalisa.morelli@marionegri.it (A.M.); mario.salmona@marionegri.it (M.S.)
2 Experimental Hepatology Unit, Division of Immunology, Transplantation and Infectious Diseases, IRCCS San Raffaele Scientific Institute, Via Olgettina 58, 20132 Milano, Italy; sitia.giovanni@hsr.it (G.S.); tran.ngoclan@hrs.it (N.L.T.)
3 Department of Instrument Science and Engineering, School of Electronic Information and Electrical Engineering, Institute of Nano Biomedicine and Engineering, Shanghai Jiao Tong University, 800 Dongchuan RD, Shanghai 200240, China; qianzhang0130@163.com (Q.Z.); dxcui@sjtu.edu.cn (D.C.)
4 Karachi Institute of Radiotherapy and Nuclear Medicine (KIRAN), Karachi 75530, Pakistan; atif_cancer@hotmail.com
5 Centro Singular de Investigación en Química Biolóxica e Materiais Moleculares (CiQUS), Departamento de Química Inorgánica, Universidade de Santiago de Compostela, 15782 Santiago de Compostela, Spain; beatriz.pelaz@usc.es
6 School of Nano Science and Technology, Indian Institute of Technology Kharagpur, Kharagpur 721302, India; chemistry.indra@alumni.iitm.ac.in
7 Center for Hybrid Nanostructures (CHyN), Universität Hamburg, Luruper Chaussee 149, 22607 Hamburg, Germany; wolfgang.parak@uni-hamburg.de
8 Vall d'Hebron Institut de Recerca (VHIR), 08035 Barcelona, Spain; neus.bastus@icn2.cat (N.G.B.); victor.puntes.icn@gmail.com (V.P.)
9 Institució Catalana de Recerca i Estudis Avançats (ICREA), 08010 Barcelona, Spain
10 Institut Català de Nanociència i Nanotecnologia (ICN2), Consejo Superior de Investigaciones Científicas CSIC and The Barcelona Institute of Science and Technology (BIST), Campus UAB, Bellaterra, 08036 Barcelona, Spain
11 CIBER en Bioingeniería, Biomateriales y Nanomedicina, CIBER-BBN, 28029 Madrid, Spain
* Correspondence: paolo.bigini@marionegri.it; Tel.: +39-02-39014221

Abstract: Titanium dioxide nanoparticles (TiO_2 NPs) are one of the main sources of the nanoparticulate matter exposure to humans. Although several studies have demonstrated their potential toxic effects, the real nature of the correlation between NP properties and their interaction with biological targets is still far from being fully elucidated. Here, engineered TiO_2 NPs with various geometries (bipyramids, plates, and rods) have been prepared, characterized and intravenously administered in healthy mice. Parameters such as biodistribution, accumulation, and toxicity have been assessed in the lungs and liver. Our data show that the organ accumulation of TiO_2 NPs, measured by ICP-MS, is quite low, and this is only partially and transiently affected by the NP geometries. The long-lasting permanence is exclusively restricted to the lungs. Here, bipyramids and plates show a higher accumulation, and interestingly, rod-shaped NPs are the most toxic, leading to histopathological pulmonary alterations. In addition, they are also able to induce a transient increase in serum markers related to hepatocellular injury. These results indicate that rods, more than bipyramidal and spherical geometries, lead to a stronger and more severe biological effect. Overall, small physico-chemical differences can dramatically modify both accumulation and safety.

Keywords: titanium dioxide nanomaterial; physico-chemical properties; biodistribution; nanotoxicity

check for updates

Citation: Violatto, M.B.; Sitia, G.; Talamini, L.; Morelli, A.; Tran, N.L.; Zhang, Q.; Masood, A.; Pelaz, B.; Chakraborty, I.; Cui, D.; et al. Variations in Biodistribution and Acute Response of Differently Shaped Titania Nanoparticles in Healthy Rodents. *Nanomaterials* **2023**, *13*, 1174. https://doi.org/10.3390/nano13071174

Academic Editor: Saura Sahu

Received: 7 March 2023
Revised: 22 March 2023
Accepted: 23 March 2023
Published: 25 March 2023

Copyright: © 2023 by the authors. Licensee MDPI, Basel, Switzerland. This article is an open access article distributed under the terms and conditions of the Creative Commons Attribution (CC BY) license (https://creativecommons.org/licenses/by/4.0/).

1. Introduction

The peculiar physico-chemical properties of engineered nanoparticles (NPs), such as composition, size, shape and surface features, make them attractive for use in the medical, agricultural, industrial and manufacturing fields [1]. These unique properties not only determine their utility for several applications, but also their toxicity [2]. Although hundreds of tons of NPs are produced and industrially processed, the connection between nanomaterial properties (in given exposure scenarios) and elementary biological responses (associated with pathological responses) are poorly known, and are used to signpost potential for hazard. In particular, knowledge of the biological interaction between different NPs derived from large-scale production processes and biological matrices (cells, tissues, whole animals) is a priority for defining their real impact on human health [3]. In the last decade, an increasing body of evidence has demonstrated the potential effect of NPs in respiratory and digestive systems, and their ability to enhance inflammatory responses in peripheral organs [4–6]. Thus, NP toxicology and the basis for their interaction with living matter became of great interest. Although the results arising from in silico and in vitro analyses are definitely pivotal to gain initial knowledge on NPs' potential toxicity (depending on their geometry or surface charge), they are quite often hardly transferable to mammals [7]. The main reasons for this mismatch stem from the impossibility of recapitulating, either in cells or through specific algorithms, the complex and only partially known interplay resulting from exposure to the final destination (accumulation, transformations—such as protein corona—clearance, and toxicity) of the NPs in multicellular organisms. In a recent study, we demonstrated the strong influence of the geometry on the biodistribution of gold NPs [8]. Interestingly, neither size nor shape led to a relevant toxicity in treated mice. Similarly, changes in the surface and the shape of gold NPs strongly influenced the biodistribution but led to a minimal effect on the overall blood count and an almost complete absence of modifications in basal hematochemistry (creatinine, bilirubin, transaminases and uric acid) [9].

Gold NPs can be considered attractive for nanomedicine due to their theranostic properties. However, these results cannot so easily be translated to assess the relationship between geometry and in vivo effect in the field of nanosafety. Indeed, other materials are produced and dispersed by environmental pollution or industrial production. Among this broad range of materials, titanium dioxide NPs (TiO_2 NPs) seem to play an even greater role in nanosafety. Due to their physico-chemical properties, TiO_2 NPs are used as food additives (chewing gums, candies, sweets, and cheeses), high refractive index products (coatings, plastics, paints), photocatalyst agents (in water treatment and air purification), sunscreens, and toothpastes [10–12]. Titanium oxide is chemically stable and very difficult to dissolve. Therefore, its inertness and the persistence inside the body may represent a critical point concerning its safety, and large-scale production plans should pay great attention to this aspect.

Similar to other nanomaterials and chemicals, its risk is strongly influenced by the mutual influence of a series of different factors, including the geometry of the NPs. In a recent study carried out in C. elegans (a nematode universally considered a reliable model of human pathophysiology [13]), we reported that rod-shaped NPs were the most toxic, greatly impairing pharyngeal function, reproduction and larval growth, whereas bipyramidal and spherical shapes were less toxic, even if no difference in terms of biodistribution and accumulation were found.

The route of exposure obviously affects the in vivo absorption, biodistribution, and toxicity of NPs. Although the main routes of entry of NPs are skin, airways or digestive tract, it is important to emphasize that a great source of risk is tightly regulated by their penetration into the bloodstream and their consequent overall distribution in many organs and cells [14]. To this end, the influence of the geometry of different synthesized TiO_2 NPs (bipyramids, plates, and rods) and their fate in terms of biodistribution, clearance, toxicity were investigated after a single intravenous treatment in healthy immunocompetent mice.

2. Materials and Methods

2.1. NP Synthesis and Characterization

Shape-controlled synthesis of TiO_2 NPs was achieved following a modified nonaqueous surfactant-assisted synthesis reported by Gordon et al. [15]. TiF_4, $TiCl_4$ and/or TTIP were used as Ti precursors, ODE (1-octadecene) as a solvent, OLA (oleic acid) as a surfactant, and OLAM (Oleylamine) or ODOL (1-octadecanol) as cosurfactants. The control of the final morphology is achieved by the choice of titanium precursor and the co-surfactant. All syntheses were performed using standard Schlenk line techniques under a nitrogen atmosphere.

Chemicals. Titanium(IV) fluoride (TiF_4, 99%, Acros, Geel, Belgium #7783633), titanium(IV) chloride ($TiCl_4$, 99%, Strem, Bischheim, France), #221150), titanium(IV) isopropoxide (TTIP, 97%) 1-octadecene (90%, Alfa Aesar, Kandel, Germany, #L11004) (1-ODE), 1-octadecanol (1-ODOL, 97%), oleylamine (OLAM, 70%, Acros, Geel, Belgium, #129541000), oleic acid (OLA, 90%, Sigma Aldrich, Milan, Italy, #O1008), and tetradecylphosphonic acid (TDPA,98%, Sigma Aldrich, Milan, Italy, #736414) were used as obtained from the supplier.

Preparation of Ti stock solutions. TiF_4 stock solution consists of 0.2 M TiF_4 and 1.0 M OLA in 1-ODE. $TiCl_4$ stock solution consists of 0.2 M $TiCl_4$ and 1.0 M OLA in 1-ODE. TTIP stock solution consists of 0.2 M TTIP and 1.0 M OLA in 1-ODE. The TiF_4 stock solution is stirred on a hot plate set to 80 °C to promote the dissolution of TiF_4. Once dissolved, the TiF_4 stock solution is orange-brown, and the $TiCl_4$ and TTIP stock solutions are dark brown.

Synthesis of TiO_2 NPs (bipyramids). Highly monodisperse anatase TiO_2 tetragonal bipyramids (10 nm side length) were synthesized using a mixture of TiF_4/$TiCl_4$ precursors in the presence of OLAM.

Synthesis of TiO_2 NPs (rods). Highly monodisperse brookite TiO_2 rods (50 nm side length, 15 nm width) were synthesized using TTIP as a precursor in the presence of OLAM.

Synthesis of TiO_2 NPs (plates). Highly monodisperse TiO_2 plates (50 nm side length) were synthesized using a mixture of TiF_4/$TiCl_4$ precursors in the presence of 1-ODOL.

General Synthetic Procedure. A general procedure for the preparation of TiO_2 NPs proceeds as follows. In a 125 mL flask, 30 mmol of cosurfactant (OLAM or 1-ODOL), 10.2 mL of 1-ODE, and 0.48 mL (1.5 mmol) of OLA are combined and degassed at 120 °C for 1 h. For a 1:1 mixture, TiF_4 and $TiCl_4$ stock solutions are mixed at equal volume in the glovebox. After degassing the flask, 1.5 mL of the desired stock solution (or mixed stock solution) is added at 60 °C. Then, the solution is quickly heated to 290 °C and held at this temperature for 10 min to allow for the formation of seed NPs. An 8 mL portion of the chosen stock solution is then pumped into the flask, which is kept at 290 °C, with a rate of 0.3 mL·min^{-1}, using a syringe pump. Afterward, the heating mantle is removed, and the flask is left to cool naturally to ambient temperature. After the synthesis, the reaction contents are first diluted with a small volume of toluene and centrifuged at 6000 rpm to separate the NPs by precipitation. The NPs are then re-dispersed through the addition of toluene and 100 µL of OLAM with sonication. Insoluble surfactant and agglomerated NPs are removed through centrifugation (i.e., the precipitate is discarded and the supernatant containing the dispersed NPs is kept). A mixture of 2-propanol and methanol is added to precipitate the NPs, and centrifugation at 6000 rpm is used to precipitate the NPs before exchanging surfactants and redispersing them in water (see next section). This washing process was repeated twice.

Ligand exchange of the TiO_2 NPs. The OLA/OLAM/ODOL ligands present in the TiO_2 NPs were exchanged with an alkylphosphonic acid via a standard ligand exchange process to further enhance their colloidal stabilities [16]. Firstly, the OLA/OLAM/ODOL coated TiO_2 NPs, as dispersed in toluene, were precipitated with methanol/ethanol by centrifugation (1000 rpm, 5 min), followed by discarding of the supernatant and redissolution of the NPs in $CHCl_3$. This washing step was repeated until the TiO_2 NPs could no longer be redispersed in $CHCl_3$ (at least six times). In this case, one can consider that the TiO_2 NPs had lost solubility through the removal of most of the original capping ligands from their surface.

Then, 2 mL of $CHCl_3$ was added to the NP precipitate under vigorous magnetic stirring at room temperature, and 1 mL of TDPA 0.2 M solution in $CHCl_3$ was added, dropwise, until the solution turned transparent. The sample was continually stirred overnight. The next day, the NPs were precipitated by methanol and centrifugation (1000 rpm, 5 min), and the supernatant was discarded. After re-dispersion of the NPs in $CHCl_3$, the washing process was repeated again by adding methanol, centrifugation, and redissolution in $CHCl_3$.

Phase transfer of TDPA coated TiO_2 NPs to water by overcoating with an amphiphilic polymer. The amphiphilic polymer poly(isobutylene–alt–maleic anhydride)–graft–dodecyl (PMA; 0.5 M monomer unit concentration in $CHCl_3$) [16,17] was added into NPs; the solution of TDPA coated TiO_2 NPs in $CHCl_3$, and more $CHCl_3$ was added to dilute the mixture according to previously published protocols [16–18]. The ratio of added PMA monomer units per effective NP surface ($R_{p/area}$) was optimized experimentally. In the case of the platelet-shape TiO_2 NPs, for example, ratio $R_{p/area}$ = 600 nm^{-2} was used. Then, the solution was placed in the rotavapor at 60 °C for 10 min, the temperature was increased to 70 °C at 950 mbar, and the solvent (i.e., chloroform) was slowly evaporated until the sample was completely dried. The resulting solid NP film in the flask was redissolved under vigorous stirring in SBB12 buffer (sodium borate buffer, 50 mM, pH 12), until the solution turned clear [16]. Finally, the sample was concentrated with 100 kDa ultrafiltration filters (Sartorius Stedim, Goettingen, Germany) by centrifugation. The eventual excess of polymer micelles was removed through agarose gel electrophoresis [19]. In a final step, the solvent was exchanged to Milli-Q water by ultrafiltration. Dynamic light scattering (DLS) was used as a control to verify that the polymer-coated TiO_2 NPs were well dispersed [16].

2.2. Animals and Treatments

The "Mario Negri" Institute for Pharmacological Research IRCCS adheres to the principles set out in the following laws, regulations, and policies governing the care and use of laboratory animals: Italian Governing Law (D.lgs 26/2014; Authorisation n.19/2008-A issued 6 March 2008 by Ministry of Health); Mario Negri Institutional Regulations and Policies providing internal authorization for persons conducting animal experiments (Quality Management System Certificate, UNI EN ISO 9001:2015, Reg. No. 6121); the NIH Guide for the Care and Use of Laboratory Animals (2011 edition), and EU directives and guidelines (EEC Council Directive 2010/63/UE). This work was reviewed by the IRCCS-IRFMN Animal Care and Use Committee (IACUC) and then approved by the Italian "Istituto Superiore di Sanità" (code: 42/2016-PR).

Eight-week-old male CD1 mice were housed in 'specific pathogen-free' animal rooms at a constant temperature of 21 ± 1 °C, humidity 55 ± 10%, with a 12 h light/dark cycle and ad libitum access to food and water. Mice were randomly divided into three groups receiving bipyramids, plates, and rods, respectively (n = 9 for each experimental group). Briefly, all animals received the same dose of each NPs preparation (6 mg/kg), diluted in 200 µL of injection grade distilled water, by intravenous injection. At the selected time points (pre injection, 1, 12, 24, 96, and 168 h), mice were anesthetized and blood was taken by retro orbital bleeding for complete blood counts, and the serum analyzed for markers of toxicity. Furthermore, at 1, 24, and 168 h after NPs injection, three mice for each group were killed and their organs collected for histological analysis.

2.3. ICP-MS Sample Preparation and %ID Calculation

Inductively coupled plasma mass spectrometry (ICP-MS) analysis, in which the amount of elemental Ti was determined, was carried out following previously published protocols for other NP materials [8,17,20,21]. The samples were first digested by the addition of 3 mL of ultra-pure (67 wt%) HNO_3 (Fisher Chemical, Milan, Italy) under constant agitation in 50 mL falcon tubes for 72 h at 22°C, until the solution became clear and no organics (i.e., rests of tissue) were left in the tube. Some 100 µL of these digested samples was taken and further digested with 100 µL of HF acid for 48 h in order to digest the TiO_2 NPs. Before ICP-MS measurements, the samples were diluted additionally by a factor of

10, using a low matrix consisting of 2 wt% HCl. This actually enhances the detection limit as well as reducing the background over all samples, and it ensures the protection of the machinery from corrosive HF. All vials and working materials had been either cleaned using freshly prepared aqua regia for 2 h, followed by boiling in Milli-Q water, or were sterile and clean non-reusable consumables. The samples were introduced into the ICP-MS setup through a perfluoroalkoxy-alkane (PFA)-based microflow spray chamber, wherein the aqueous sample was nebulized, introduced into the argon gas flow, and transported to the torch, where it was ionized in an argon plasma of around 6000 °C. After ionization, the sample was presorted using an omega lens, separated element-wise in a quadrupole field through the mass to charge rate, sorted again using kinetic barriers and a charged lens system, and finally detected with either an analog or a digital detector depending on the count rate. The percent of injected dose (%ID) was calculated as the percentage of Ti found in one organ referring to the total amount of injected Ti [17].

2.4. Blood Analysis and Histopathology

The extent of hepatocellular injury and toxicity was monitored by measuring serum alanine aminotransferase (sALT). Markers of cell toxicity such as serum aspartate aminotransferase (sAST) and lactate dehydrogenase (LDH) activity were measured at the indicated time points after NP injection. sALT, sAST and LDH activity were measured using a IFCC (International Federation of Clinical Chemistry and Laboratory Medicine) optimized kinetic UV method in an Aries chemical analyzer (Werfen Instrumentation Laboratory S.p.A., Milan, Italy) and expressed as U/L (Units/Liter). Complete cell counts were measured in whole blood collected in EDTA coated microvettes (Sarstedt, Nümbrecht, Germany) utilizing an automated cell counter (IDEXX Procyte Dx, IDEXX Laboratories).

Each analysis was validated by a certified biochemical chemistry and haematology specialist using quality control serums (CQI) or blood, in the San Raffaele Mouse Clinic (http://research.hsr.it/en/services/mouse-clinic/hematologic-testing.html, accessed on 21 October 2021).

At time of autopsy for each mouse, different organs were sampled, fixed in zinc-formalin, processed, embedded in paraffin, cut and stained with hematoxylin/eosin, or further processed for immunohistochemical analyses as previously described [22]. A Picrosirius Red (0.5 g Sirius Red F3B (C.I. 35782) + 500 mL picric acid solution—Sigma Aldrich, Milan, Italy) staining method was performed to reveal collagen deposition. Immunohistochemical staining was performed utilizing the following antibody: anti-F4/80 (clone A3-1, AbD Serotec, Milan, Italy). All images were acquired using an Aperio Scanscope CS2 system (Leica Biosystems, Milan, Italy) available at the SRSI Advanced Light and Electron Microscopy BioImaging Center (ALEMBIC). The images were identified as representative areas of interest within the total area of the specimen analyzed and exported as ImageScope snapshots.

2.5. Statistics

All the tests carried out for the physico-chemical characterization of the NPs were performed at least in triplicates. For in vivo experiments, the number of animals sacrificed at each data point was minimized (n = 3) according to the 3Rs principle. p values < 0.05 were considered statistically significant and reported on graphs. Data are presented as mean values ± standard error of the mean (SEM) and analyzed using GraphPad Prism Software (version 7). The differences in Ti levels measured by ICP-MS were analyzed with a one-way ANOVA followed by a Bonferroni post hoc test (** $p < 0.01$, *** $p < 0.001$). For blood cell analysis, a one-way ANOVA followed by Dunn's post hoc test was carried out, (* $p < 0.05$, ** $p < 0.005$), while for hepatic toxicity, an unpaired T-test was carried out (** $p < 0.01$).

3. Results

3.1. Synthesis and Characterization

For this study, we synthesized and characterized a set of TiO_2 NPs. Figures 1–3 report representative images of bipyramids, rods, and plates, respectively, acquired using scanning transmission electron microscopy (STEM).

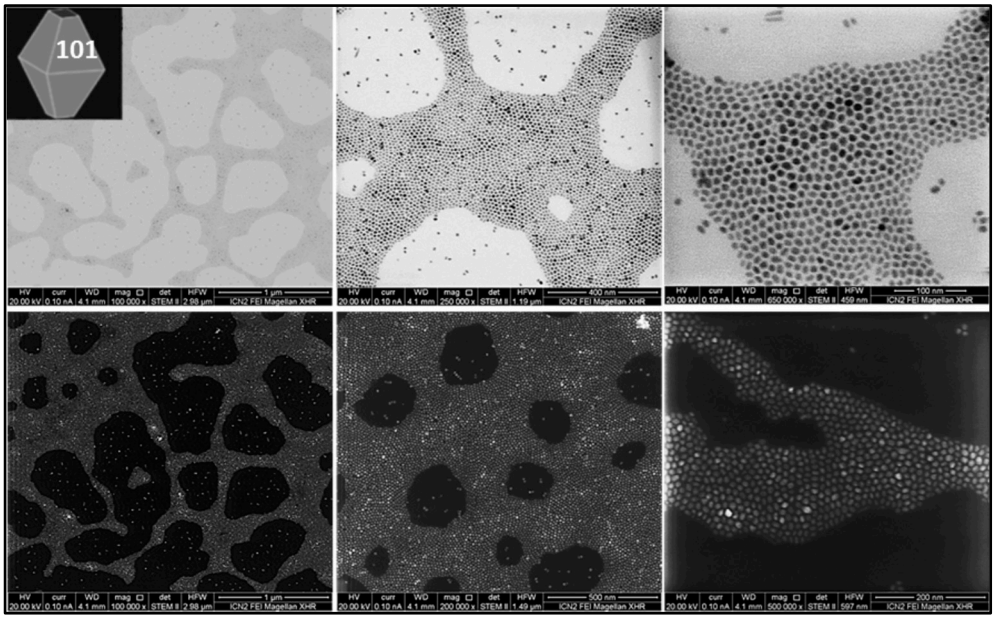

Figure 1. TiO_2 bipyramids. STEM images of TiO_2 NPs synthesized using TiF_4 as a precursor in the presence of OLAM. In the presence of the co-surfactant OLAM, TiF_4 produces highly uniform tetragonal bipyramidal anatase NPs (10 nm side length), which are significantly truncated perpendicular to the [001] direction.

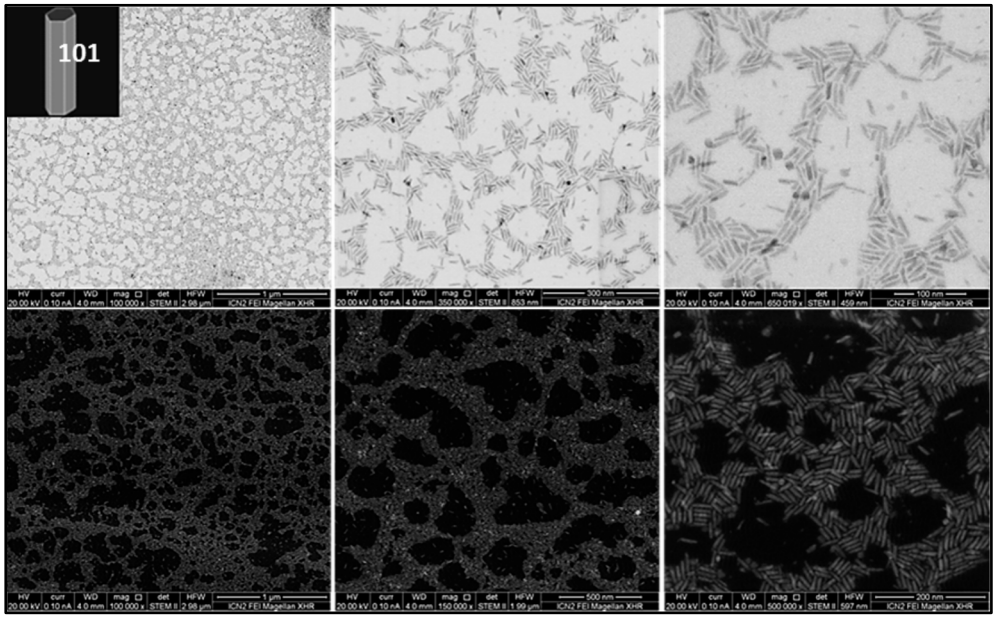

Figure 2. TiO_2 rods. STEM images of TiO_2 NPs synthesized using TTIP as precursor in the presence of OLAM. In the presence of the co-surfactant OLAM, pure phase brookite rods (50 nm side length, 15 nm width) are formed using $TiCl_4$ as precursor.

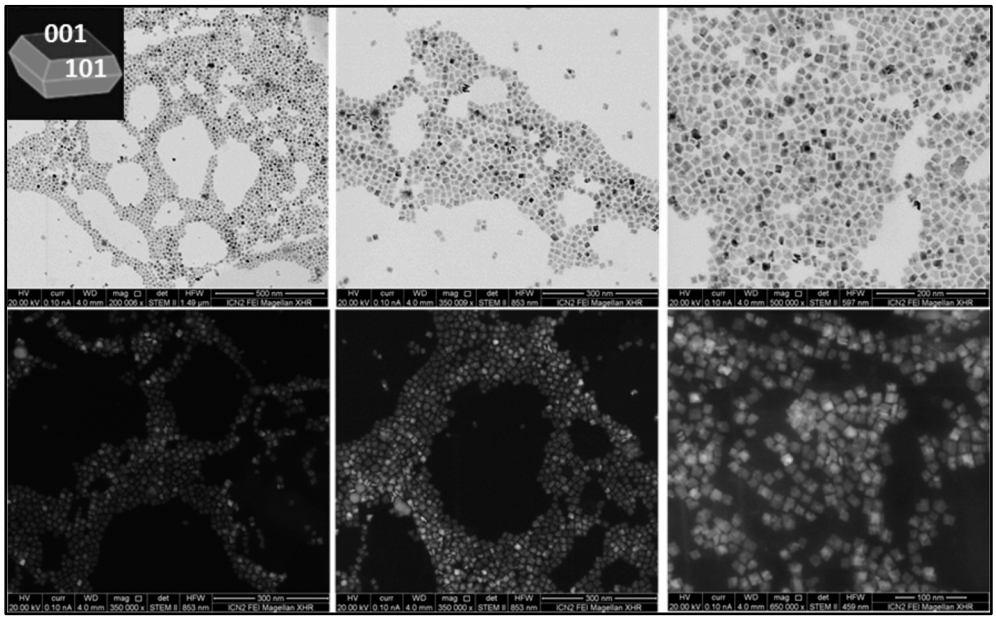

Figure 3. TiO_2 plates. STEM images of TiO_2 NPs synthesized using $TiF_4/TiCl_4$ as precursors in the presence of 1-ODOL. The use of the mixed $TiF_4/TiCl_4$ precursor in combination with 1-ODOL forms plates (50 nm side length, 10 nm width).

The table below (Table 1) clearly reports TiO_2 NP size. Measurements were performed counting at least 100 particles, and the average size and the standard distribution were obtained.

Table 1. Dimensional characterization of TiO_2 NPs administered to mice.

Sample	Size Distribution
TiO_2 bipyramids	7.5 ± 0.7 nm side
TiO_2 rods	27.8 ± 2.1 nm length 6.3 ± 1.0 nm width
TiO_2 plates	13.6 ± 2.1 nm side 4.5 ± 0.3 nm thickness

3.2. Influence of the "Shape" on TiO_2 NP Biodistribution

To quantitatively determine the biodistribution of the NPs in the main organs, ICP-MS analysis of the tissue digests was performed to measure the elemental titanium concentrations. Figure 4 shows the obtained results reported as percentage of the injected dose (%ID) in mice sacrificed at 1, 24, and 168 h after a single administration of bipyramids, rods, and plates. Vehicle-treated mice (n = 3) were intravenously injected with normal saline and studied as an inner control to exclude a bias due to the natural presence of titanium in the body. As expected, no titanium was detected in all tissues of saline-administered mice (data not shown).

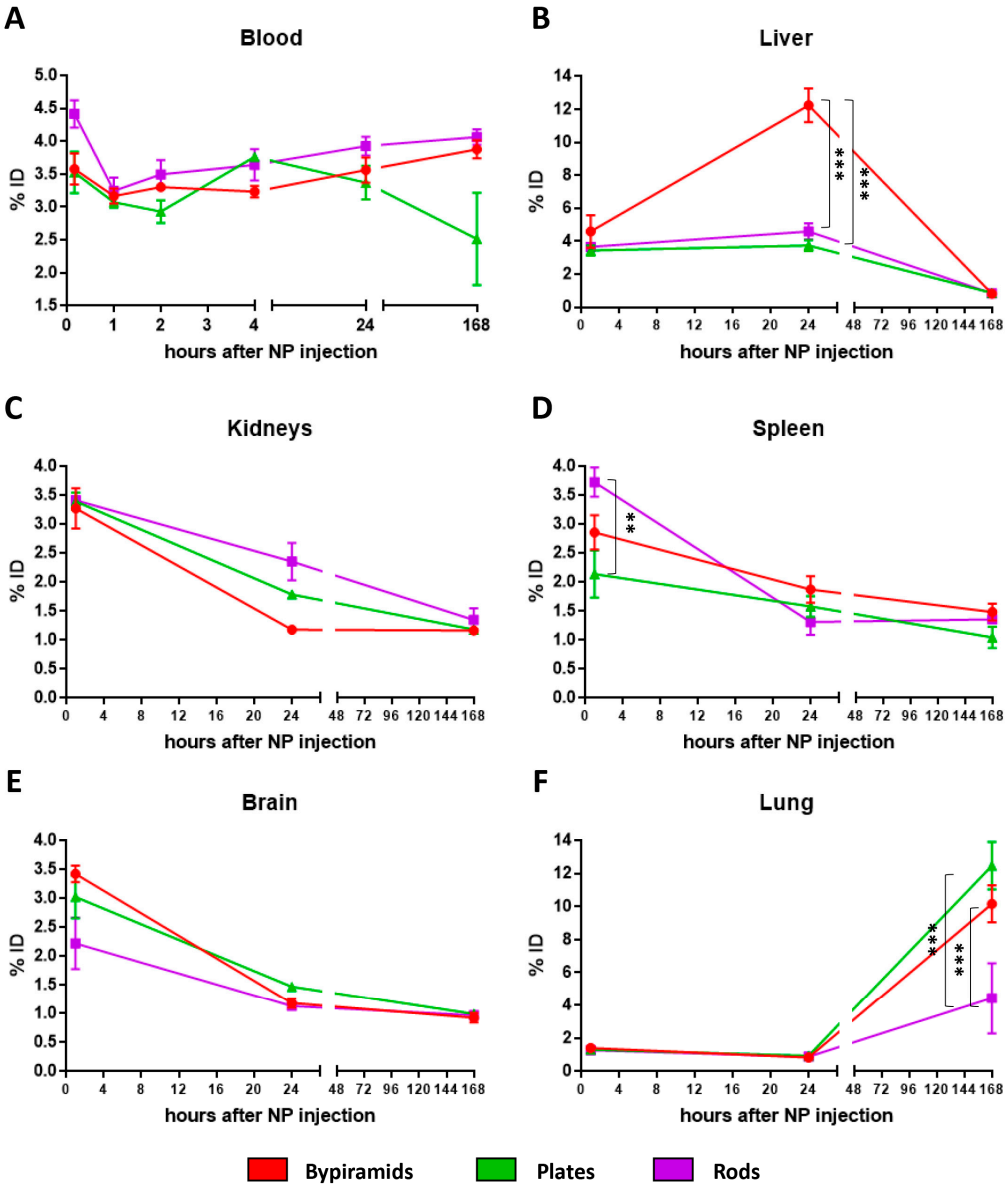

Figure 4. Ti organ content. Percentage of injected dose (%ID) measured by ICP-MS in blood derived from mice treated with different TiO_2 NPs at 10′, 1, 2, 4, 24, and 168 h after treatment (**A**) and in the following collected organs ((**B**–**F**): liver, kidneys spleen, brain, and lung) derived from mice treated with different TiO_2 NPs at 1, 24, and 168 h after treatment. The data are reported as mean ± SEM. A one-way ANOVA followed by a Bonferroni post hoc test was carried out. Significant difference (** $p < 0.01$, *** $p < 0.001$) when comparing the different shapes at the same time point is indicated.

The content of TiO_2 NPs in the whole blood is reported in Figure 4A. Because circulating immunocompetent cells may actively interact with NPs through cellular uptake and their efficiency can be influenced by the NP geometry, we decided to collect whole blood (serum and cellular components) instead of the exclusive evaluation of plasmatic levels. All NP shapes exhibit a short circulation time with a very rapid clearance and a modest uptake from blood components, with a concentration falling to 4%ID. Interestingly, a slight but detectable increase in NP content was observed over time in mice treated with rods and bipyramids, while the animals treated with plates showed a less marked and only transient interaction with blood cells.

Direct injection in the bloodstream leads to a fast and progressive penetration of NPs in different organs. Overall, the highest Ti concentration was found in the liver, followed

by lung, kidney, spleen, and brain. As expected, the liver plays the main role in the capture of NPs after intravenous administration; similarly to a recent study performed by our group [8], a shape-dependent effect was observed when comparing bipyramids to plates and rods (Figure 4B). Whereas at the first hour, no difference was found among the groups, 24 h after administration, animals receiving bipyramids showed a drastic increase in Ti content as compared to the other experimental groups. However, the strong decrease in Ti levels at 168 h after injection suggests that TiO_2 NPs, independently of their geometry, do not lead to long-lasting accumulation in liver parenchyma.

Considering the %ID, the NP kinetic found in the kidney and spleen (Figure 4C,D) is very similar; TiO_2 NPs rapidly reach these organs, but their presence is extremely transient, and independent of their shape, they rapidly disappeared at the latter time-points. It is likely that renal and splenic filtering through resident macrophage uptake does not occur in these experimental conditions.

As expected, the brain showed a drastic reduction in the levels of Ti from 1 to 24 h after administration (Figure 4E). This trend was similar in each shape, and may be determined by the sharp decrease in the NP levels in blood. It is therefore likely that the contribution measured at 1 h was almost exclusively related to the presence of blood in the brain vessels. The lack of NP accumulation in brain is confirmed by their levels measured in animals sacrificed at 24 and 168 h after NP injection.

The process of accumulation of TiO_2 NPs in lungs is very interesting (Figure 4F). Both bipyramid and plate levels strongly increased from the 1st to the 7th day after treatment. This accumulation cannot be attributed to the effect of circulating NPs in the bloodstream. Rods showed a lower amount of Ti accumulation compared to the two other shapes. However, accumulation over the time is also noticeable for this type of NP. The reason for this particular penetration in lung parenchyma cannot be elucidated by our studies. However, it is widely known that the lung is one of the most irrigated organs in the body, and it is therefore possible that the major accumulation of particulate matter happens in this tissue. On the other hand, it is unlikely that an active passage through the pulmonary barrier occurs in this latter phase [23].

In vivo, the majority of the injected dose is cleared from the bloodstream by cells of the mononuclear phagocyte system, a network of immune cells located in organs such as the liver, spleen and bone marrow. Conversely, the accumulation of these TiO_2 NPs in filter organs is manifold lower if compared to many other classes of soft and metallic NPs of similar geometry and size [8,24–26]. Moreover, they do not pass biological barriers such as the blood–brain barrier, but have a great ability to accumulate in the lung parenchyma. The influence of the shape is moderate but not negligible. An interesting aspect to underline is that the ability of a specific type of NP to penetrate and accumulate is greatly influenced by the target organ. However, on the whole, bipyramids demonstrate greater accumulation than plates and rods.

3.3. Influence of the "Shape" on TiO_2 NP Biological Effect

The main components of whole blood are blood cells and plasma. Blood cells include red blood cells, white blood cells (among which lymphocytes, neutrophils, and monocytes) and platelets. In Figure 4A, we reported the accumulation of the three types of TiO_2 NPs with different shape in the blood, while in Figure 5, the impact of this accumulation is evaluated by directly counting the white blood cells from the blood withdrawn 12 h after administration.

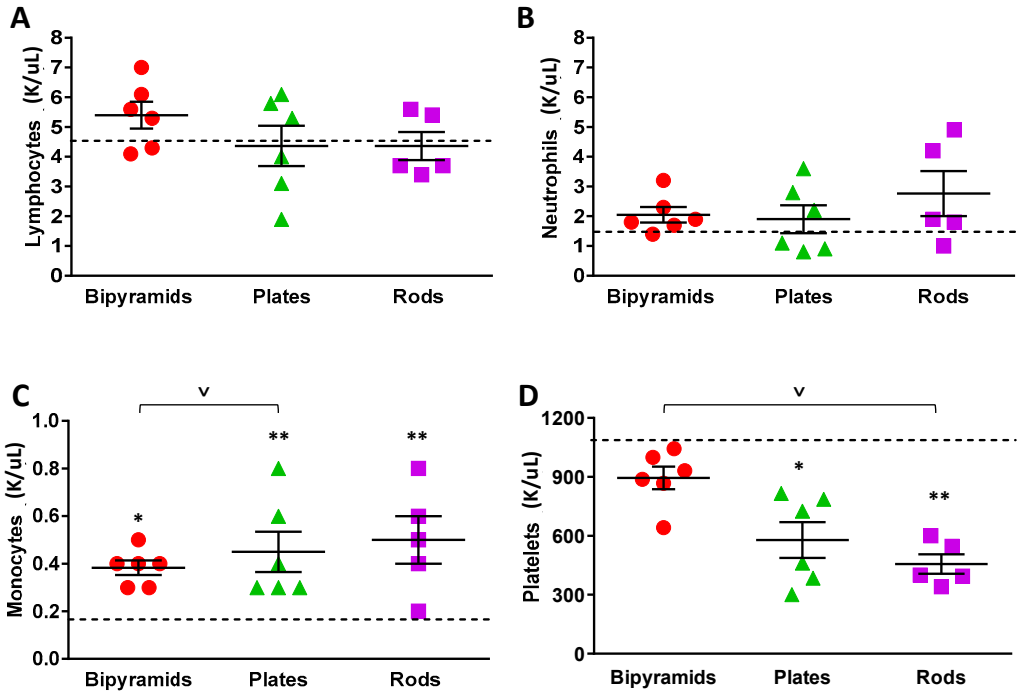

Figure 5. Complete blood cell analysis. Twelve hours after intravenous administration of TiO_2 NP, six mice from each experimental group were phlebotomized, and blood was analyzed for total number of lymphocytes (**A**), neutrophils (**B**), monocytes (**C**), and platelets (**D**). Data are presented as mean ± SEM. A one-way ANOVA followed by Dunn's post hoc test was carried out. This indicated significant difference (* $p < 0.05$, ** $p < 0.005$) between the NP-treated and vehicle-treated mice; (v $p < 0.05$) when comparing the different shapes. The means of each variable measured in control mice are depicted as hatched lines.

Complete blood cell analysis showed that the total number of circulating lymphocytes was not altered by NP injection (Figure 5A); a little and non-significant increase was observed in mice treated with bipyramids, with no specific biological relevance.

A trend of neutrophils increasing was instead observed for all types of NPs compared to vehicle-treated mice (Figure 5B). Although not statistically significant, this seems slightly influenced by the NPs' shape.

In contrast to circulating lymphocytes and neutrophils, a marked increase in monocytes was observed in all three experimental groups treated with TiO_2 NPs compared to vehicle mice (Figure 5C), and this is particularly evident after plate and rod administration. Monocytes are the circulating cells devoted to the removal and the phagocytosis of many exogenous molecules by an active uptake process occurring after the opsonisation of the target. The behavior of rods is somehow correlated with the levels of Ti in blood, wherein a clear increase in Ti content was measured in animals treated with NPs of this shape (Figure 4A). It is therefore possible to hypothesize that a rapid adaptation of the system consisting of an increase of monocytes is needed to remove the NPs from the circulation. The reason why rods lead to a stronger activation is unknown. It is likely that the contact with plasma proteins may somehow modify the interaction between nanomaterials and monocytes. Regarding the relationship between protein corona and NP shape, it is important to mention a previous study carried out by our group, which revealed that silver wires strongly affect alveolar epithelial cells, whereas spherical particles have no effect. This supports the hypothesis that shape is one of the important factors that determine particle toxicity [27].

In contrast to this overall trend of monocytes increasing, a significant decrease in circulating platelets was observed after TiO_2 NP injection in comparison with vehicle-injected mice (Figure 5D). Similar to monocyte measurement, animals treated with rods and

plates showed a marked alteration of platelets. To this end, it is reasonable to speculate that platelets, by recognizing and interacting with NPs with an irregular 3D structure, become activated and degraded in the circulation.

As shown in Figure 4B, the levels of Ti accumulation in the liver of treated mice were transient, with the peak of accumulation at 24 h after the administration of NPs. Importantly, a shape-dependent accumulation was observed, with bipyramids reaching highest levels than plates and rod-shaped NPs. To define if this accumulation was associated with liver toxicity, a time-course was carried out to determine the levels of both alanine aminotransferase (sALT, Figure 6A) and aspartate aminotransferase enzymes (sAST, Figure 6B). These two transaminase levels are commonly measured to make a first diagnostic evaluation of hepatocellular injury. sALT is a more specific indicator of hepatocyte cell death than sAST, which may be released in the circulation by the death of other cell types along with lactate dehydrogenase (LDH, Figure 6C).

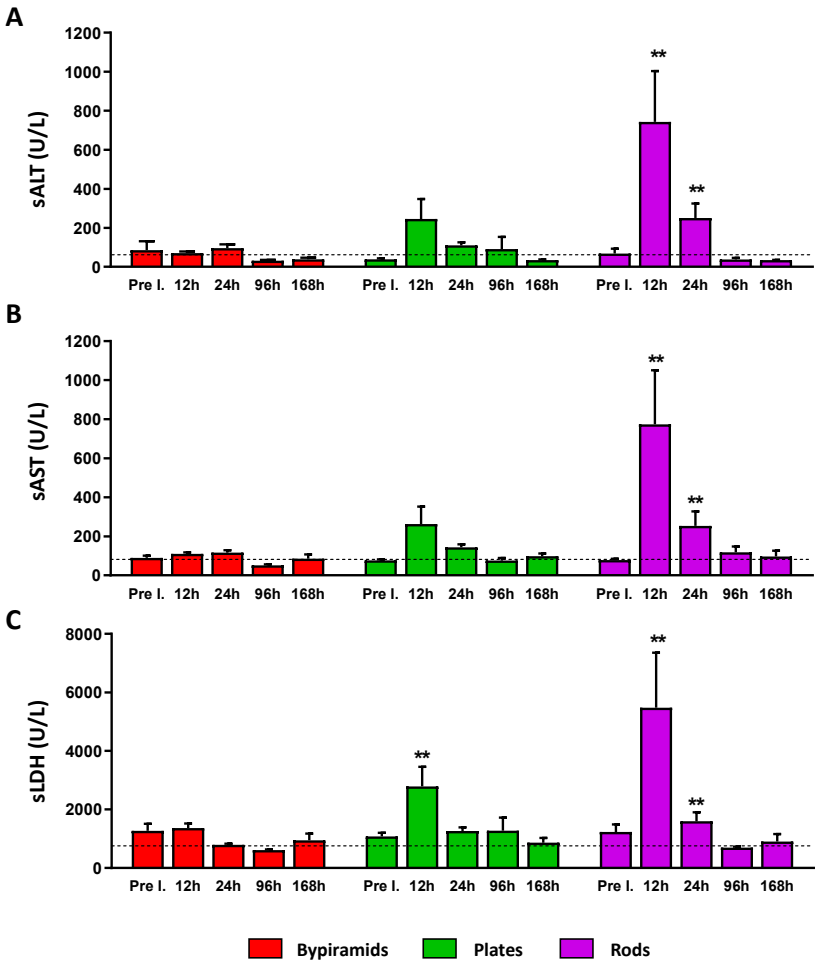

Figure 6. In vivo hepatic toxicity. Activity (Units/Liter [U/L]) of serum ALT (**A**), AST (**B**), and LDH (**C**) measured at the indicated time points in groups of mice injected with bipyramids, plates, and rods. The dashed lines indicate the upper value of normality of each variable (70 U/L for ALT, 83 U/L for AST, and 750 U/L for LDH). Pre I. = Pre injection. The values are expressed as mean ± SEM. An unpaired T-test was carried out; significant difference (** $p < 0.01$) when comparing NP-treated and vehicle-treated mice at the same time point is indicated.

The dashed lines indicate the upper value of normality of each variable. Higher levels of all these markers compared to physiological ones were measured 12 and 24 h following rod injection, while only the LDH value was found to be higher after 12 h following plate treatment. Notably, these levels rapidly returned to normal values in the next time points, indicating that the administration of TiO_2 NPs generates only a transient

injury with the NPs of plate and rod shape. However, this result should be strongly taken into consideration in cases of chronic exposure. Interestingly, no effect was induced by bipyramids for all the hepatic markers at all the time points (red bars).

To determine liver pathology associated with the increase of liver enzymes induced by TiO_2 NPs, groups of mice were killed at 1, 24, and 168 h after NP injection, and their livers were analyzed by histopathological analysis. Since inflammation and activation of tissue macrophages are often tightly related, immunohistochemistry for F4/80 (a well-characterized membrane protein, extensively used as a marker for mature tissue macrophages and Kupffer cells) was carried out in consecutive sections previously stained with hematoxylin and eosin (H&E). As shown in Figure 7, two consecutive representative sections of liver, respectively processed for H&E or F4/80, are reported for each experimental condition and at each time point. Microgranulomas are depicted as red hatched lines, while micronecrotic areas are depicted with yellow-hatched lines.

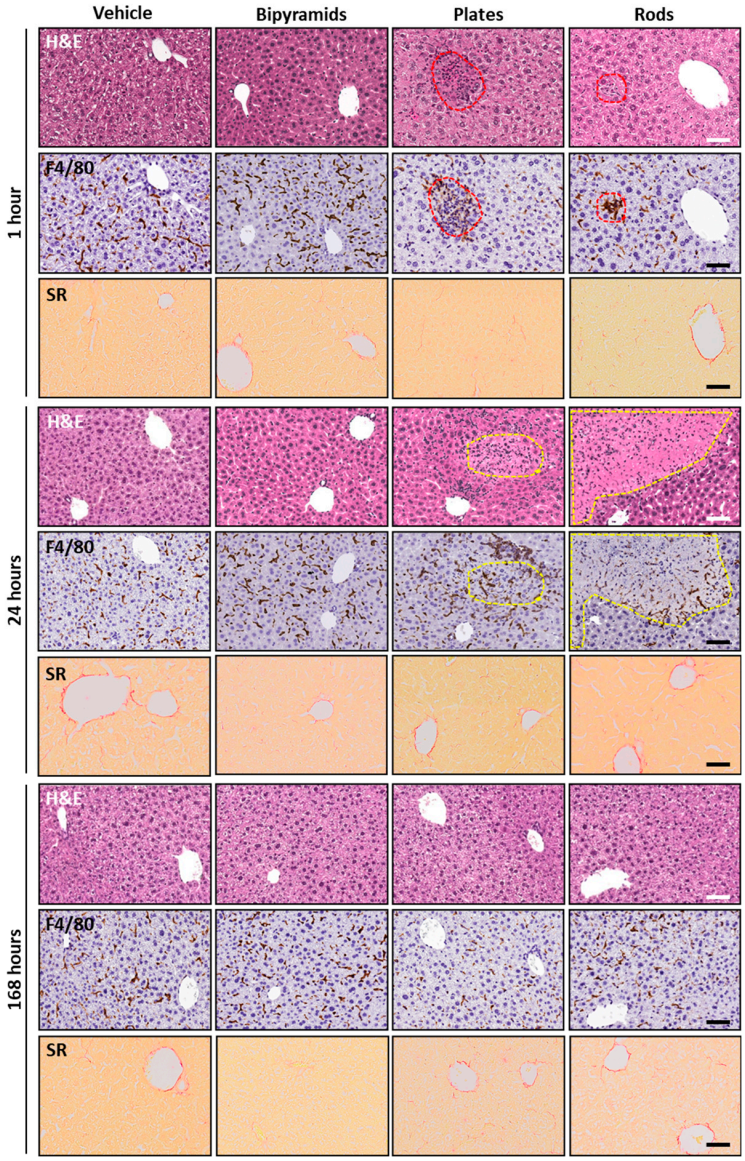

Figure 7. Liver histopathology and immunohistochemistry. Representative micrographs (H&E, upper panels, immunohistochemical staining, F4/80, middle panels and Sirius Red, lower panels) of the liver from mice injected with bipyramids, plates and rods, compared to vehicle-treated mice sacrificed at 1, 24 and 168 h after NP injection. Red hatched lines indicate microaggregation of F4/80 positive macrophages; yellow hatched lines indicate areas of hepatic infarcts. The scale bars represent 100 µm.

As expected, no relevant hallmarks of inflammation, steatosis, and other tissue alterations were observed in pathogen-free immunocompetent mice treated with vehicle. Moreover, no difference between sections from vehicle- and bipyramid-treated mice was detected. Indeed, in accordance with the measurement of blood cells and liver enzymes (Figures 5 and 6), the hepatic parenchyma from mice treated with bipyramids showed neither morphological alterations nor variations in the amount and the localization of macrophages.

Very interestingly, small microgranulomas can be detected since from first hour of treatment with plates; these are characterized by a clustering of macrophages inside the liver parenchyma (red circle) of treated mice. They are associated with a modification of the parenchyma itself, as shown by H&E staining. Histological alteration becomes even more pronounced in mice sacrificed 24 h after the treatment, where hallmarks of necrosis occur (yellow circle) with peripheral aggregates of F4/80 immunopositive cells. In the early phase, microgranulomas (red circle) were also observed in the liver of rod-treated mice. At 24 h after treatment, the relatively big lesions (yellow circle) appear similar to micro-necrotic areas or small infarcts. This implies that rods must have induced a vascular event (i.e., platelets and coagulation cascade activation with the occlusion of relatively large hepatic vessels). For both plates and rods, the perturbation effect was nearly limited to the first days and completely reversed along the first week after the administration of NPs. This transient effect is very interesting, because it seems that NP injection was able to produce an acute response but does not seem to trigger a chronic inflammatory state despite their persistence. Notably, the lack of relevant alterations in mice treated with bipyramids seemed to exclude the relationship between NP penetration and accumulation (higher and sharper, even if transient, compared to the other shapes, Figure 4B) and toxic effects on the liver parenchyma.

In addition, to assess the extent of fibrosis in liver, Sirius Red staining was performed to detect collagen distribution in the samples. No evidence of collagen overexpression was observed in all TiO_2 NP-treated groups compared to vehicle-treated mice. The typical feature characterized by the presence of collagen around liver vessels was detected. On the contrary, interlobular collagen deposition (marker for fibrosis onset) was absent in all experimental groups (Figure 7).

ICP-MS measurements (Figure 4F) clearly demonstrate that there is also difference concerning their long-lasting accumulation in lungs between differently shaped NPs. To verify both if this accumulation can lead to a direct modification of the parenchyma and if there is a correlation between the levels and the toxicity of TiO_2 NPs, histopathological analyses were carried out (Figure 8).

Figure 8A shows representative images of lung parenchyma processed with both H&E, Sirius Red and the F4/80 antibody from mice killed 1, 24, and 168 h after treatment. The graph in Figure 8B reports the measurement of the level of immunoreactivity in mice sacrificed at the last time point. From the first hour after treatment, a marked pulmonary tissue alteration was observed following the treatment with rods, whereas both plates and bipyramids did not seem to produce the same effect. However, all treatments tend to modify the tissue over time; the lower panel describing the last time point clearly reveals a well detectable difference between the parenchyma structure of vehicle-treated and TiO_2 NP-treated mice. This gradual modification may be due the progressive accumulation in this organ. In contrast to what is observed in the liver, interstitial inflammation with recruitment of F4/80 positive cells was weaker, mainly pronounced 168 h after treatment, and mostly enhanced in animals receiving bypiramids and rods. While the lungs from mice treated with bipyramids show a pronounced interstitial immunoreactivity in the alveoli only after 168 h, rod-treated mice showed an earlier alteration that seemed to have a trend of attenuation over time. Similarly to what was found in liver, no features of fibrosis were observed in all experimental groups tested; collagen fibers were substantially associated exclusively with physiological structures (the basement membrane, alveolar wall and alveolar septa).

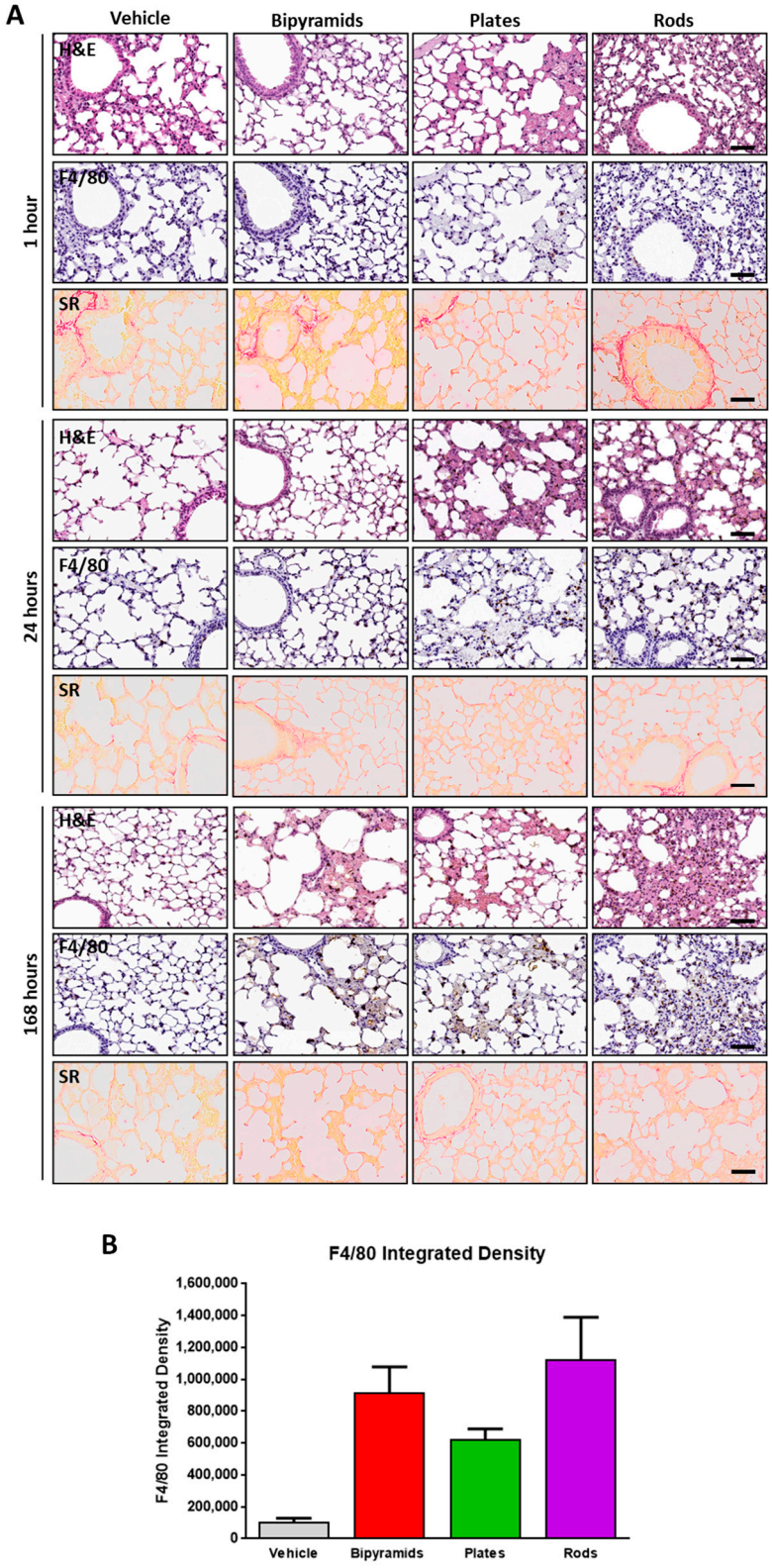

Figure 8. Lung histopathology and immunohistochemistry. (**A**) Representative micrographs (H&E, upper panels), immunohistochemical staining (F4/80, middle panels) and Sirius Red (lower panels) of the lungs of mice injected with bipyramids, plates, and rods, compared to vehicle-treated mice sacrificed at 1, 24, and 168 h after NP injection. The scale bars indicate 50 µm. (**B**) Histogram showing the spread of the pattern of immunoreactivity from sections of mice sacrificed 168 h after NP injection. The values were expressed as mean ± SEM.

4. Discussion

The aim of the study was to evaluate the interaction of different TiO_2 NP shapes and host tissues after systemic injection in healthy, immunocompetent and specific pathogen-free (SPF) mice. To deeply characterize this interaction, we focused our attention on well-defined parameters such as NP kinetics (penetration, accumulation, and clearance) and alterations in specific targets. It is well known that titanium dioxide is used in many products that have a potential impact through different entry routes (skin, airways, gastrointestinal tract) [28]; after absorption by capillaries and vessels, it can diffuse into many organs [29].

It is widely known that most industrial TiO_2 NPs have an extremely heterogeneous nature in terms of geometry. We have recently demonstrated that gold NPs with different shapes had specific distribution, peculiar accumulation, and different kinetics [8]. However, they did not appear to produce toxic effects on the main filter organs (kidney, liver, lung, and spleen) at least up to 5 days after intravenous administration. Based on this study, we resumed the same experimental model and approximately the same range of time points from the treatment to the sacrifice. Our previous study and, more generally, the extensive characterization of the behavior of gold NPs recently published by Tsoi et al. [30], confirmed the strong tropism of hard materials towards the liver and their ability to be internalized in reticulum endothelial system (RES) cells. Quite surprisingly, compared to the gold NPs kinetics, in this work, ICP-MS measurements revealed a low uptake of TiO_2 NPs from livers and a complete disappearance from the 1st to the 7th day after administration. This transient phenomenon seems to exclude an efficient uptake from liver macrophages. The difference in biodistribution could be related to the smaller size of these TiO_2 NPs (around 10 nm) compared to the AuNPs (about 50 nm).

Reduced absorption capacity by liver components could suggest (1) a greater filtering efficiency of the kidneys or spleen, which are the other two main target organs of the largest percentage of intravenously injected nanomaterials [31,32], and/or (2) a very fast clearance and excretion that would support the possibility of a safe exploitation of these materials. The very low splenic and renal levels of Ti do not seem to confirm the first hypothesis, even in spite of the lack of TiO_2 measurements from feces and urine. The whole blood %ID was quite low for each type of NP; however, this was not unexpected, and was similar to that observed in mice treated with gold NPs. Therefore, the long-lasting permanence of the TiO_2 levels in the whole body cannot be justified with the hypothesis that circulating NPs remain in plasma for 7 days. It is therefore possible that they remain somehow entrapped in the endothelium to be then progressively released and captured by the lungs from the 1st to the 7th day. Unexpectedly, an almost shape-independent accumulation (excluding rods) in the lungs was observed after systemic administration. Another possible hypothesis to explain the late accumulation in lungs is the progressive uptake from circulating cells, their activation, and their homing toward pulmonary parenchyma. The efficient penetration of human mesenchymal stem cells loaded with polymeric NPs in the lung has been demonstrated [33,34]. A delayed cell-mediated transport of NPs uptaken from circulating cells is therefore the most likely assumption.

Overall, our data concerning the measurement of NPs in different organs confirm that (1) in this type of administration, the accumulation of TiO_2 NPs is low compared to many other hard materials, and they can be rapidly cleared up by kidneys; (2) the shape seems to affect only partially and transiently the general trend of accumulation. Interestingly, the behavior of rods is similar to that observed after the administration of gold nanorods, and therefore it could be a peculiarity of this shape; (3) tissue macrophages do not seem to play a crucial role in filtering TiO_2 NPs, and; (4) the only process of long-lasting accumulation could be exclusively attributed to the lungs. In several cases of liver and lung injuries, the immunomodulatory response and the alteration of transaminases can lead to necrosis and fibrotic rearrangements of the tissue. Although in our study, the animals receiving TiO_2 NPs showed altered levels of transaminases, some macrophage activation and infiltrates,

the nature of them seems to be transient and at least upon a single treatment does not suggest a relevant tissue damage.

Kinetics and the biodistribution are important parameters to be considered in studies of bio–nano interaction. However, similarly to toxicology and pharmacology, the concentration can be somehow unrelated to their overall effect. For this reason, a deep survey of the effect of TiO_2 treatment in the blood, liver and lungs has been carried out. Since the blood is the first tissue interacting with NPs after intravenous administration, we have evaluated the direct effect on the white blood cell and platelet count 12 h after treatment. Very interestingly, a slight tendency toward an increased number of white cells was found in treated animals, and this was more marked with regard to monocytes. Notably, monocytes are circulating macrophages, and their primary functions are the neutralization and the degradation/clearance of a large plethora of non-self elements. Increasing monocytes after injection is therefore not a surprising situation in SPF immunocompetent mice. This tendency does not appear to be exclusively influenced by NP geometry, even if plates and rods seem to have a similar effect both on the monocytes' increase and in the simultaneous circulating platelets' reduction. A very broad range of stimuli can lead to drastic reduction in platelets. However, this result is extremely interesting in light of the recent overview of the NP effect on platelets' activation and coagulation trigger [35]. More specifically, experiments with both anatase and rutile TiO_2 NPs mainly suggest the aggregation of platelets, whereas our study seems to show an increase in number without particular morphological differences or aggregations. Regarding the physico-chemical parameters that induce such changes, it is important to emphasize that an increase in platelets, particularly after chronic exposure, can have strong health effects in subjects with cardiovascular risk [36].

Alterations in white blood cells and platelets are not the only effect of TiO_2 NP treatment. Despite the low accumulation in the liver parenchyma, early histological changes associated with transient inflammatory reaction and granulomas formation were clearly observed in mice sacrificed 1 and 24 h after NP administration. Although rods seem to produce a greater effect compared to other geometries, no evidence of long-lasting effect was suggested by single administration by any of the shapes. It is possible to argue that the extremely fast effect observable at 1 h after injection is caused by a bystander effect, and it is not associated with NP penetration. To understand whether accumulation and histopathological alterations could affect liver function, we performed kinetics on circulating levels of transaminases in all experimental groups. A transient increase in sALT and sAST levels was almost exclusively observed in mice treated with rods, and to a lesser extent, in those treated with plates.

Another target of these NPs is the lung. It is interesting to see that compared to many other studies, a persistent bioaccumulation in the animals treated with TiO_2 NPs appears to be greater in the lung than in other filter organs. This result is quite surprising but very interesting, and the interaction with the lung is also shown by the relevant histological changes and the activation of the macrophages seen in animals treated with TiO_2 NPs.

We also need to explain the significance and relevance of "shape" in the context of our study. The three types of NPs used here in fact had clearly different shapes. However, apart from shape, the other physicochemical parameters of these three types of NPs were also different, namely the volume per NP and also the surface area per NP. All of these parameters can influence the interaction of the NPs with cells. In fact, results depend on which metrics are used to distinguish between the different types of NPs [37,38]. Unfortunately, it is highly complicated to vary only one parameter, such as shape, while keeping all other parameters such as volume, surface area, etc. constant. Here, large multi-dimensional NP libraries, in which all parameters are varied, may help. However, studies on such libraries show that it is often not possible to relate biological effects to just one single physicochemical property [17]. Thus, "shape" in our study refers to the fact that three types of different NPs were used, all of which had different shapes. Any observed biological effect, however, cannot be directly correlated to shape only, but rather refers to the type of NP.

5. Conclusions

Overall, this study demonstrates that TiO_2 geometry can alter the accumulation and response of the host; however, this effect may have different kinetics, depending on the considered organ. The reversibility of all these the effects can be easily explained by the nature of the treatment (single administration), but their potential risk through chronic exposure cannot be neglected. Although many other experiments should be carried out, selecting specific ways of administering and performing chronic exposure, this analysis could be a step-by-step platform for assessing the guidelines related to the chemical and physical parameters of NPs. The obtained results can be exploited by the industry in order to limit those NPs that are more dangerous to human health.

Author Contributions: Conceptualization, G.S., W.J.P., V.P., M.S. and P.B.; methodology, M.B.V., L.T., N.L.T., Q.Z., A.M. (Atif Masood), B.P., I.C. and D.C.; formal analysis, M.B.V., L.T., A.M. (Annalisa Morelli), N.L.T., Q.Z., A.M. (Atif Masood), B.P., I.C. and D.C.; data curation, M.B.V.; writing—original draft preparation, M.B.V. and L.T.; writing—review and editing, W.J.P., V.P., P.B. and N.G.B.; supervision, W.J.P., V.P., P.B. and N.G.B.; funding acquisition, W.J.P., V.P. and P.B. All authors have read and agreed to the published version of the manuscript.

Funding: This research was funded by National Key Research and Development Program of China (No. 2017FYA0205301), Projects of International Cooperation and Exchanges NSFC (No. 82020108017), National Natural Science Foundation of China (No. 82272821); MCIN/AEI (PID2019-111218RB-I00 and RYC-2017-23457) and Centro Singular De Investigación de Galicia Accreditation 2019−2022, and ED431G 2019/03. Moreover, parts of this work were funded by the Cluster of Excellence 'Advanced Imaging of Matter' of the Deutsche Forschungsgemeinschaft (DFG)-EXC 2056-project ID 390715994; by Deutscher Akademischer Austauschdienst (DAAD); and by an Alexander von Humboldt fellowship. G.S. is supported by the Italian Association for Cancer Research (AIRC), grants 22820 and 22737. NGB and VP receive financial support from the Spanish Ministerio de Ciencia, Innovación y Universidades (MCIU) (RTI2018-099965-B-I00, AEI/FEDER, UE) proyectos de I + D + i de programación conjunta internacional MCIN/AEI (CONCORD, PCI2019-103436), co-funded by the European Union. P.B. is supported by the CONCORD project (EuroNanoMed III).

Data Availability Statement: The datasets presented in this study can be found in online repositories.

Conflicts of Interest: The authors declare no conflict of interest. The funders had no role in the design of the study; in the collection, analyses, or interpretation of data; in the writing of the manuscript; or in the decision to publish the results.

References

1. Pelaz, B.; Alexiou, C.; Alvarez-Puebla, R.A.; Alves, F.; Andrews, A.M.; Ashraf, S.; Balogh, L.P.; Ballerini, L.; Bestetti, A.; Brendel, C.; et al. Diverse Applications of Nanomedicine. *ACS Nano* **2017**, *11*, 2313–2381. [CrossRef] [PubMed]
2. Rivera Gil, P.; Oberdörster, G.; Elder, A.; Puntes, V.; Parak, W.J. Correlating Physico-Chemical with Toxicological Properties of Nanoparticles: The Present and the Future. *ACS Nano* **2010**, *4*, 5527–5531. [CrossRef] [PubMed]
3. Xia, T.; Li, N.; Nel, A.E. Potential Health Impact of Nanoparticles. *Annu. Rev. Public Health* **2009**, *30*, 137–150. [CrossRef]
4. McClements, D.J.; Xiao, H. Is Nano Safe in Foods? Establishing the Factors Impacting the Gastrointestinal Fate and Toxicity of Organic and Inorganic Food-Grade Nanoparticles. *Npj Sci. Food* **2017**, *1*, 6. [CrossRef] [PubMed]
5. Nho, R. Pathological Effects of Nano-Sized Particles on the Respiratory System. *Nanomed. Nanotechnol. Biol. Med.* **2020**, *29*, 102242. [CrossRef] [PubMed]
6. Ajdary, M.; Moosavi, M.; Rahmati, M.; Falahati, M.; Mahboubi, M.; Mandegary, A.; Jangjoo, S.; Mohammadinejad, R.; Varma, R. Health Concerns of Various Nanoparticles: A Review of Their in Vitro and in Vivo Toxicity. *Nanomaterials* **2018**, *8*, 634. [CrossRef]
7. Horvath, P.; Aulner, N.; Bickle, M.; Davies, A.M.; Nery, E.D.; Ebner, D.; Montoya, M.C.; Östling, P.; Pietiäinen, V.; Price, L.S.; et al. Screening out Irrelevant Cell-Based Models of Disease. *Nat. Rev. Drug Discov.* **2016**, *15*, 751–769. [CrossRef]
8. Talamini, L.; Violatto, M.B.; Cai, Q.; Monopoli, M.P.; Kantner, K.; Krpetić, Ž.; Perez-Potti, A.; Cookman, J.; Garry, D.; Silveira, C.P.; et al. Influence of Size and Shape on the Anatomical Distribution of Endotoxin-Free Gold Nanoparticles. *ACS Nano* **2017**, *11*, 5519–5529. [CrossRef]
9. Wang, J.; Bai, R.; Yang, R.; Liu, J.; Tang, J.; Liu, Y.; Li, J.; Chai, Z.; Chen, C. Size- and Surface Chemistry-Dependent Pharmacokinetics and Tumor Accumulation of Engineered Gold Nanoparticles after Intravenous Administration. *Metallomics* **2015**, *7*, 516–524. [CrossRef]
10. Fiordaliso, F.; Foray, C.; Salio, M.; Salmona, M.; Diomede, L. Realistic Evaluation of Titanium Dioxide Nanoparticle Exposure in Chewing Gum. *J. Agric. Food Chem.* **2018**, *66*, 6860–6868. [CrossRef]

11. Tucci, P.; Porta, G.; Agostini, M.; Dinsdale, D.; Iavicoli, I.; Cain, K.; Finazzi-Agró, A.; Melino, G.; Willis, A. Metabolic Effects of TiO2 Nanoparticles, a Common Component of Sunscreens and Cosmetics, on Human Keratinocytes. *Cell Death Dis.* **2013**, *4*, e549. [CrossRef] [PubMed]
12. Rompelberg, C.; Heringa, M.B.; van Donkersgoed, G.; Drijvers, J.; Roos, A.; Westenbrink, S.; Peters, R.; van Bemmel, G.; Brand, W.; Oomen, A.G. Oral Intake of Added Titanium Dioxide and Its Nanofraction from Food Products, Food Supplements and Toothpaste by the Dutch Population. *Nanotoxicology* **2016**, *10*, 1404–1414. [CrossRef] [PubMed]
13. Iannarelli, L.; Giovannozzi, A.M.; Morelli, F.; Viscotti, F.; Bigini, P.; Maurino, V.; Spoto, G.; Martra, G.; Ortel, E.; Hodoroaba, V.-D.; et al. Shape Engineered TiO_2 Nanoparticles in Caenorhabditis Elegans: A Raman Imaging Based Approach to Assist Tissue-Specific Toxicological Studies. *RSC Adv.* **2016**, *6*, 70501–70509. [CrossRef]
14. De Matteis, V. Exposure to Inorganic Nanoparticles: Routes of Entry, Immune Response, Biodistribution and In Vitro/In Vivo Toxicity Evaluation. *Toxics* **2017**, *5*, 29. [CrossRef]
15. Gordon, T.R.; Cargnello, M.; Paik, T.; Mangolini, F.; Weber, R.T.; Fornasiero, P.; Murray, C.B. Nonaqueous Synthesis of TiO_2 Nanocrystals Using TiF_4 to Engineer Morphology, Oxygen Vacancy Concentration, and Photocatalytic Activity. *J. Am. Chem. Soc.* **2012**, *134*, 6751–6761. [CrossRef]
16. Hühn, J.; Carrillo-Carrion, C.; Soliman, M.G.; Pfeiffer, C.; Valdeperez, D.; Masood, A.; Chakraborty, I.; Zhu, L.; Gallego, M.; Yue, Z.; et al. Selected Standard Protocols for the Synthesis, Phase Transfer, and Characterization of Inorganic Colloidal Nanoparticles. *Chem. Mater.* **2017**, *29*, 399–461. [CrossRef]
17. Xu, M.; Soliman, M.G.; Sun, X.; Pelaz, B.; Feliu, N.; Parak, W.J.; Liu, S. How Entanglement of Different Physicochemical Properties Complicates the Prediction of in Vitro and in Vivo Interactions of Gold Nanoparticles. *ACS Nano* **2018**, *12*, 10104–10113. [CrossRef]
18. Lin, C.-A.J.; Sperling, R.A.; Li, J.K.; Yang, T.-Y.; Li, P.-Y.; Zanella, M.; Chang, W.H.; Parak, W.J. Design of an Amphiphilic Polymer for Nanoparticle Coating and Functionalization. *Small* **2008**, *4*, 334–341. [CrossRef]
19. Fernández-Argüelles, M.T.; Yakovlev, A.; Sperling, R.A.; Luccardini, C.; Gaillard, S.; Sanz Medel, A.; Mallet, J.-M.; Brochon, J.-C.; Feltz, A.; Oheim, M.; et al. Synthesis and Characterization of Polymer-Coated Quantum Dots with Integrated Acceptor Dyes as FRET-Based Nanoprobes. *Nano Lett.* **2007**, *7*, 2613–2617. [CrossRef]
20. Kreyling, W.G.; Abdelmonem, A.M.; Ali, Z.; Alves, F.; Geiser, M.; Haberl, N.; Hartmann, R.; Hirn, S.; de Aberasturi, D.J.; Kantner, K.; et al. In Vivo Integrity of Polymer-Coated Gold Nanoparticles. *Nat. Nanotechnol.* **2015**, *10*, 619–623. [CrossRef]
21. Sitia, G.; Fiordaliso, F.; Violatto, M.B.; Alarcon, J.F.; Talamini, L.; Corbelli, A.; Ferreira, L.M.; Tran, N.L.; Chakraborty, I.; Salmona, M.; et al. Food-Grade Titanium Dioxide Induces Toxicity in the Nematode Caenorhabditis Elegans and Acute Hepatic and Pulmonary Responses in Mice. *Nanomaterials* **2022**, *12*, 1669. [CrossRef]
22. Sitia, G.; Iannacone, M.; Aiolfi, R.; Isogawa, M.; van Rooijen, N.; Scozzesi, C.; Bianchi, M.E.; von Andrian, U.H.; Chisari, F.V.; Guidotti, L.G. Kupffer Cells Hasten Resolution of Liver Immunopathology in Mouse Models of Viral Hepatitis. *PLoS Pathog.* **2011**, *7*, e1002061. [CrossRef] [PubMed]
23. Brain, J.D.; Molina, R.M.; DeCamp, M.M.; Warner, A.E. Pulmonary Intravascular Macrophages: Their Contribution to the Mononuclear Phagocyte System in 13 Species. *Am. J. Physiol. Lung Cell. Mol. Physiol.* **1999**, *276*, L146–L154. [CrossRef]
24. Hoshyar, N.; Gray, S.; Han, H.; Bao, G. The Effect of Nanoparticle Size on in Vivo Pharmacokinetics and Cellular Interaction. *Nanomedicine* **2016**, *11*, 673–692. [CrossRef] [PubMed]
25. Black, K.C.L.; Wang, Y.; Luehmann, H.P.; Cai, X.; Xing, W.; Pang, B.; Zhao, Y.; Cutler, C.S.; Wang, L.V.; Liu, Y.; et al. Radioactive ^{198} Au-Doped Nanostructures with Different Shapes for In Vivo Analyses of Their Biodistribution, Tumor Uptake, and Intratumoral Distribution. *ACS Nano* **2014**, *8*, 4385–4394. [CrossRef] [PubMed]
26. Kaga, S.; Truong, N.P.; Esser, L.; Senyschyn, D.; Sanyal, A.; Sanyal, R.; Quinn, J.F.; Davis, T.P.; Kaminskas, L.M.; Whittaker, M.R. Influence of Size and Shape on the Biodistribution of Nanoparticles Prepared by Polymerization-Induced Self-Assembly. *Biomacromolecules* **2017**, *18*, 3963–3970. [CrossRef]
27. Stoehr, L.C.; Gonzalez, E.; Stampfl, A.; Casals, E.; Duschl, A.; Puntes, V.; Oostingh, G.J. Shape Matters: Effects of Silver Nanospheres and Wires on Human Alveolar Epithelial Cells. *Part. Fibre Toxicol.* **2011**, *8*, 36. [CrossRef]
28. Shakeel, M.; Jabeen, F.; Shabbir, S.; Asghar, M.S.; Khan, M.S.; Chaudhry, A.S. Toxicity of Nano-Titanium Dioxide (TiO2-NP) Through Various Routes of Exposure: A Review. *Biol. Trace Elem. Res.* **2016**, *172*, 5. [CrossRef]
29. Iavicoli, I.; Leso, V.; Bergamaschi, A. Toxicological Effects of Titanium Dioxide Nanoparticles: A Review of In Vivo Studies. *J. Nanomater.* **2012**, *2012*, 964381. [CrossRef]
30. Tsoi, K.M.; MacParland, S.A.; Ma, X.-Z.; Spetzler, V.N.; Echeverri, J.; Ouyang, B.; Fadel, S.M.; Sykes, E.A.; Goldaracena, N.; Kaths, J.M.; et al. Mechanism of Hard-Nanomaterial Clearance by the Liver. *Nat. Mater* **2016**, *15*, 1212–1221. [CrossRef]
31. Bertrand, N.; Leroux, J.-C. The Journey of a Drug-Carrier in the Body: An Anatomo-Physiological Perspective. *J. Control. Release* **2012**, *161*, 152–163. [CrossRef] [PubMed]
32. Blanco, E.; Shen, H.; Ferrari, M. Principles of Nanoparticle Design for Overcoming Biological Barriers to Drug Delivery. *Nat. Biotechnol.* **2015**, *33*, 941–951. [CrossRef] [PubMed]
33. Violatto, M.B.; Santangelo, C.; Capelli, C.; Frapolli, R.; Ferrari, R.; Sitia, L.; Tortarolo, M.; Talamini, L.; Previdi, S.; Moscatelli, D.; et al. Longitudinal Tracking of Triple Labeled Umbilical Cord Derived Mesenchymal Stromal Cells in a Mouse Model of Amyotrophic Lateral Sclerosis. *Stem Cell Res.* **2015**, *15*, 243–253. [CrossRef] [PubMed]

34. Nold, P.; Hartmann, R.; Feliu, N.; Kantner, K.; Gamal, M.; Pelaz, B.; Hühn, J.; Sun, X.; Jungebluth, P.; del Pino, P.; et al. Optimizing Conditions for Labeling of Mesenchymal Stromal Cells (MSCs) with Gold Nanoparticles: A Prerequisite for in Vivo Tracking of MSCs. *J. Nanobiotechnol.* **2017**, *15*, 24. [CrossRef] [PubMed]
35. Fröhlich, E. Action of Nanoparticles on Platelet Activation and Plasmatic Coagulation. *CMC* **2016**, *23*, 408–430. [CrossRef]
36. Renga, B.; Scavizzi, F. Platelets and Cardiovascular Risk. *Acta Cardiol.* **2017**, *72*, 2–8. [CrossRef] [PubMed]
37. Parakhonskiy, B.; Zyuzin, M.V.; Yashchenok, A.; Carregal-Romero, S.; Rejman, J.; Möhwald, H.; Parak, W.J.; Skirtach, A.G. The Influence of the Size and Aspect Ratio of Anisotropic, Porous CaCO3 Particles on Their Uptake by Cells. *J. Nanobiotechnol.* **2015**, *13*, 53. [CrossRef]
38. Feliu, N.; Hühn, J.; Zyuzin, M.V.; Ashraf, S.; Valdeperez, D.; Masood, A.; Said, A.H.; Escudero, A.; Pelaz, B.; Gonzalez, E.; et al. Quantitative Uptake of Colloidal Particles by Cell Cultures. *Sci. Total Environ.* **2016**, *568*, 819–828. [CrossRef]

Disclaimer/Publisher's Note: The statements, opinions and data contained in all publications are solely those of the individual author(s) and contributor(s) and not of MDPI and/or the editor(s). MDPI and/or the editor(s) disclaim responsibility for any injury to people or property resulting from any ideas, methods, instructions or products referred to in the content.